

NASA/CR-2015-218769



Acoustically Tailored Composite Rotorcraft Fuselage Panels

*Stephen Hambric, Micah Shepherd, Kevin Koudela, and Denis Wess
Penn State University, State College, Pennsylvania*

*Royce Snider, Carl May, Phil Kendrick, and Edward Lee
Bell Helicopter Textron Inc., Fort Worth, Texas*

*Liang-Wu Cai
Kansas State University, Manhattan, Kansas*

NASA STI Program . . . in Profile

Since its founding, NASA has been dedicated to the advancement of aeronautics and space science. The NASA scientific and technical information (STI) program plays a key part in helping NASA maintain this important role.

The NASA STI program operates under the auspices of the Agency Chief Information Officer. It collects, organizes, provides for archiving, and disseminates NASA's STI. The NASA STI program provides access to the NTRS Registered and its public interface, the NASA Technical Reports Server, thus providing one of the largest collections of aeronautical and space science STI in the world. Results are published in both non-NASA channels and by NASA in the NASA STI Report Series, which includes the following report types:

- **TECHNICAL PUBLICATION.** Reports of completed research or a major significant phase of research that present the results of NASA Programs and include extensive data or theoretical analysis. Includes compilations of significant scientific and technical data and information deemed to be of continuing reference value. NASA counter-part of peer-reviewed formal professional papers but has less stringent limitations on manuscript length and extent of graphic presentations.
- **TECHNICAL MEMORANDUM.** Scientific and technical findings that are preliminary or of specialized interest, e.g., quick release reports, working papers, and bibliographies that contain minimal annotation. Does not contain extensive analysis.
- **CONTRACTOR REPORT.** Scientific and technical findings by NASA-sponsored contractors and grantees.

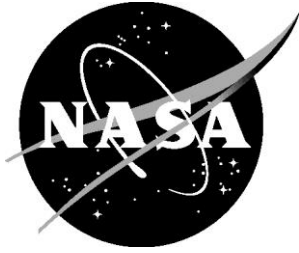
- **CONFERENCE PUBLICATION.** Collected papers from scientific and technical conferences, symposia, seminars, or other meetings sponsored or co-sponsored by NASA.
- **SPECIAL PUBLICATION.** Scientific, technical, or historical information from NASA programs, projects, and missions, often concerned with subjects having substantial public interest.
- **TECHNICAL TRANSLATION.** English-language translations of foreign scientific and technical material pertinent to NASA's mission.

Specialized services also include organizing and publishing research results, distributing specialized research announcements and feeds, providing information desk and personal search support, and enabling data exchange services.

For more information about the NASA STI program, see the following:

- Access the NASA STI program home page at <http://www.sti.nasa.gov>
- E-mail your question to help@sti.nasa.gov
- Phone the NASA STI Information Desk at 757-864-9658
- Write to:
NASA STI Information Desk
Mail Stop 148
NASA Langley Research Center
Hampton, VA 23681-2199

NASA/CR–2015-218769



Acoustically Tailored Composite Rotorcraft Fuselage Panels

*Stephen Hambric, Micah Shepherd, Kevin Koudela, and Dennis Wess
Penn State University, State College, Pennsylvania*

*Royce Snider, Carl May, Phil Kendrick, and Edward Lee
Bell Helicopter Textron Inc., Fort Worth, Texas*

*Liang-Wu Cai
Kansas State Univeristy, Manhattan, Kansas*

National Aeronautics and
Space Administration

Langley Research Center
Hampton, Virginia 23681-2199

Prepared for Langley Research Center
under Contract NNL11AA02C

July 2015

The use of trademarks or names of manufacturers in this report is for accurate reporting and does not constitute an official endorsement, either expressed or implied, of such products or manufacturers by the National Aeronautics and Space Administration.

Available from:

NASA STI Program / Mail Stop 148
NASA Langley Research Center
Hampton, VA 23681-2199
Fax: 757-864-6500

Contents

Abstract.....	1
1 Introduction	2
2 Baseline Composite Panel.....	4
2.1 Design and Construction.....	4
2.2 Structural Material Properties	11
2.3 Structural Modeling (Finite Elements).....	13
2.3.1 Bell Structural FE model.....	13
2.3.2 Penn State Structural-Acoustic Model.....	15
2.4 Acoustic Modeling (Boundary Elements).....	16
2.5 Measurements	16
2.6 Vibro-acoustic behavior	16
2.6.1 Effective Flexural Wavespeeds	16
2.6.2 Resonances	18
2.6.3 Damping Loss Factors	23
2.6.4 Forced Response Simulations and Measurements.....	25
3 Panel Optimized for Reduced Noise	32
3.1 Design Optimization Goals.....	32
3.2 Quieting Technologies	32
3.2.1 Traditional Treatments Attached to Panel.....	33
3.2.2 Reduced Stiffness Core Materials	33
3.2.3 Embedded Viscoelastic Treatments.....	34
3.2.4 Band-Gap/Phononic Crystal Structure-borne Sound Barriers	43
3.2.5 Split Panel Concept for Airborne Sound Transmission Reduction.....	69
3.3 Final Optimized Panel Design.....	72
3.3.1 Structural Modeling	73

3.3.2	Structural Integrity Calculations	77
4	Optimized Panel Performance	87
4.1	Measured Modes, Loss Factors, and Mobilities	87
4.2	Radiated Sound Power	91
4.3	Analytic Diffuse Field Panel TL Modeling	95
5	Summary and Conclusions	99
6	References	101
Appendix A – Baseline and Optimized Panel Testing		103
A.1	Modal Analysis	103
A.2	Transmission Loss Testing	104
A.3	Shaker Testing	105
Appendix B – Virtual Transmission Loss for an Aluminum Panel		107
Appendix C – Determination of Panel Wavespeed and Young’s Modulus		111
C.1	Theory	111
C.2	Implementation using measured mode shapes	112
Appendix D: Evaluation of Diffusivity and Angular Weighting Factors using Intensity Measurements ..		115
D.1	Introduction	115
D.2	Intensity Measurements	115
D.3	Limitations of intensity measurements	117
D.4	Intensity Results – Panel Installed	118
D.5	Intensity Results – Open Aperture	125
D.6	Future work	127
Appendix E – Formulation for Multiple Scattering of Flexural Waves in a Thin Plate		129

Abstract

A rotorcraft roof sandwich panel has been redesigned to optimize sound power transmission loss (TL) and minimize structure-borne sound for frequencies between 1 and 4 kHz where gear meshing noise from the transmission has the most impact on speech intelligibility. The roof section, framed by a grid of ribs, was originally constructed of a single honeycomb core/composite facesheet panel. The original panel has coincidence frequencies near 700 Hz, leading to poor TL across the frequency range of 1 to 4 kHz. To quiet the panel, the cross section was split into two thinner sandwich subpanels separated by an air gap. The air gap was sized to target the fundamental mass-spring-mass resonance of the double panel system to less than 500 Hz. The panels were designed to withstand structural loading from normal rotorcraft operation, as well as 'man-on-the-roof' static loads experienced during maintenance operations. Thin layers of VHB 9469 viscoelastomer from 3M were also included in the facesheet ply layups, increasing panel damping loss factors from about 0.01 to 0.05. Measurements in the NASA SALT facility show the optimized panel provides 6-11 dB of acoustic transmission loss improvement, and 6-15 dB of structure-borne sound reduction at critical rotorcraft transmission tonal frequencies. Analytic panel TL theory simulates the measured performance quite well. Detailed finite element/boundary element modeling of the baseline panel simulates TL slightly more accurately, and also simulates structure-borne sound well.

1 Introduction

Commercial rotorcraft are powered by drive systems comprised of complex transmissions, which contain sets of gears and shafts supported by bearings. As the gears rotate at high rates of speed, they induce vibration and noise in the transmission and throughout the rotorcraft. An example of a rotorcraft transmission region and roof section is shown in Figure 1.

The goal of this work was to develop and evaluate acoustically tailored composite rotorcraft panels to reduce noise transmitted into the passenger cabin of a rotorcraft. The focus is on the structural roof panels, which are mechanically connected to the transmission, allowing strong gear meshing tones emanating from the transmission to pass into the panels and radiate into the cabin. Sound radiated by the transmission housing also impacts the ceiling panels acoustically, which transmit a portion of that sound into the interior.

Composite materials are sometimes used to construct lightweight stiff panels for rotorcraft, which reduce weight, but also lead to increased sound radiation into the rotorcraft due to their reduced impedances and increased sound radiation efficiencies. Trim panels constructed of layers of foams and thin plates are often attached to the panels to reduce sound transmission, but are expensive, bulky, and heavy. The scope of this work is to design composite fuselage panels which do not require trim panels, and actually reduce, rather than increase, the noise from transmission tones.



Figure 1. View of the inside of the transmission region in a commercial rotorcraft.

A sample of in-flight test data which illustrates key frequencies of interest for noise reduction is shown in Figure 2. While several tones are present, two frequencies were identified based on sound quality assessments as most critical in this example – those of the main rotor bull gear mesh (at around 1060 Hz) and the input pinion gear mesh (at around 3100 Hz). Modeling and measurements of the baseline and optimized panels will therefore focus on frequencies between 1 and 4 kHz.

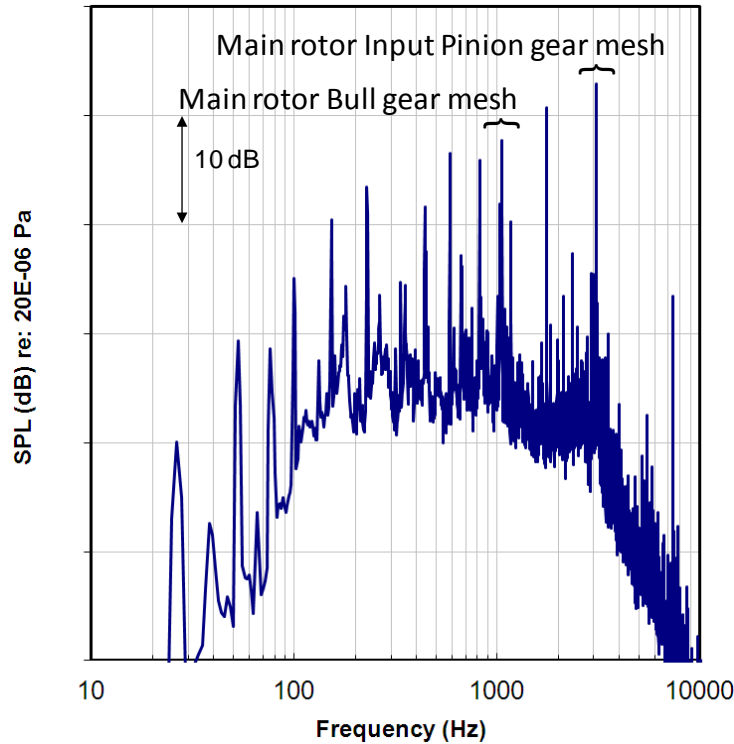


Figure 2. Sample of in-flight sound pressure data for a commercial rotorcraft.

In this work, we have developed and demonstrated technologies and methodologies for designing composite fuselage panels which radiate less sound into the rotorcraft interior. We constructed and tested two 4-ft by 4-ft roof panels— one using current composite manufacturing approaches, and a second panel based on the optimized acoustic technologies applied under this project. The program has achieved the following specific overall objectives:

- 1.** A baseline, 4-ft by 4-ft, flat, composite, beam-stiffened panel representative of the roof panel in a commercial helicopter was designed. The baseline panel meets the same requirements, including weight and structural integrity, as the roof panels in commercial helicopters.
- 2.** The baseline composite panel was fabricated using standard manufacturing techniques used at Bell Helicopter.
- 3.** Methods for designing composite panels were developed that reduce the vibrational energy propagating into and through the panels while improving the sound radiation characteristics.
- 4.** An optimized composite roof panel was designed and fabricated to minimize vibration transmissibility and sound radiation over frequencies spanning the dominant gear meshing tones of a typical rotorcraft (1-4 kHz). Practical constraints (weight and structural integrity) were included in the optimization.

This work provides NASA and the rotorcraft community with design methods that can be used to acoustically tailor composite panels for rotorcraft. This work also provides NASA with representative composite panels that can be used to evaluate future treatment concepts.

2 Baseline Composite Panel

2.1 Design and Construction

A baseline composite panel with geometry and properties representative of those of a Bell Helicopter 429 roof structure has been designed and constructed. A cross-section within the desired region of the 429 roof assembly was selected as the basis for the panel design, as shown in Figure 3. Equivalent composite materials were chosen to replace the existing metallic materials for the upper and lower skins, edge band laminate, and core. Thicknesses and surface densities of the materials in the center sandwich panel are listed in Table 1, and equivalent structural material properties are discussed in Section 2.3. Note that Table 1 includes a layer of viscoelastomer attached to the inner surface which is typical of that bonded to many Bell roof panels to mitigate noise transmission.

The upper and lower skins of the center sandwich panel are made of plies of Cytec G30-500/5276-1 Carbon/Epoxy Fabric. A layup of plies was used which provides the best equivalent stiffness, as measured by the product of Young's Modulus and Moment of Inertia, to that of the 429 core-stiffened metallic panel. The core thickness is the same as that of the production panel, so that equivalent stiffness is controlled by the panel face sheet properties. Face sheet stiffness is defined using:

$$E_M A_M = E_C A_C \quad \text{and} \quad G_M A_M = G_C A_C ,$$

where E is the extensional modulus (nominally 8.2 Msi for the Cytec fabric), G is the shear modulus (nominally 400 ksi), A is the area, M indicates metallic properties and C indicates composite properties. Since the area is the product of width and thickness (t), and the panel maintains the same width, these equations may be rewritten as:

$$E_M t_M = E_C t_C \quad \text{and} \quad G_M t_M = G_C t_C .$$

Several composite laminates were evaluated to find the layup with the best match to that of the production panel. A three ply layup with orientation angles (in degrees) of [0/45/0] was eventually chosen to provide the best combination of extensional and shear stiffness in comparison to the metallic panel.

A similar analysis was performed for the edge band laminate, except that instead of shear or extensional stiffness, equivalent bending stiffness is the critical parameter. The equation for determining equivalent bending is:

$$E_M t_M^3 = E_C t_C^3 .$$

The layup that best satisfies this constraint is [0/45/45/0/0]_s, where 'S' indicates symmetry about the center ply for the remaining angles. The edge, therefore, is constructed of 10 total layers of Cytec.

The last component in the composite baseline panel design is an equivalent composite core material. It is not practical to achieve a stiffness comparable to that of an Aluminum core with a composite core, so the next critical driver for design is strength. Hexcel Kevlar core with a density of 47 kg/m³ (2.9 lb/ft³)

and a mean Shear modulus of 96.5 MPa (14 ksi) was found to have the best equivalent strength to that of the metallic core.

Design loads for the core stiffened panel area are critical for the upper skin in compression. Upper skin applied ultimate loads are set to 150% of the flight limit loads, and include components in both in-plane directions, and in-plane shear. Design loads for the edge laminates are also based on flight load limits, and include in-plane forces as well as a moment applied about the fore-aft direction. A margin of safety greater than 1 is required for both core and edge fabric laminates based on an elevated temperature wet open hole compression allowable. Other design constraints are (a) local skin wrinkling stability, (b) core crush in the ramp area, and (c) core shear due to a man-load on the roof panel. The baseline panel meets all of these requirements.

Standard size aluminum I-beams were chosen with cross-sectional properties that best matched the properties of the variable cross-section production roof beams and transverse intercostal beams. In the baseline panel, the roof beams are 1016 mm (40 inches) long, and the intercostal beams are 762 mm (30 inches) long. The flange widths of the roof and intercostal beams are 76.2 mm (3 inches) and 50.8 mm (2 inches) respectively. Both beams are 102 mm (4 inches) high, with 3.96 mm (0.156 inch) flange and web thicknesses. The roof beams and transverse intercostal beam webs are connected by aluminum shear clips, and the top flanges are connected by four aluminum splice straps that provide an economical representation of the joints at the transmission mounting points. The beams, shear straps and splices are shown in Figure 4. The panel design is detailed in Figure 5 and Figure 6. The roof beams are connected to the panel with 5/16" diameter titanium protruding shear head pins and titanium collars spaced at a nominal 6.5 Diameter pitch. These fasteners and spacing are representative of the majority of the Bell model 429 roof beam to panel fasteners.

Figure 7 shows the composite portion of the baseline panel construction, and Figure 8 shows the fully assembled panel. The total panel mass is 15.8 kg (34.7 lb), with 5.64 kg (12.4 lb) in the composite, 10.1 kg (22.3 lb) in the beams, and 0.60 kg (1.33 lb) in the fasteners and shear straps. The completed panel is coated with an Epoxy VOC Compliant Primer (MIL-P-85582, TY I) Light Green (water-base).

Table 1. Cross-sectional materials, thicknesses, and surface densities for center region of baseline panel.

Material	Thickness (in)	Thickness (cm)	Surface density (lb/in ²)	Surface density (kg/m ²)
Paint			0.00006	0.042
Face sheet	0.0079	0.0201	0.000443	0.311
Face sheet	0.0079	0.0201	0.000443	0.311
Face sheet	0.0079	0.0201	0.000443	0.311
Adhesive		0.0000	0.00035	0.245
Honeycomb	0.500	1.2700	0.00048	0.671
Adhesive		0.0000	0.00035	0.245
Face sheet	0.0079	0.0201	0.000443	0.311
Face sheet	0.0079	0.0201	0.000443	0.311
Face sheet	0.0079	0.0201	0.000443	0.311
Paint			0.00006	0.042
Visco	0.04	0.1016	0.00222	1.56
Total	0.587	1.49	0.00618	4.67

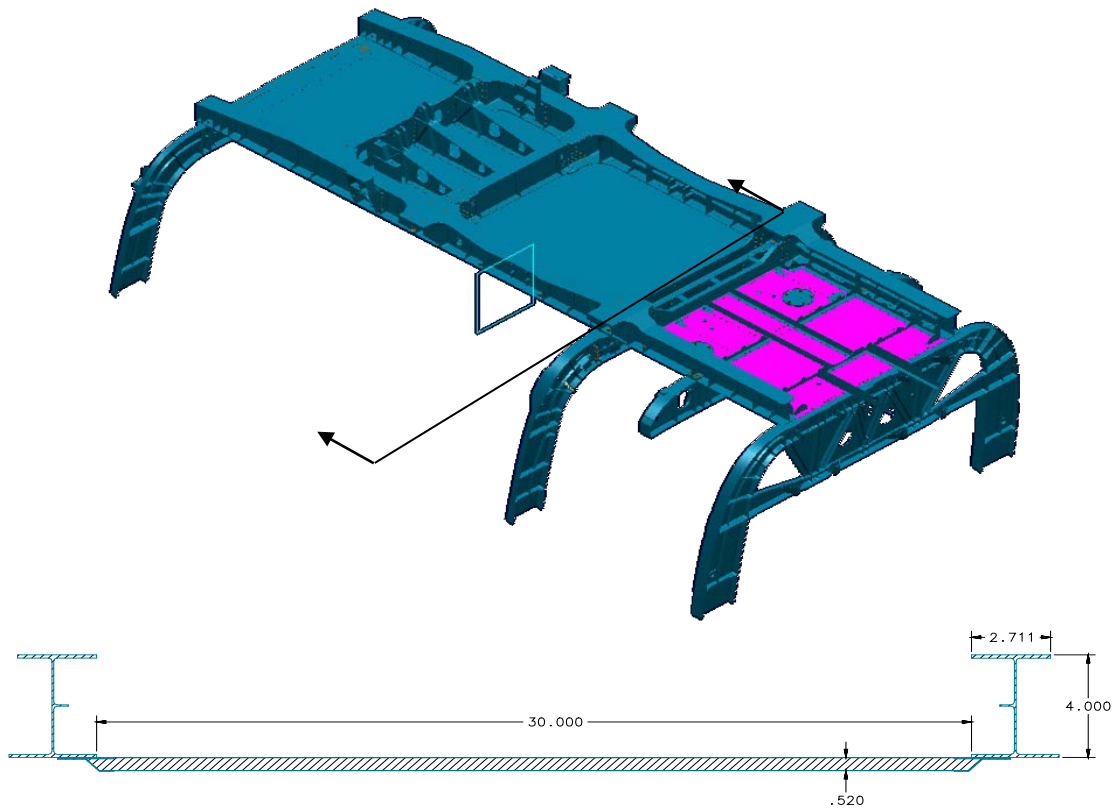


Figure 3. Cross-section of Bell 429 Roof Assembly, dimensions in inches.

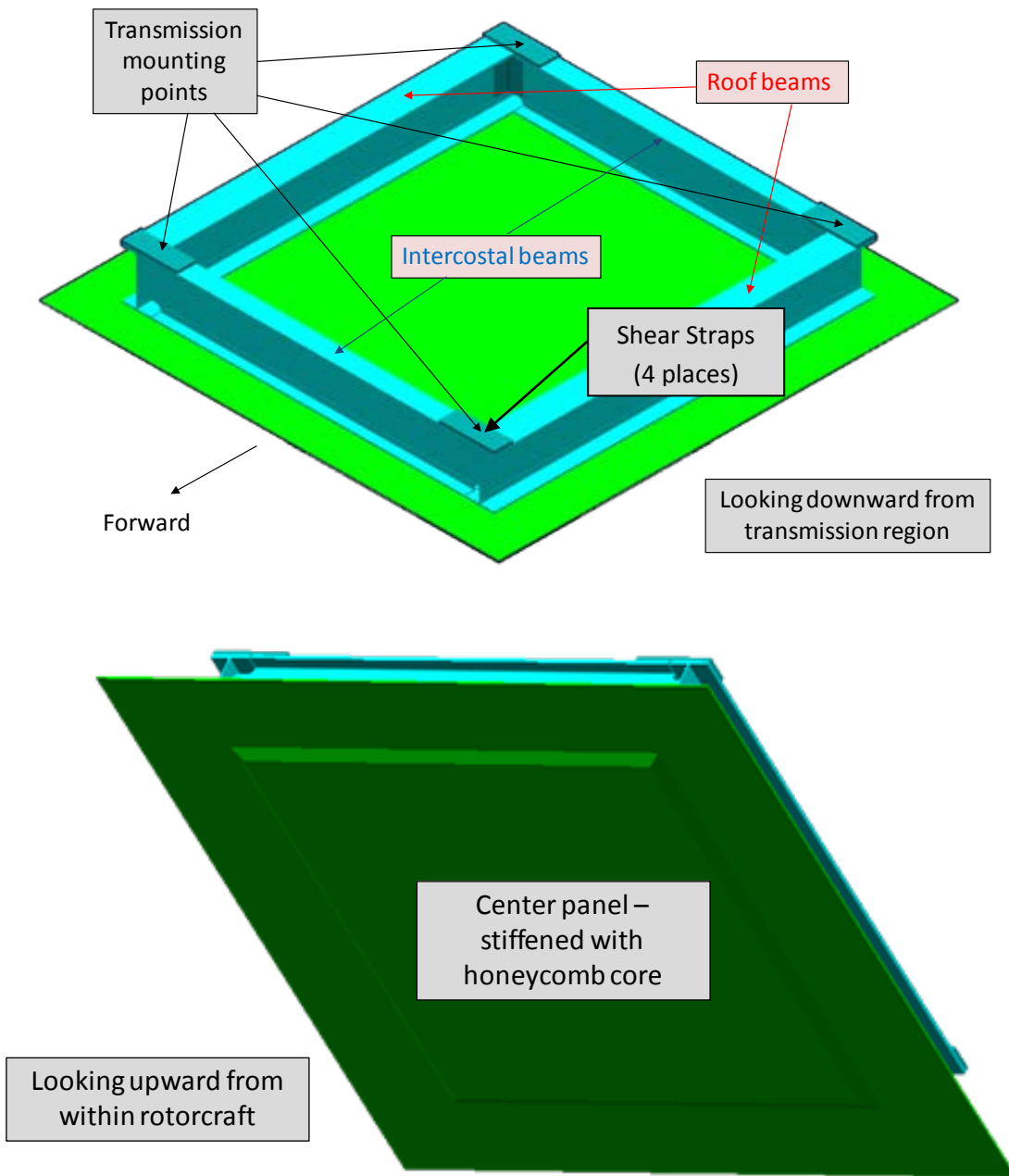


Figure 4. Baseline panel viewed from above (top) and below (bottom).

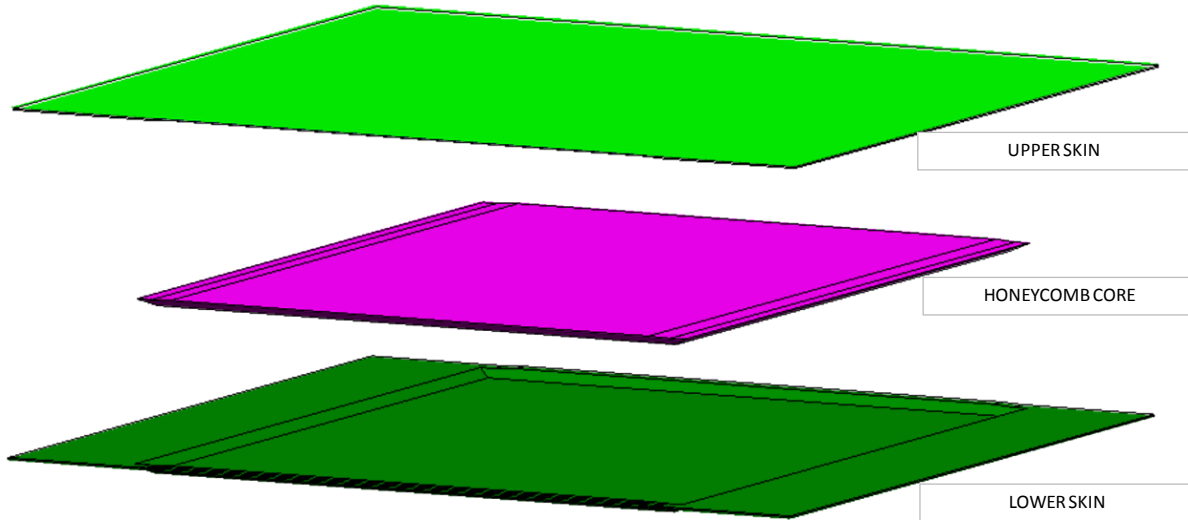


Figure 5. Stackup of skins and honeycomb core.

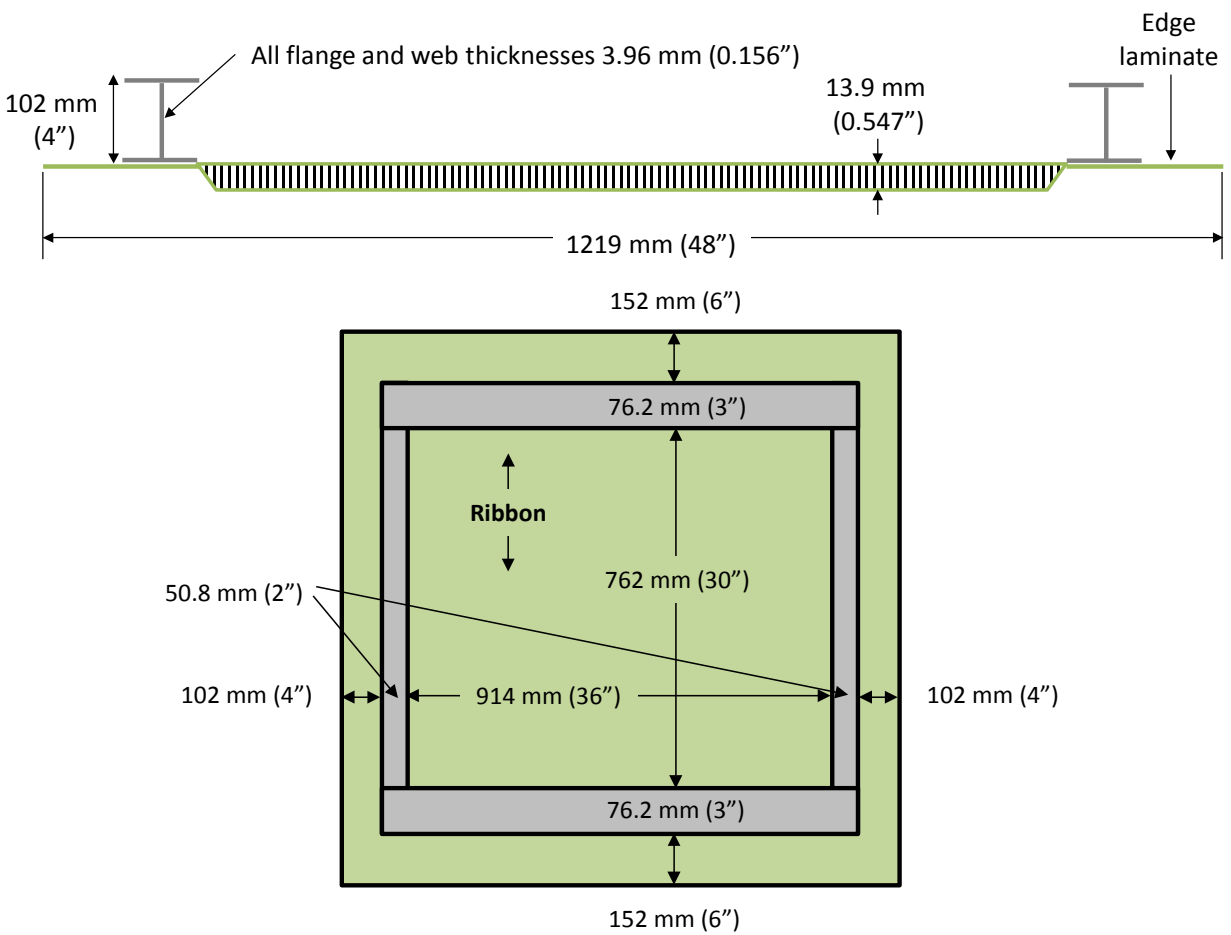


Figure 6. Baseline panel geometry (not to scale).

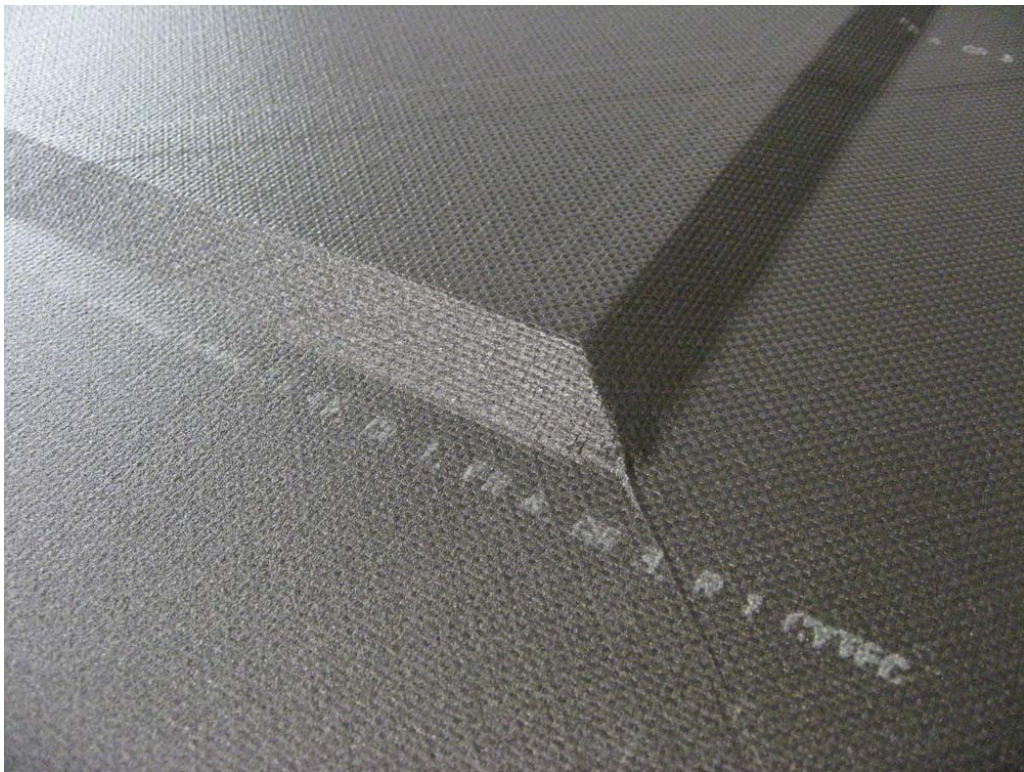


Figure 7. Composite portion of baseline panel.

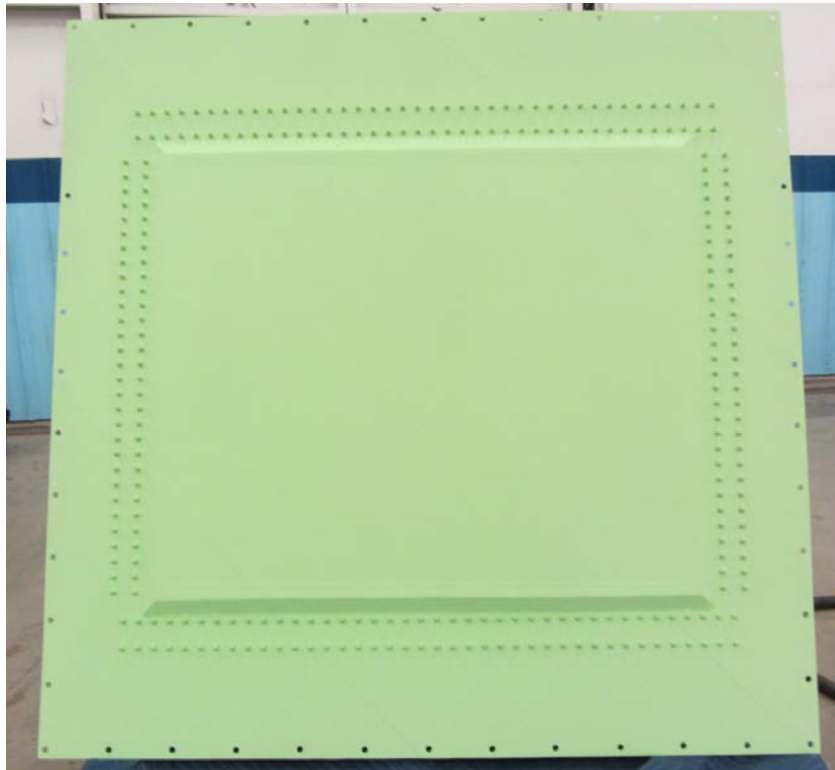


Figure 8. Fully assembled baseline panel viewed from above (top) and below (bottom).

2.2 Structural Material Properties

A finite element (FE) model was constructed of the baseline panel to analyze its sound transmission characteristics. An original FE model had several errors, including inaccurate and incomplete material properties, incorrect orientation of the core ribbon and warp directions, and incorrect beam thicknesses. The errors led to the FE model overestimating resonance frequencies by 20-30%. To better determine the actual structural material properties, two 4" x 8" coupon panels cut from a 12" x 12" newly constructed panel intended to be identical to that of the baseline panel were tested statically to compare static stiffnesses, as well as dynamically to compare measured and simulated resonance frequencies of the fundamental panel modes. The panels were cut so that the length of one was aligned along the ribbon direction of the core, and the length of the other aligned with the warp direction.

Since the test panels are quite small and extremely light, traditional modal testing with attached accelerometers was impractical, since the mass loading from the accelerometers would have been significant. Instead, the panels were suspended from wire adjacent to a loudspeaker, which ensonified the surfaces with airborne white noise. A Laser Doppler vibrometer (LDV) measured the resulting panel surface vibration, shown in Figure 9. Four modes of vibration are visible for each panel – two near 2 kHz, and two near 3.5 kHz.

FE models of the test coupons were generated, and the modal frequencies were compared to those extracted from the measurements. The model was initially corrected to include the mass density of the layers of adhesive (Cytec FM 300K film adhesive, .05 lb/ft², estimated to be nominally .008 inches thick, http://www.cemselectorguide.com/pdf/FM_300_081211.pdf), as well as the paint. The stiffnesses of the paint and adhesive are ignored. The adhesive is assumed to rigidly connect the face sheets and core. Adjusting the surface mass density led to improved agreement between measured and simulated resonance frequencies, but the FE model was still about 10-15% too stiff. This meant that either or both of the face sheet and core stiffnesses provided by the material suppliers were incorrect.

Bell conducted static measurements of the core and face sheet materials, and updated the material properties. Notable changes include:

- a heavier core, with a 10% increase in density;
- a softer core, with about a 20-30% decrease in stiffness; and
- softer face sheets, with about a 10% reduction in stiffness. Also, Bell discovered that the laminate stiffness differs slightly (about 6%) for the 'tool' and 'bag' sides.

The updated material properties greatly improves the agreement between the measured and simulated test coupon modes (within +/-5%). The final structural material properties for the laminates and core are listed in Table 2. The compression and tension moduli, as well as the tool and bag side moduli, were averaged to compute the values used in structural FE dynamic analyses. The variation in the tool/bag/compression/tension moduli is small – about 4%. Also, the in-plane Poisson's ratio for the face sheet is a smeared estimate based on the stack of three plies. A key lesson learned from this experience is that FE modeling and test coupons are invaluable for insuring material properties are properly characterized.

Table 2. Final laminate and core material properties used for analysis. Directions 1 and 2 are in-plane, and 3 is through the thickness. Note the face sheet Poisson’s ratio is smeared over the full set of three plies. The edge material has material properties identical to those of the face sheets.

Table 2a – Selected center panel material properties

Property	Face Sheets	Kevlar Core
E_{11}, E_{22} (GPa/Msi)	57 / 8.3	-
ν_{12}	0.21	-
G_{13} (MPa/ksi)	-	139 / 20.1 (ribbon)
G_{23} (MPa/ksi)	-	68 / 9.8 (warp)
ρ (kg/m ³ / lb/in ³)	1550 / 0.0560	47 / 0.0017

Table 2b – Edge panel properties

Property	Value
E_{11}, E_{22} (GPa/Msi)	54 / 7.8
ν_{12}	0.21
ρ (kg/m ³ / lb/in ³)	1550 / 0.0560
t (mm / in)	2.0 / .079

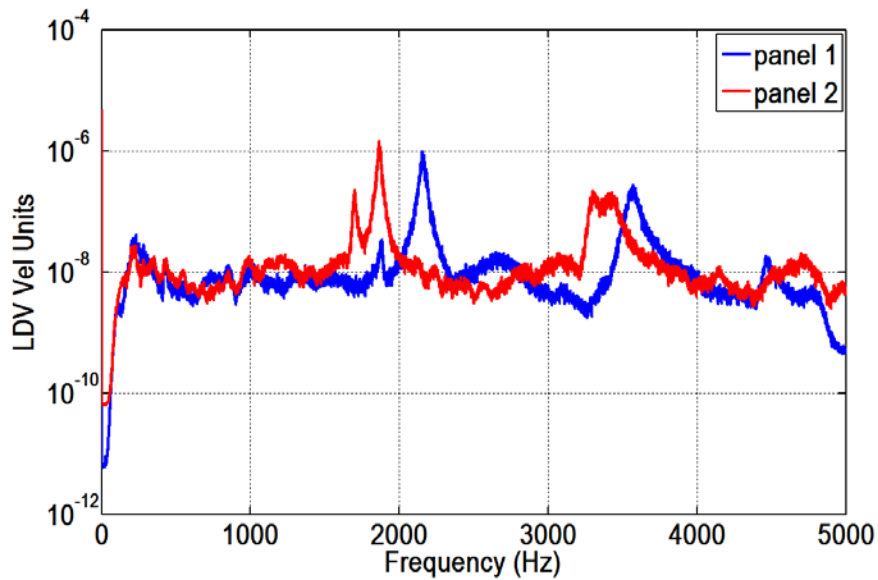


Figure 9. Vibration of test coupons ensouified with acoustic field. The length of panel 1 is aligned with the ribbon direction of the core, and the length of panel 2 aligned with the warp direction of the core. The LDV normal velocity units are uncalibrated.

2.3 Structural Modeling (Finite Elements)

2.3.1 Bell Structural FE model

A structural FE model of the baseline panel was constructed at Bell, as shown in Figure 10. All components are modeled with quadratic solid elements, with a 0.5" spacing along the width and length. The upper and lower skin plies were each discretely modeled with a single element through the thickness. The core was modeled with one element through the thickness. The edge band laminate was modeled with six elements through the thickness. A cross-section of the panel is shown in Figure 11. The I-beams were modeled with a single element through the thickness, and are connected to the panel in the locations of the fasteners using CBUSH (spring) elements to represent the bolts. The stiffnesses of the spring elements are based on the bolt material and cross-section. The beam cross-section and CBUSH elements (shown as red circles) can be seen in Figure 12.

Initially, the model was created with elements with an aspect ratio which conforms to Bell standard practices. However, this led to an unacceptably large number of degrees of freedom, so the model was then remeshed with a 20:1 aspect ratio through the thickness (the element edge length along the width and length of the panel is 20 times that of the element thickness). The transition area from the upper and lower skins to the edge band region was simulated by discretely modeling all plies in the edge band and then tapering the plies to the upper and lower skins as shown in Figure 13.

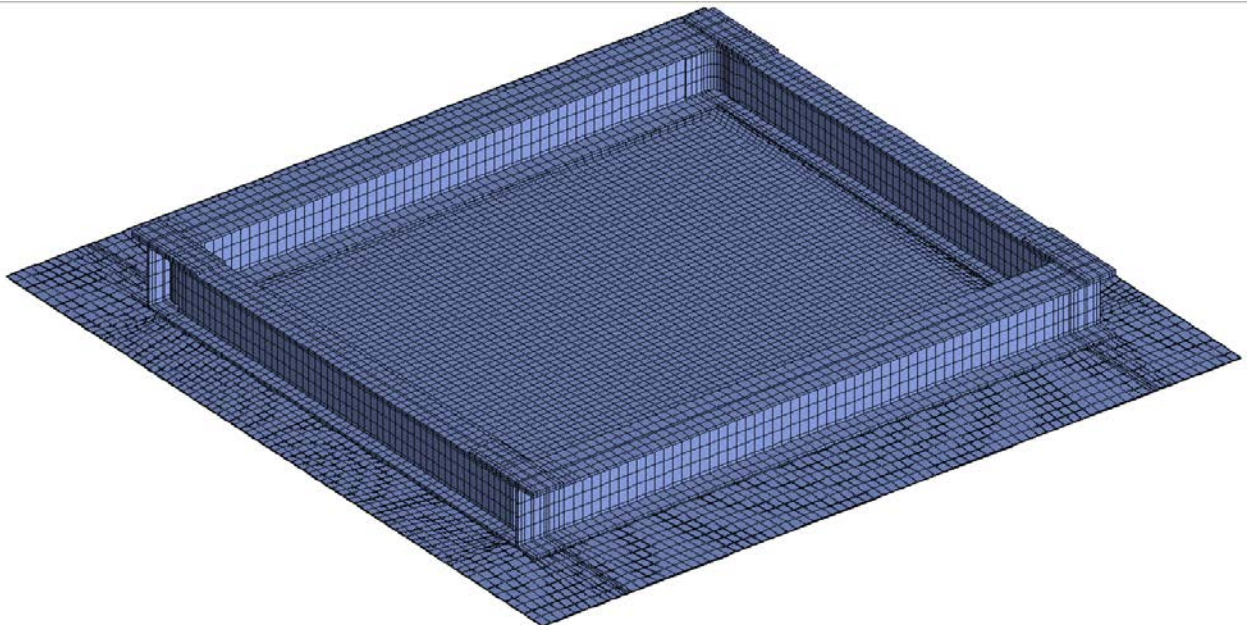


Figure 10. Finite element model of baseline panel.

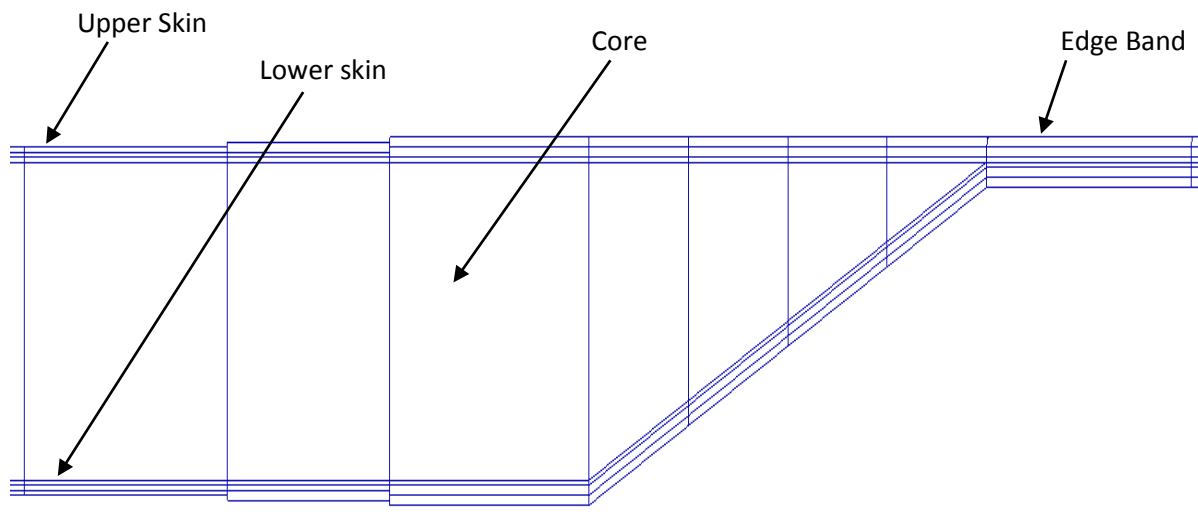


Figure 11. Panel cross-section near edges.

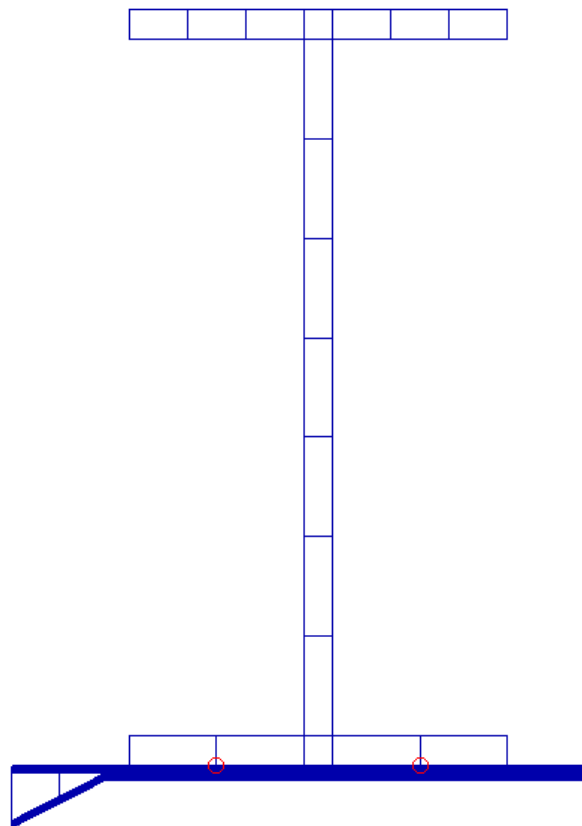


Figure 12: CBUSH locations connecting roof beams to panel.

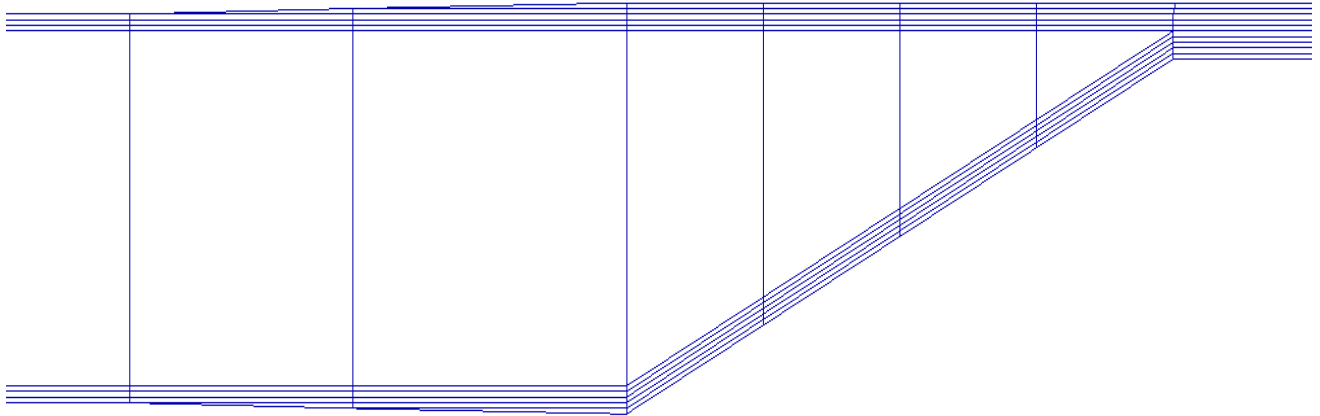


Figure 13: Final panel cross-section near edges.

2.3.2 Penn State Structural-Acoustic Model

The Bell FE model resolves all face sheet plies individually, and is suitable for structural integrity analysis. Penn State analyzed Bell's FE model of the baseline panel using NX/NASTRAN. Unfortunately, the model required over a day to compute normal modes for frequencies up to 1 kHz. Since the project requires analysis of frequencies up to 4 kHz, and the Bell model cannot be analyzed easily for those frequencies, Penn State generated a lower-resolution FE model for acoustics analysis. The lower resolution model represents the face sheets with fewer through-thickness elements, reducing the model size by over 60%. Quadratic solid elements are still used, however, consistent with Bell's model. Here are the details of the modeling reductions:

- The edge laminate regions (without honeycomb core) are now modeled with two through-thickness elements, with aggregate material properties computed based on Bell's orientations and material properties (see Table 2).
- The inner panel face sheets are modeled with a single element on the inner and outer surfaces, rather than three, with aggregate material properties computed based on Bell's orientations and material properties (see Table 2).
- The honeycomb core is modeled with a single through-thickness element.

Based on Penn State's experiences with similar structures, little error was anticipated with using aggregate face sheet properties rather than modeling each ply layer individually. The Aluminum beams are modeled with the same mesh resolution as Bell's model, and are connected to the panel using the same spring definitions, representing the bolts.

In addition to Bell's bolts, Penn State also applied a spatial stiffness in the transverse and in-plane directions to represent the frictional coupling of the beams and panel, which are compressed together by the bolts. The interface stiffness is based on an assumed percentage of the faces of the mating

materials faces in contact, which is related to an assumed surface roughness. We use guidance from Garvey [1], who measured the effects of preload on the overall elastic moduli of stacked motor laminate sheets. Our baseline structure differs from stacked common laminate sheets, however, since the beam and panel materials are different. We therefore use the stiffnesses of the softest of the two materials in contact – the composite, as this will be the limiting value. Since the surface roughness is not known, we assume the interface elastic moduli are 5% of those of the composite moduli (1.3 Msi in compression and 0.41 Msi in shear) and assume an interface thickness of 0.079 in. To convert to an array of springs between the nodes of the beams and the panel, the stiffnesses are combined with the ratios of the interface areas and the number of springs between interface nodes.

2.4 Acoustic Modeling (Boundary Elements)

To compute the sound radiated by the panel and its effects on panel radiation damping, an acoustic boundary element (BE) model was constructed. Every structural element has a corresponding acoustic element. The overall model is assumed to be baffled by the adjacent fuselage sections (or by walls in a Transmission Loss Test Chamber). The fluid loading and sound radiation were computed using the lumped parameter approach of Koopmann and Fahline [2]. The resulting fluid loading matrices were applied to the FE model using the component mode synthesis approach in ARL/Penn State's CHAMP (Combined Hydroacoustic Modeling Programs) analysis procedure [3, 4].

2.5 Measurements

Several types of vibroacoustic measurements were conducted on the baseline panel, including experimental modal analysis, surface averaged vibration response functions, radiated sound power, and sound power transmission loss. The modal analyses were conducted for free and clamped boundary conditions. The free boundary condition data were used to validate and guide updates to the FE model. The clamped data were used to confirm the edge boundary conditions applied to the panel when mounted in the NASA SALT facility [5]. Finally, the sound power and transmission loss (TL) measurements made in SALT validate the overall FE/BE model, and act as a baseline for future optimized panel performance assessments.

See Appendix A for detailed test procedures for these measurements.

2.6 Vibro-acoustic behavior

2.6.1 Effective Flexural Wavespeeds

The effective flexural wavespeeds are examined to better understand the nature of sound transmission through the panel. A cross section of a honeycomb core, composite facesheet panel is shown in Figure 14. The wavespeeds of honeycomb core/composite facesheet sandwich panels are dominated by moment effects at low frequencies, where the facesheets contract and expand in flexure, and by shear effects at high frequencies, where the core rigidity resists transverse motion. The effective bending wavespeed c_b may be determined from:

$$c_b^2 = \frac{2N}{\rho_s h + \sqrt{(\rho_s h)^2 + \frac{4\rho_s h N^2}{\omega^2 D}}}, \quad (1)$$

where $D = \frac{Et(h+t)^2}{2(1-\nu^2)}$, $N = G_{core} h(1+t/h)^2$, and $G_{core} \cong \sqrt{G_{ribbon} G_{warp}}$. ρ_s is the overall panel mass density, h is the honeycomb core thickness, N is the shear rigidity, D is the flexural rigidity, E is the Young's Modulus, t is the overall facesheet section thickness, ν is Poisson's ratio (in the in-plane, or '1-2' direction spanning the overall facesheet sections), and G are the transverse shear moduli in the different directions of the honeycomb 'weave' (ribbon and warp). Note the importance of core thickness to D , and correspondingly to c_b .

The critical frequency, where the effective bending wavespeeds match the sound speed in air (c_o), is:

$$\omega_{cr}^2 = \frac{c_o^4 \rho_s h}{D} \frac{1}{1 - \frac{c_o^2 \rho_s h}{N}}. \quad (2)$$

Using the material properties in Table 1 and Table 2, the baseline panel flexural rigidity D is nominally 3200 N-m, the mean shear rigidity N varies from 0.94 to 1.93 MN-m (the shear modulus is different in the warp and ribbon directions), the facesheet section effective Poisson's ratio is 0.21, and the overall mass density per unit area is 3.11 kg/m² (this includes the mass of adhesive and paint, but not of any added external layers of viscoelastomer). Figure 15 compares the center and edge panel bending wavespeeds computed using these properties, with the edge panel (no honeycomb core) in-plane Poissons ratio of 0.25. The mean shear and effective bending wavespeeds, along with upper and lower bounds based on the variable shear moduli in the in-plane directions, are shown. The center panel bending waves become supersonic at frequencies above about 700 Hz, with the edge panel section waves remaining subsonic up to 5 kHz. Also, the effective bending wave speed begins to approach the shear wave speed upper limits above 5 kHz.

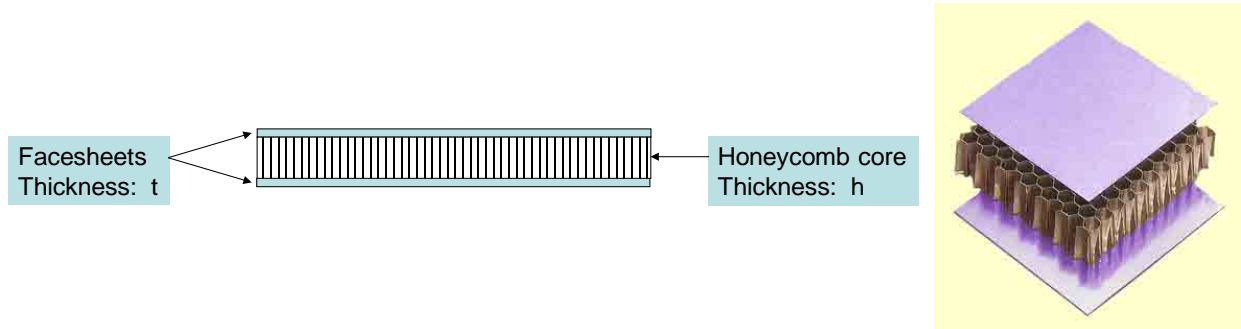


Figure 14. Schematic of typical honeycomb core/composite facesheet panel.

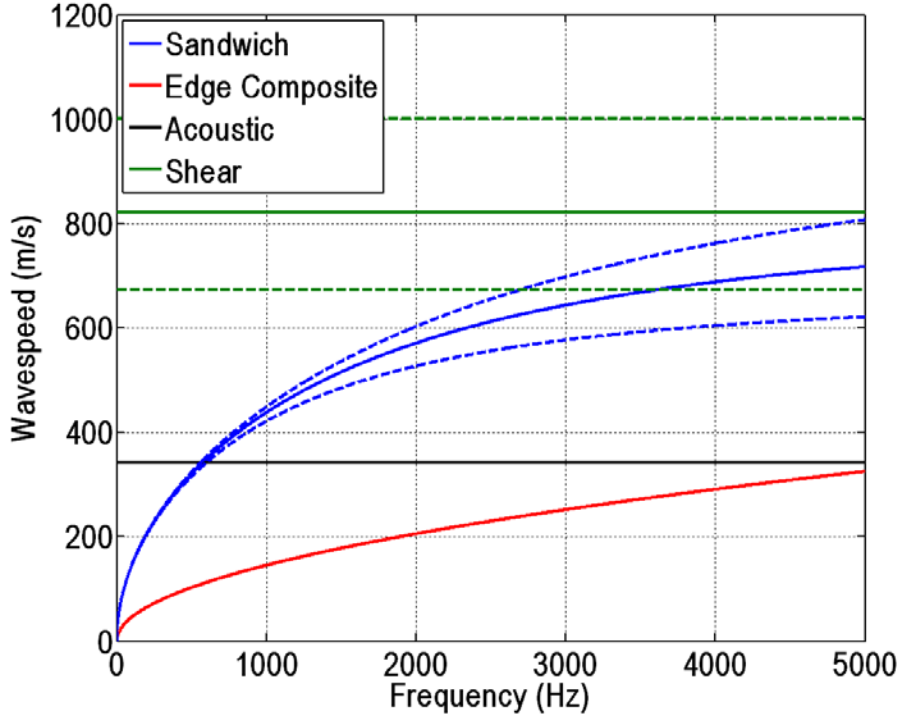


Figure 15. Analytic wavespeeds for the center panel and edge panels; the mean and upper and lower bounds on the shear and effective sandwich bending wavespeeds are shown.

2.6.2 Resonances

The reduced version of the FE model does not explicitly model every composite ply, but groups them into combined layers to reduce model size. To ensure the simplified version is accurate, Figure 16 compares a set of low frequency modes extracted from both Bell’s original model and Penn State’s model with free boundary conditions. The modal frequencies are nearly identical. The modes of the panel may be subdivided into categories – central panel (with stiffening honeycomb core), as shown in Figure 17, and edge panels (composite material only), as shown in Figure 18. There are also modes of the beam structure (Figure 19). The low-order center panel mode shapes resemble simply supported panel modes, with the ribs acting as the simple supports. Also, the outer edge mode shapes resemble those of clamped-free panels. Figure 20 compares the measured and simulated center panel resonance frequencies, and shows that the FE model captures the frequencies within 10% uncertainty.

The resonance frequencies and panel dimensions may be used to estimate flexural wavespeeds in the center panel by assuming edge boundary conditions. For example, the wavespeed c_{mn} of a given mode shape at its resonance frequency ω_{mn} may be inferred from:

$$c_{mn} = \frac{\omega_{mn}}{k_{mn}}, \quad (3)$$

where k_{mn} depends on the assumed boundary conditions. The center panel is connected to the beam stiffeners via a transition region between the honeycomb core and pure facesheet material, as shown in

Figure 21. To assess whether the boundary condition best emulates simply supported or clamped conditions, the modal wavespeeds were computed assuming:

$$k_{mn} = \sqrt{\left(\frac{m\pi}{a}\right)^2 + \left(\frac{n\pi}{b}\right)^2} \quad (4)$$

for simply supported boundary conditions and

$$k_{mn} = \sqrt{\left(\frac{(2m+1)\pi}{2a}\right)^2 + \left(\frac{(2n+1)\pi}{2b}\right)^2} \quad (5)$$

for clamped conditions, where a is the width (nominally 38 inches) and b is the length (nominally 33 inches). The flange half-widths were added to the center panel width to compute the nominal a and b dimensions for the wavenumber analysis since the flange is thin and moves with the center panel.

Figure 22 compares inferred modal wavespeeds to those computed using analytic formulae for infinite panels, and shows that the panel modes are effectively simply supported. The figure also shows the range of flexural wavespeeds in the panel due to the differing honeycomb core stiffnesses in the ribbon (stiffest) and warp (weakest) directions. The data are shown again in Figure 23, but are limited to modes with only a half wave across either the length ($m=1$) or width ($n=1$). The $m=1$ modes feature bending waves which travel predominantly along the width, or ribbon (stiffer) direction, and the $n=1$ modes are aligned primarily along the length, or warp (weaker) direction. Figure 23 shows that these modes follow the analytic curves fairly well, particularly the $n=1$ modes.

This exercise shows that the center panel region is indeed effectively simply supported, with minor mode shape length and width variations. This means that simple analytic formulas for simply supported panels may be used to guide optimized panel design.

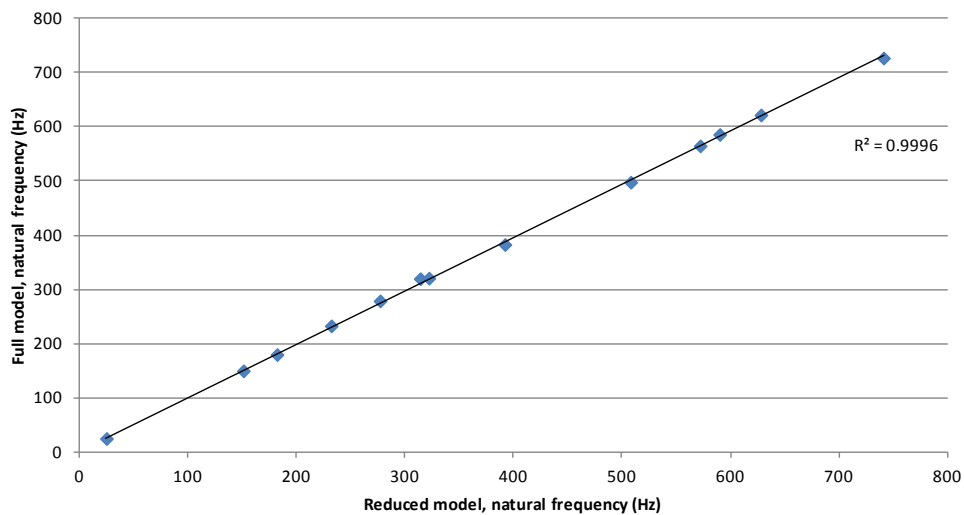


Figure 16. Comparison of low-frequency modal frequencies extracted from Bell rigorous FE model and Penn State approximate FE model; diagonal line indicates perfect agreement (slope of 1.0).

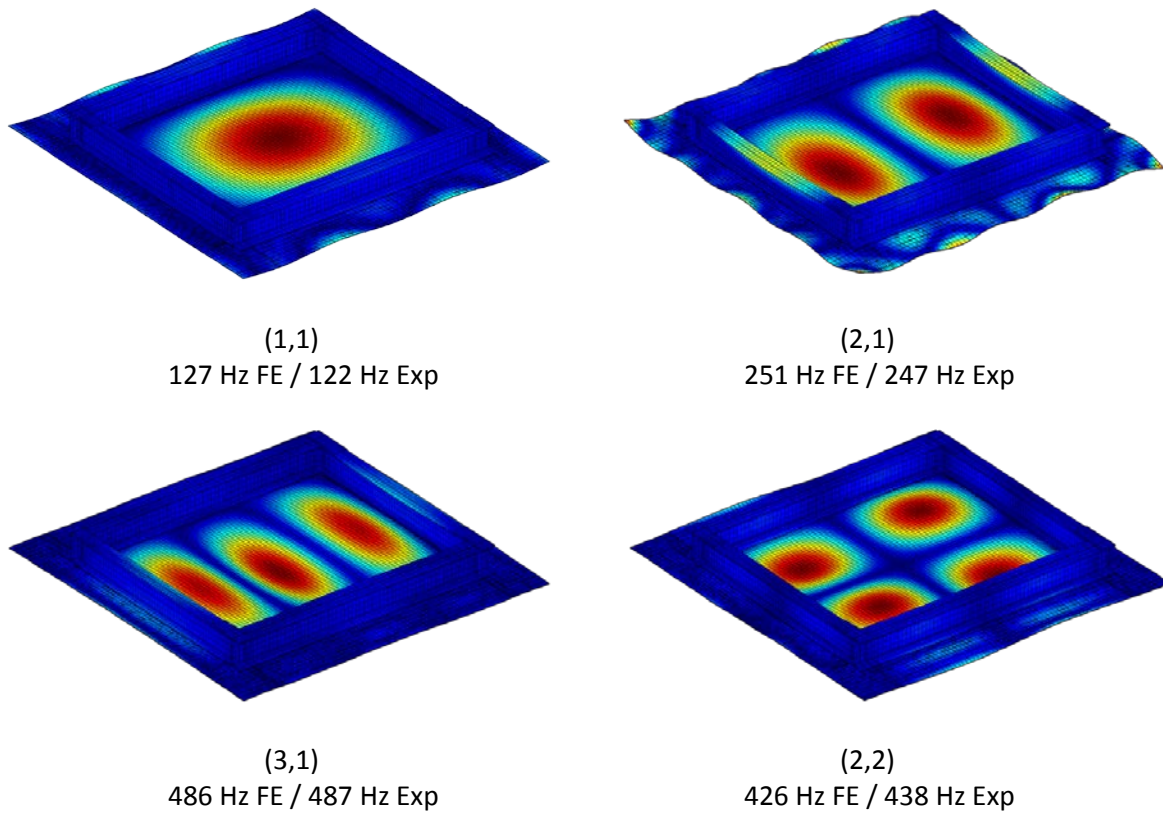


Figure 17. Low-order center panel modes of baseline panel, FE simulations and FE and experimental resonance frequencies. Values in parenthesis indicate the number of half-waves along the length and width of the panel respectively.

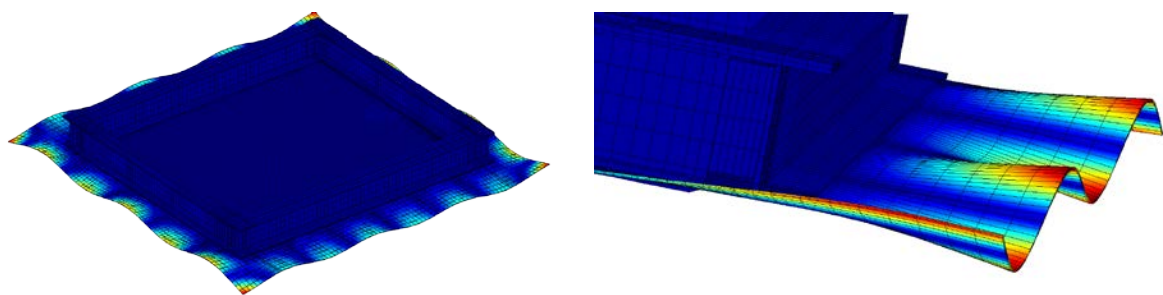
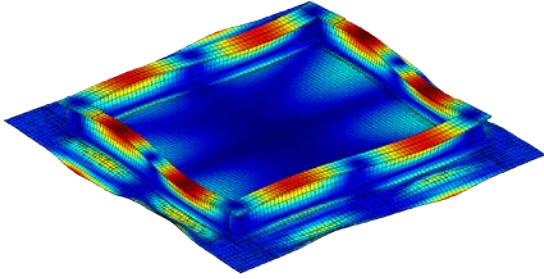
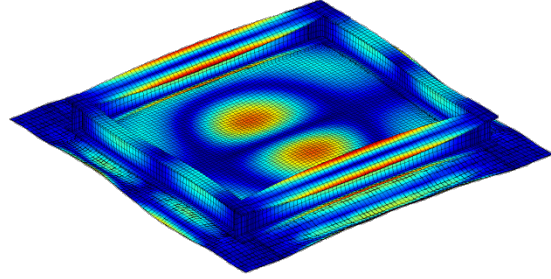


Figure 18. Example of mode shapes in edge material; left image zooms on edge material.



Beam in-plane bending, 593 Hz



Beam flange twisting, 668 Hz

Figure 19. Examples of beam modes of baseline panel, FE simulations. Comparable experimental mode shapes were not identified since the beams were not part of the measurements.

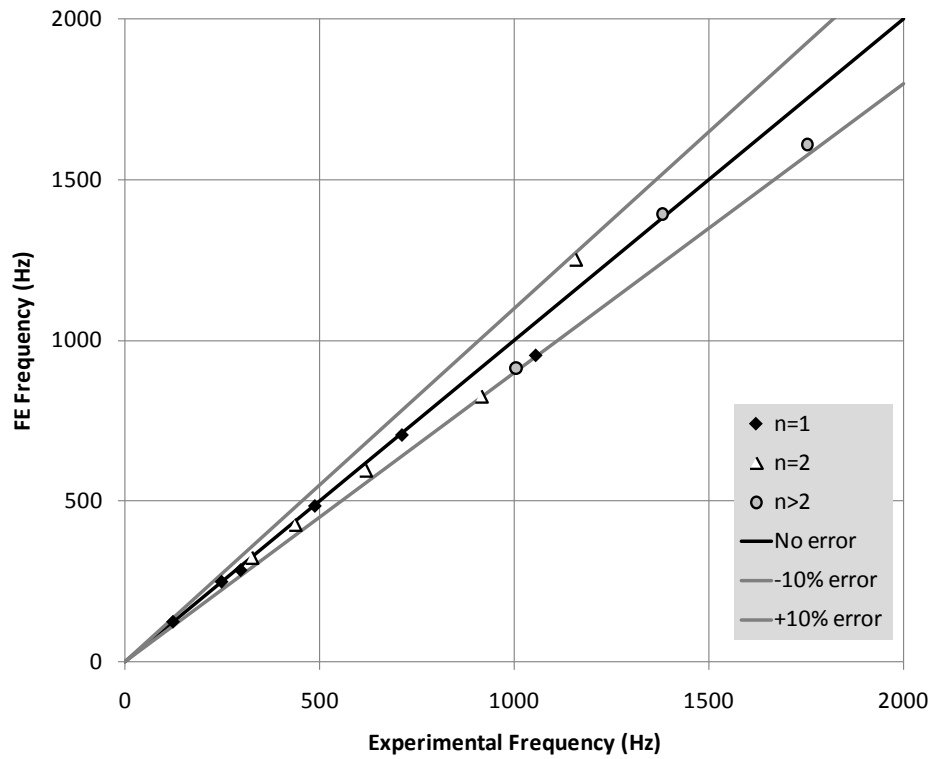


Figure 20. Measured vs. simulated center panel resonance frequencies for baseline panel. 'n' corresponds to the mode order along the width direction of the center panel.

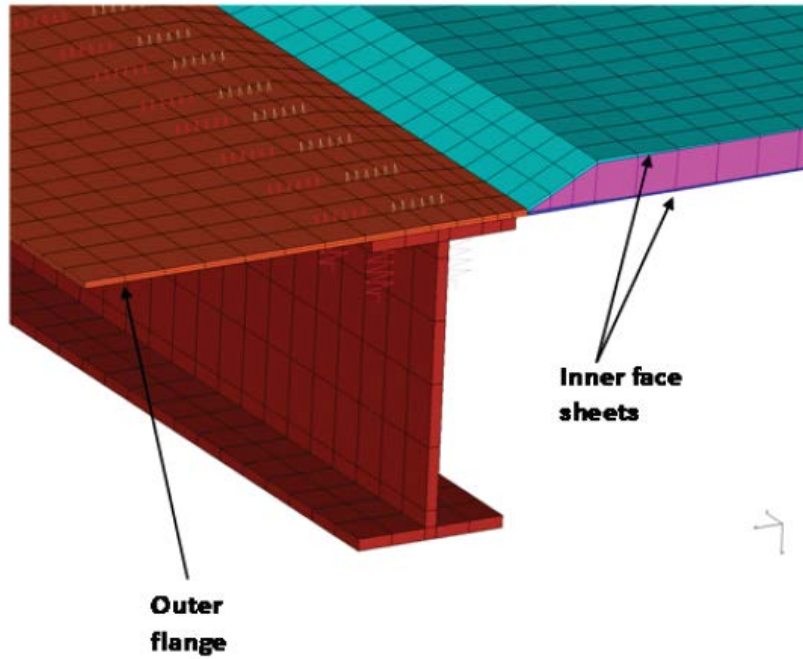


Figure 21. Connections between beam and center and edge composite panels.

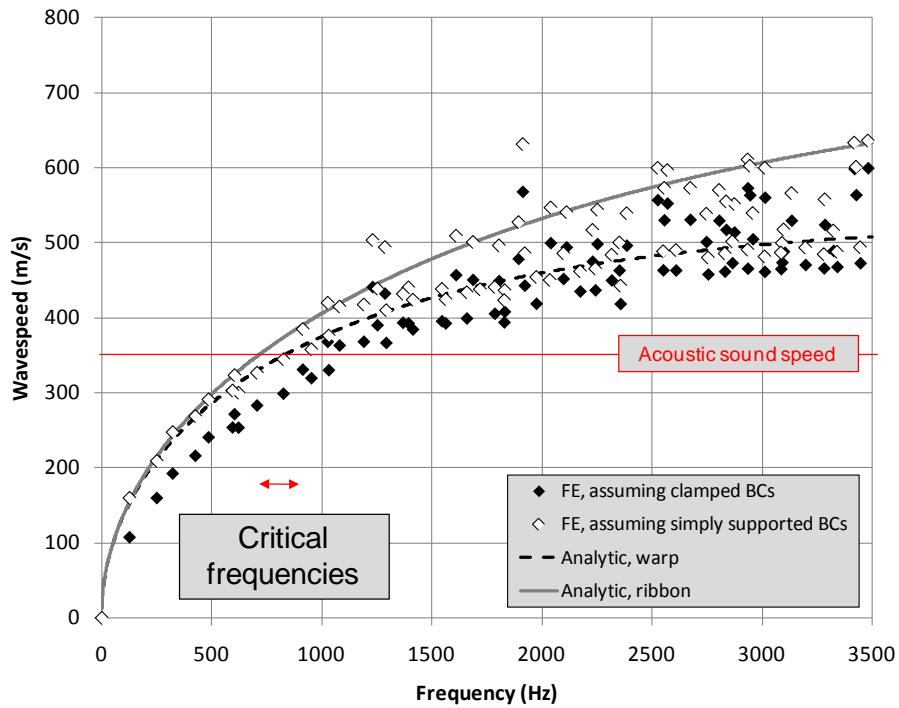


Figure 22. Flexural wavespeeds of the center panel inferred from resonance frequencies and assumed modal wavenumbers for simply supported and clamped conditions. The inferred wavespeeds are compared to analytic estimates in the warp and ribbon honeycomb directions.

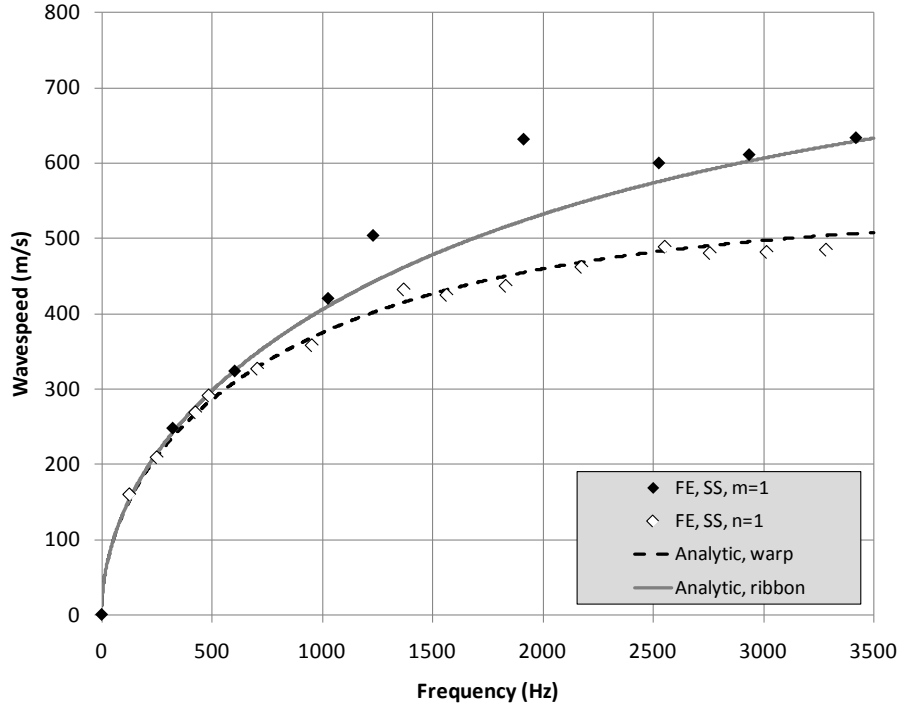


Figure 23. Same as Figure 22, except that only modes with a half wave in the length ($m=1$) or width ($n=1$) directions are shown.

2.6.3 Damping Loss Factors

Overall damping loss factors were extracted from the experimental modal analysis data, and are shown in Figure 24. The center panel modes are labeled in the figure, and are highly damped near 500 Hz, slightly below the acoustic coincidence frequency. Above about 2 kHz, all modes have damping loss factors between nominally 0.006 and 0.035. Figure 25 shows the center panel damping only, along with estimates of the damping induced by sound radiation using the relation:

$$\eta_{rad} = \sigma_{rad} \frac{\rho_o c_o}{\omega \rho_s h}, \quad (6)$$

where σ_{rad} is the sound power radiation efficiency of the center panel modes, ρ_o is the mass density of air, and c_o is the sound speed in air. At and above coincidence, we assume σ_{rad} is 1 (as shown in the acoustic BE calculation in Figure 26), and see that the estimated radiation loss factor is generally an upper bound of the center panel mode loss factors. However, the actual center panel modes, particularly at higher frequencies, couple strongly with the beams and edge panels, as seen in Figure 17 and Figure 19. This coupling increases the effective modal masses of those modes. Increasing the panel mass density by 50% to approximate this effect reduces the radiation damping, and provides a better match with the higher frequency panel modes above 800 Hz. Rigorous calculations of individual modal masses would provide improved agreement, but this simple comparison is sufficient to illustrate the importance of radiation damping on the center panel vibration. It is critical, therefore, that acoustic BE (or similar) modeling be included in any panel vibration calculation to account for radiation damping.

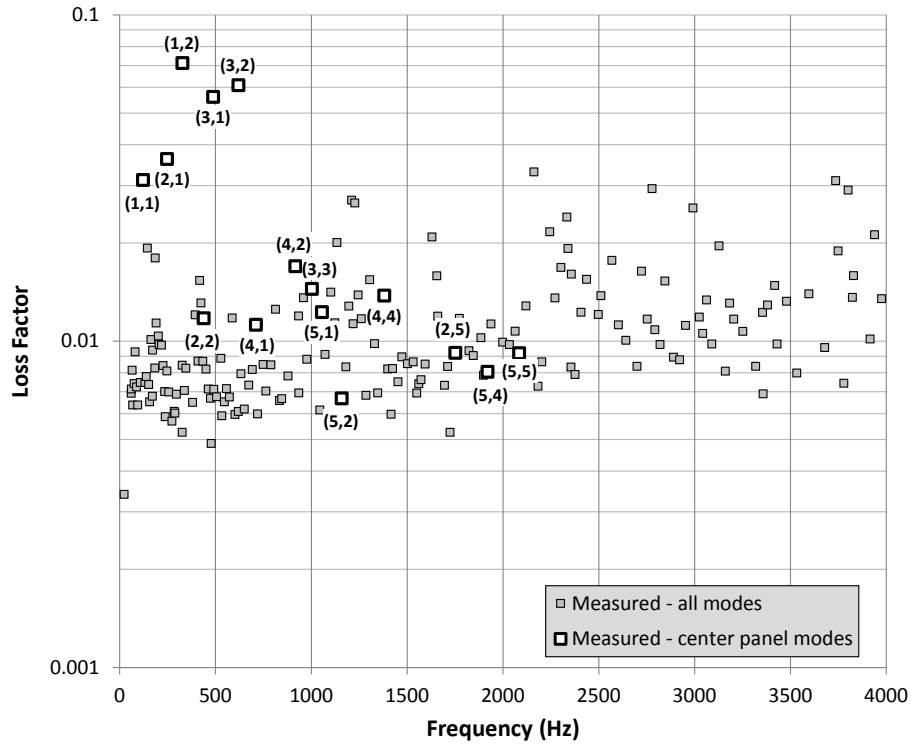


Figure 24. Measured modal damping loss factors. Center panel modes are distinguished by their (m,n) mode orders

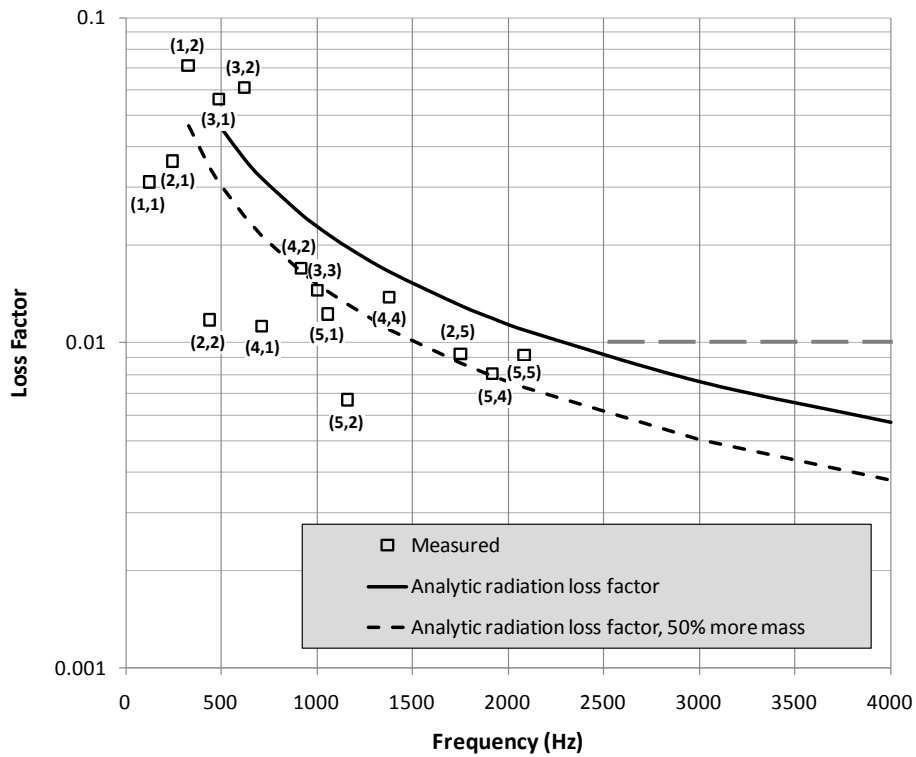


Figure 25. Measured center panel modal damping loss factors vs estimates of radiation damping.

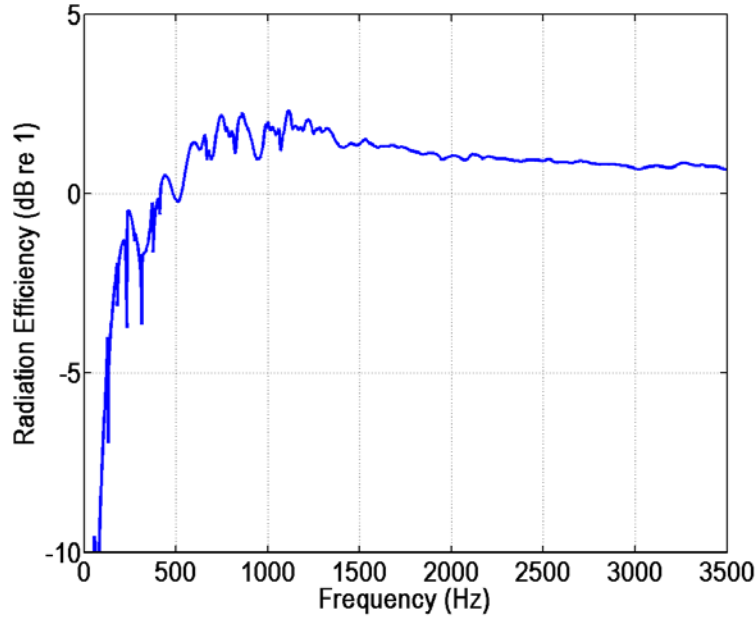


Figure 26. BE calculation of radiation efficiency of baseline panel for diffuse drive in dB (0 dB indicates radiation efficiency of 1).

2.6.4 Forced Response Simulations and Measurements

Two forced response calculations were used to better understand the critical sound transmission paths through the baseline panel and to guide design optimization efforts: a structural drive at one of the beam joints (mimicking transmission drives as shown in Figure 27), and a diffuse acoustic field applied over the surface of the center panel (shown in Figure 28), as well as both the center and edge paneling. All radiated sound transfer functions were computed using ARL/Penn State’s CHAMP analysis capability [3, 4] (see Figure 29). Based on the loss factor measurements, we assume a global mechanical loss factor of 0.01, and apply the acoustic BE model to the structural FE model to capture the effects of radiation damping.

The simulated and measured point mobilities for three center panel drives are averaged and compared in Figure 30. The measurements and simulations agree well, and are also mostly bounded by the infinite panel mobilities above 1 kHz. Upper and lower bound infinite panel mobilities are computed using:

$$G_{\text{inf}} = \frac{\omega}{8\rho_s h c_b^2} \quad (7)$$

and the variable core shear moduli in the ribbon and warp directions. The upward trending of the conductance is caused by the increasing dominance of the core shear modulus with increasing frequency. The mobilities above 1 kHz (the important frequency range for this project) are influenced by many modes, with only modest variability. This high modal overlap, along with all modes being supersonic (with unit radiation efficiency) indicates that any quieting strategy must target nearly all modes equally, rather than a few strong sound radiators.

The sound power radiated by the panel due to excitation by a diffuse acoustic loading field is measured in NASA Langley's SALT [5] facility, and simulated using the CHAMP software. To simulate the boundary conditions in the SALT facility, the outer edges of the panel are fixed in the FE model. Only the panel regions (center and edge) are driven with the diffuse loading; the beams are unloaded. Figure 31 shows the simulated sound power radiated by the center panel and the edge region for frequencies above 400 Hz (the lower frequency limit of the NASA reverberant room), and shows that, as expected, the faster bending waves in the center panel are responsible for much higher transmitted sound than the subsonic waves along the edges.

The powers in Figure 31 are compared to the usual assumption of incident sound power in a reverberant room:

$$P_{inc} = \frac{c_o w_{in}}{4} S \quad (8)$$

where w_{in} is the reverberant room energy density and S is the panel surface area. Using the blocked pressure assumption we can approximate w_{in} as:

$$w_{in} \cong \frac{|p|^2}{\rho_o c_o^2}, \quad (9)$$

where p is the acoustic pressure at the boundary. Since we apply a unit pressure loading to the panel, the squared pressure must be unity.

The transmission coefficient is then

$$\tau = \frac{P_{rad}}{S / 4\rho_o c_o} \quad (10)$$

where P_{rad} is computed by CHAMP. The virtual transmission loss (VTL) is the inverse of the transmission coefficient expressed in dB:

$$VTL = 10 \log \left(\frac{S / 4\rho_o c_o}{P_{rad}} \right). \quad (11)$$

The computed VTL for the center panel region is compared in Figure 32 to that of the analytic infinite panel estimate in Fahy and Gardonio [6], integrated over all angles of incidence:

$$\tau_d(\omega) = \frac{\int_0^{\pi/2} \tau(\phi, \omega) \sin \phi \cos \phi d\phi}{\int_0^{\pi/2} \sin \phi \cos \phi d\phi} = \int_0^{\pi/2} \tau(\phi, \omega) \sin 2\phi d\phi. \quad (12)$$

More details on the VTL procedure are in Appendix B.

The FE/BE-based VTL is similar to the analytic estimate, establishing confidence in the modeling. However, the small TL of the panel shows that sound sources are poorly attenuated, and that panel redesign to mitigate transmission noise is clearly warranted. Finally, Figure 33 shows that the overall VTL (which includes the center and edge panels) is for most frequencies within 3 dB of that measured in the NASA SALT facility, establishing further confidence in the modeling procedures. The coincidence dip of the edge paneling near 5.5 kHz is not as strong in the measured data, likely because the edge paneling is not a large continuous section, but a narrow frame, such that simplified infinite panel TL techniques are no longer accurate near coincidence.

Figure 31 and Figure 33 also include analytic estimates of radiated sound power and TL from infinite panel representations of both the center and edge regions. The total panel analytic TL estimates are computed by summing the total power radiated by the total areas of each region. The analytic estimates show that the edge paneling radiates more power above about 4 kHz. Optimizing the TL of the center panel, therefore, will only significantly improve overall panel TL below 4 kHz.

Finally, radiated sound power simulations and measurements for a transverse structural drive at a rib joint are compared in Figure 34. The measurements were made using an intensity probe on the anechoic side of the SALT facility. As with the diffuse drive, the simulated and measured data are generally within 3 dB (except at 500 Hz and 1 kHz, which show up to 5 dB differences).



Figure 27. Typical rotorcraft installation. Roof panel is in green below the strut. Yellow arrow denotes oscillatory transverse force.

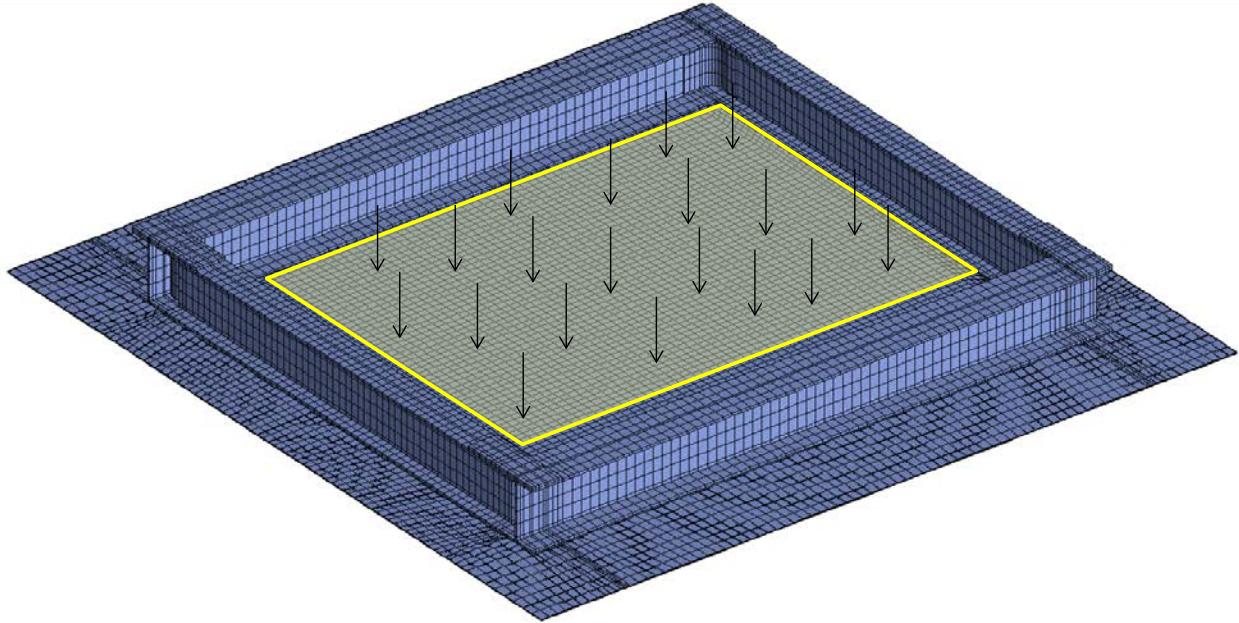


Figure 28. Diffuse acoustic loading applied to center region of baseline panel.

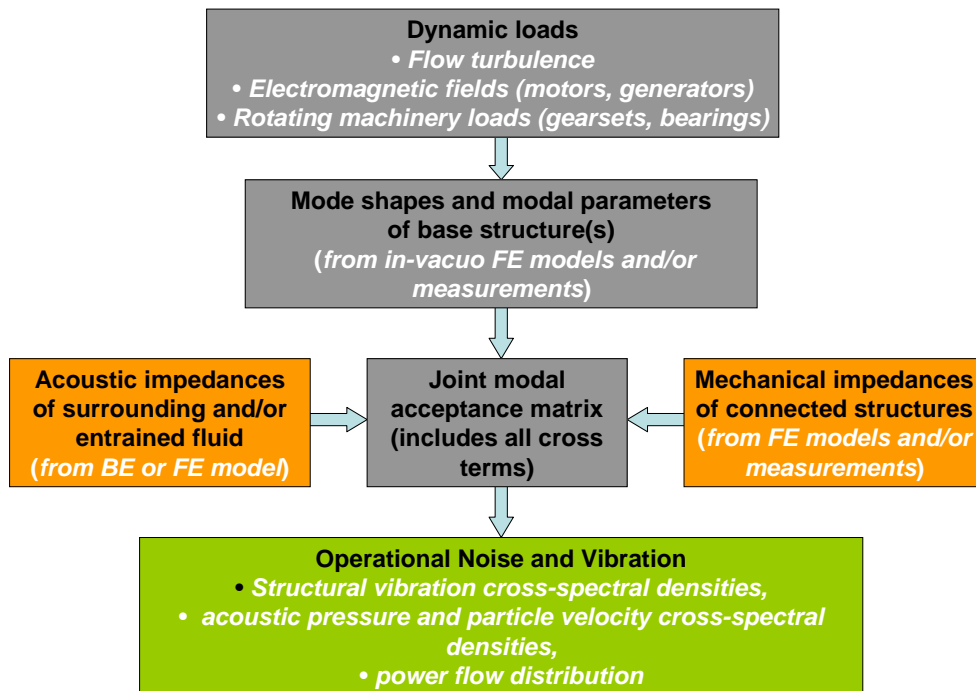


Figure 29. ARL/Penn State's CHAMP analysis capability [3].

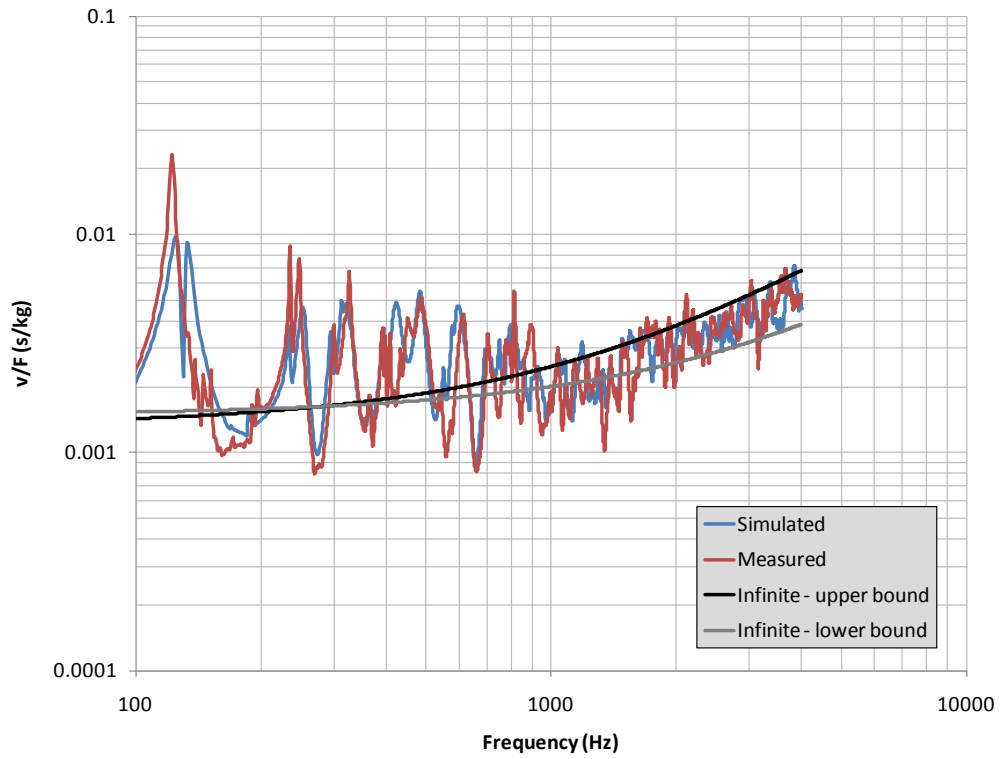


Figure 30. Simulated and measured drive point mobilities, averaged over three drive locations. Infinite panel upper and lower bound mobilities computed for core ribbon and warp directions.

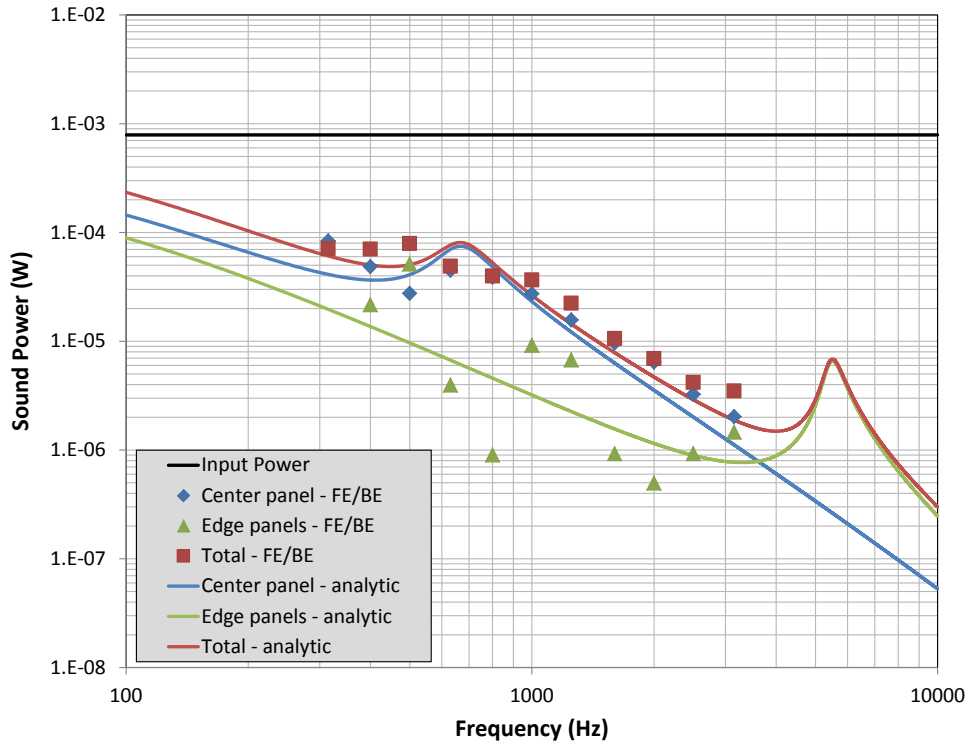


Figure 31. Simulated input and radiated sound power.

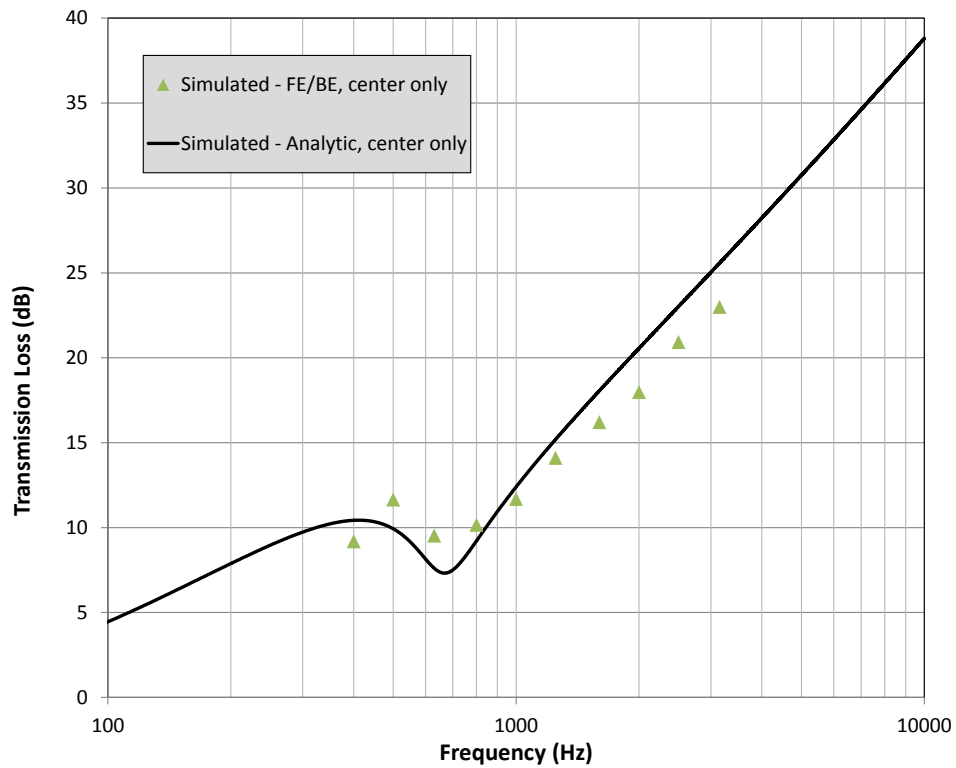


Figure 32. TL for center panel only, FE/BE VTL vs. analytic simulations.

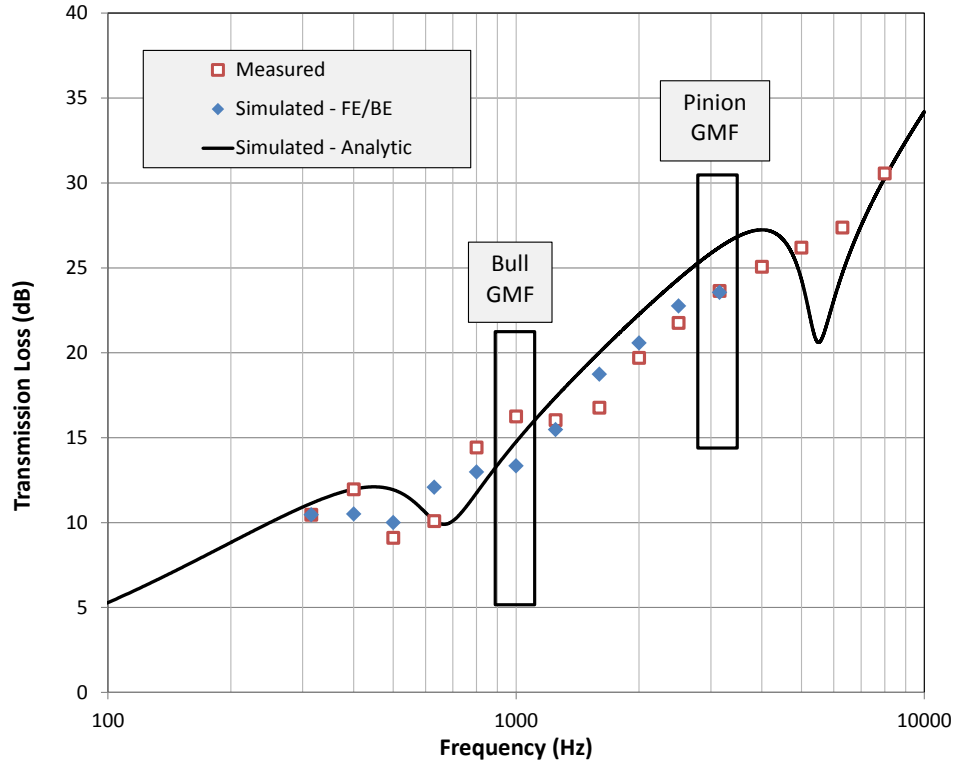


Figure 33. Measured vs. simulated TL for center and edge regions for diffuse acoustic drive.

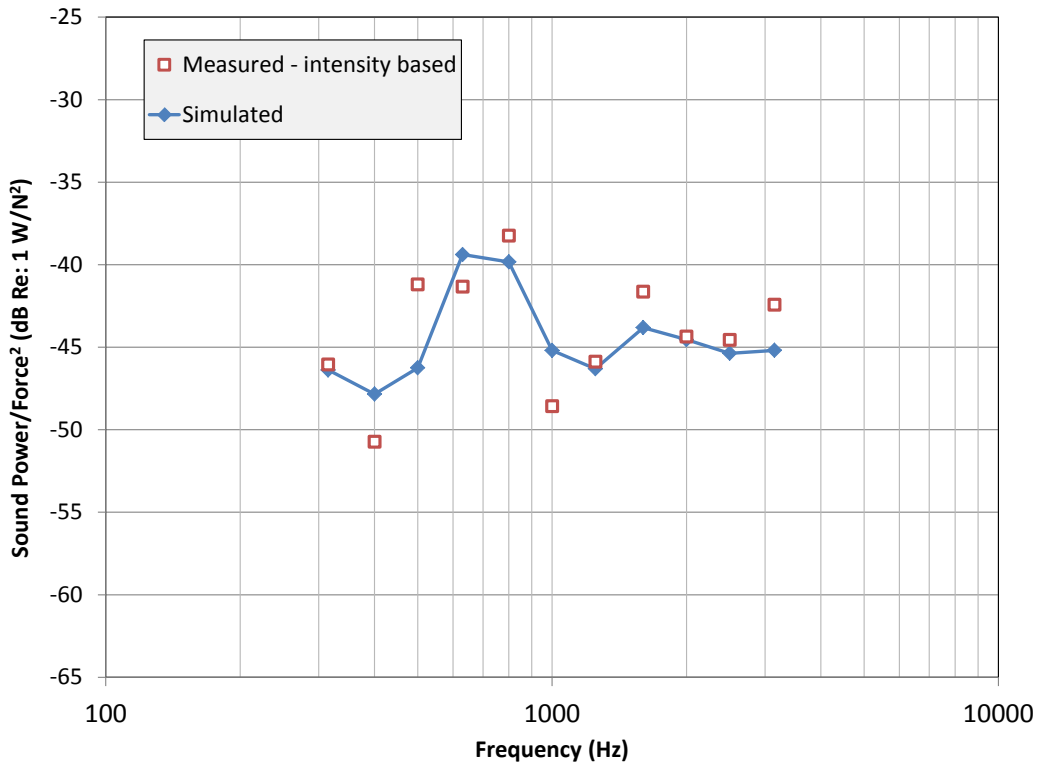


Figure 34. Measured vs. simulated sound power for structural drive at beam joint.

3 Panel Optimized for Reduced Noise

3.1 Design Optimization Goals

Design options were pursued which balance vibroacoustic reductions with weight and structural integrity constraints. The center region of the panel was adjusted to minimize structure-borne and air-borne sound transmission without adding excessive weight. In this context, net weight is defined as the offset between additional weight of the optimized panel (as compared to the baseline panel) and the weight of soundproofing insulation and/or damping materials that can be eliminated as a result of increased vibro-acoustic performance of the optimized panel:

Net Weight = Optimized Panel Weight – Baseline Panel Weight – Insulation/Damping Eliminated Weight

Typical surface weights range from 1 – 2.4 kg/m² (0.2 – 0.5 lb/ft²) for standard soundproofing packages and 3.4 – 9.7 kg/m² (0.7 – 2 lb/ft²) for VIP applications. One objective of the design optimization was to reduce or eliminate soundproofing materials based on the vibro-acoustic performance of the optimized panel. The following generic soundproofing configuration would typically be applied to the baseline panel to improve vibro-acoustic performance:

1. 60% coverage constrained layer damping material, 1.56 kg/m² (0.32 lb/ft²) 3M Aearo Technologies C-2206-03PSA, 1 mm (0.04 in) thick, and
2. 2.54 cm (1 in) thick, 6.7 kg/m³ (0.42 lb/ft³) Johns Manville Microlite AA fiberglass insulation blanket.

During the optimization study, the cross-sectional materials used in the center panel were varied, while ensuring that the flexural rigidity was maintained, and that material strength constraints were met (see Section 2.1 for a discussion of structural design constraints). An important design constraint is to ensure symmetric laminates with a minimum of 10% fibers in each direction. Also, lamina data factored with open hole ‘knockdown factors’ conservatively approximates Bell’s typical allowable design curves. Typical critical design allowable is for an open or filled hole in compression at an elevated temperature and moisture soaked condition.

3.2 Quieting Technologies

Based on the analysis results to date, the baseline panel represents a challenging noise reduction problem. The center panel bending waves are supersonic at frequencies above about 700 Hz, so that all modes of vibration radiate sound strongly throughout the key frequency range of interest (1 – 4 kHz).

There are several design changes that could reduce sound transmission of the panel, including:

- attaching treatments to the panel;
- reducing the shear stiffness of the core material to reduce the effective panel flexural wavespeeds, increasing the coincidence frequencies and reducing sound power radiation efficiencies;
- adding structural damping to the panel, reducing vibration and therefore radiated sound power;

- introducing structural barriers adjacent to the roof beams to reduce the structure-borne energy flow into the center panel; and
- splitting the panel into two subpanels separated by an air gap.

The design changes must not (a) add significant weight or thickness, and (b) reduce structural integrity.

3.2.1 Traditional Treatments Attached to Panel

There are currently two typical methods of reducing cabin noise – applying thin sheets of constrained layer damping (CLD) material and/or layer(s) of fiberglass insulation to the interior face of the panel. The damping material reduces vibration amplitudes at panel resonances, thereby reducing radiated sound. The mass of the insulation reduces the sound power transmitted through the center panel, particularly at high frequencies.

Common off-the-shelf CLD material is ISODAMP C-2206 from E-A-R Aearo Technologies (owned by 3M). The material is 1 mm thick with a surface density of 1.56 kg/m^2 , and according to the vendor, provides an added damping loss factor of 0.115 to a thin sheet of Aluminum at 1 kHz. The added mass to the panel by the CLD is significant, since the bare panel surface density is only 2.48 kg/m^2 . This added mass will also slow down the panel flexural waves, but not to the point where the coincidence frequency is increased enough to reduce radiation efficiency above 1 kHz.

A commonly used acoustic blanket is the Microlite AA from Johns Manville. The lightest Microlite AA blanket weighs 0.168 kg/m^2 (small compared to the panel surface density), and provides about 4.5 dB of sound attenuation at 1 kHz and about 12 dB at 3 kHz. The blankets are mounted within a thin plastic covering which is attached to the edges of the panel.

3.2.2 Reduced Stiffness Core Materials

The classical approach for increasing sound power transmission loss in honeycomb sandwich panels is to slow down the shear waves in the core material to the point where they are subsonic [7, 8]. The Kevlar core used in the baseline panel has an effective mean shear wave speed of 821 m/s, which is well above the air sound speed of 344 m/s. Reducing the mean core shear modulus from 97 MPa to 15 MPa would reduce the shear wave speed to 287 m/s, eliminating the panel coincidence frequency such that all flexural/shear waves are subsonic. Using infinite panel theory, the TL curves in Figure 35 show the potential effects of slowing down the core shear waves.

The results show that the upper bound for sound power transmission loss is dictated by simple mass law theory. Further reductions of airborne sound power are only possible with added noise barriers, such as the acoustic blankets commonly used by industry, or by adding other structural panels, with an accompanying airgap, normal to the panel. Also, it is unlikely that a panel with a core with a mean shear modulus of 15 MPa would meet the structural integrity constraints described in Section 2.1.

In an alternative approach investigated by NASA Langley Research Center, voids may be machined into the core material to reduce the transmission of energy through the panel [9]. This approach, however, reduces the panel overall bending stiffness, and may not be acceptable for a rotorcraft roof panel.

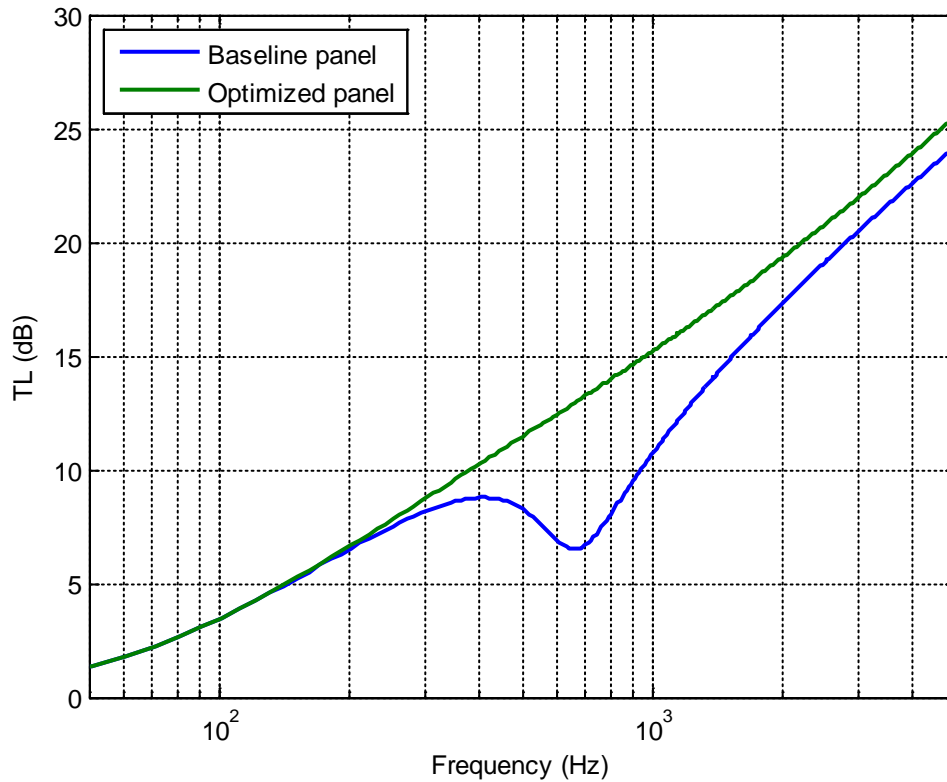


Figure 35. TL for baseline panel, and optimized panel with soft core and subsonic wave speeds.

3.2.3 Embedded Viscoelastic Treatments

Thin layers of viscoelastomer may be embedded within the facesheet sections, or within the core itself. Peters et. al. [8] reported loss factors of 0.05 and greater with core-embedded viscoelastomer, and showed a 3-5 dB transmission loss improvement over more lightly damped panels. Reducing radiated sound at low frequencies via structural damping improvements will be difficult due to the dominance of the radiation damping (in cases of high core shear stiffness). To investigate the potential benefits of added structural damping, the structural loss factor was increased from 0.01 (measured in the baseline panel) to 0.05 over all frequencies in the FE model. Figure 36 and Figure 37 show simulated reductions in radiated sound power for structural and acoustic diffuse drives on the FE/BE model. As expected, sound power reductions due to added structural damping are most pronounced at higher frequencies, with a mean reduction of 2-3 dB, and a reduction at resonance peaks of 4-6 dB. These results are promising, and consistent with those of Peters [8].

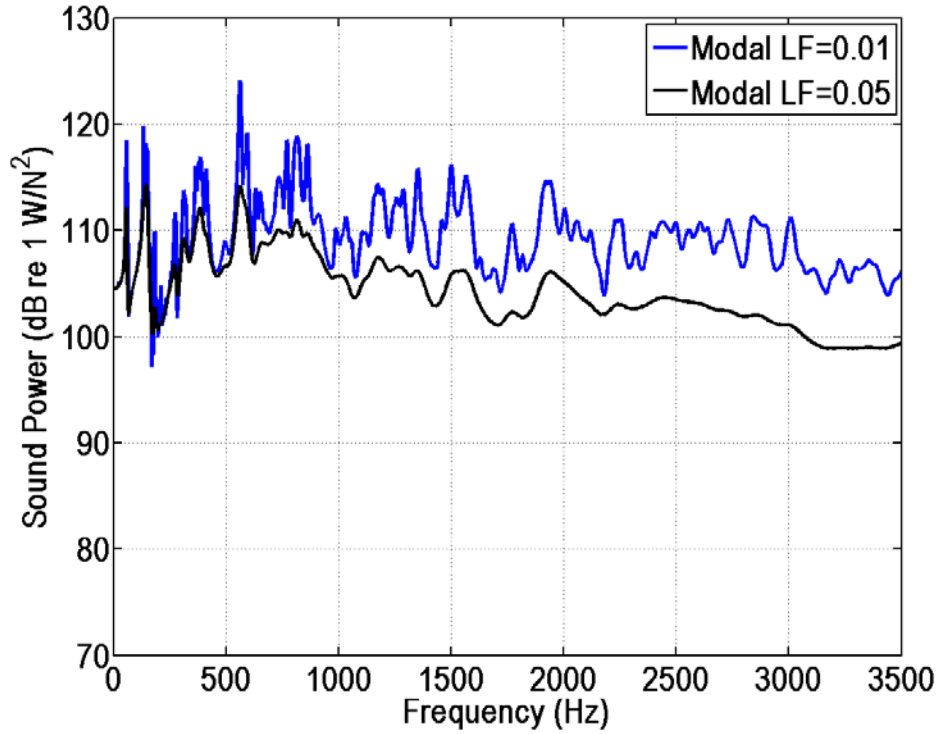


Figure 36. Effects of added structural damping on radiated sound power due to structural drive at beam intersection.

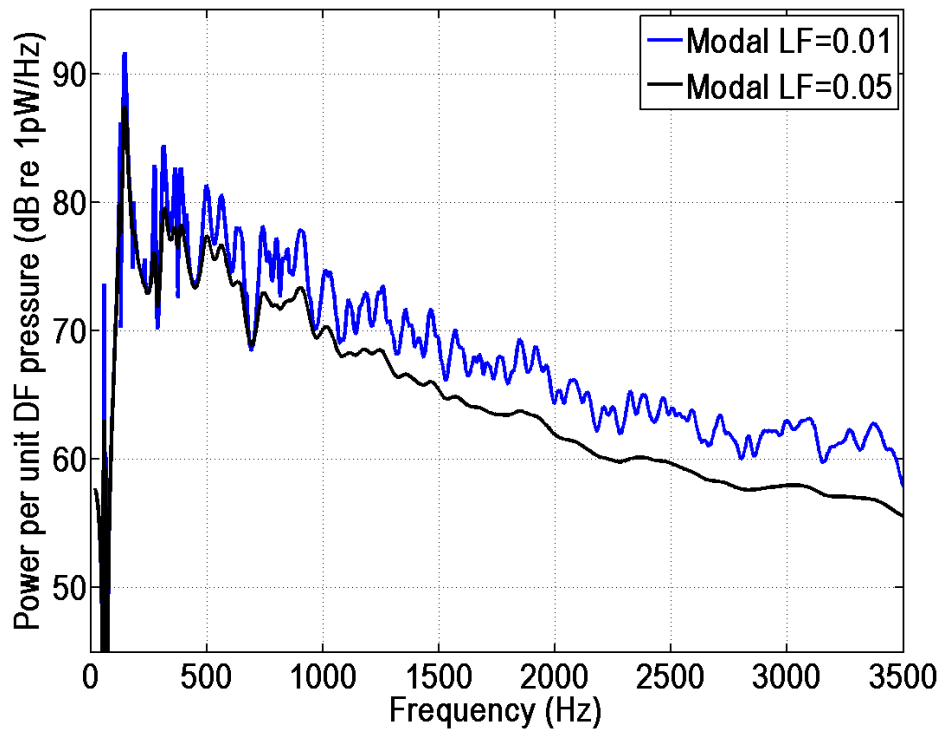


Figure 37. Effects of added structural damping on radiated sound power due to acoustic diffuse drive.

3.2.3.1 VHB Viscoelastomer from 3M

The FE/BE results indicate that inserting layers of thin viscoelastic material in the face sheets, as well as between the beam stiffeners and panel, will lead to improved acoustic performance. The face sheets used in helicopter sandwich panels, however, are extremely thin and lightweight (each ply in the baseline panel is 0.0079 inches thick). Replacing one of the layers, in this case the center ply, with a layer of viscoelastomer requires similarly thin and light damping material. 3M corporation recommended using their VHB 9469 adhesive, which is formulated to have high damping properties near room temperature and at frequencies between 1 and 4 kHz. Replacing the center layer of each face sheet with a layer of the VHB material (which is nominally 0.005" thick) leaves outer and inner carbon layers with 0 and 90 degree ply orientations. There are no 45 degree ply orientations in the new design, however. Structural integrity calculations described in Section 3.3.1 confirm the acceptability of this approach.

Figure 38 shows the temperature- and frequency-dependent shear modulus and loss factor for the VHB material. Shear Moduli (computed assuming a Poisson's ratio of 0.499 and Young's Moduli from DMA testing) and loss factors are compared at 20 and 30 degrees C in Figure 39. The loss factors are quite high, ranging between 0.7 and 1.1 between 1 and 4 kHz. Though promising, the damping benefits of the VHB material were checked by performing experimental modal analyses on two test coupons constructed by Bell.

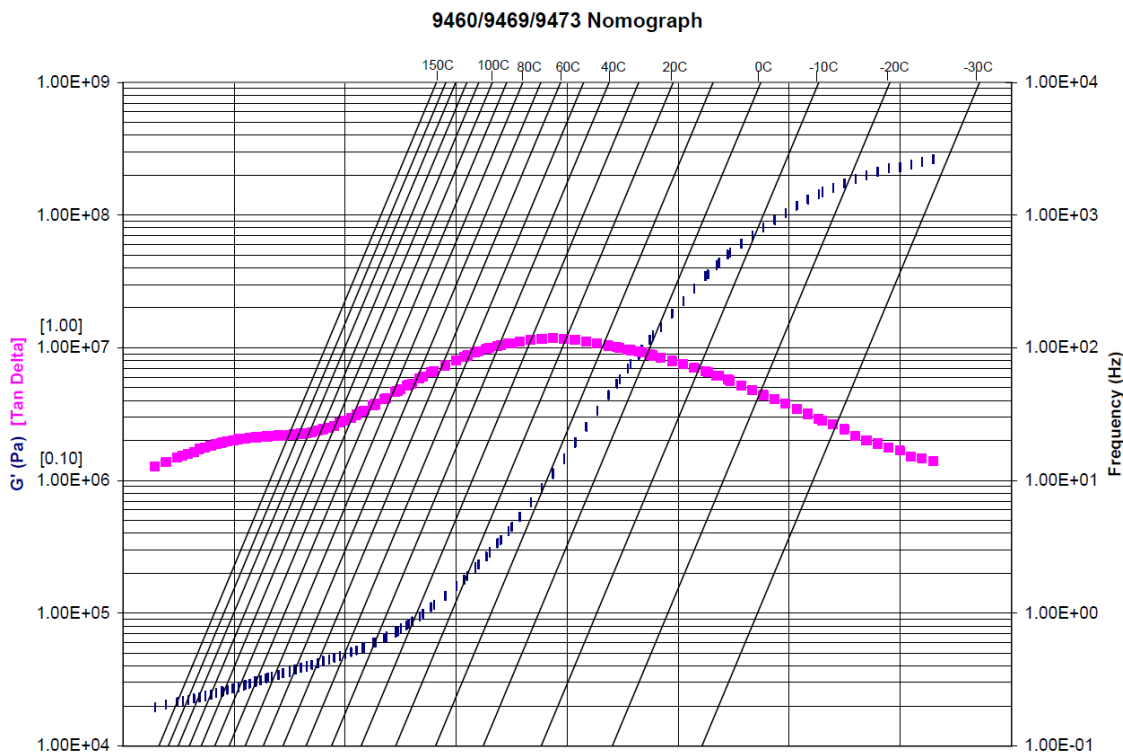


Figure 38: Shear modulus and loss factor nomograph for 3M VHB 9469 (provided by 3M).

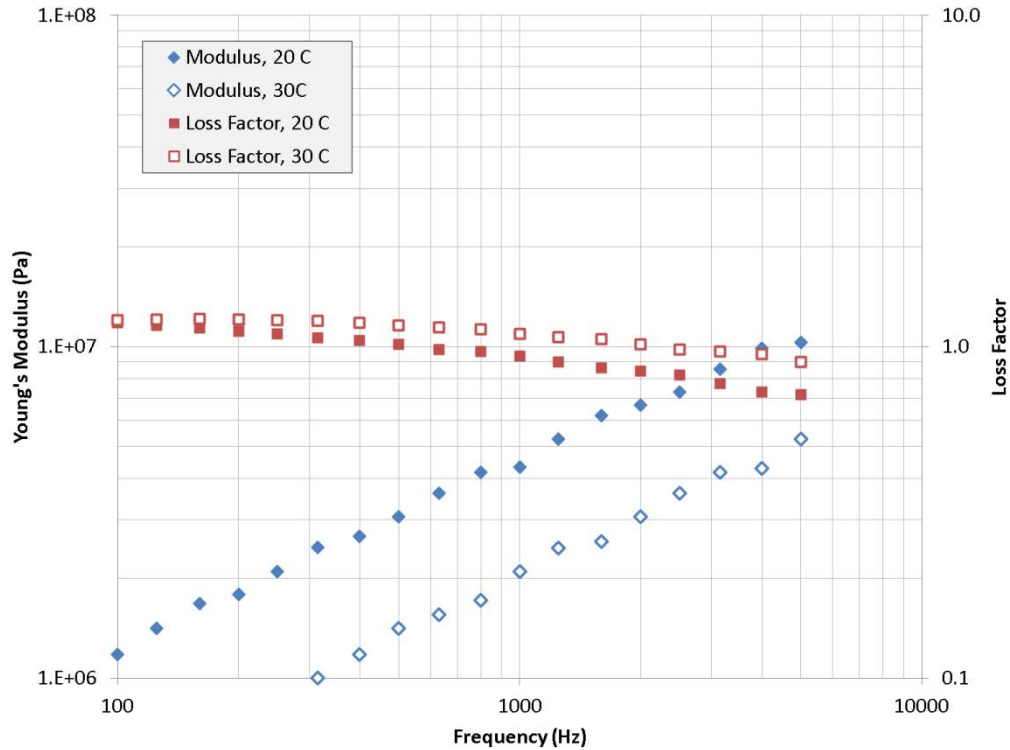


Figure 39: Young's modulus and loss factor for 3M VHB 9469 at 20 C and 30 C.

3.2.3.2 Coupon Testing and Analysis

Two test coupons constructed with layers of the 3M VHB 9469 material sandwiched between sheets of carbon fiber plies (the same material used in the baseline panel) were tested using experimental modal analysis at Penn State. The panel dimensions (19" x 23") were chosen to avoid modal degeneracy, so that each structural mode is distinct in frequency and easily identified. The same Hexcel Kevlar 0.5" thick core (1/8" cell size, 3.3 lb/ft³) used in the baseline panel was used for the test coupons. The two coupons were constructed using different approaches. The first panel has facesheets with cocured carbon fiber and VHB, such that part of the VHB fused with epoxy in the carbon fiber sheets. This formed a hybrid structure with uncertain properties. A second panel with pre-cured carbon fiber sheets post-bonded with the VHB was therefore also constructed. A non-destructive inspection (NDI) of the post-bond panel was conducted to ensure complete adhesion. An image of the NDI test is shown in Figure 40, and indicates excellent contact between the plies and VHB, with no voids (blue colored regions) detected.

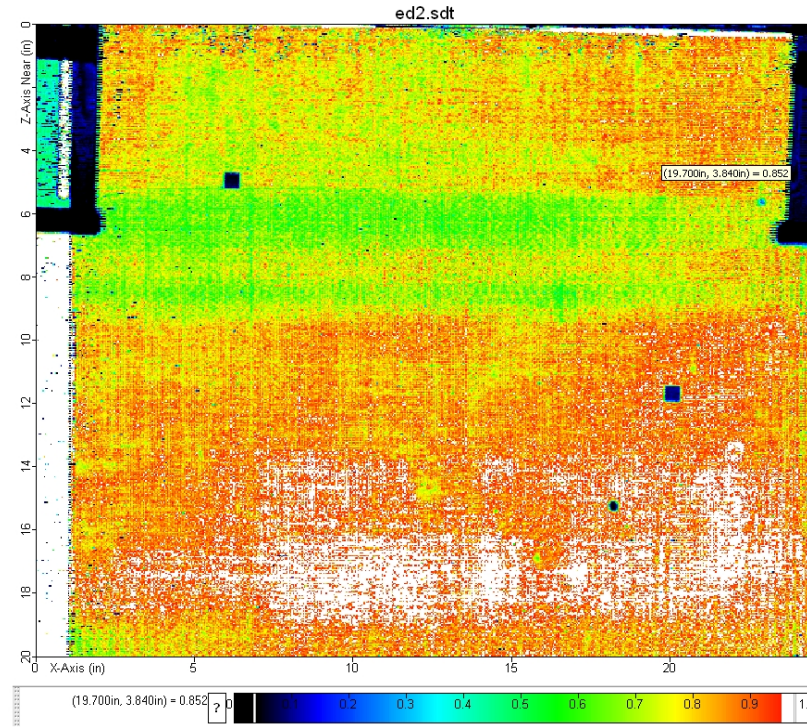


Figure 40: NDI scan of improved post-bonded face-sheet/VHB/face-sheet layup. Small blue squares are pads used for testing, and not voids. White regions are above sensing range, but still indicate excellent adhesion.

Complex modes were extracted from experimental modal analysis data, and loss factors and resonance frequencies were compared for the two panels. Figure 41 shows a few of the measured mode shapes, which are clean and symmetric, providing confidence in the quality of the panel construction. Figure 42 compares the modal loss factors for the two panels for frequencies up to about 5 kHz. The post-bond approach consistently yields higher damping, and both construction approaches lead to strong damping improvements at 1 and 3 kHz, where the dominant transmission tones occur. Based on these data, the post-bond approach was used for the optimized panel, and a nominal panel structural damping value of 0.05 is assumed for acoustic performance simulations. However, this construction technique is costlier and more time consuming than a co-cured approach. Bell will weigh performance and cost should it decide to pursue the optimized panel concept in future rotorcraft.

Replacing the center carbon layer reduces the face sheet stiffness, thereby reducing the flexural wavespeeds. The measured mode shapes may be used to estimate modal wavenumbers, which combined with modal frequencies determine modal wavespeeds (see Appendix C for details on the approach). Figure 43 shows the inferred modal wavespeeds for the two panels along with a least-squares data fit using thin plate theory and the wavespeed of the baseline sandwich panel. The baseline panel properties were used to infer the modulus for the optimized panel facesheets, which have the center ply replaced with 3M VHB 9469 adhesive. Using the baseline sandwich panel properties, it was found that the sample panel wavespeed reasonably matches the modal wavespeed estimates if the sample panel facesheet wavespeed is about 80% of the baseline panel facesheet wavespeed and the

shear wavespeed is the same. To infer the sample panel facesheet modulus, thin plate theory was used along with the ratio of the wavespeeds:

$$\frac{c_{b,fs,sample}}{c_{b,fs,baseline}} = \frac{\sqrt[4]{D_s/\rho_s h_s}}{\sqrt[4]{D_b/\rho_b h_b}} = \frac{\sqrt[4]{E_s h_s^2/12(1-\nu_s^2)\rho_s}}{\sqrt[4]{E_b h_b^2/12(1-\nu_b^2)\rho_b}} = 0.8. \quad (13)$$

The panel thicknesses and Poisson’s ratio are approximately the same while the ratio of the densities is about 0.75. The final estimate of the facesheet modulus then becomes $E_s=0.3E_b$, a significant reduction. The reduced stiffness and wavespeed will lead to higher acoustic coincidence frequencies.

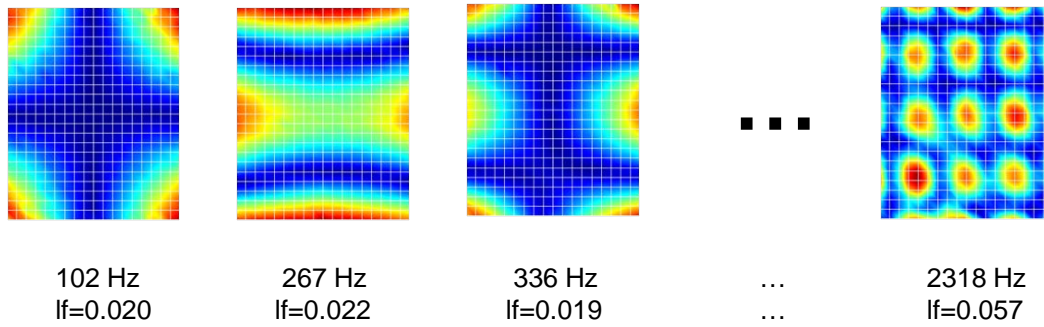


Figure 41: Selected measured mode shapes and loss factors of post-bond test coupon.

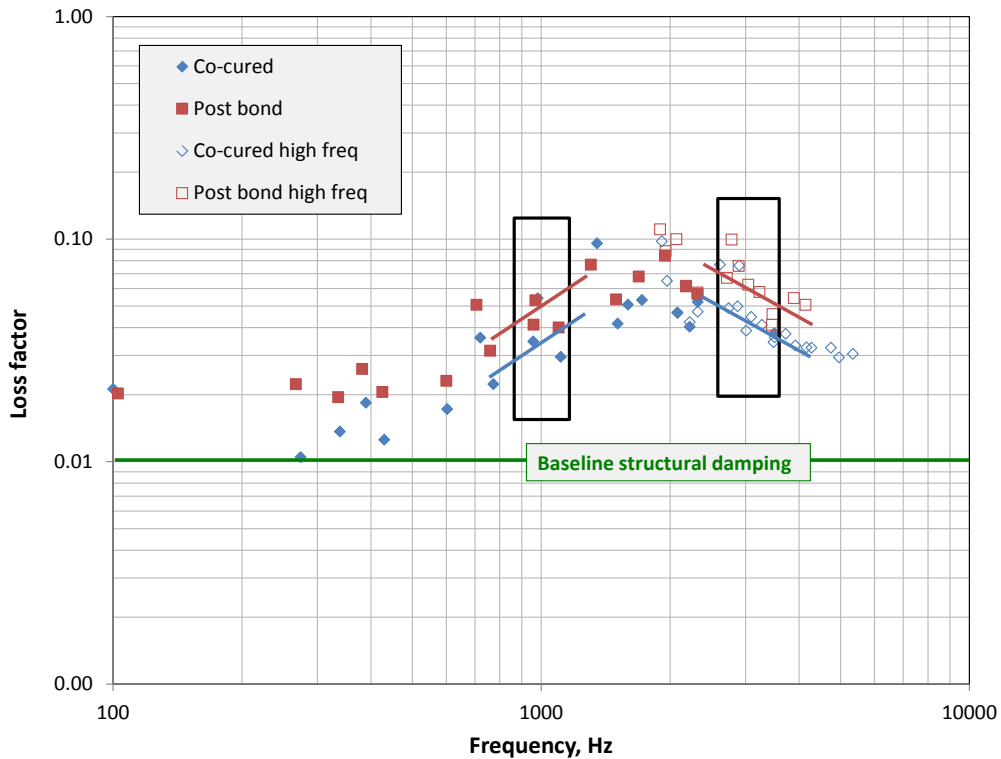


Figure 42: Measured structural loss factors for two test coupons with embedded VHB 9469.

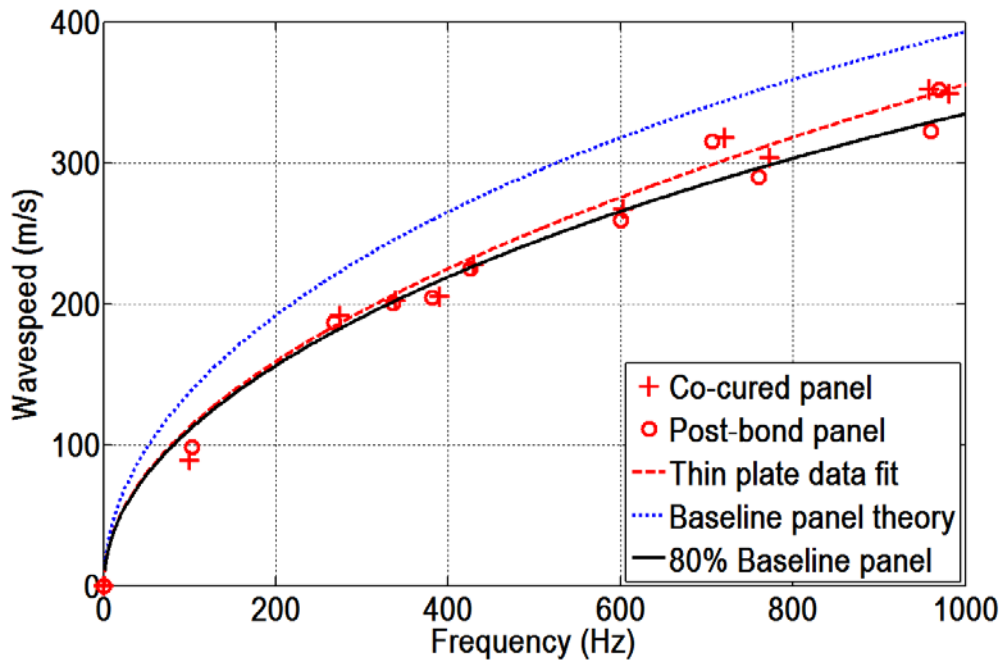


Figure 43: Flexural wavespeeds for baseline and test coupon cross-section.

The panels also provide an opportunity to verify the FE modeling procedure for sandwich panels with layers of VHB material. Figure 44 shows a schematic of the cross-sectional modeling of the panels. The coupon was modeled with 4,370 parabolic solid elements. Each ply layer was modeled with one element through its thickness, and four elements represent the Kevlar core. The ribbon direction was modeled along the length of the panel. The adhesive layers between the inner plies and the core were not modeled explicitly, but the layer masses were simulated instead by increasing the adjacent ply mass densities from 0.311 kg/m^2 (0.000443 lb/in^2) to 0.558 kg/m^2 (0.000793 lb/in^2). The final modeled (0.757 kg) and measured (0.753 kg) masses match almost exactly.

The viscoelastomer Young's Moduli were varied over several center frequencies per the data shown in Figure 39. The Poisson's ratio was set to 0.499. Modes of the panel with free boundary conditions were extracted using NASTRAN for each property set, and modal frequencies were determined based on proximity to the center frequency of each set. Figure 45 compares the measured and simulated resonance frequencies, which agree to within $\pm 4\%$. Figure 46 compares measured and simulated structural loss factors, which agree well for frequencies above 1 kHz. Below 1 kHz, the simulated loss factors are higher than the measured ones. However, since this project focuses on frequencies between 1 and 4 kHz, we have not pursued the cause of this discrepancy. Overall, the good agreement between measured and predicted resonance frequencies and loss factors confirm the modeling procedure and the underlying material properties.

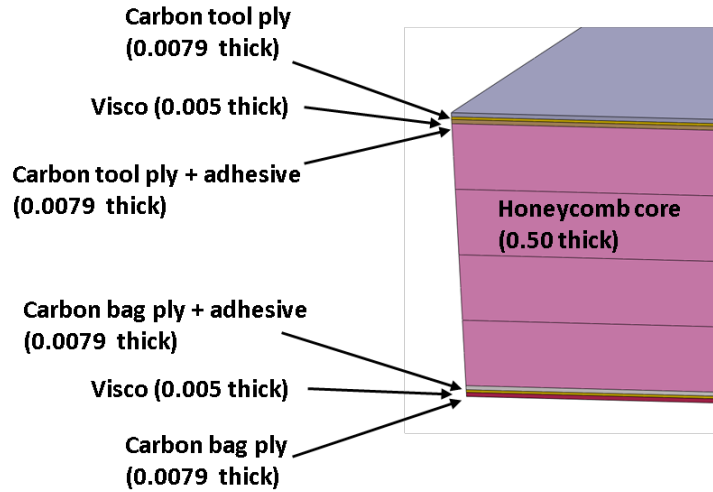


Figure 44: FEM model for test coupons with embedded VHB material.

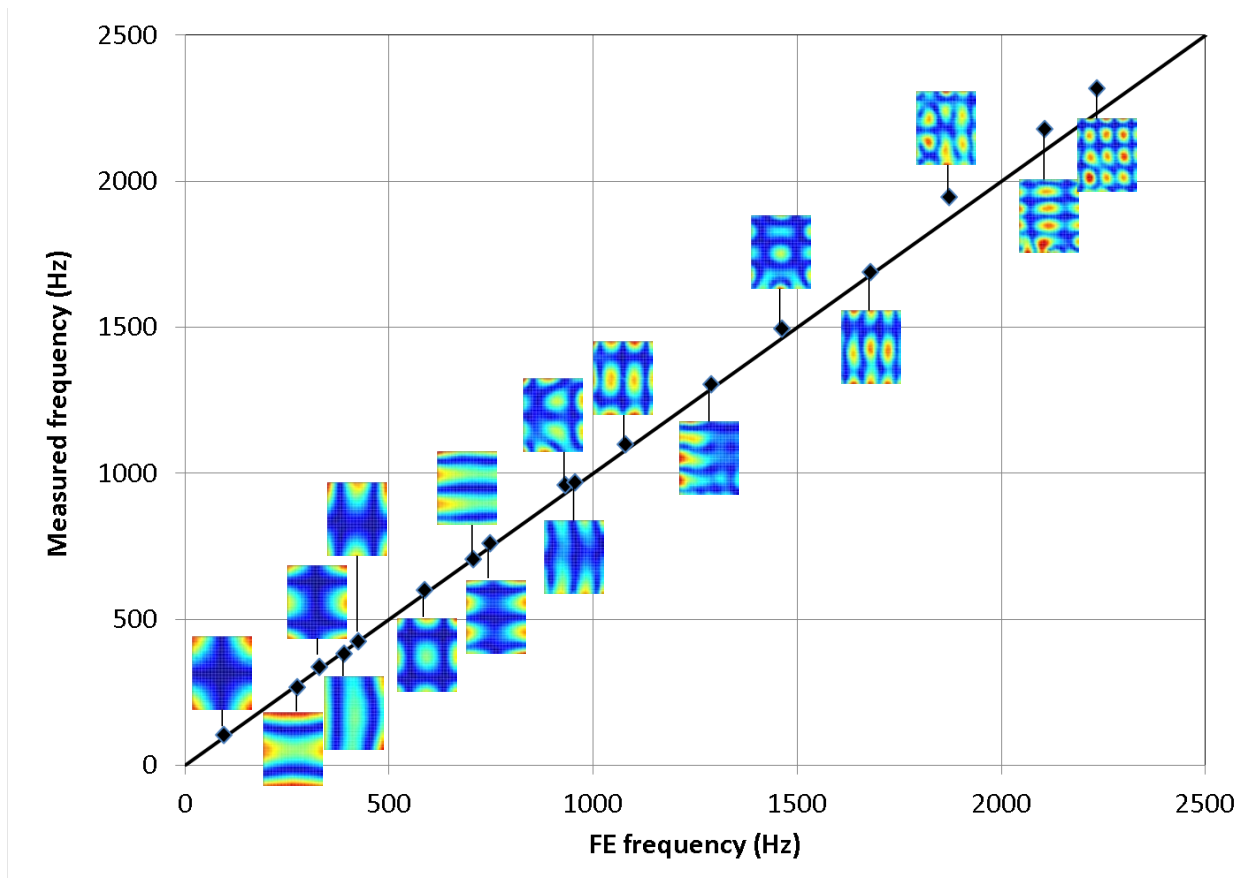


Figure 45: FE vs. measured resonance frequencies for test coupon with embedded VHB 9469 and free boundary conditions.

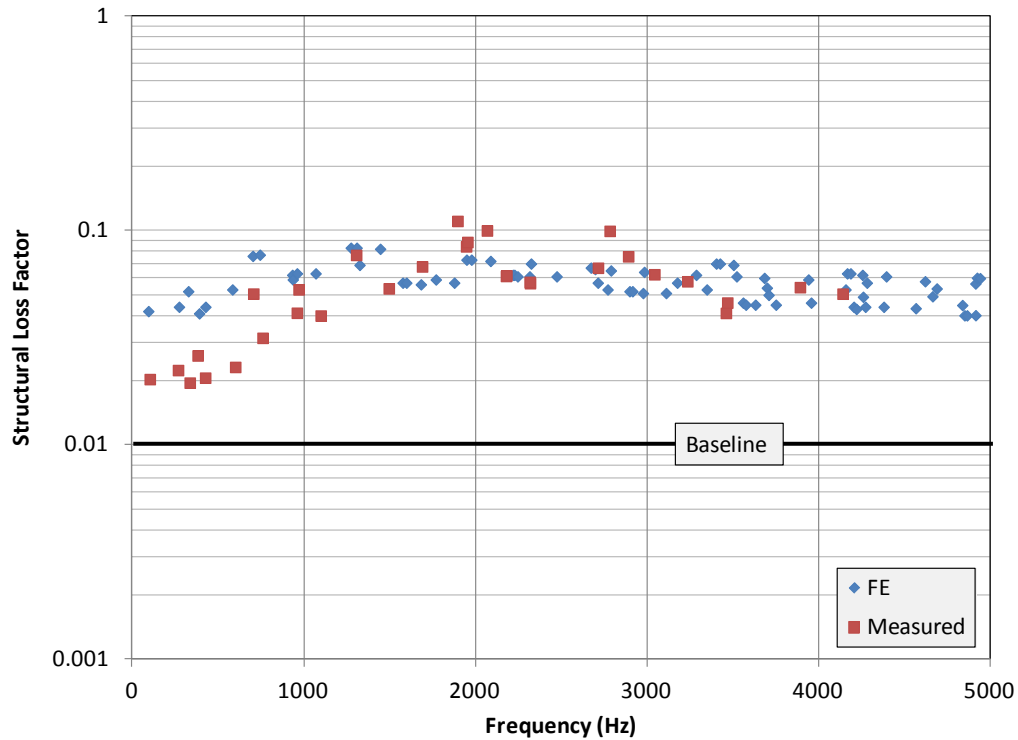


Figure 46: FE vs. measured damping loss factors for test coupon with embedded VHB 9469.

3.2.3.3 Projected performance improvement with embedded VHB 9469

The structural damping of the baseline panel FE/BE model was increased from 0.01 to 0.05 based on the test coupon measurements. The acoustic sound power transmission loss calculations were repeated, and compared to the baseline panel TL in Figure 47. The increased damping leads to about a 4 dB noise reduction, which while helpful, is not spectacular. Other means of improving noise transmission are therefore still required.

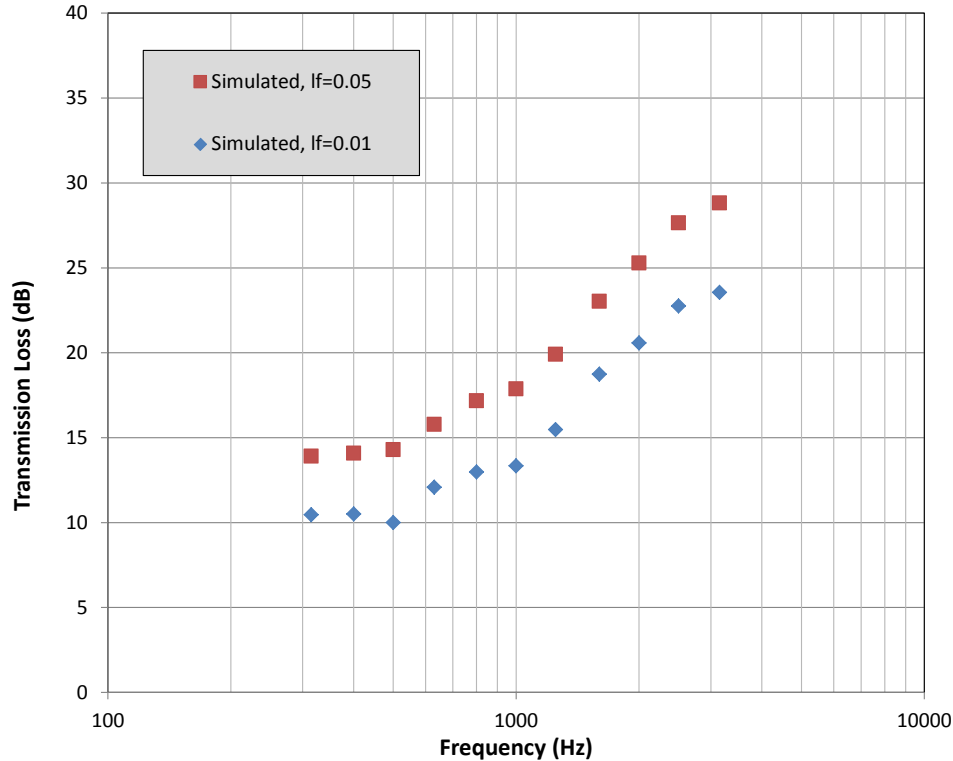


Figure 47: CHAMP simulations of the effects of VHB on baseline panel.

3.2.4 Band-Gap/Phononic Crystal Structure-borne Sound Barriers

Phononic crystals, or arrays of structural discontinuities, can mitigate structure-borne sound transmission of waves in certain frequency ranges. A formulation for the exact solution for multiple scattering of flexural waves in a thin plate has been obtained. A technical report that contains all the details of the formulation is provided in Appendix E. The problem consists of an array of inclusions, of an arbitrary number and arrangement, embedded in a thin plate, and the multiple scattering of a planar incident wave is analyzed. The key assumptions in the formulation include: the plate is thin (hence the classical thin-plate theory is used), uniform in its mechanical and geometrical properties, and has an infinite extent. Three types of inclusions (scatterers) have been included in the formulation:

- **Voided:** mathematically this assumes that the perimeter of the inclusion is free of forces and moments. Physically this represents drilled through-thickness holes in the plate.
- **Rigid:** mathematically this assumes that the perimeter of the inclusion is clamped, and hence both the displacement and slope vanish.
- **Elastic:** this assumes that inclusions are thin plates. Mathematically this requires the continuation of the displacement and slopes across the interface. Although the classical thin-plate theory may not be valid for the inclusions when the diameter of the inclusions is in the same order as their thickness, it is assumed that the classical thin-plate theory remains valid as the first order approximation.

The formulation has been implemented as computer code so that simulations for the wave transmission effects with various material and geometric configurations can be performed. In the simulations here, the inclusions are considered rigid. Some preliminary simulation results are presented and discussed in the following. In this set of simulations, only a simple geometry is considered: the scatterers are all identical, of a radius of 0.015 m (30 mm diameter), and are spaced 0.05 m apart, in a square arrangement. The simulations are run at a few discrete frequencies of interest: 1 kHz, 3 kHz, 6 kHz, and 10 kHz.

3.2.4.1 Voided Inclusions

The amplitude of the wave field in the vicinity of the voids is shown in Figure 48. In this figure, the upper left corner is for $f = 1$ kHz, the upper right corner is for $f = 3$ kHz, the lower left corner is for $f = 6$ kHz, and the lower right corner is for $f = 10$ kHz. The color scale has a maximum of 2.5 (red), and minimum of 0 (blue).

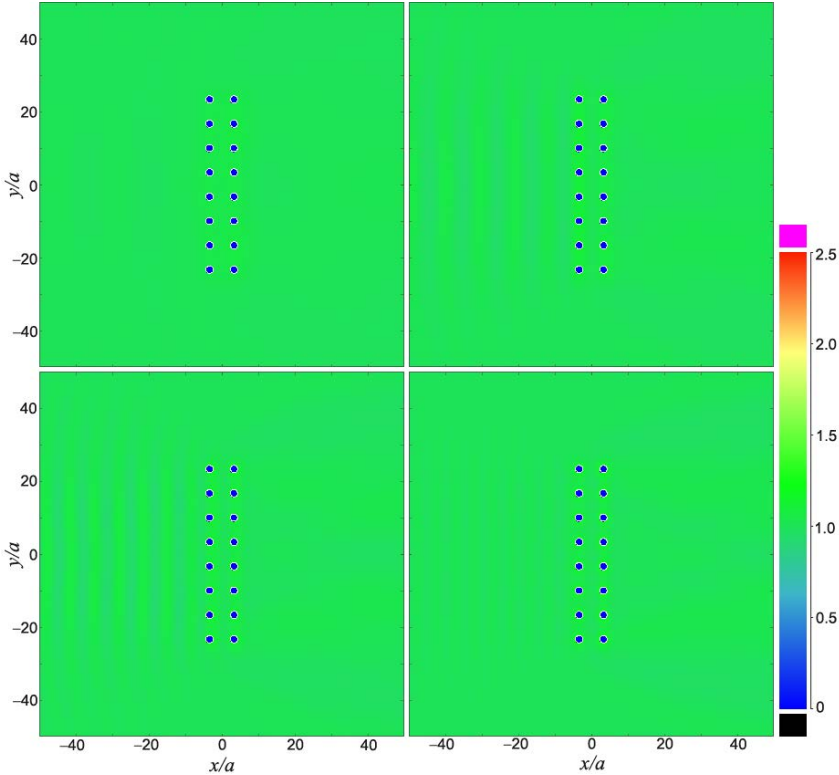


Figure 48: Amplitude of acoustic pressure surrounding the void inclusions at four frequencies: 1 kHz (upper-left), 3 kHz (upper-right), 6 kHz (lower left), and 10 kHz (lower-right).

It can be seen from this figure that the scattering effects are extremely weak at all four frequencies. There are only slight traces of reflection at 3 kHz and 6 kHz.

3.2.4.2 Rigid Inclusions

Similarly, Figure 49 shows the amplitude near the rigid inclusions at the same four frequencies. In this case the scattering effects are very strong. In fact they are so strong that wave transmission is prohibited almost entirely. And they are effective in all the four frequencies computed. In other words, there is virtually no frequency dependency. In essence, the scatterers effectively form a wall that blocks the transmission of the wave.

3.2.4.3 Elastic Inclusions

For elastic materials, there are wide ranges of values for different material properties. A series of simulations are performed in which the inclusion's flexural rigidity and mass density change proportionally relative to those of the plate, which represent a most common characteristic in natural materials. Results of two most representative cases are presented here. In the first case, the inclusion's flexural rigidity is 100 times of that of the plate, and the mass density is 10 times of the plate. This case is designated as "hard elastic" case. In the second case, the inclusion's flexural rigidity is 0.01 times of that of the plate, and the mass density is 0.1 times of the plate. This case is designated as the "soft elastic" case. The resulting wave fields at those four frequencies near these elastic inclusions are shown in Figure 50 and Figure 51. It can be seen that neither case provides an effective barrier for the wave transmission. Furthermore, it appears that a hard elastic inclusion is not as strong a scatterer as a soft elastic inclusion.

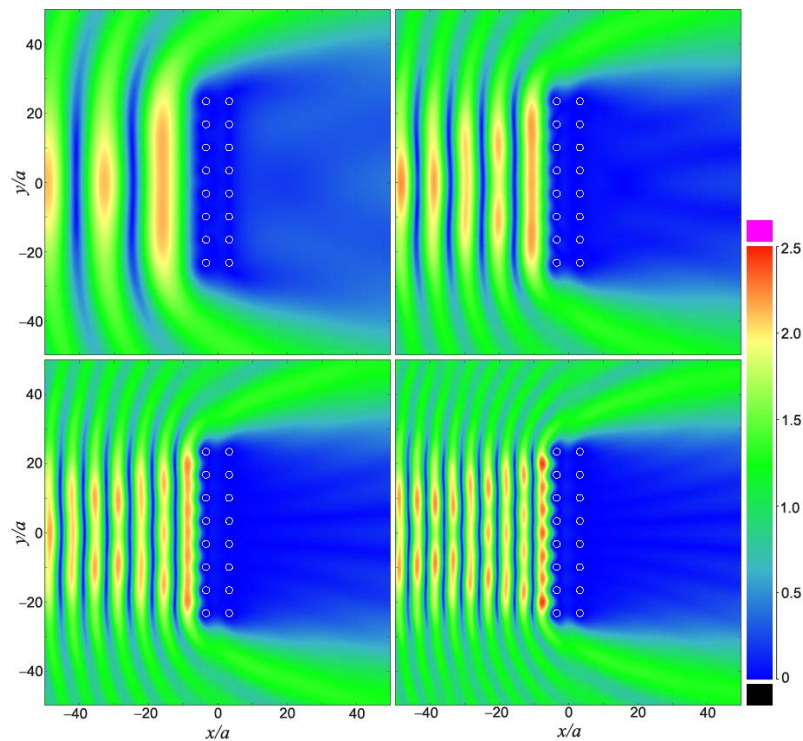


Figure 49: Amplitude of acoustic pressure surrounding the rigid inclusions at four frequencies: 1 kHz (upper-left), 3 kHz (upper-right), 6 kHz (lower left), and 10 kHz (lower-right).

3.2.4.4 Discussion of Simulation Results

This set of cursory (preliminary, rather than systematic) simulations indicates that, except the case of rigid inclusions, the scattering effects in all other cases are very weak. Aside from the obvious reason that the inclusions in those cases are “weak scatterers,” the more important reason is that the arrangements do not match the conditions that are needed for band gap formation. Typically a phononic band gap forms when the wavelength in the host (the thin plate) approaches the spacing between the adjacent scatterers. In the base sandwich panel, at 3 kHz, the wave speed is around 650 m/s (according to Figure 15), which gives a wavelength of ~ 0.22 m. This wavelength is much greater than the spacing and hence in the low-frequency regime, the inclusions provide very little impedance. Even at 10 kHz, the highest frequency in the simulations, the wavelength is ~ 0.14 m, still far greater than the spacing.

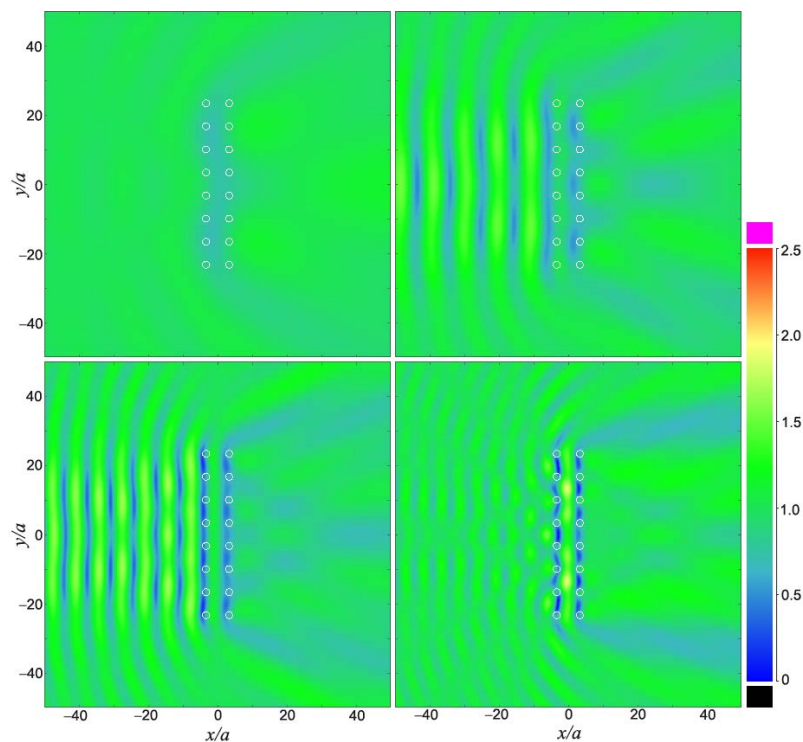


Figure 50: Amplitude of acoustic pressure surrounding the soft elastic inclusions at four frequencies: 1 kHz (upper-left), 3 kHz (upper-right), 6 kHz (lower left), and 10 kHz (lower-right).

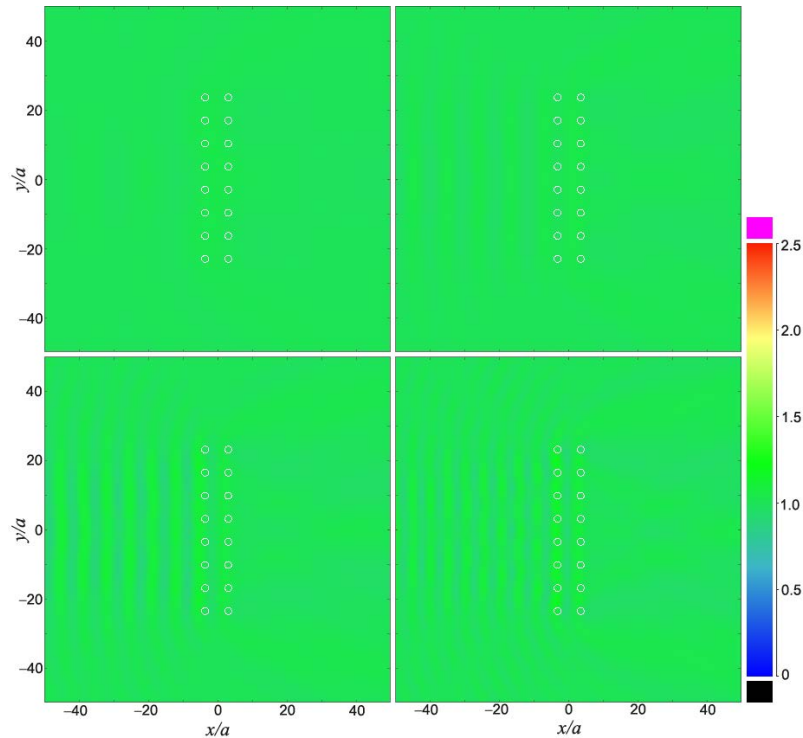


Figure 51: Amplitude of acoustic pressure surrounding the hard elastic inclusions at four frequencies: 1 kHz (upper-left), 3 kHz (upper-right), 6 kHz (lower left), and 10 kHz (lower-right).

There are two directions that can be explored to address this issue and to bring a band gap into the picture. One is to reduce the sound speed in the sandwich panel. The potential challenge with this direction is that the changes thus incurred to the sandwich panel compromise the structural stiffness requirements. The second direction is to enlarge the spacing. For example, for targeting the noise reduction at 3 kHz, the scatterers can be arranged with a spacing of $\sim 0.25\text{-}0.27\text{m}$. The potential problems with this direction are that an increasing the spacing usually would correspondingly require a larger inclusion size; and that the overall size of the sandwich panel ($0.9\text{m} \times 0.9\text{m}$) may not allow a sufficient number of inclusion for the band gap to form. Of course, it is also possible to explore the combination of these two directions.

3.2.4.5 Proposed Design to Rigidify the Inclusions

Probably the most feasible, and if successful, the most effective, way to introduce the band gap effect for suppressing the wave transmission is to take a closer look at the “exception case”: the rigid inclusions.

In many theoretical studies, an elastic solid can be used to approach void or a rigid body by setting its material properties to extreme. However, in the set of simulations that has been performed for elastic inclusions, setting the flexural rigidity of the elastic inclusion to an extremely high value (such as 10^9 times of the thin plate) does not bring a scattering effect that even remotely resembles the rigid inclusion case.

A closer look reveals the following underlying reason: the boundary conditions for the rigid inclusions are a mathematical idealization, and actually are not a real physical rigid inclusion. For a physical inclusion of extremely high rigidity but having the same thickness of the plate, the inclusion may undergo rigid body translations and rotations, collectively called rigid body motions. However, the mathematical boundary conditions for the so-called rigid inclusion prevent such rigid-body motions completely. This set of mathematical boundary conditions can be physically realized as having the inclusions not only rigid, but also fixed in space. This insight prompted the proposal of the following mechanism to prohibit or impede rigid body motions of the inclusions.

In the proposed design, called *stiffened inclusions*, the inclusions are much longer than the thickness of the plate so their ends protrude out of the thin plate. These ends are bound to a stiffening panel, one on each end of an inclusion. Finally, to reduce the added weight, the center portions of the stiffening panels are eliminated. A 3D rendering of this conceptual design of such stiffened inclusions is shown in Figure 52.

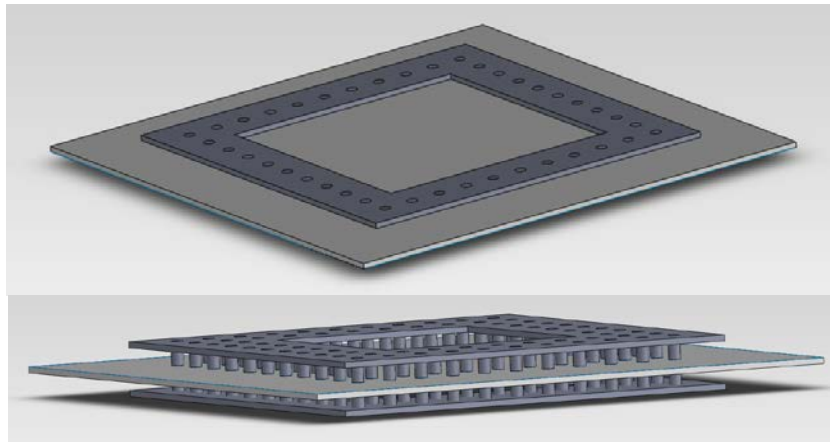
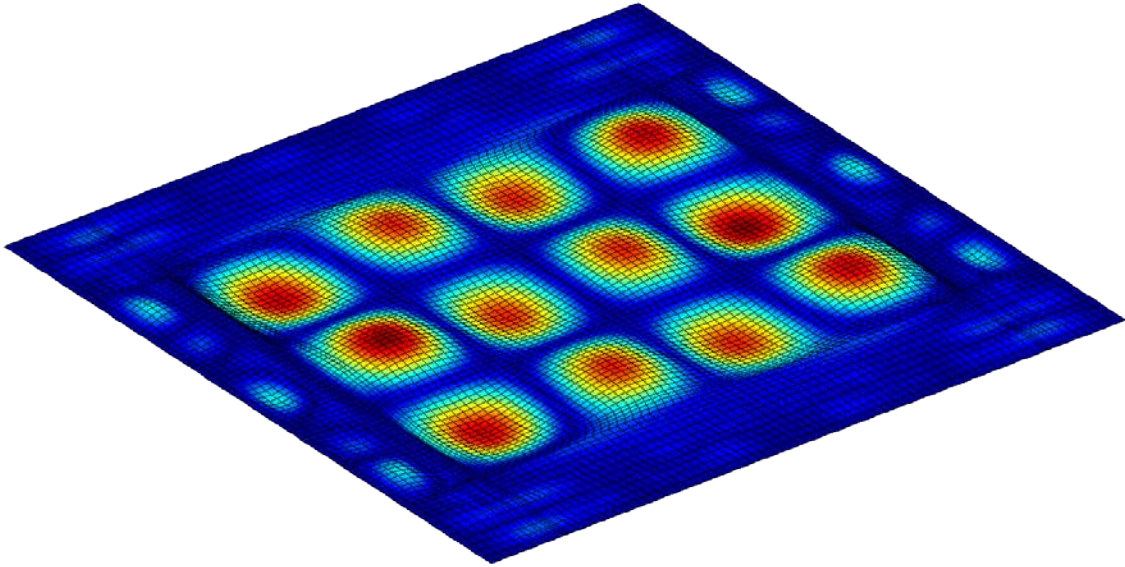


Figure 52: 3-D solid model rendering of "stiffened inclusions" concept design.

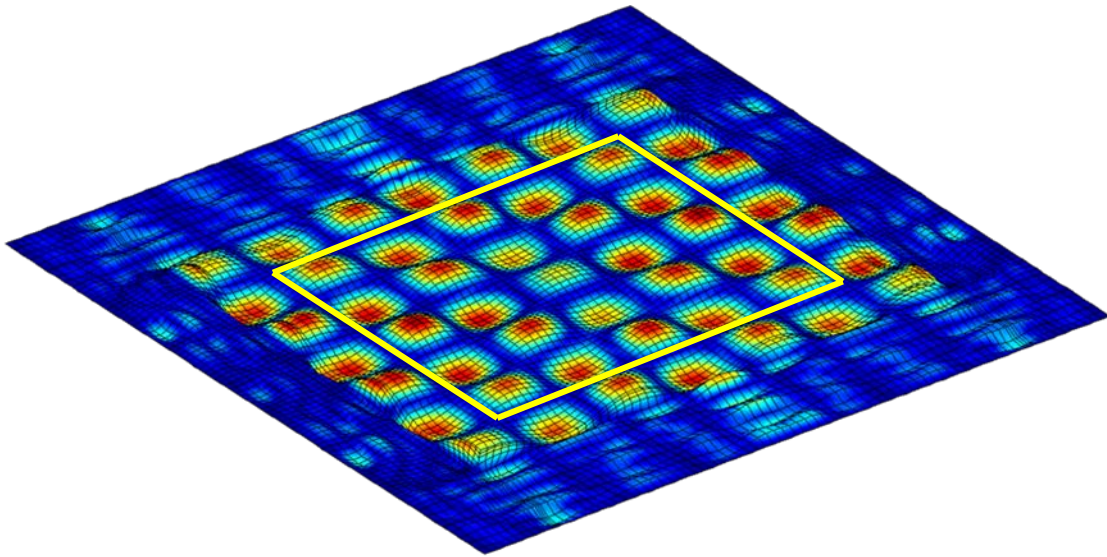
In this proposed structure, because the ends of the inclusions are all tied together, the rigid body rotation of individual inclusions is essentially eliminated, and the only possible motion is the rigid body translation. The rigid body translations of individual inclusions are further greatly impeded because those stiffening panels, along with the inclusions, form another sandwich panel with significantly higher rigidity (because of much larger thickness), and in essence, eliminates the rigid body translation.

3.2.4.6 Band-gap target frequency range

The stiffened inclusion concept was evaluated using the baseline panel design. There are two main frequencies of interest near critical transmission noise tones - 1 and 3 kHz. Typical mode shapes of the baseline panel near those frequencies are shown in Figure 53. While the structural wavelengths are too long for a practical inclusion array to be effective, a 3 kHz array seems feasible. To minimize interaction of the array with nearfield evanescent waves near the beams, an offset of a few inches is required.



Acoustic wavelengths are $\sim 4/5$ that of structural wavelengths at 1 kHz



Acoustic wavelengths are $7/16$ that of structural wavelengths at 3 kHz

Figure 53: Structural and acoustic wavelength estimates at 1 and 3 kHz. Yellow rectangle indicates potential region for stiffened inclusion array.

3.2.4.7 Effective Panel Properties

The multiple scattering analysis/simulation is based on the classical thin-plate model, in which the thin plate is assumed to be uniform and isotropic. However, the sandwich roof panel behaves more like a thick panel. Fortunately, we can still use the plate scattering analysis simulation procedure near a target frequency (3 kHz for this application) by computing an equivalent flexural rigidity at that frequency. The

parameters that characterize the wave propagation are the thickness h , the mass density ρ and the flexural rigidity D of the plate. The total thickness and the mass density are calculated based on the physical configuration of the panel, giving $h = 13.9$ mm and $\rho = 223.3$ kg/m³. The equivalent flexural rigidity is calculated according to sandwich panel bending wave speed c_b based on the following relation in the thin-plate model:

$$D = \frac{c_b^4 \rho h}{\omega^2} \quad (14)$$

where $\omega = 2\pi f$, and f is the wave frequency. The thus-retrieved flexural rigidity is shown in Figure 54. The sonic crystal will be targeted to have a stop band centered around 3000 Hz. From Figure 54, a flexural rigidity of 836 N-m is chosen for the thin-plate model, which gives a wave speed of 556 m/s at 3000 Hz. The wave speed in the thin-plate model for frequencies up to 8000 Hz is plotted in Figure 55, where the wave speed based on thick-plate model is also plotted for comparison, showing a good match at 3000 Hz.

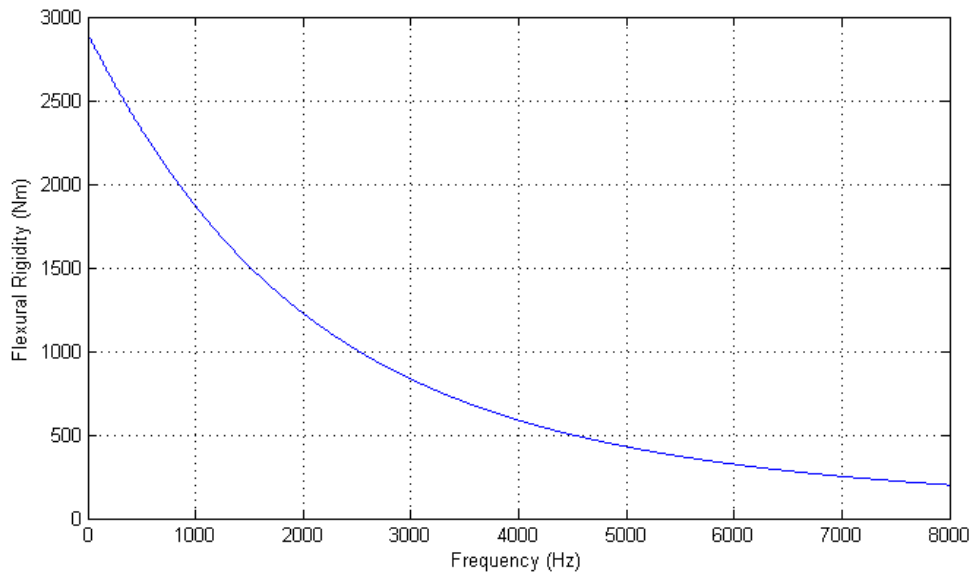


Figure 54: Equivalent flexural rigidity from the wave speed based on a thick-plate model.

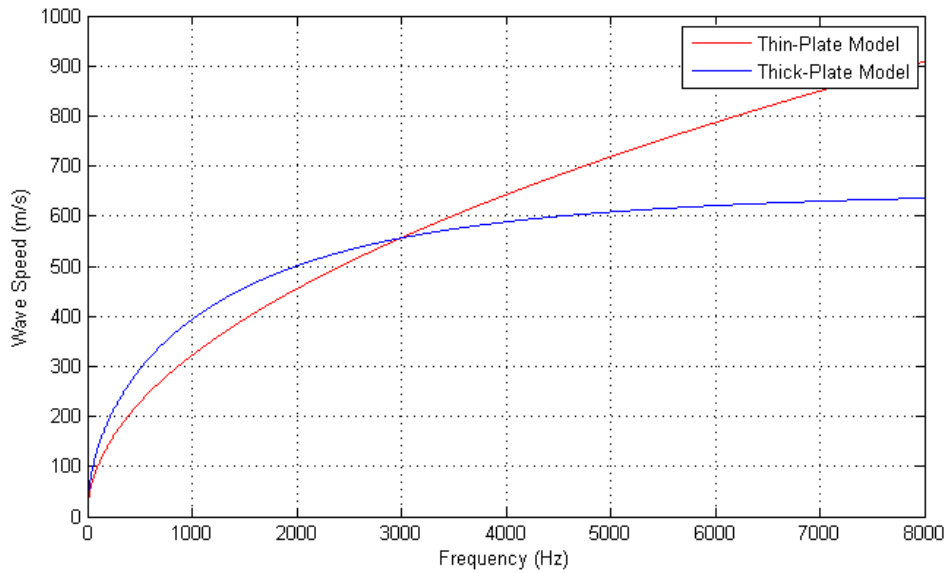


Figure 55: Wave speed for the thin-plate model based on the equivalent flexural rigidity at 3000 Hz (red), compared with estimate based on the thick-plate model (blue).

3.2.4.8 Initial Design

Commercial off-the-shelf inserts, such as those shown in Figure 56, may be used as the array elements. Such inserts provide the entire surface of the through hole in the inserts as an adhesion surface. The weaknesses of this choice are the added weight and the significant reduction of the radius of the rods, reducing the rigidity of the overall inclusion assemblage. In numerical simulations, the inclusion's radius will be the radius of the insert, which is somewhere between those of the flanges and the housing. In this choice, the inclusion will be solid steel or fiber reinforced composite rods.



Figure 56: Various forms of potted inserts for sandwich panels. (Taken from the web site of the provider: http://www.clipnuts.com/potted_in_inserts.html)

Some of the parameters used in the simulation are selected in advance:

- At least two rows of inclusions are required based on preliminary scoping studies. Three rows can achieve a better performance but takes up significantly more of the panel's surface.
- The spacing of the inclusions is between 50.8 and 152.4 mm (2 and 6 inches). Denser packing would enhance the wave blockage effect, but risks reducing the overall structural integrity of the panel. Larger spacing would reduce the wave blockade effect.
- The radius of the inclusions is between 5 and 15 mm (diameter: from 10 to 30 mm).

Two initial designs, both of square arrangements, are assessed for the optimized panel

- **Design A:** $r = 15$ mm, $d = 56$ mm; and
- **Design B:** $r = 15$ mm, $d = 100$ mm.

where r is the radius of the rigid inclusion, and d is the side length in a square unit cell. The difference between the two designs is that, physically, Design A targets the first band gap (3 kHz); whereas Design B targets the second band gap (1 kHz). Their transmission spectra for the baseline panel are shown in Figure 57. The band gap central frequency for Design A (red) is already near 3000 Hz (actually 3500 Hz).

Next, the arrangements are finely tuned such at the central frequency is located closer to 3000 Hz.

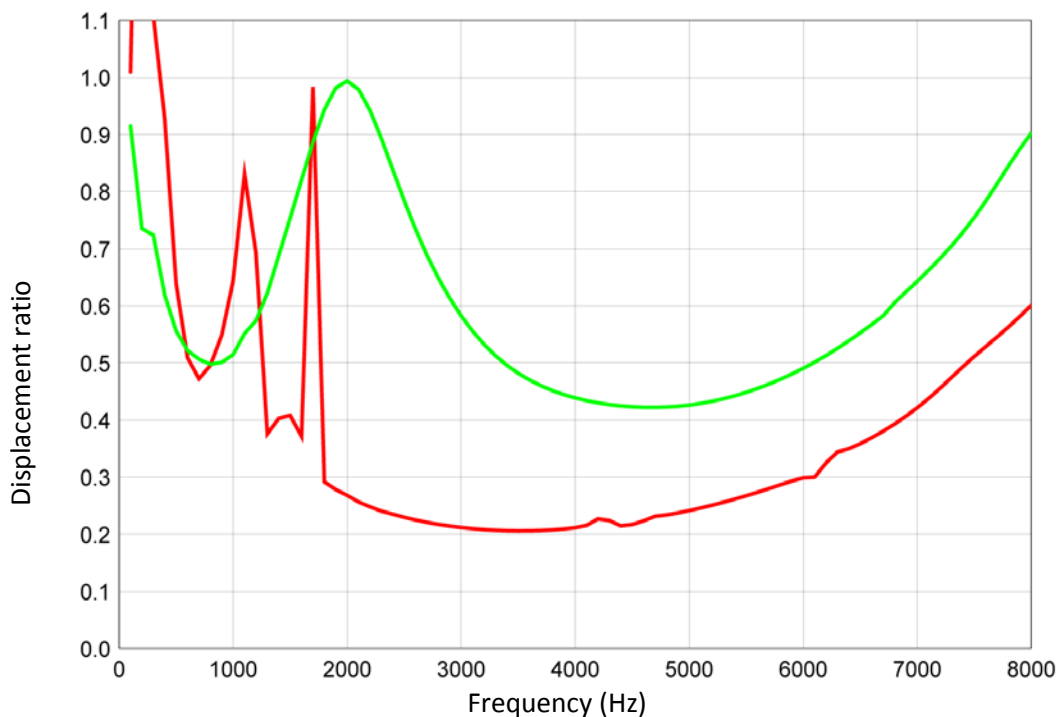


Figure 57: The forward displacement power ratios for the two initial designs. Red: Design A; Green: Design B.

3.2.4.9 Tuning Design A

The radius of the inclusion is varied while the spacing remains unchanged. The radius r is varied in both directions, ranging from 13 mm to 17 mm in 1 mm increments. The resulting spectra are shown in Figure 58. The variation of the gap's central frequency with the radius is shown in Figure 59. It is also noted that as r increases, the bottom of the gap appears very flat.

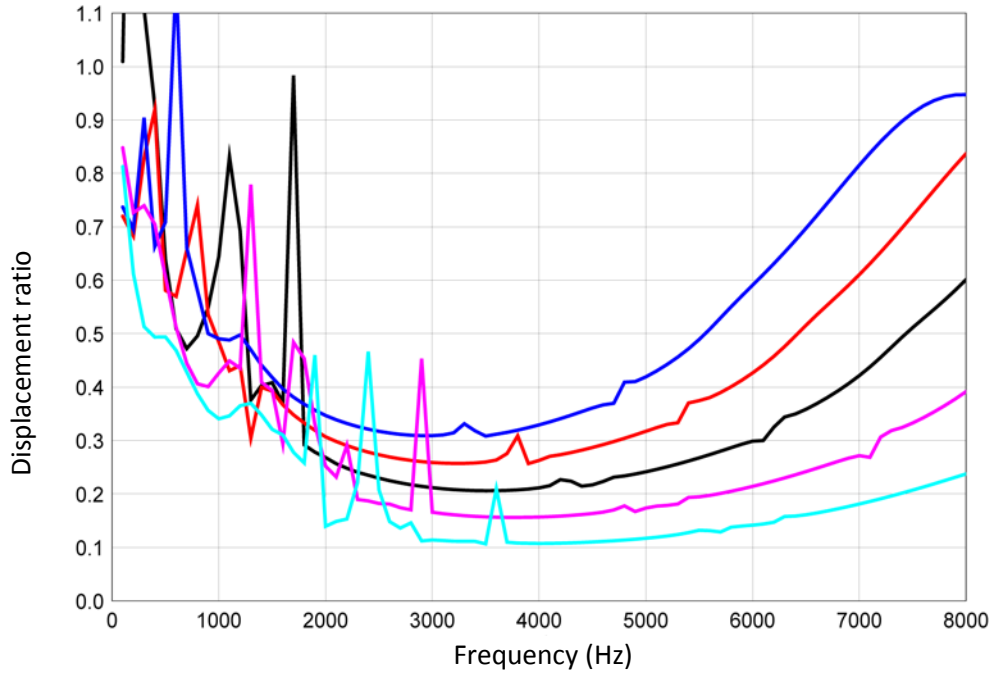


Figure 58: Forward displacement spectra with different inclusion radius: blue: $r = 13$ mm, red: $r = 14$ mm; black: $r = 15$ mm; purple: $r = 16$ mm; turquoise: $r = 17$ mm.

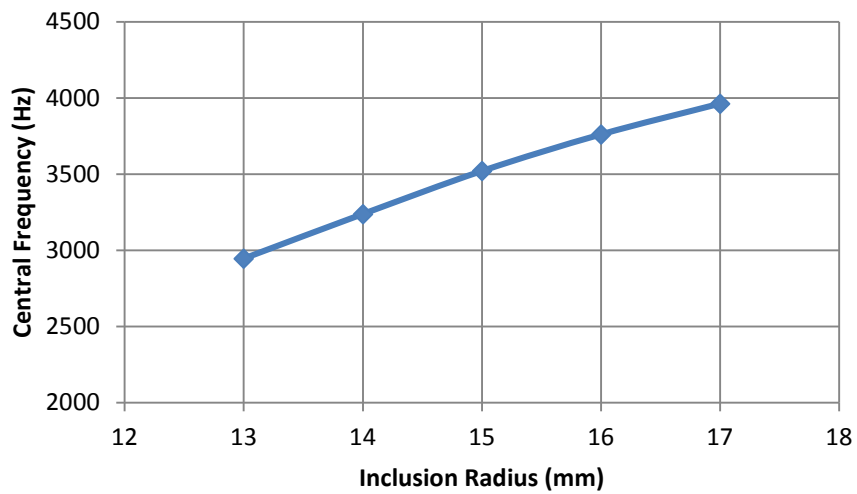


Figure 59: Variation of the central frequency of the band gap with the inclusion radius r .

Similarly, while r remains unchanged (at $r = 15$ mm), the spacing d is varied, from 56 mm to 64 mm in 2 mm intervals. The resulting spectra are shown in Figure 60; and the variation of the central frequencies with the spacing d is shown in Figure 61.

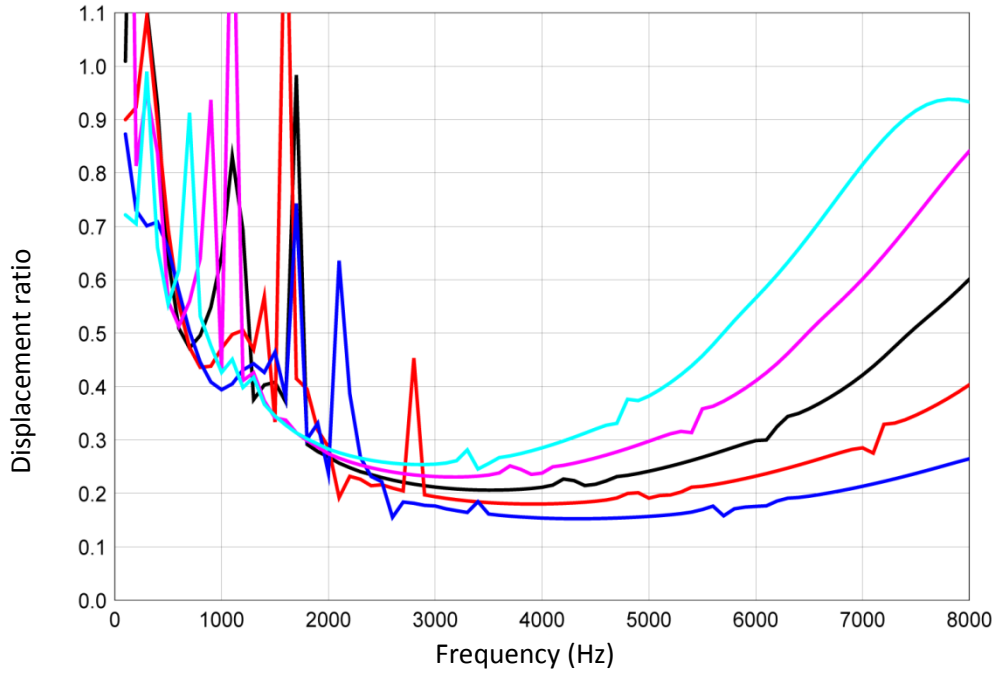


Figure 60: Forward displacement spectra at different spacing at a fixed inclusion radius $r = 15$ mm. Blue: $d = 56$ mm; Red: $d = 58$ mm; Black: $d = 60$ mm; Purple: $d = 62$ mm; Turquoise: $d = 64$ mm.

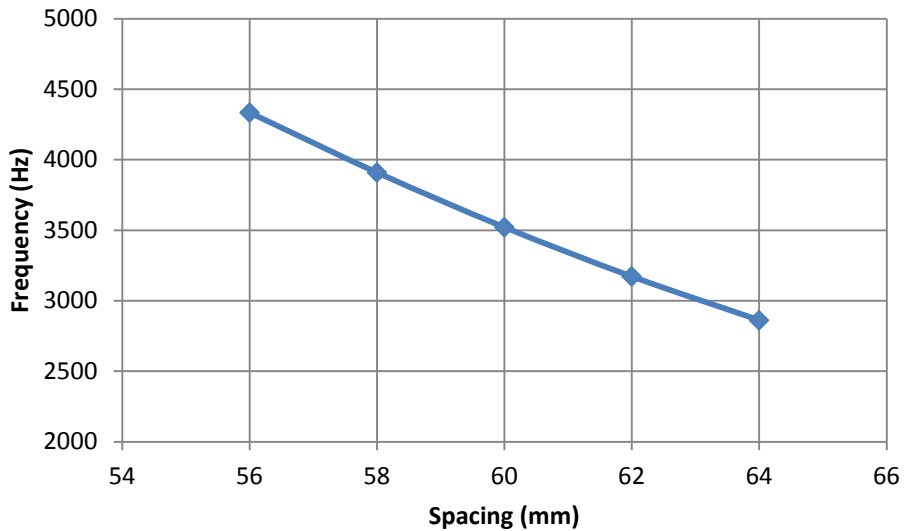


Figure 61: Variation of the band's central frequency with spacing while the inclusion radius is fixed at $r = 15$ mm.

It can be seen that adjusting either r or d can fine tune the band gap. In general, a larger inclusion radius results in a lower transmission coefficient. Thus, $r = 15 \text{ mm}$ is selected, and the spacing, based on a simple interpolation in Figure 61, is chosen as $d = 63 \text{ mm}$.

3.2.4.10 Tuning Design B

The radius of the inclusions is varied, from 15 mm to 20 mm in 1 mm increments, while the spacing is fixed at $d = 100 \text{ mm}$. The resulting spectra are collected in Figure 62. The variation of the central frequency with the radius is shown in Figure 63. It can be seen that shift of the central frequency is rather limited by varying the radius. Since the gap has a central frequency near 4700 Hz, it would require a significant decrease in radius to shift the band gap to the left. This would deteriorate the performance of the band gap. In other words, it is impractical to move the band gap by adjusting the radius alone.

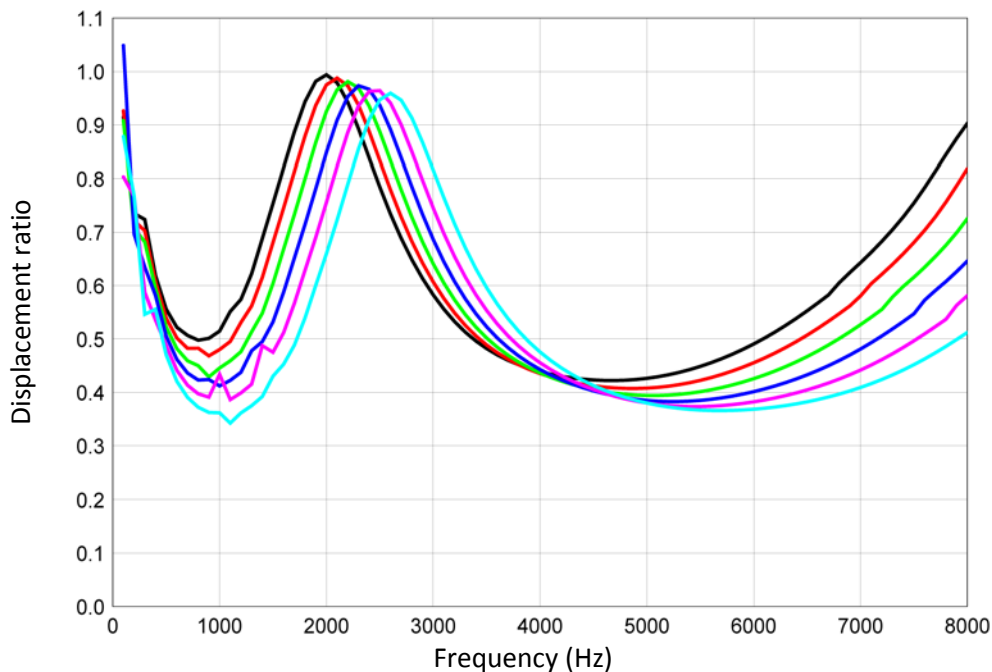


Figure 62: Forward displacement spectra with different inclusion radius: black: $r = 15 \text{ mm}$, red: $r = 16 \text{ mm}$; green: $r = 17 \text{ mm}$; blue: $r = 18 \text{ mm}$; purple: $r = 19 \text{ mm}$; turquoise: $r = 20 \text{ mm}$.

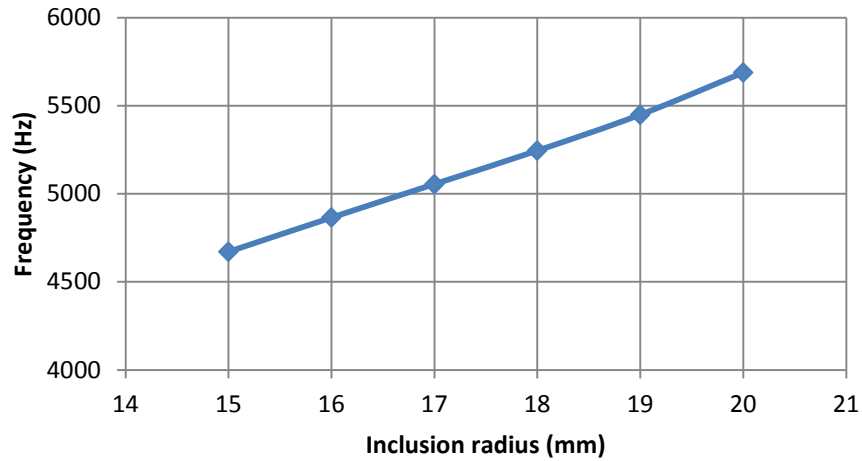


Figure 63: Variation of the central frequency of the band gap with the inclusion radius r .

Increasing the spacing would shift the central frequency to the lower range. Since this is the only parameter to be adjusted, variable step sizes are used. The calculated spacings are $d = 100$ mm, 110 mm, 115 mm, 120 mm. By 120 mm, the central frequency is below 3000 Hz. The collected spectra are shown in Figure 64. The variation of the central frequency with spacing is shown in Figure 65.

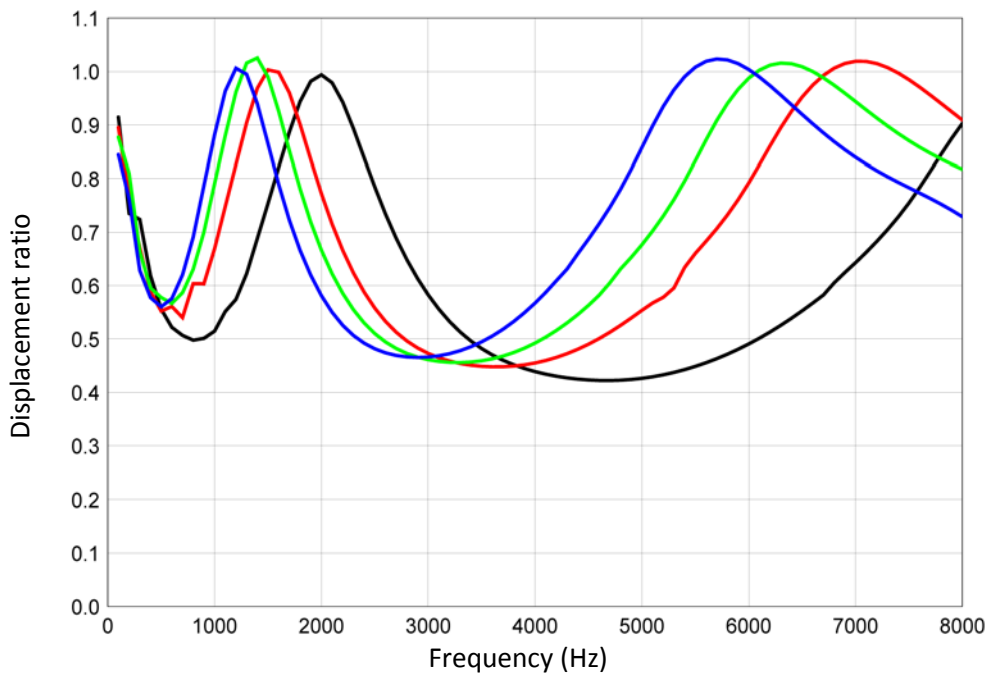


Figure 64: Forward displacement spectra with different spacing while the inclusion radius is kept at $r = 15$ mm. Black: $d = 100$ mm, red: $d = 110$ mm; green: $d = 115$ mm; blue: $d = 120$ mm.

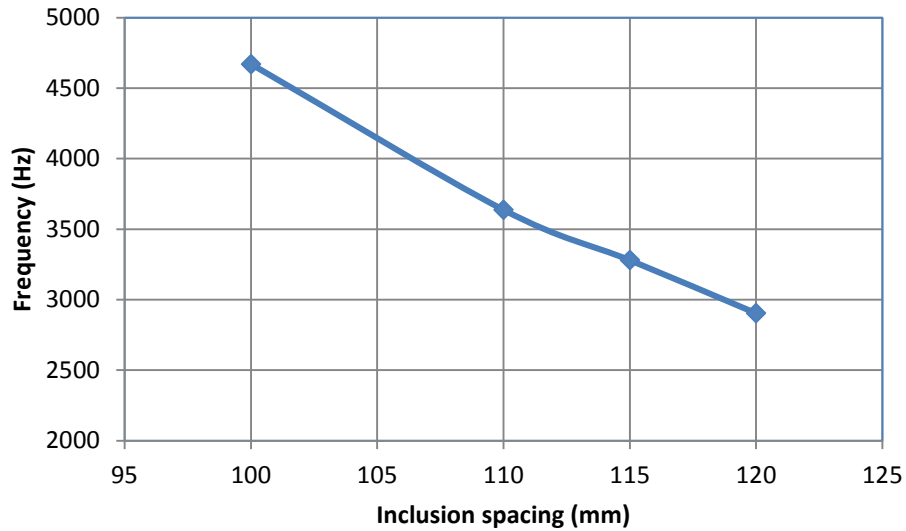


Figure 65: Variation of the central frequency of the band gap with the inclusion spacing d .

Using spacing $d = 120$ mm, the central frequency is around 2900 Hz. According to Figure 64, increasing the radius by 1 mm, the central frequency increases approximately by 200 Hz. Thus, the final parameters for design B are chosen as: $r = 15.5$ mm; $d = 120$ mm.

3.2.4.11 Final Designs

The forward displacement spectra for the two final designs are compared in Figure 66. In plotting these curves, a finer frequency step size is used. Based on the spectra alone, both designs offer significant wave blockage. At the lower point, the transmission coefficients are approximate 0.45 and 0.25, respectively. This is the transmission coefficient for the displacement. In terms of power, they would be 0.21 and 0.06; or, 6 and 12 dB reductions.

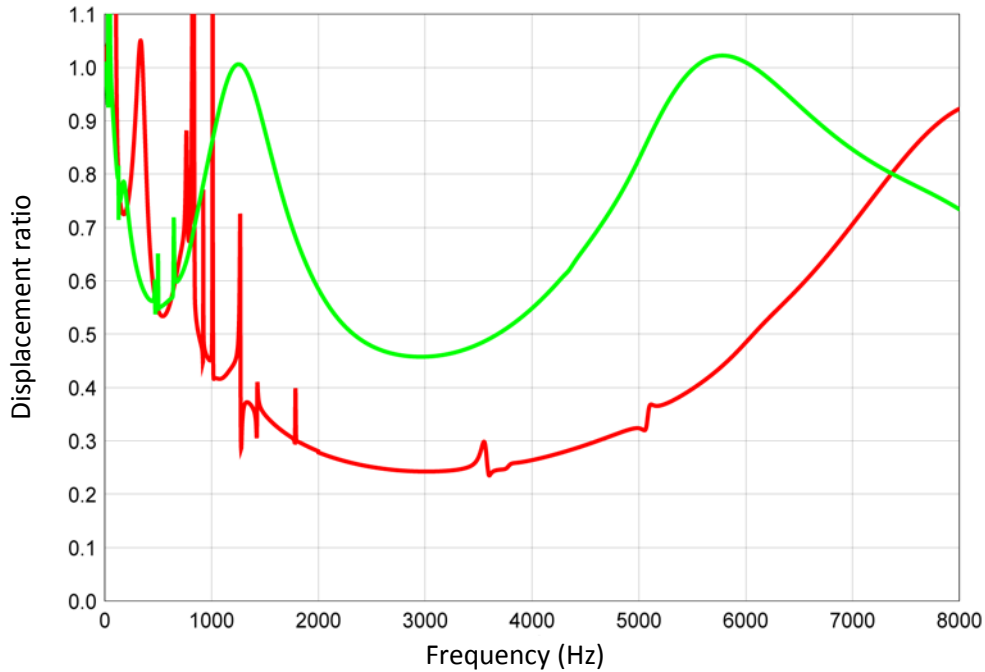


Figure 66: Forward displacement spectra for the final designs. Red: Design A. Green: Design B.

The panel has an overall size of 762 mm x 941 mm (30"x36") between the beams. Leaving a space of 100 mm between the loading beam and the sonic crystal, this leave 562 mm x 741 mm that can be occupied by the sonic crystal. For Design B, this would leave 5 inclusions in the short side and 7 on the long side. The second row would have 3 inclusions in short side and 5 inclusions on the long side. This essentially occupies the entire area. This design is not practical.

For Design A, there are 10 inclusions in the shorter side, and 12 inclusions in the longer side. The second row would have 8 inclusions in the shorter side and 10 inclusions on the longer side. This seems to be a reasonable design. The overall layout is shown in Figure 67.

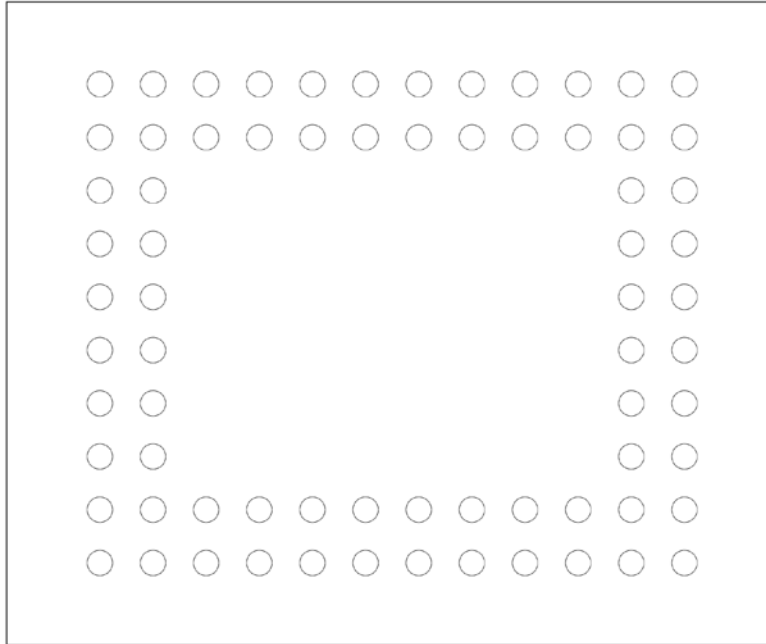


Figure 67: Overall layout of the sonic crystal (Design A) on the 30"x36" area of the panel. The black border represents the 30"x36" (762 mm x 914.2 mm) area. The distance between the sonic crystal and the shorter side is 110.6 mm, and the longer side is 97.5 mm. The spacing is 63 mm.

3.2.4.12 Evaluation of Commercial Insert Geometry

A metallic insert was identified, Shur-Lok Part #5169-S-8, as shown in Figure 68, with a shank outer diameter of 20.6 mm, and enlarged ends of diameter of 23.0 mm to allow wrenching holes; and a flange diameter of 41.3 mm. Using a slightly larger diameter is to account for the increase of the effective radius due to the flange, a diameter of 23.0 mm is used in the simulations. All other modeling parameters remain the same.

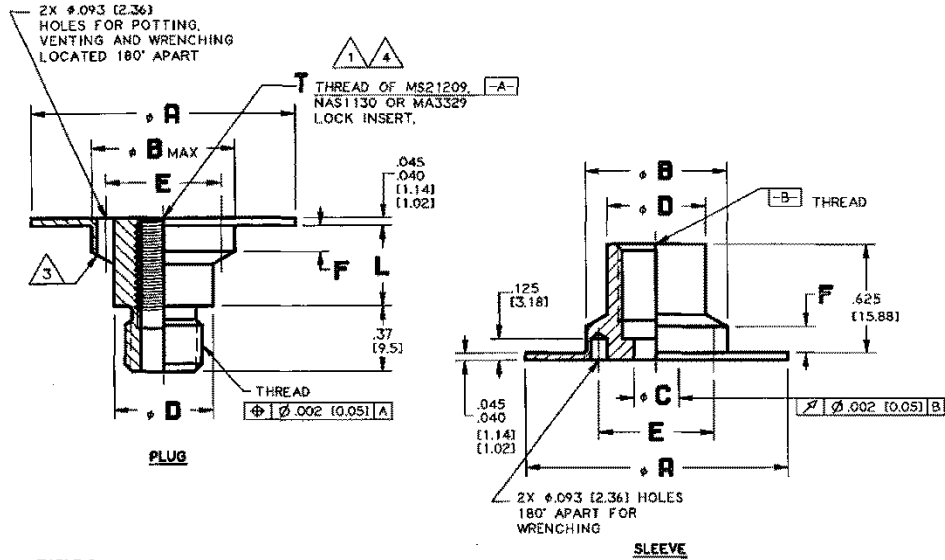


TABLE 1


SIZE CODE	T THREAD 	ϕA	ϕB MAX	ϕC	ϕD	E	F	INSTALLATION HOLE SIZE
4	.2500-28UNF-3B	1.500 [38.10]	.810 [20.57]	.257 [6.53]	.562 [14.27]	.656 [16.66]	.150 [3.81]	.811 - .817 [20.60] - [20.75]
M6	M6X1 4H5H	1.500 [38.10]	.935 [23.75]	.377 [9.58]	.687 [17.45]	.781 [19.84]	.240 [6.10]	.936 - .942 [23.77] - [23.93]
6	.3750-24UNF-3B	1.500 [38.10]	.935 [23.75]	.377 [9.58]	.687 [17.45]	.781 [19.84]	.240 [6.10]	.936 - .942 [23.77] - [23.93]
M10	M10X1.25 4H5H	1.500 [38.10]	.935 [23.75]	.377 [9.58]	.687 [17.45]	.781 [19.84]	.240 [6.10]	.936 - .942 [23.77] - [23.93]
8	.5000-20UNF-3B	1.625 [41.28]	1.060 [26.92]	.515 [13.08]	.812 [20.62]	.906 [23.01]	.240 [6.10]	1.061 - 1.067 [26.95] - [27.10]
M12	M12X1.25 4H5H	1.625 [41.28]	1.060 [26.92]	.515 [13.08]	.812 [20.62]	.906 [23.01]	.240 [6.10]	1.061 - 1.067 [26.95] - [27.10]

Figure 68: Diagram and geometry of the selected insert from Shur-Lok catalog (size 8 is used here). Diameter E is used in the simulations.

Since one of the key variables, the radius of the inclusions, has been fixed, simulations are run when the other primary design parameter, the spacing d , is varied from 40 mm to 60 mm in 5mm increments. The resulting spectra for the displacement amplitude in the forward direction are show in Figure 69. It can be seen that the central frequency of the band gap occurs at around 3400 Hz for $d = 55$ mm (brown curve); and around 2600 Hz for $d = 60$ mm (dark purple). When the spacing is small, the first band gap is located at a much higher frequency.

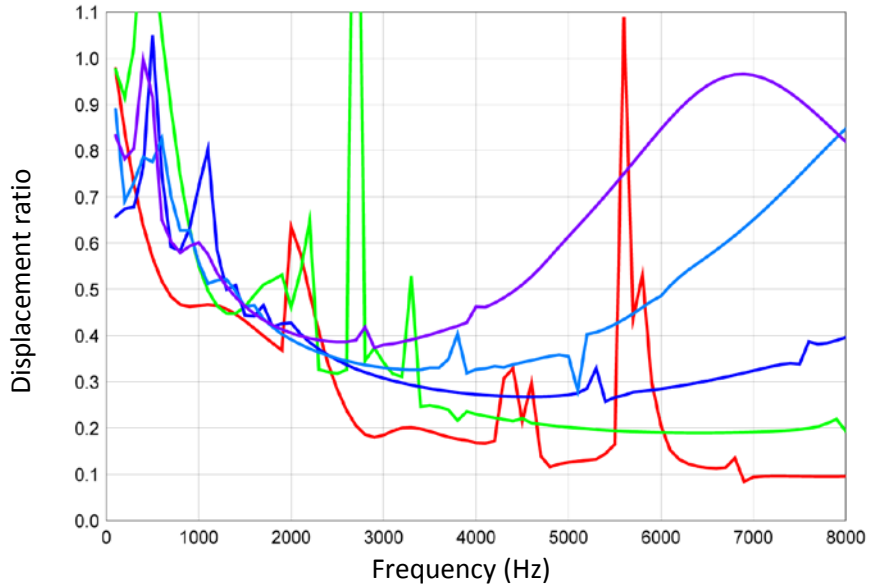


Figure 69: Spectra for different scatterer spacing: red: $d = 40$ mm, green: $d = 45$ mm; blue: $d = 50$ mm; light blue: $d = 55$ mm; dark purple: $d = 60$ mm.

With interpolation, it is expected that a spacing of 57 mm would be about right. The spectrum is calculated in a finer step size in the same frequency range for $d = 57$ mm and is shown in Figure 70. The numerical data show that the central frequency of the band gap is located between 2980 and 3000 Hz in a computation using 20 Hz as the step size.

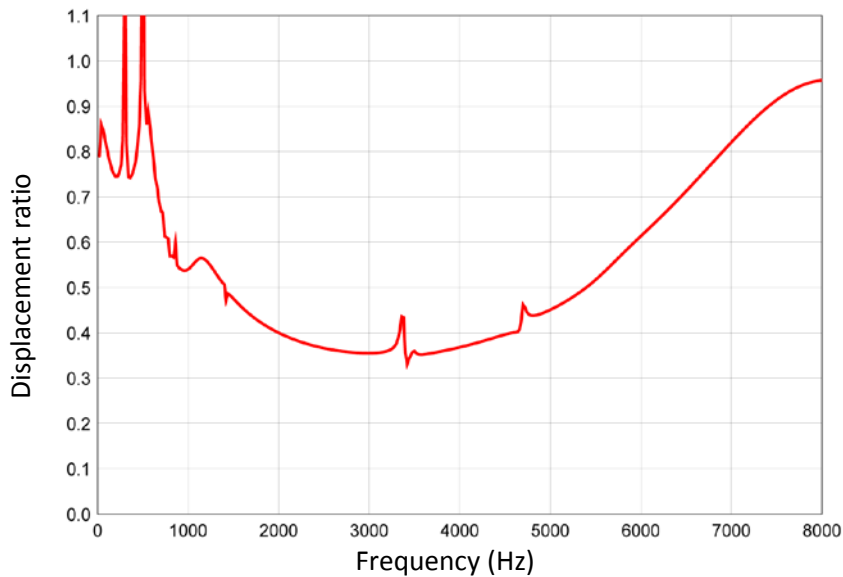


Figure 70: Spectrum for the final design: $r = 11.5$ mm, $d = 57$ mm.

3.2.4.13 Practical Design Considerations

The retaining panel concept shown in Figure 52 is not practical for a commercial rotorcraft roof panel due to weight and space constraints. Alternate approaches include attaching the retaining frame directly to the outside surfaces of the inner and outer face sheets, effectively creating a 'doubler' picture-framed region over the insert array. Also, the honeycomb core in the insert region may be realigned so that the cells are perpendicular, rather than parallel to, the inserts. The doublers and the realigned honeycomb core both serve to mitigate rotational motion near the inserts. It is doubtful, however, that a perfectly irrotational array can be practically constructed.

3.2.4.14 Effects of Finite Boundaries on Wave Scattering

The effects of finite boundaries on wave scattering by an array of inclusions may be approximated by using additional wave sources to represent reflections from boundaries. A point source is produced by a concentrated time harmonic lateral force acting at a particular point on the plate. A series of such forces acting along a line segment forms a line source, which, by incorporating different phases, can represent a clamped edge or free edge. Furthermore, a series of not so closely located point sources could also mimic the effect of a row of rivets that holds a stiffening rib to a panel.

Comparing Point Sources with Planar Incident Wave

The first set of simulations explores the feasibility of using point source as a wave source, and also helps validate the sonic crystal design. For this, a side-by-side comparison is made for an array of two rows of inclusions. On one side, a planar incident wave is the wave source; on the other; a series of point sources are lined up parallel to the rows of the inclusions. Figure 71 shows an example of such comparison, in which the displacement amplitude is shown at the target frequency of 3000 Hz. The left figure has a planar wave as the source; and the right figure has an array of 17 equally spaced point sources, of the same strength and phase as the source. The point sources are spread out along a line segment that is noticeably longer than the inclusion array. This ensures an almost-planar wave form impinging onto the sonic crystal, which allows the comparison with the planar incident wave case. Note that each of the point source results in a singular wave field. In the computations, the amplitude of the incident wave due to these wave sources is normalized by the amplitude of the source 10 mm away.

In a series of simulations, the distance from the point source array to the sonic crystal is varied. The simulations show that the wave field passing through the sonic crystal is essentially unchanged. The distance affects the reflected wave field in the space between the point source array and the sonic crystal, largely due to the change in the pattern for the standing wave between the line source array and the inclusion array. In the case of the planar incident wave, there is no standing wave but just interference of the two waves, the incident and the reflected wave, traveling in opposite directions. This observation confirms that the filtering effects of the band gap due to the inclusions are independent of the incident wave forms.

Note that due to the singular nature of the point loads, the normalization schemes used in the two cases are different and hence the direct comparison of values (or the exact colors) between the two cases are not meaningful. All comparisons focus on the pattern and the relative displacement amplitude within each figure.

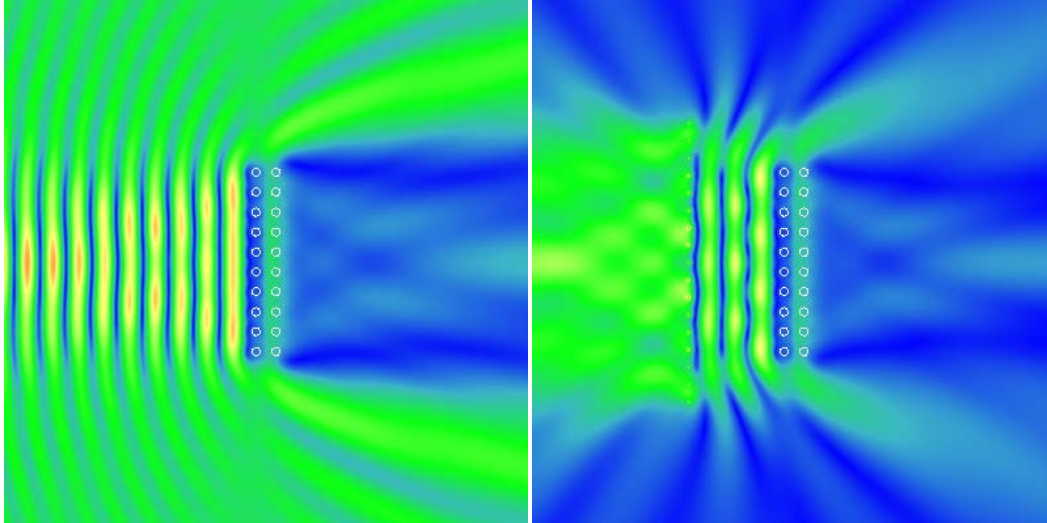


Figure 71. Distribution of displacement amplitude in vicinity of rigid inclusions at frequency $f=3000$ Hz. Left: planar incident wave. Right: incident due to an array of point sources

Two Sonic Crystal Arrays

In this set of simulations, two sonic crystals, each consisting of two rows of inclusions in square arrangement, are embedded in the panel, and one array of point sources is placed on the outside of each sonic crystal. In essence, the configuration adds a mirrored image of the sonic crystal and point source arrays as in the right image in Figure 71.

In the first of this set of simulations, the location of the point source arrays is varied. Figure 72 compares the displacement field of the entire panel for different locations of the source array, identified by the distance to the center of the panel. The sonic crystals are at fixed locations, with the sonic crystal rows located 271.5 mm and 328.5 mm away from the center of the panel, but with the point source arrays located 350 mm, 400 mm, 450 mm and 500 mm, respectively, from the center.

Figure 73 shows the distributions of the displacement amplitude along the x -axis (horizontal symmetry line of the panel) for the four cases shown in Figure 72. In this figure, the locations of the inclusions are marked by the magenta vertical dashed lines; and the locations of the point source arrays are marked by the vertical dashed lines in the color matching that of the curve. The wave fields inside the two sonic crystals are essentially the same, with the exception of the first case in which the source arrays are located extremely close to the sonic crystal. Again the result suggests that the source location is an unimportant factor; and that the sonic crystals exhibit desired filtering effects at the target frequency of 3000 Hz. Due to the space limit on the panel, there is not enough room to fit in a third row of sonic crystals. Otherwise, the filtering effect could be improved.

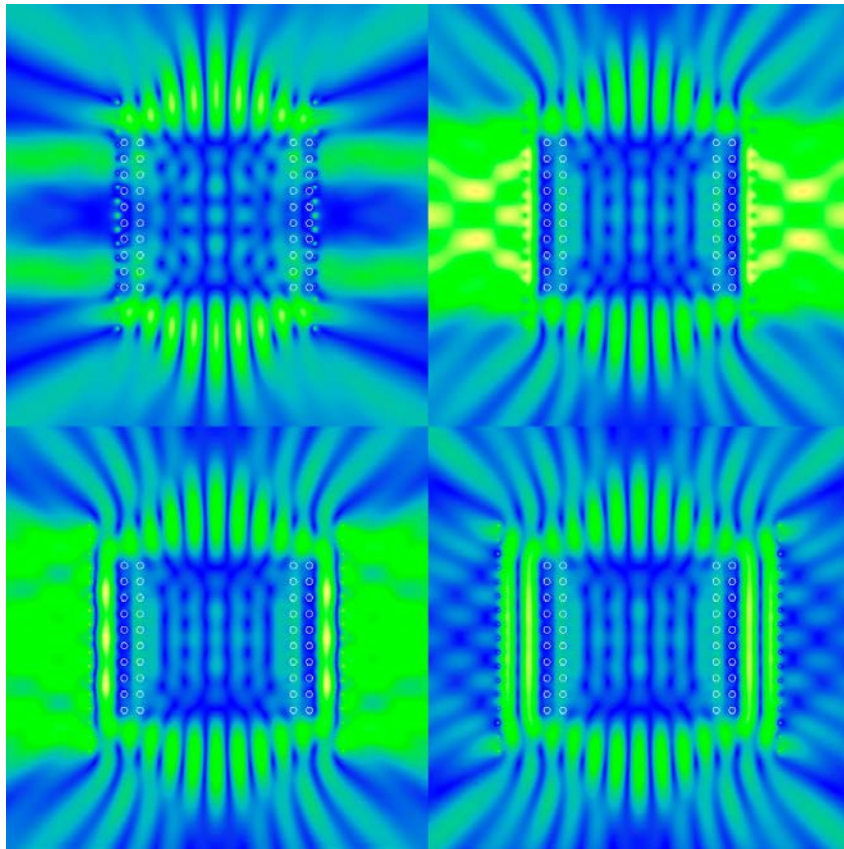


Figure 72. Displacement amplitude in the panel at 3000 Hz for the four locations of the point source arrays.
 Top left: 350 mm; top right: 400 mm; bottom left: 450 mm; bottom right: 500 mm.

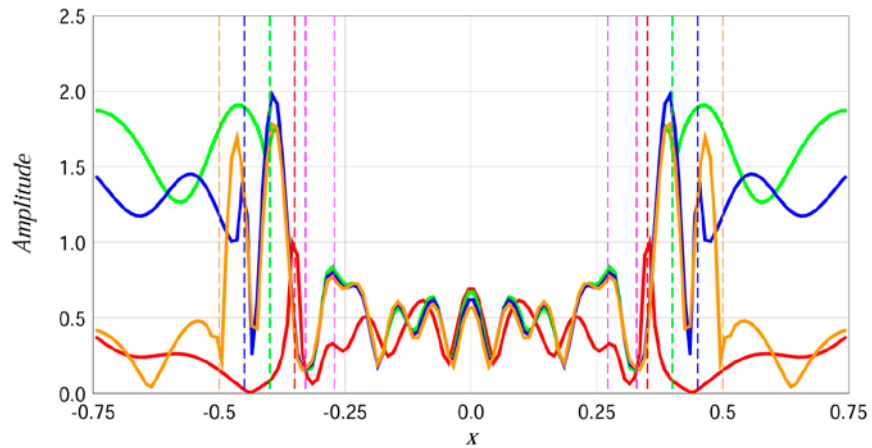


Figure 73. Distribution of relative displacement amplitude along x -axis for the cases shown in Figure 72.
 Vertical dashed lines represent the locations of the source arrays (in matching color), and inclusions (magenta). Legend: red: 350 mm; green: 400 mm; blue: 450 mm; and orange: 500 mm.

Full-Panel Simulation

To observe the behavior of the panel with the embedded sonic crystal, in the next series of simulations, the full panel is used. The sonic crystal now consists of two rings of inclusion. Based on the design of the sonic crystal, and the available space in the panel, four configurations as shown in Figure 74 are simulated. In the full panel, the load is transmitted into the panel through a set of I-beams that form a rectangular enclosure of dimensions 762 mm \times 914.4 mm (30 in \times 36 in). The four configurations have 11, 12, 13 and 14 inclusions respectively in the horizontal directions, and 11 inclusions in the vertical direction, on the outer ring. The inner rings have two less inclusions in each direction. Two arrays of point sources are located 914.4 mm apart, one on each side of the sonic crystal. Within each array, 17 point sources are equally spaced 50 mm apart, aligned in parallel with the sonic crystal.

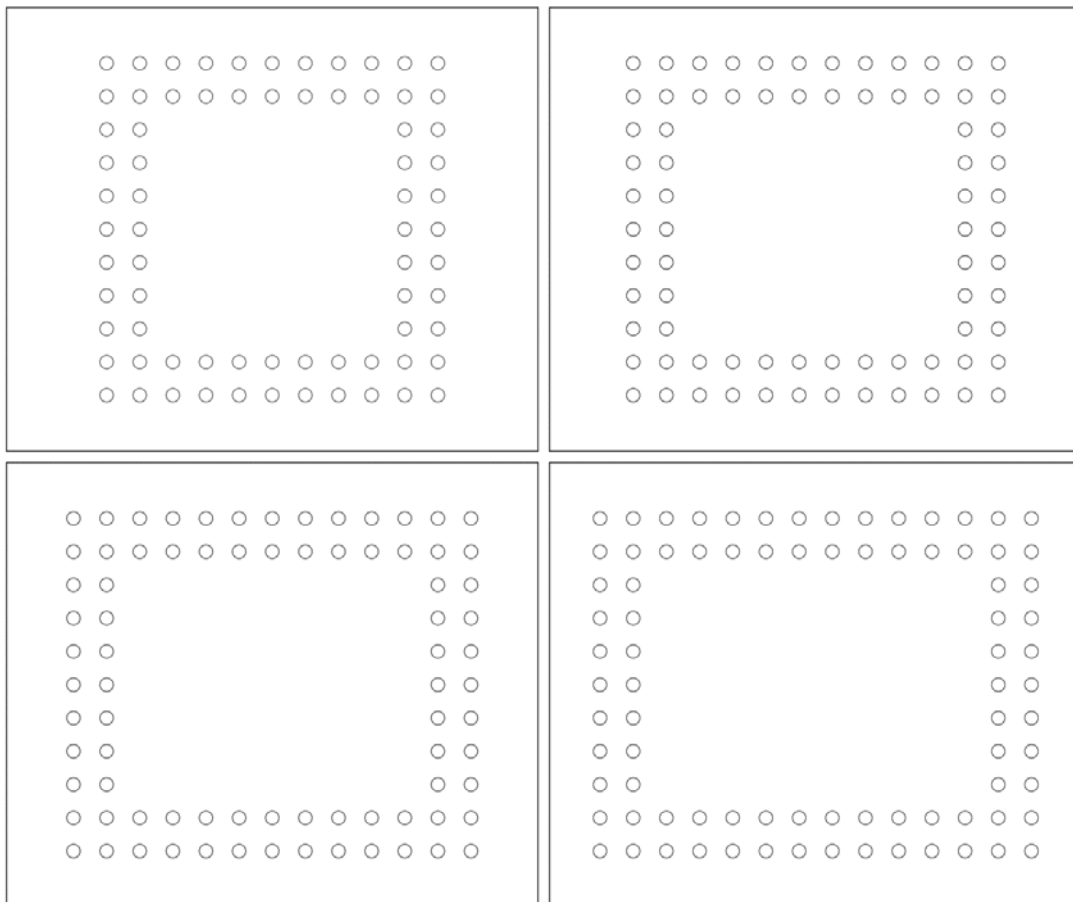


Figure 74. Layouts of four configurations. In each configuration, the outline represents the portion of the roof panel within the I-beams through which the load is transmitted into the panel. Top left: 11 \times 11 inclusions in the outer ring. Top right: 12 \times 11 inclusions in the outer ring. Bottom left: 13 \times 11 inclusions in the outer ring; Bottom right: 14 \times 11 inclusions in the outer ring.

Figure 75 shows the displacement field over the entire panel when the point source arrays are excited at the target frequency of 3000 Hz. Similarly, Figure 76 shows the distribution of the displacement amplitude along the x-axis in the panel. This set of simulations show a very different scenario compared

to Figure 72 and Figure 73. The most prominent difference is the strong resonance pattern formed inside the enclosure of the sonic crystal. This suggests, since the filtering cannot entirely block the wave from transmitting into the space enclosed by the sonic crystal, that the transmitted wave can resonate under appropriate conditions (when wavelengths align with the span of the geometry).

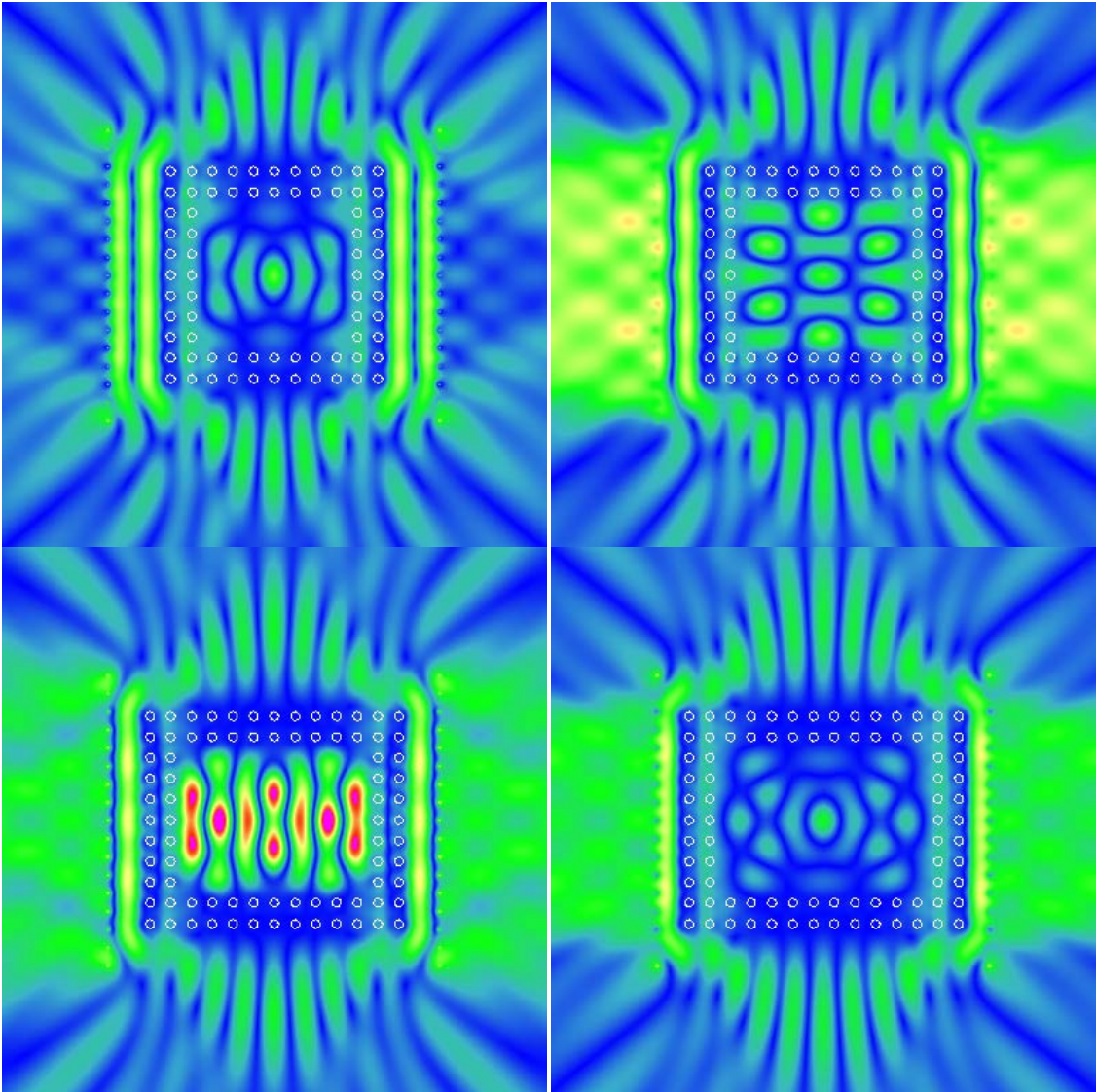


Figure 75. Displacement amplitude in the panel at frequency 3000 Hz for the four configurations shown in Figure 74.

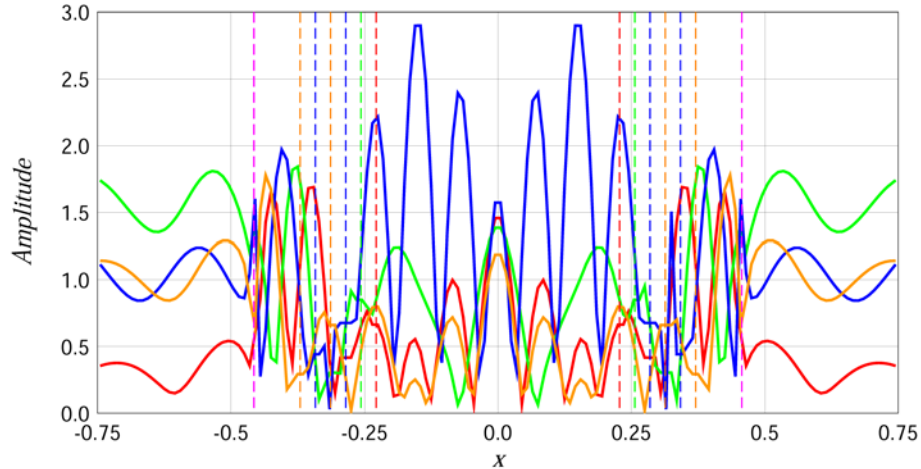


Figure 76. Distribution of relative displacement amplitude along the x-axis in the four configurations shown in Figure 75. The vertical dashed lines show the locations of the point source arrays (magenta) and the inclusion (in matching colors). Legend: red – 11x11, green – 12x11, blue – 13x11, orange – 14x11.

Circular Sonic Crystal

In light of the above observations on the importance of the space enclosed by the sonic crystal, it is clear that a rectangular arrangement has two characteristic lengths, which leads to a higher probability of matching the bending wavelength to one of characteristic lengths. For this reason, a different geometry is explored: circular arrangements of the sonic crystal. In the simulations, the circular shape is omnidirectional and has only one characteristic length: the radius (or the diameter) of the ring.

Two configurations are explored. In both configurations, the outer ring is located at a radius nearest to $762/2 = 381$ mm such that distance between two adjacent inclusions is 57 mm. In the computations, the arc length is used to approximate the linear distance. As the result, 42 inclusions are placed at an angular distance of $360^\circ/42 = 8.5714^\circ$ apart at a radius of 381 mm. The first inclusion is placed at the polar coordinate (381 mm, $8.5714^\circ/2$) such that the upper and lower halves of the space are mirror images of each other. The two different configurations come in different arrangements as the inner ring. In the first configuration, the inner ring follows the same angular arrangement of the outer ring but is 57 mm shorter in radius: that is, it has 42 inclusions arranged at a radius of 324 mm. In the second configuration, the inclusions are also located at radius of 324 mm, but the distance between adjacent inclusions is kept as close to 57 mm as possible. 36 total inclusions are used, placed 10° apart, at an arc length of 56.55 mm. Overall, the first configuration maintains the appearance of the “square” grid of the sonic crystal; the second configuration maintains the lattice constant as designed.

The simulation results for both configurations at the target frequency of 3000 Hz are shown in Figure 77. Figure 78 shows the corresponding displacement amplitude distribution along the x-axis. In this figure, the magenta vertical dashed line represents the location of the point source arrays; and the green dashed lines represent the extents of the inclusions in the sonic crystals.

The results show that it is still possible to form a configuration resonance. The second configuration, which maintains the designed “lattice constant” in both directions, achieves significantly better filtering. Although the two configurations have almost identical overall geometrical shapes for the enclosed space, the resonance patterns and strengths are very different.

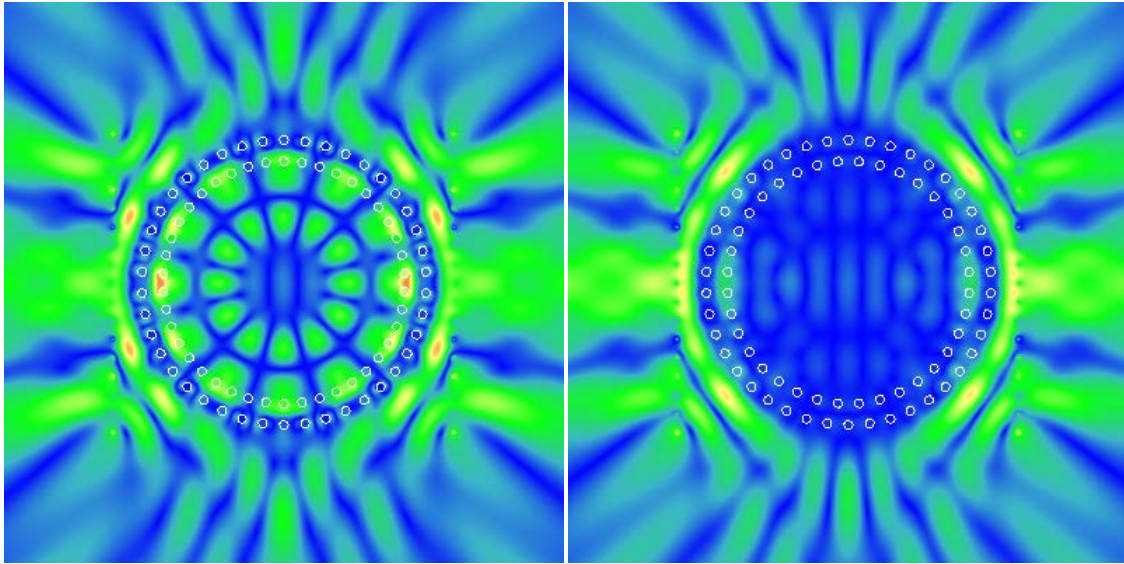


Figure 77. Displacement amplitude with the presence of circular sonic crystals, at frequency of 3000 Hz. Left: maintaining the appearance “square” grid; Right: maintaining the lattice constant as designed.

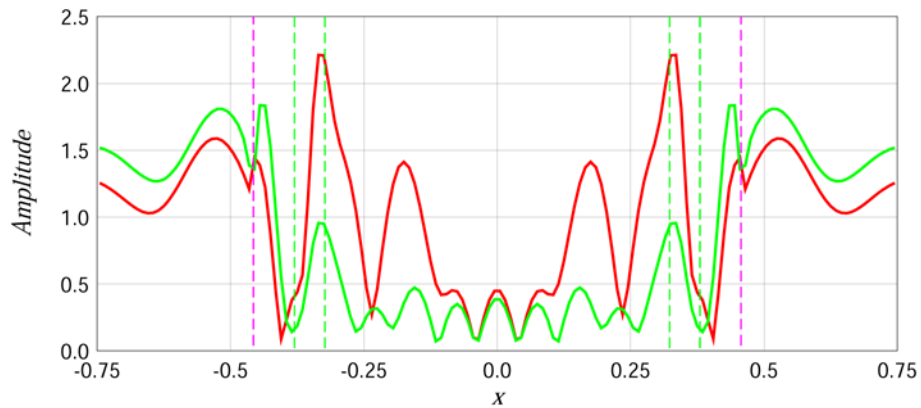


Figure 78. Distribution of relative displacement amplitude along the x -axis for two configurations shown in Figure 77.

Concluding Remarks

These simulations demonstrate the feasibility of using an array of point sources to simulate a planar incident wave. Results also indicate that a sonic crystal design based on a single array can perform similarly to designs based on planar incident waves that originate infinitely far from the array. In other

words, the designed sonic crystal exhibits the bad gap effect regardless of the type of the incident wave form. What is important is the frequency of the designed band gap.

However, when implementing sonic crystal designs in practical finite structures, some practicality limitations might significantly degrade performance. In this series of studies, two effects have been encountered. The first is due to limited available space to embed the sonic crystal, where only two rings of inclusions may be used. This design exhibits the desired band gap but the gap does not act as a total blockade. A fraction of the wave can still penetrate the sonic crystal. The second effect is when the sonic crystal must be formed as an enclosure around a finite space, where the transmitted waves can form standing wave patterns at or near resonance frequencies. In such cases, the filtering effect diminishes further. An effective solution to the problem might be to use multiple rows of inclusions. It would be worthwhile in the future to explore the effect of having more rows of inclusions, such as using three rings of scatterers.

3.2.5 Split Panel Concept for Airborne Sound Transmission Reduction

It is well known in the acoustic sound power transmission loss community, and particularly by glass window manufacturers, that ‘double glazed’ panels are preferable to single panels. The same amount of mass is spread between two panels with an air gap between them. Using two panels nearly doubles the TL when compared to a single panel with the same mass. Figure 79 shows two sandwich panels, with thinner 6.35 mm (0.25 inch) cores, with a 12.7 mm (0.5 inch) air gap between them. Each face sheet is treated with a center layer of the VHB 9469 discussed in Section 3.2.3. Table 3 lists the thicknesses and surface densities of each layer of the optimized panel.

The 12.7 mm gap is chosen to ensure that sound transmission degradation associated with the mass-spring-mass resonance of a double panel system is well below the first transmission tone frequency at 1 kHz. The resonance frequency, where each panel acts as a lumped mass connected by the stiffness of the air gap, is:

$$f_o = \frac{1}{2\pi} \sqrt{\frac{\rho c^2 / d}{m_1 m_2 / (m_1 + m_2)}}, \quad (15)$$

where ρc^2 is the bulk Modulus of air, d is the gap thickness, and m_1 and m_2 are the two outer panel area densities. In the equation, the numerator represents the gap stiffness per unit area, and the denominator represents the effective total mass per unit area. The resonance amplifies the sound transmission through the double panel system at and around its resonance frequency. The effects of the gap thickness on the mass-spring-mass resonance, and on the overall panel thickness, are summarized in Table 4. A 12.7 mm gap shifts the resonance below 500 Hz, which is sufficiently below the 1 kHz target so that degradation should not occur.

Rather than leave the air gap empty, Bell suggested filling it with a 9.5 mm (0.375 inch) thick layer of Amber Microlite AA insulation (24 kg/m³) from Johns Manville. The insulation provides both thermal, as well as reduced sound transmission through its added mass. Bell often adds an extra layer of Microlite contained within a thin plastic covering on the inside surfaces of its rotorcraft roof panels. However, the

layers are costly, and must often be removed when servicing the panels. Including the insulation inside the panel is preferable. The added acoustic transmission loss benefits are modest, and due mostly to the added mass of the material, as shown in Table 5. In the Table, the 'Mass Law' column corresponds to estimated transmission loss due to the mass of the material, computed using the well-known infinite panel formulas [6].

An initial analytically based estimate of the performance benefits of the split panel damped design, using the analytic tools validated against the baseline panel measurements, is shown in Figure 80. The optimized panel coincidence dip is higher in frequency, since the split panel cores are half the thickness of that of the baseline panel. Also, the face sheet rigidities are lower due to the softer center VHB layers. However, the coincidence dip was targeted to lie between the two transmission tones at 1 and 3 kHz. Future designs may also adjust core thickness and material to shift the coincidence dip to benign source locations. The double panel concept nearly doubles TL at both 1 and 3 kHz. Adding the Microlite may also improve TL, but it remains to be seen how well it works above the coincidence dip. Finally, the effects of sound transmission through the edge composite is not included in this estimate, but will be addressed in final calculations compared to measurements.

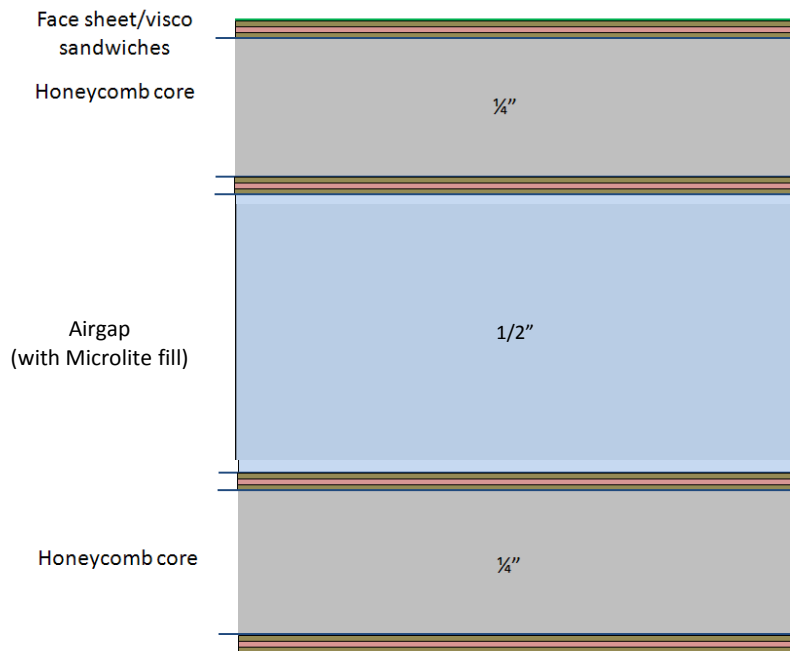


Figure 79: Split panel concept.

Table 3. Thicknesses and surface densities of optimized panel.

Material	Thickness (in)	Thickness (cm)	Surface density (lb/in ²)	Surface density (kg/m ²)
Paint			0.00006	0.042
Face sheet	0.0079	0.0201	0.00044	0.311
Visco	0.005	0.0127	0.00020	0.14
Face sheet	0.0079	0.0201	0.00044	0.311
Adhesive	0	0.0000	0.00035	0.245
Honeycomb	0.25	0.6350	0.00048	0.3355
Adhesive	0	0.0000	0.00035	0.245
Face sheet	0.0079	0.0201	0.00044	0.311
Visco	0.005	0.0127	0.00020	0.14
Face sheet	0.0079	0.0201	0.00044	0.311
Adhesive	0	0.0000	0.00035	0.245
Microlite (3/8") in 1/2" gap	0.5	1.2700	0.00033	0.228
Adhesive	0	0.0000	0.00035	0.245
Face sheet	0.0079	0.0201	0.00044	0.311
Visco	0.005	0.0127	0.00020	0.14
Face sheet	0.0079	0.0201	0.00044	0.311
Adhesive	0	0.0000	0.00035	0.245
Honeycomb	0.25	0.6350	0.00048	0.3355
Adhesive	0	0.0000	0.00035	0.245
Face sheet	0.0079	0.0201	0.00044	0.311
Visco	0.005	0.0127	0.00020	0.14
Face sheet	0.0079	0.0201	0.00044	0.311
Paint			0.00006	0.042
Total	1.083	2.75	0.00785	5.501
total face sheets				2.488
total honeycomb				0.671
Total visco				0.560
Total adhesive				1.470
Total Microlite				0.228
Total allowable	0.625	1.59	0.00814	5.700

Table 4. Effects of airgap thickness on mass-spring resonance frequency and overall panel thickness of optimized panel.

Air gap thickness (mm)	Resonance Frequency (Hz)	Overall panel thickness (mm)
3.18	911	18.0
6.35	644	21.2
12.7	456	27.5

Table 5. Measured and mass-law based sound transmission loss improvements due to use of MicroLite.

Frequency (Hz)	dB, Measured by vendor	dB, Mass Law
500	2.4	2.4
1000	4.6	4.7
2000	6.6	6.8
4000	8.8	10.5

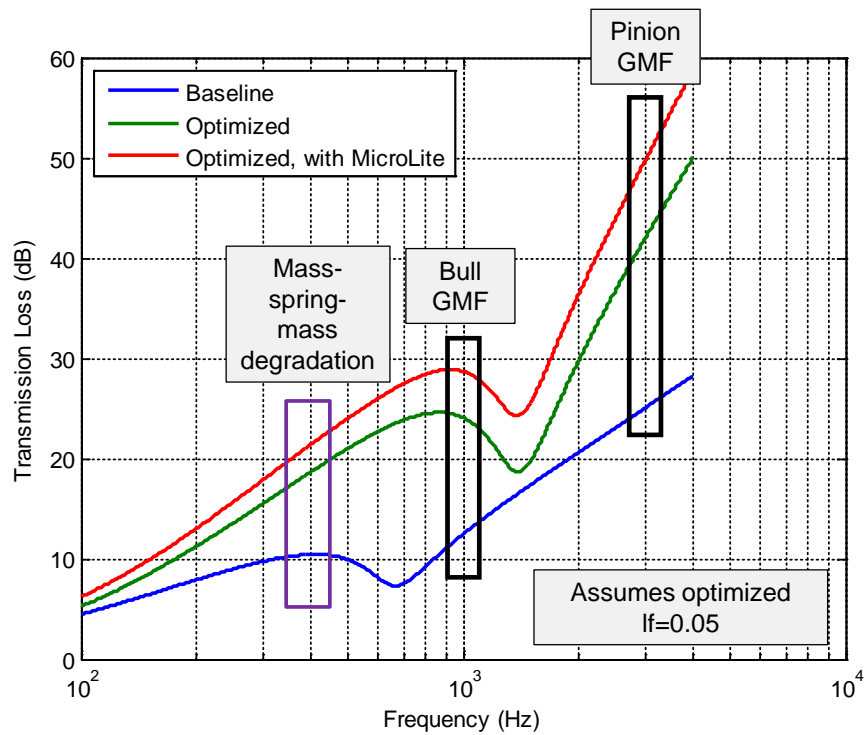


Figure 80: Analytic estimates of transmission loss benefits of split panel concept, center panel only.

3.3 Final Optimized Panel Design

The final optimized panel balances acoustic performance with structural integrity constraints, as well as meeting weight and space goals. The split panel concept is augmented with damped face sheets which include embedded VHB viscoelastic material, and filled with MicroLite blankets. The final surface density is 5.5 kg/m², which is within the allowable goal of 5.7 kg/m². Schematics of the baseline and optimized panel cross sections are shown in Figure 81. Although the optimized panel is thicker than the baseline panel, the excess thickness is shifted to outside the fuselage. Bell has confirmed that the extra thickness will not affect the transmission or other electrical, mechanical, or hydraulic elements in the roof cavity region.

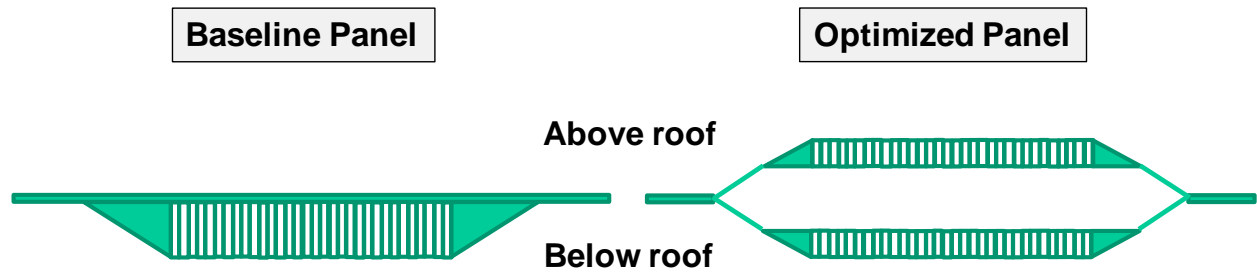


Figure 81: Schematics of baseline (left) and optimized (right) panel cross sections (not to scale).

3.3.1 Structural Modeling

The optimized panel was modeled using hexahedron, wedge, and tetrahedron finite elements, as shown in Figure 82. Each ply of fabric and each layer of VHB were discretely modeled with a single layer of elements through the thickness. Each core was modeled with two elements through the thickness. Adhesive plies were not included in the model, as they have negligible effect on the structural performance of the panel. The panel is symmetric except for an extra ply of VHB at the midplane, so the lower half of the panel was modeled and then mirrored with an offset for the VHB ply to create the upper half. The uppermost surface of the panel was used to create a two-dimensional mesh of quadrilateral elements. These elements were extruded to create hexahedron elements. This ply was then copied and translated downward to create the remaining plies in the upper half of the panel. The core was created by applying a hexahedron and wedge mesh to geometry imported from the CAD software Catia. Once all layers were created, each layer was modified to match the design by removing the edgeband for the pre-cured plies and removing the center section and ramping down the edgeband plies. To create the ply ramps, the hexahedron elements were split into wedge elements along the length of the sides and tetrahedron elements in the corners of the panel.

Beams, straps and angle brackets, as shown in the top of Figure 83, were used to represent the support structure of the 429 roof. The beams were modeled with hexahedron elements, with a single element through the thickness of the webs and flanges. The beams were connected with straps across the top flanges and angle brackets across the webs. These were each modeled with a single hexahedron element through the thickness as well.

The brackets, straps, beams, and panel are connected with fasteners. These elements are connected together in the FEM using CBUSH spring elements in the fastener locations. The bottom of Figure 83 shows the CBUSH elements, represent by yellow circles. Nodes from connected elements are made coincident and then a CBUSH, oriented in the direction of the fastener axis, is used to attach them together. Then a PBUSH property is assigned to represent the fastener stiffness, computed using the bolt material and area. It is important to note that since these CBUSH elements are connected to nodes of solid elements, they will not run properly in NASTRAN SOL 101 (Static Analysis), but they will work in NASTRAN SOL 103 (Real Normal Modes Analysis) and was the most efficient way to configure the model for dynamic analysis. For static analysis, the panel was analyzed in NASTRAN SOL 101, supported with Single Point Constraints (SPCs) at the location of the fasteners that would attach it to the beams.

The elements were divided into six material families as shown in Figure 82. The carbon/epoxy (C/Ep) is divided into three regions for nominal, bag side, and tool side properties. Plies that are cured with VHB or as a solid laminate have nominal carbon/epoxy properties. Plies cured between the core and the pre-cured laminates have tool side properties. Plies cured between the core and the bag have bag side properties. The nominal smeared properties used for dynamic modeling are similar to those listed in Table 2.

It was observed during the test correlation of the baseline panel that the dynamic response is sensitive to the total panel weight. While they are not typically discretely modeled for static analysis, the weights of the adhesive, paint, and fasteners are accounted for in the FEM for dynamic performance. A CONM2 point mass element is added at each fastener location to include its weight. The adhesive and paint weights are included by adjusting the density of the elements adjacent to them. Separate material cards were created for each modified density section using the mass densities listed in Table 3. The weight of the optimized panel assembly was estimated from nominal volume and density of each part. The densities were modified so that the weights of each part in the FEM equaled the calculated weights. A summary of the weights is shown in Table 6.

Table 6. Optimized panel weight summary.

Material	Weight (kg)	Weight (lb)
Carbon/Epoxy face sheets	3.08	6.80
Adhesive	1.89	4.18
Paint	1.02	2.24
VHB	0.466	1.03
Honeycomb Core	0.422	0.931
Stiffeners + paint	9.46	20.9
Clips & Angles	0.712	1.57
Fasteners	0.373	0.823
Total Weight	17.4	38.4

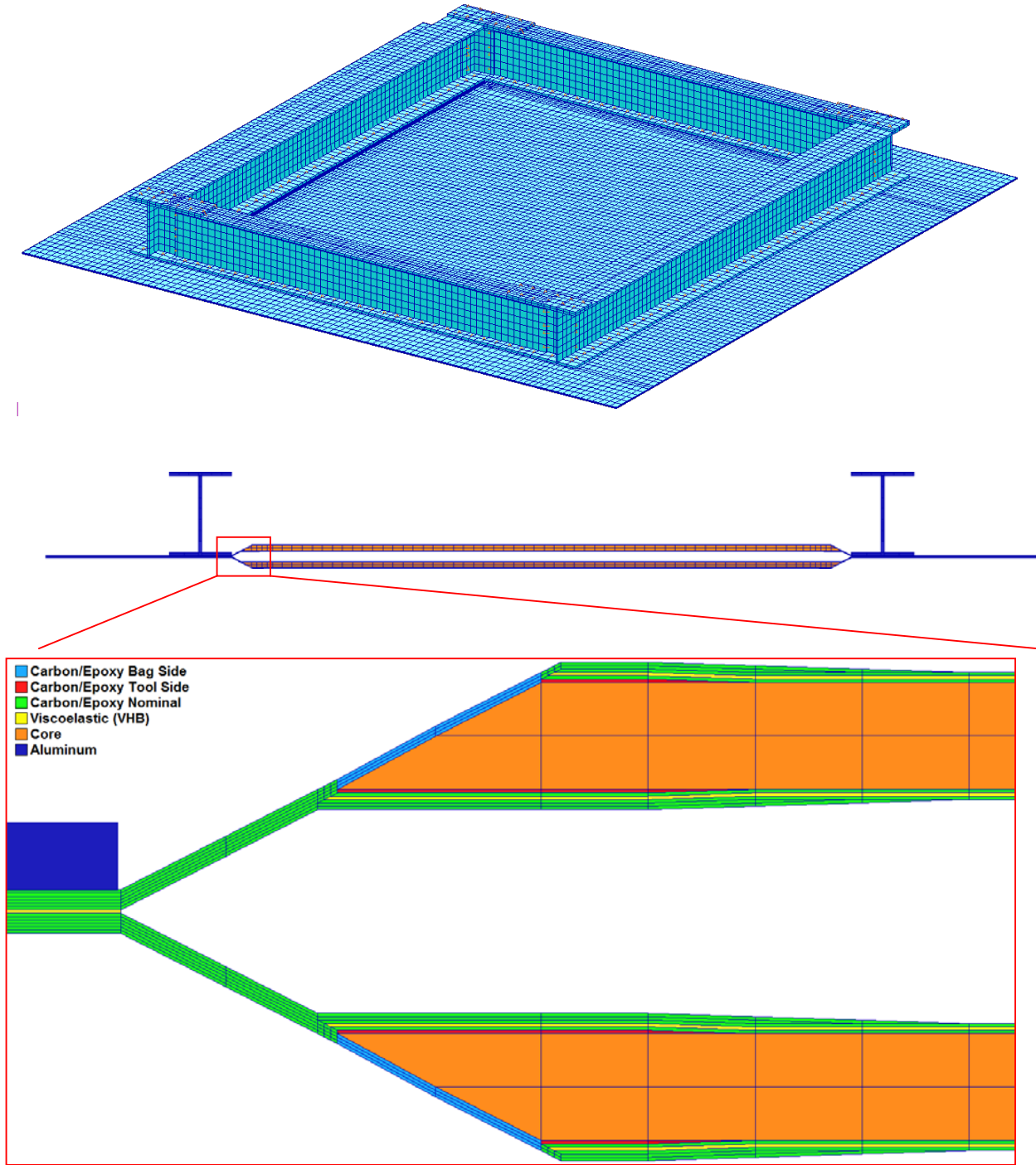


Figure 82: FE model of optimized panel.

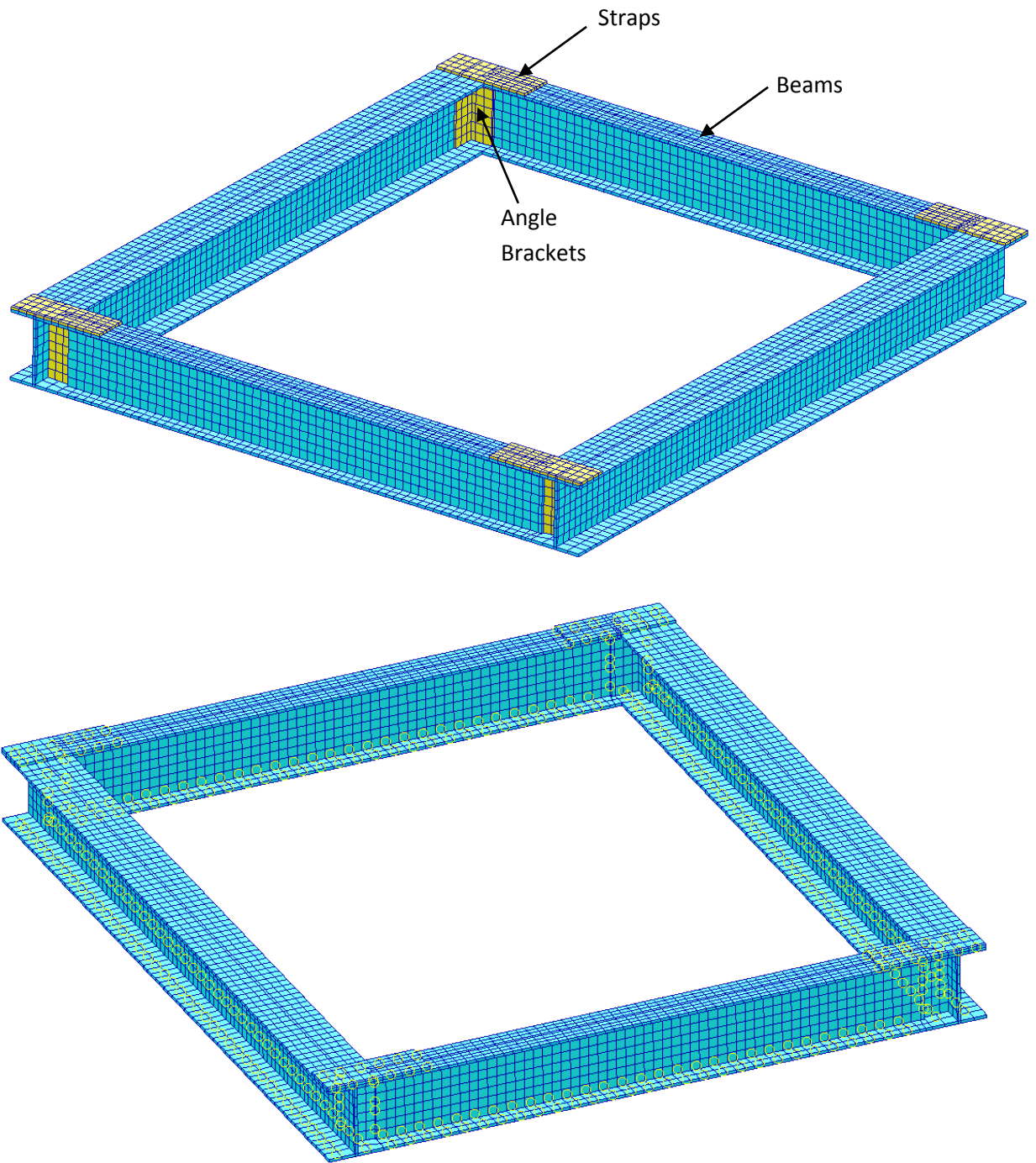


Figure 83: FE model of roof structure. Top – brackets and straps, Bottom – CBUSH springs highlighted in yellow.

3.3.2 Structural Integrity Calculations

While the focus of this project is on the acoustic performance of the panel, it is still necessary to analyze the structural integrity of the panel with the critical design loads for the representative roof panel. Skin panel strength, ramp strength, edgeband fiber and bearing strength, panel stability and step load response have been analyzed. The skin panel (regions 1-4), ramp (region 5), and edgeband (region 6) are shown in Figure 84. The ramp is least critical of the three, since the skin panel and edgeband both have positive margins (see sections 3.3.2.1 and 3.3.2.2) the ramp strength is considered good by comparison. The ramp is critical for buckling in the stability analysis in section 3.3.2.4.

3.3.2.1 Skin Panel Strength Analysis

The skin panel refers to the skin plies over the core. The skin plies can be divided into four different regions, each having a different ply layup as shown in Figure 76. The most critical layup is from region 1 as this area has the least number of plies and less support than the skins in regions 2 through 4. Design loads for the core stiffened panel were critical for the upper skin in compression. Upper skin applied ultimate loads were based on 150% of limit flight loads and were used to analyze the critical skin region using an elevated temperature wet open hole compression allowable. The strength based margin of safety for fibers in the x (fwd/aft) direction is +0.2.

3.3.2.2 Edgeband Strength Analysis

The edgeband fiber strength analysis is similar to the skin panel strength analysis, except that the loading moment is applied to the edgeband instead of being coupled out by the upper and lower panels. The strength based margin of safety for this load condition was +0.73 for the fibers in the forward/aft direction utilizing an elevated temperature wet open hole compression allowable.

3.3.2.3 Edgeband Bearing Strength Analysis

The roof beams are attached to the panel using 0.414 cm (0.163 inch) diameter titanium pins through the edgeband. The peak fastener applied ultimate load in the roof panel was 4827 N (1086 lbf), also for the jump take-off load condition. The strength based margin of safety for this ultimate load was +0.19 for the laminate in bearing.

3.3.2.4 Stability Analysis

With the addition of an air gap, the ramp down of the laminate from the core to the edgeband becomes unsupported. This was deemed a buckling critical area, so a stability analysis of the panel was performed. The panel was held fixed at the points where the panel is fastened to the beams and then critical loads and moments as determined from previous analysis were applied. A NASTRAN SOL 105 (Static Buckling Analysis) solution was computed. The resulting critical buckling eigenvalues are both about 1.95, which are substantially greater than 1.0, demonstrating that the six plies in the ramp will provide adequate stability under the worst case conditions.

3.3.2.5 Step Load Analysis

The panel has the potential to be stepped on when installed in the aircraft. While this is unlikely to occur, it is still necessary to ensure that the panel can withstand this step load. To simplify the analysis, only the center portion of the top sandwich panel was considered, as shown in Figure 86. The nodes of the upper and lower face sheets are fixed from translating vertically at their supported edges. The panel is also fixed in all three translational directions at two nodes. The critical condition for a step load is a 2670 N (600 lbf) unit load applied to the center of the panel. This represents a 90.7 kg (200 lb) person with a gravitational load of 2.0 and an ultimate to limit factor of 1.5. The step load is applied as a pressure load distributed across a 12.7 cm (5 inch) diameter area on the upper surface of the panel.

A NASTRAN SOL106 (Non-Linear Static Analysis) solution was run with this condition. The analysis results show that the maximum deflection of the panel is 2.72 cm (1.07 inches), as shown in Figure 87. This means that the top panel will contact the bottom panel (since the 1.27 cm [0.5 inch] gap is less than 2.72 cm [1.07 inch] deflection), and they will share the load. This simplified analysis assumes the top panel carries the entire load, therefore the results are conservative.

The stresses at the center point of the panel for the limiting 2.72 cm (1.07 inch) deflection are:

$$\begin{aligned}\sigma_x &= -5296 \text{ psi} \\ \sigma_y &= -8374 \text{ psi} \\ \tau_{xy} &= -10.27 \text{ psi}\end{aligned}$$

The maximum forces in the upper face sheet were calculated from the local stresses as shown. The face sheet thickness is 0.0079 inches.

$$N_x = \sigma_x t = (-5296 \text{ psi})(0.0079 \text{ in}) = -41.84 \frac{\text{lb}}{\text{in}}$$

$$N_y = \sigma_y t = (-8373 \text{ psi})(0.0079 \text{ in}) = -66.15 \frac{\text{lb}}{\text{in}}$$

$$N_{xy} = \tau_{xy} t = (-10.27 \text{ psi})(0.0079 \text{ in}) = -0.0812 \frac{\text{lb}}{\text{in}}$$

These loads were used to calculate the critical strain in the upper face sheet, $\epsilon_{crit} = -907 \mu\epsilon$. The allowable strain for the face sheet materials is $-3575 \mu\epsilon$. The positive margin of safety calculated below indicates the face sheet is of adequate strength for the step load condition.

$$MS = \frac{\epsilon_{allow}}{\epsilon_{crit}} - 1 = 2.94.$$

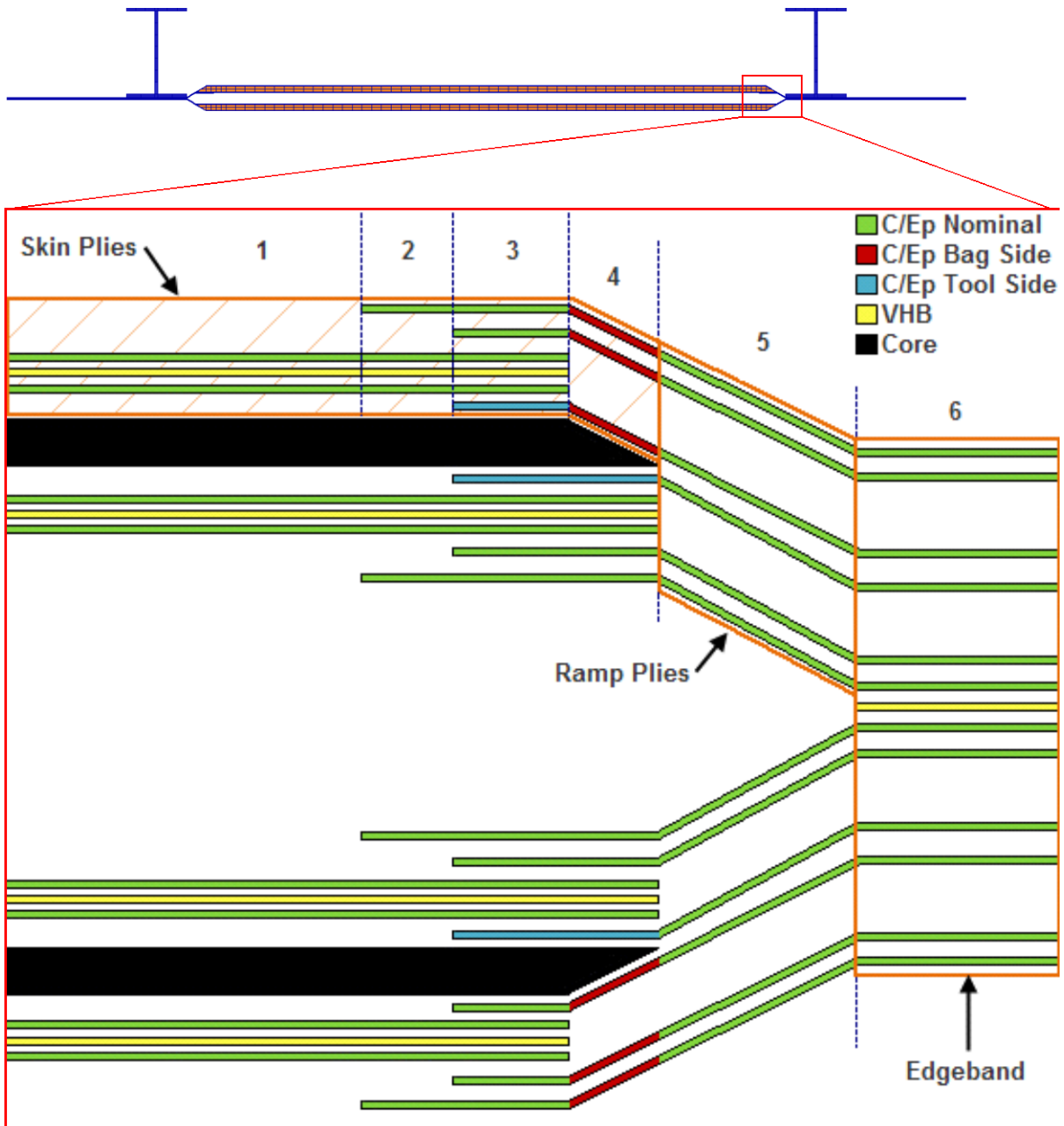


Figure 84: Upper skin plies.

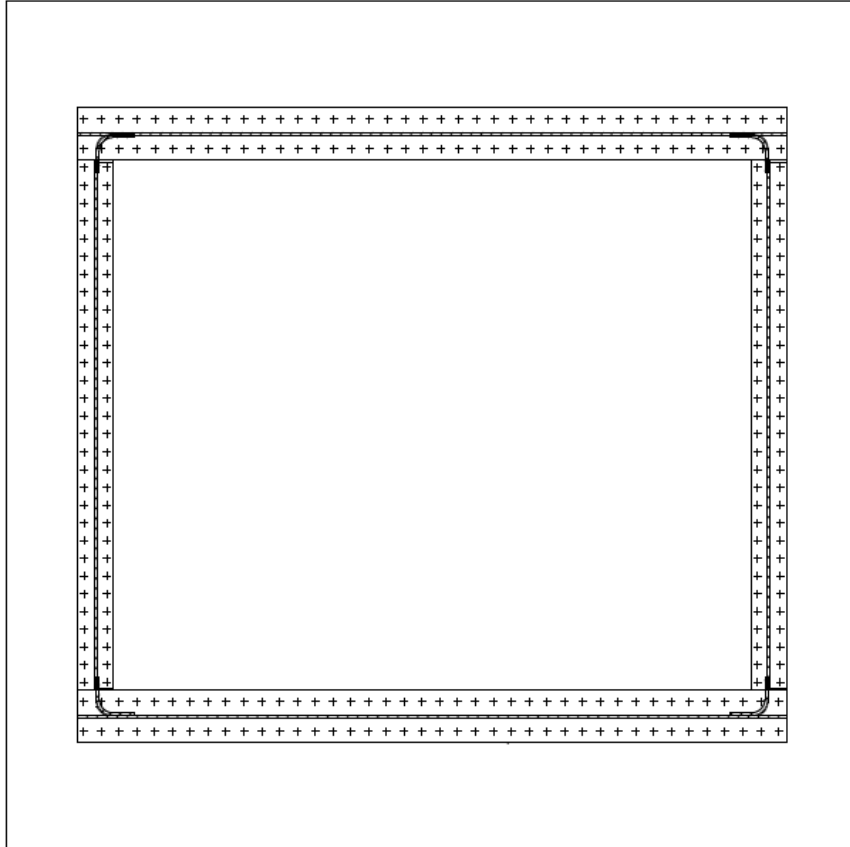


Figure 85: Fasteners through roof beams and edgeband.

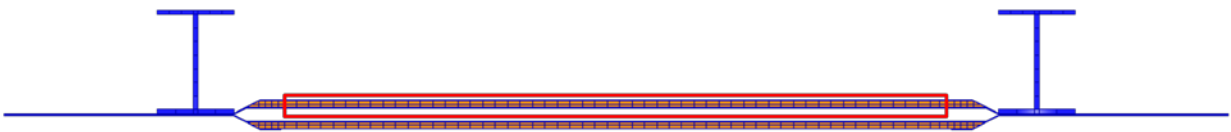


Figure 86: Panel section for step load analysis.

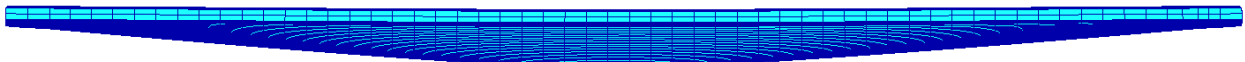


Figure 87: Non-linear analysis deflection results.

3.3.2.6 Optimized Panel Manufacturing

The optimized panel was made from two subpanels, joined together along the outer edge with VHB, and via fasteners to the beam frame. Figure 88 - Figure 92 summarize the manufacturing process at Bell-Textron. First, an Aluminum tool was machined to facilitate the subpanel layups. Layers of pre-cured fabric and VHB were laid on the flat portion of the tool, and vacuum compacted between layups. Uncured fabric was laid in the transition region and edges, and hand worked to ensure proper shaping. The honeycomb core was attached, and the rest of the plies overlaid. Each subpanel was then vacuum sealed and cured in an autoclave. The two panels were assembled with VHB, which is also an adhesive, and the frame was overlaid to match-drill holes for the fasteners. The fasteners were attached and checked for tightness. Finally, holes were drilled along the edges to match those in the NASA SALT facility. The final optimized panel is shown in Figure 93.

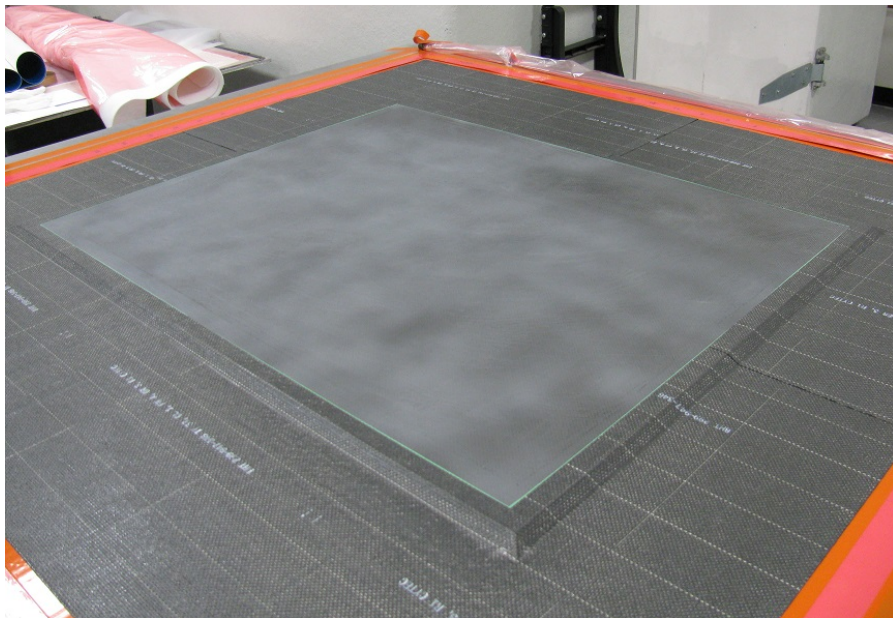
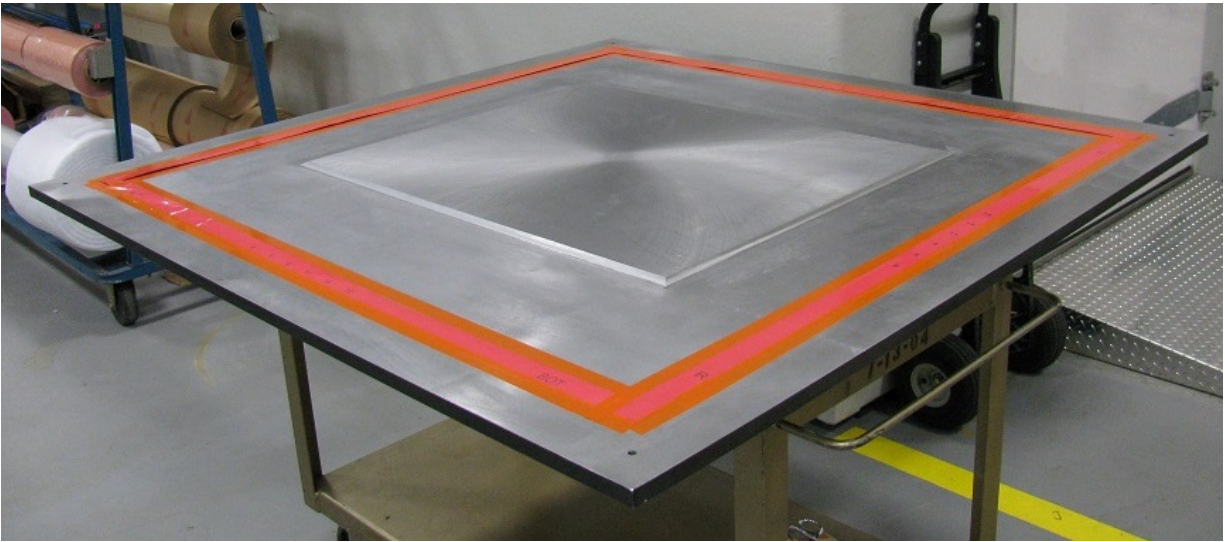


Figure 88. Aluminum tooling (top), with layers of fabric and VHB applied (bottom).

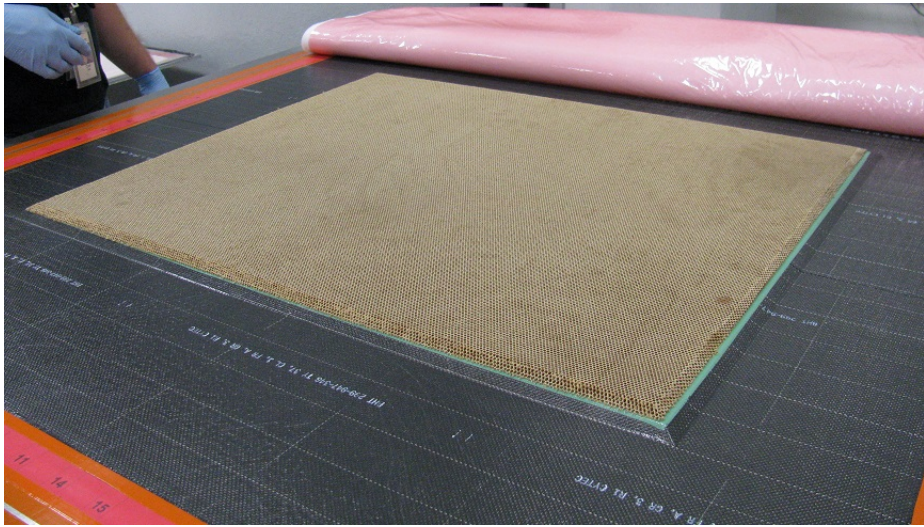


Figure 89. Top – hand working of edge material, Bottom – application of honeycomb core.

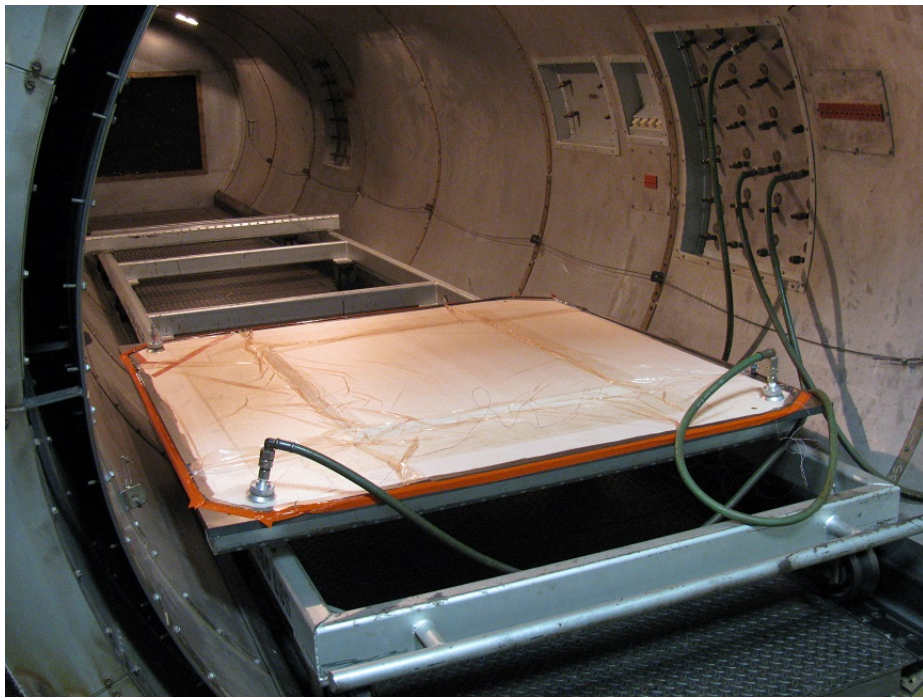
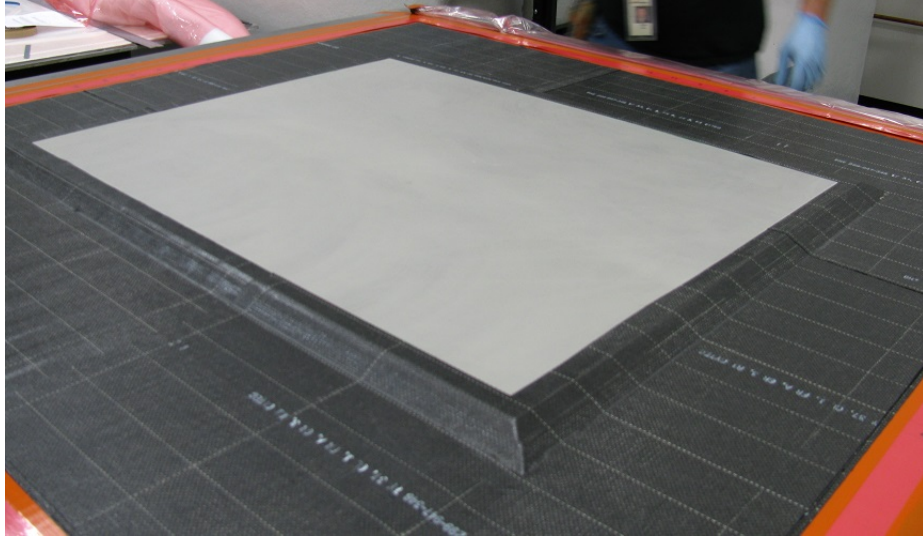


Figure 90. Top – Completed single subpanel, Bottom – Curing of vacuum-sealed subpanel.

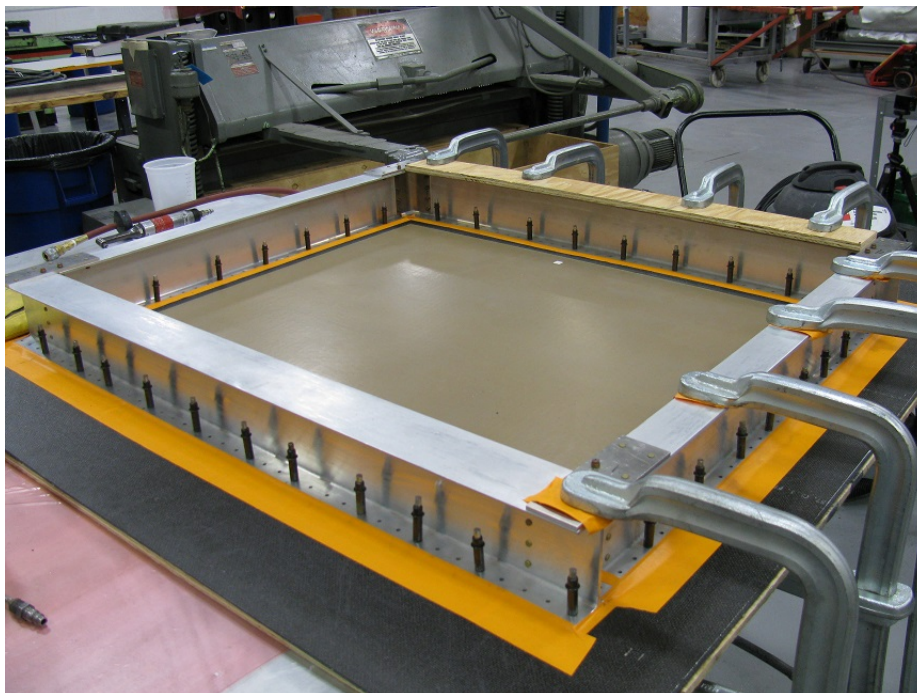
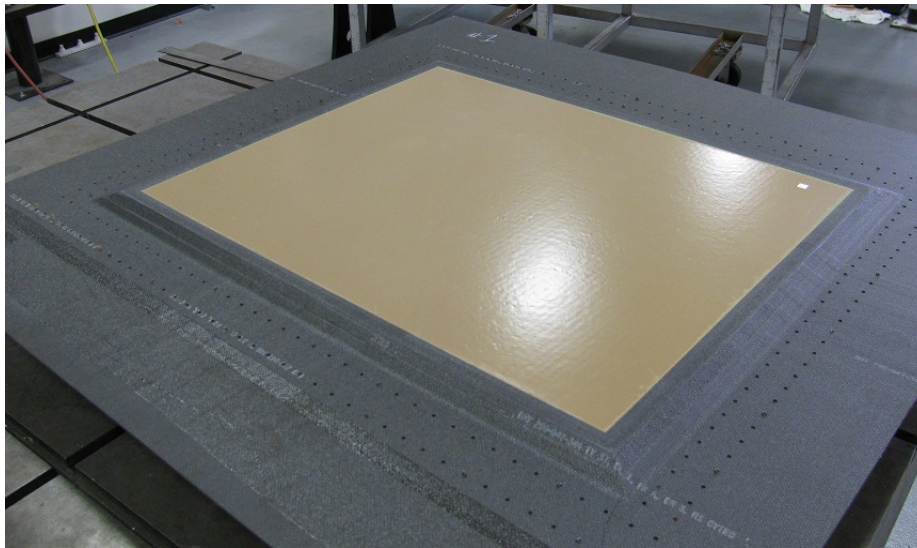


Figure 91. Match drilled holes for framing.

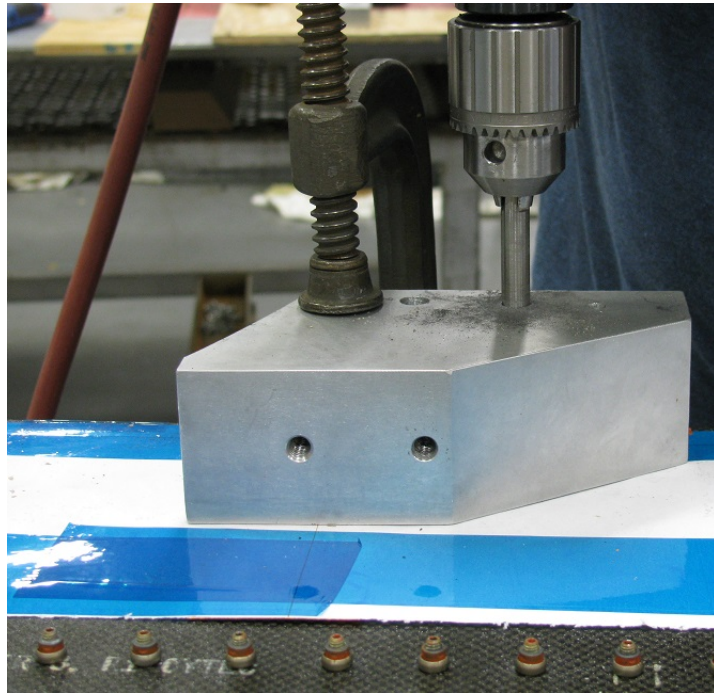


Figure 92. Top – tightness check of frame fasteners, Bottom – drilling of mounting holes for NASA SALT facility.

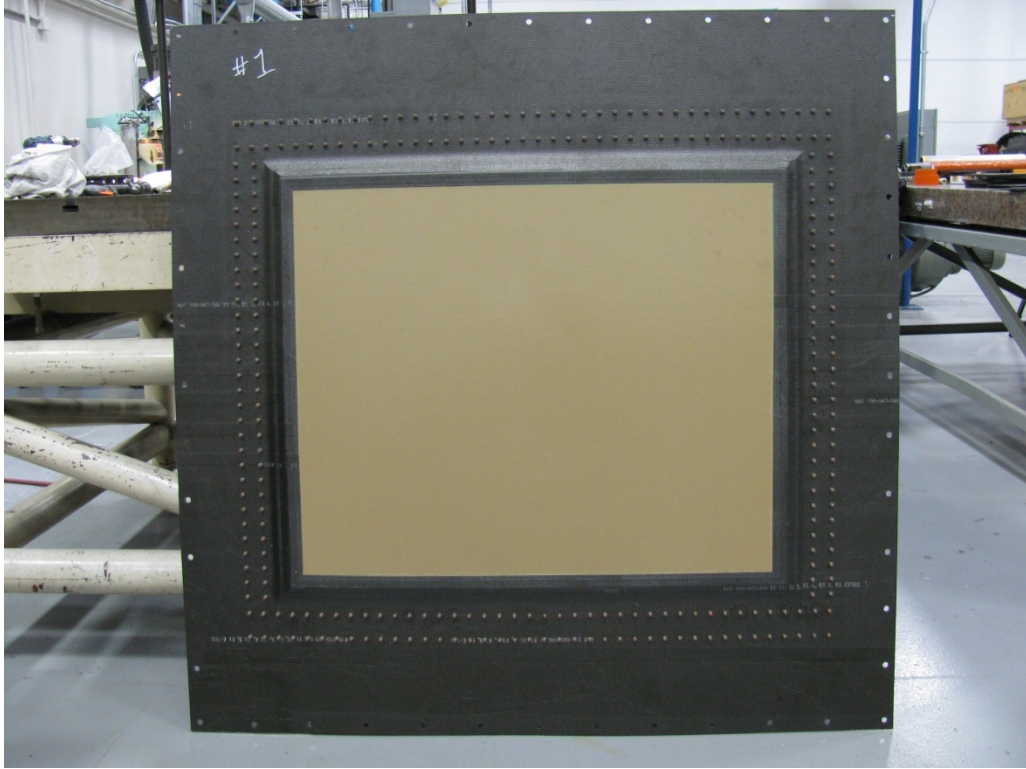


Figure 93. Final optimized panel – top – interior face, bottom – exterior face (with frame).

4 Optimized Panel Performance

4.1 Measured Modes, Loss Factors, and Mobilities

Modal and sound power measurements for the optimized panel were made at ARL/Penn State and in NASA's SALT facility. A rectangular grid of measurement points with 2 inch spacing was used for the modal measurements. Modes were measured for free and mounted conditions. Samples of the extracted modes are shown in Figure 94.

Resonance frequencies and loss factors for the free panel measurements are shown in Figure 95. The modes are split into those dominated by the panel edges and the center panel region. Damping in the edge modes is high, ranging between 0.15 and 0.30, while damping in the center panel region ranges between 0.04 and 0.07, similar to that in the test coupon with treated face sheets. Recall the baseline panel damping without embedded VHB is about 0.01. Modal loss factors of the center panel modes measured in the free and mounted panel are also compared in Figure 95. The center panel modal frequencies do not change significantly when the panel is mounted, but mounting in SALT does increase loss factors slightly. The edge modes, of course, are much stiffer when the panel is mounted, and are not readily extracted from the data due to the extremely high loss factors.

In fact, the damping is so high that all modes become difficult to extract and identify above 500 Hz. Edge, center, and beam modes are strongly cross-coupled and the panel response due to drives on the center panel and edge regions becomes nearly constant with frequency, as shown in Figure 96. The nearly constant response indicates high modal overlap, caused by high damping as well as high modal density. Figure 97 compares the averaged center panel transverse vibration response, averaged over three drive locations. The figure shows that the optimized back panel response is several dB lower than that of the driven front panel above 500 Hz, with reductions increasing with increasing frequency. The subpanels are therefore well isolated from each other, which should lead to reduced noise transmission. The driven center panel response in the optimized panel is comparable to that of the baseline panel below 2 kHz, and mitigated above 2 kHz. The optimized panel response is clearly more highly damped than that of the baseline panel.

Note that the response in Figure 96 and Figure 97 rolls off significantly with increasing frequency. This may be due to low input forces from the shaker. Mobilities above 3 kHz may therefore be biased low.

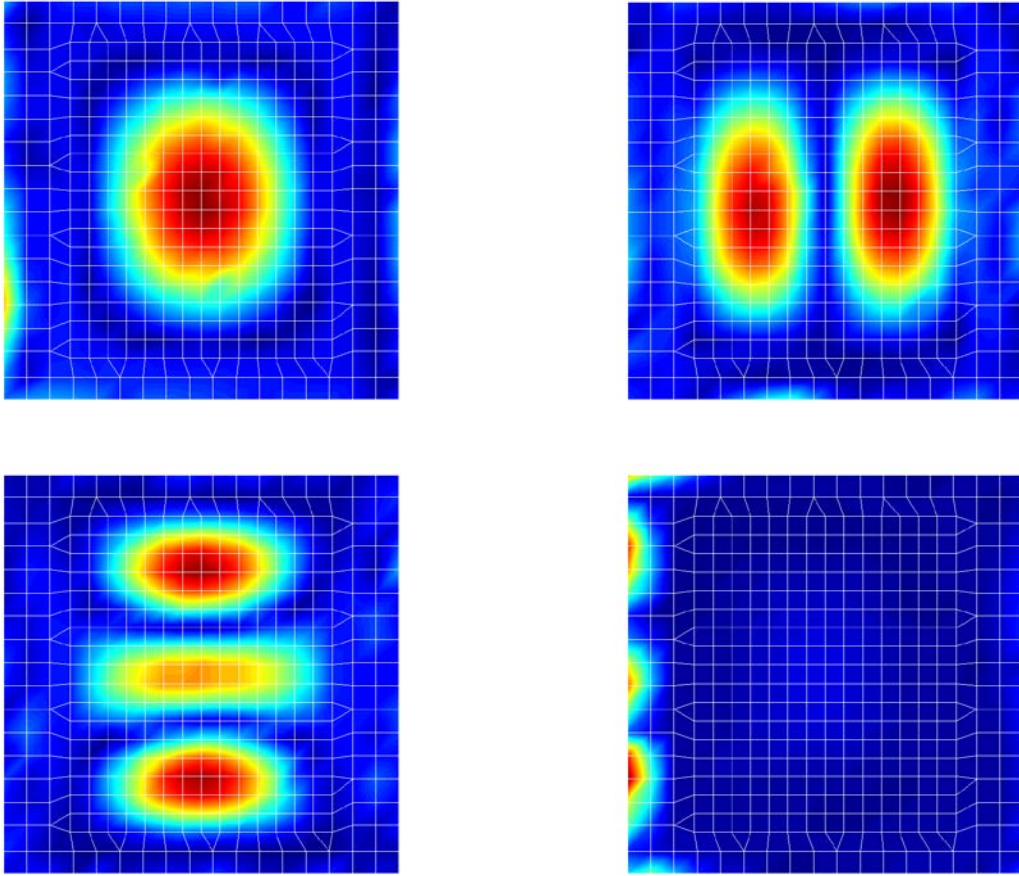


Figure 94. Mode shapes of optimized panel. Upper left (1,1); upper right (2,1); lower left (1,3), lower right – edge mode.

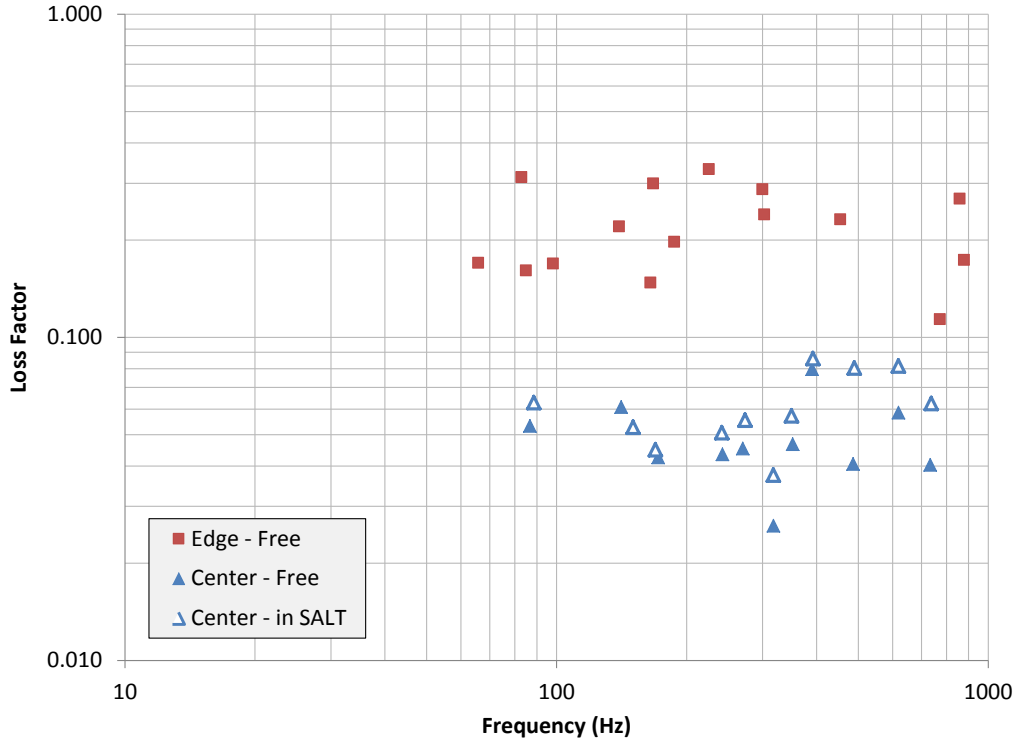


Figure 95. Modal loss factors of optimized panel, free and fixed (in SALT) edge boundary conditions.

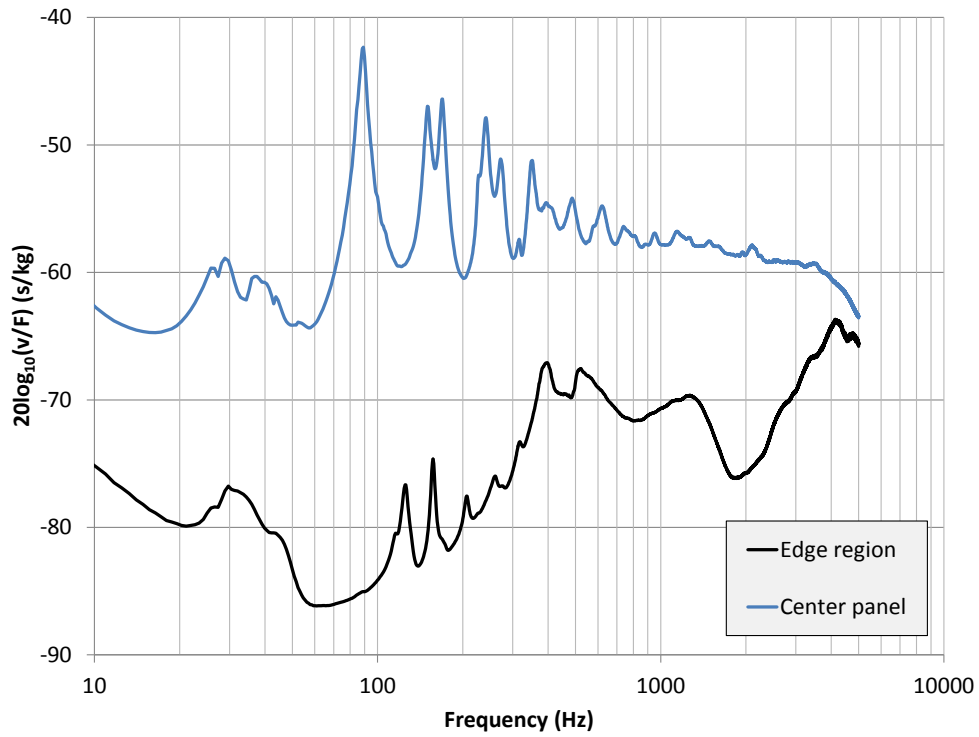


Figure 96. Surface-averaged transverse v/F for center and edge regions of optimized panel with free boundaries.

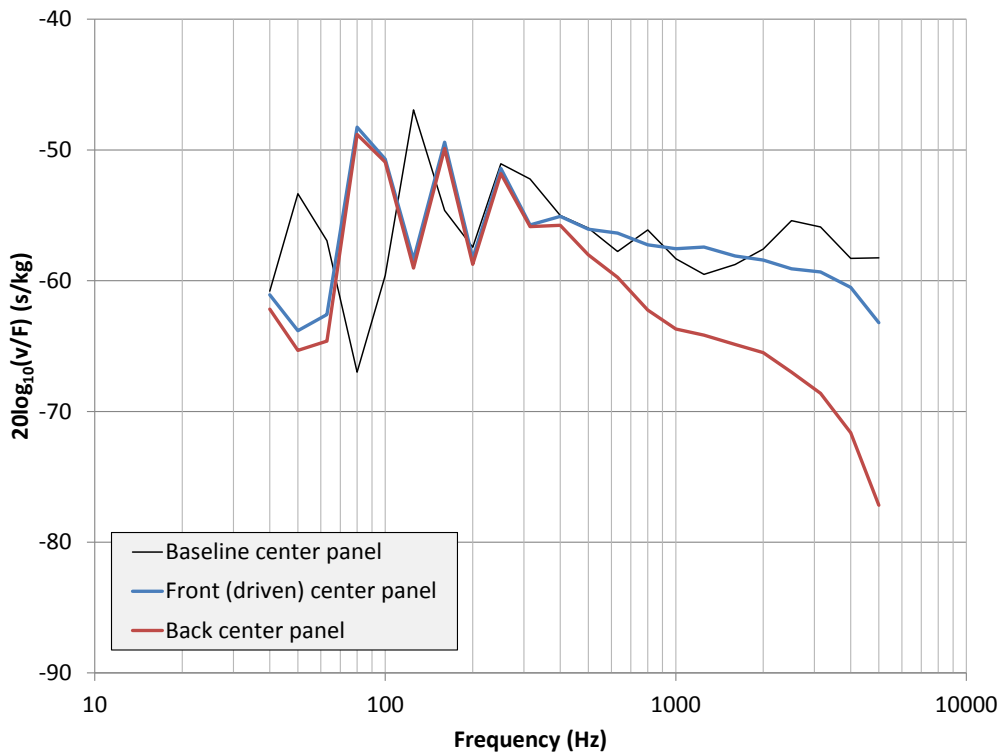
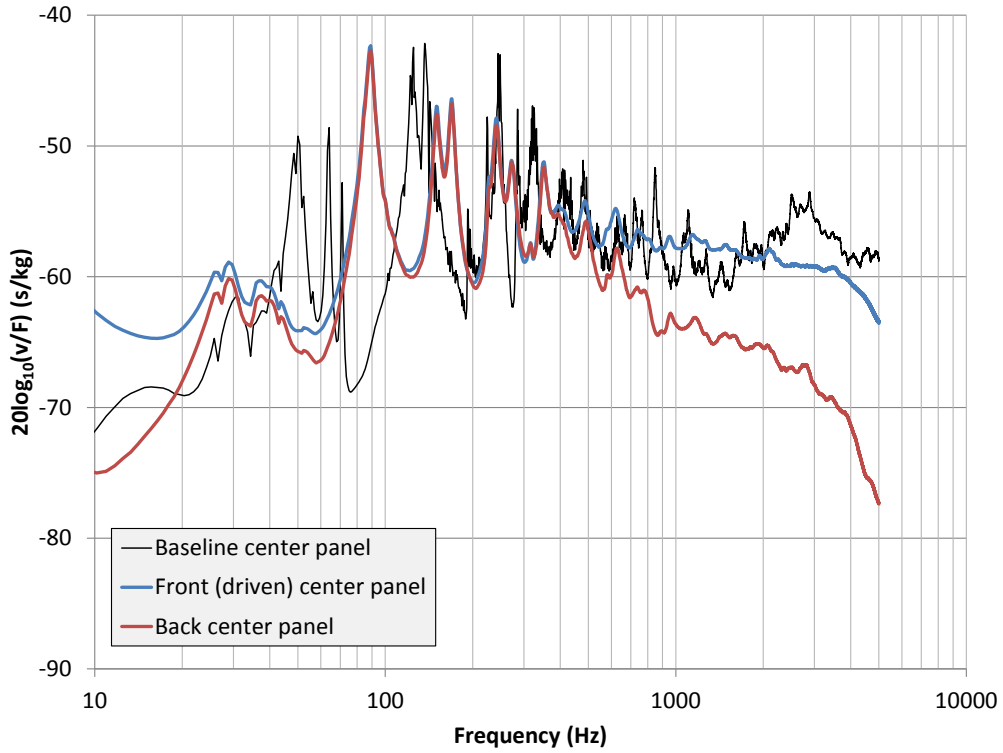


Figure 97. Surface averaged center panel transverse v/F averaged over three center panel drives, optimized (front and back center panels) and baseline panels with free boundaries. Top – narrow-band, Bottom – one-third octave band.

4.2 Radiated Sound Power

Both structural and acoustic (diffuse field) drives were applied to the panel while mounted in the SALT facility (Figure 98 and Figure 99). Transverse forces drove the panel at each of the four joints (representing the mounting locations of the transmission) to measure drive point mobility, shown in Figure 100. The shaker drive data is useful up to 5 kHz. Given the similarity between the mobilities (with the exception of joint 2, which was likely measured at a slightly different location along the beam flange), radiated sound power was measured for a drive on a single joint (joint 4). Radiated sound power for the structural and diffuse field excitations was computed by summing over a square array of intensity measurements. The convergence study for a diffuse drive in Figure 101 shows that a 10.16 cm (4 inch) spacing, corresponding to a 13 x 13 array of measured intensities, provides accuracy within 0.1 dB. The convergence study also shows the presence of the panel-cavity-panel resonance near 400 Hz. However, since the SALT facility Schroeder frequency is about 350 Hz, subsequent plots are limited to frequencies from 315 Hz upward.

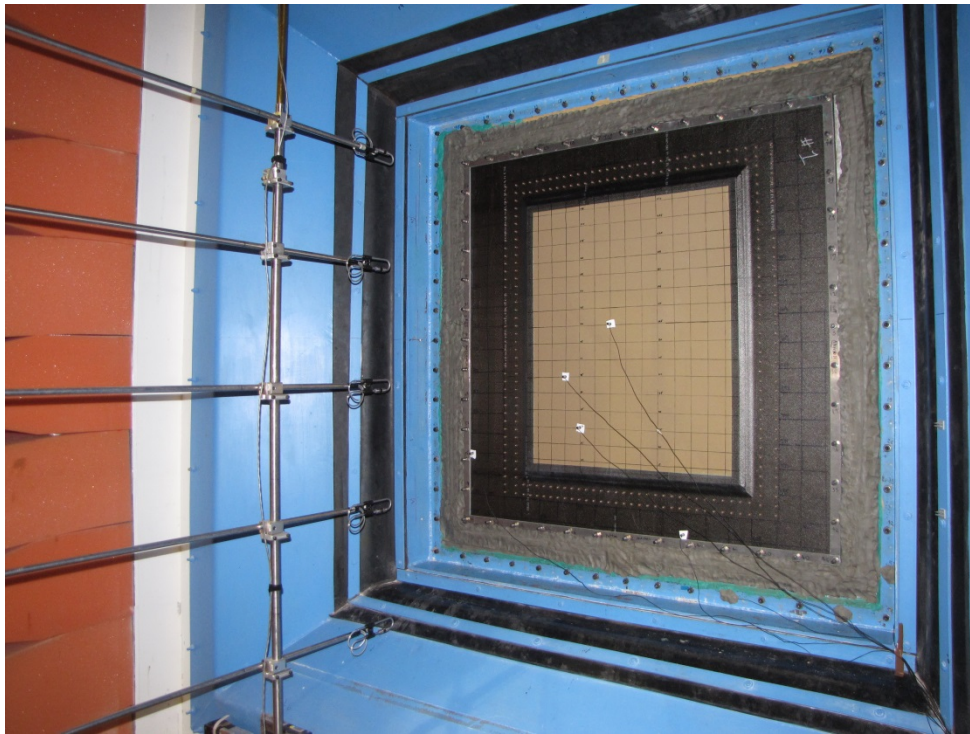


Figure 98. Optimized panel (inner surface shown) mounted in NASA SALT facility. Reference accelerometers are placed on center and edge panel regions. Intensity probe array is to the left.

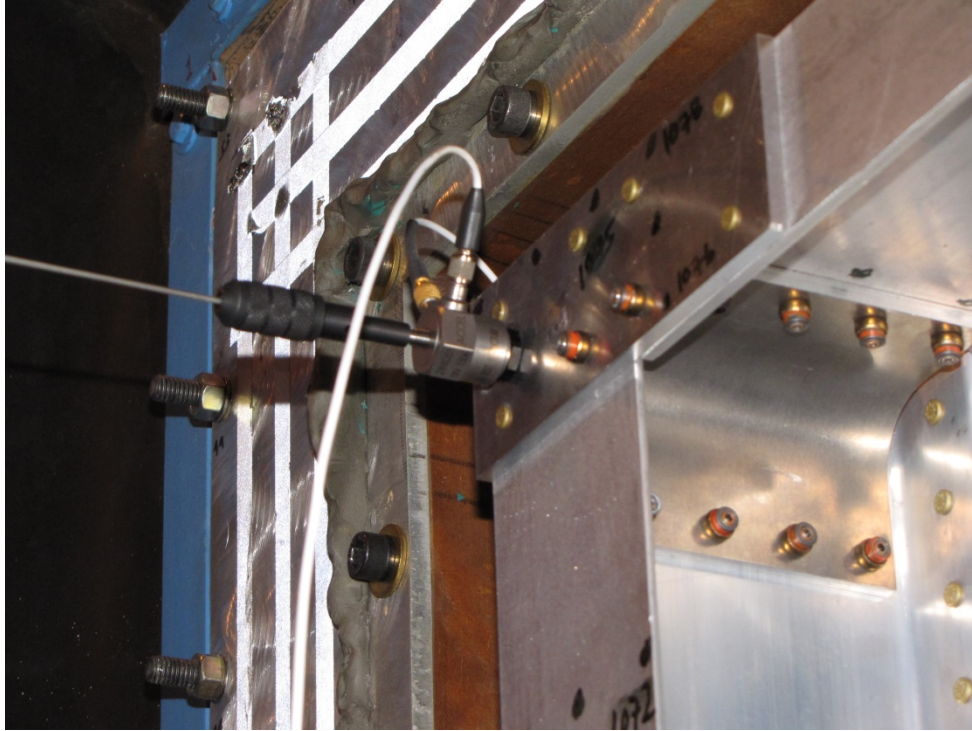


Figure 99. Shaker drive (via stinger and impedance head) on upper left frame corner.

The sound radiated from the baseline and optimized panels for a transverse joint drive is compared in Figure 102. The sound radiated by the optimized panel is much lower than that from the baseline panel, with improvements ranging from 6 to 20 dB, with the highest improvements above 2 kHz. The reduced sound power for structure-borne drives is due to the significant added damping in the panel, as well as damping sandwiched between the beams and panel.

The sound power transmission loss (power input by the diffuse field divided by the power radiated by the panel) for the baseline and optimized panels is shown in Figure 103, and the noise reduction for both structural and acoustic drives is compared in Figure 104. Once again, the sound power radiated by the optimized panel is much lower than that of the baseline panel, with 6-12 dB improvements. The frequency with the smallest improvement is the coincidence dip at 2500 Hz, which was positioned by design to be between the 1 and 3 kHz gear mesh tones of highest interest. The TL improvements are due to a combination of the split panel design, as well as the increased structural damping and MicroLite blanket in the air cavity. The improvements are not as high as anticipated prior to the testing, however. Analytic modeling of the transmission loss is therefore used to analyze the performance in more detail.

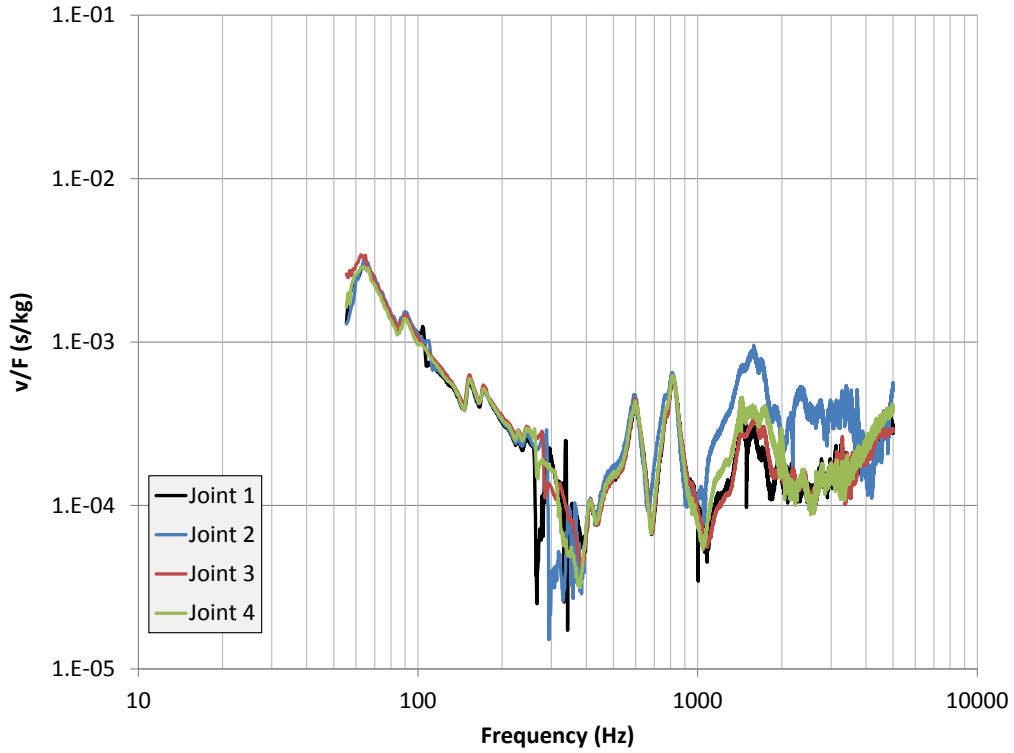


Figure 100. Drive point mobilities at each of the four beam joints.

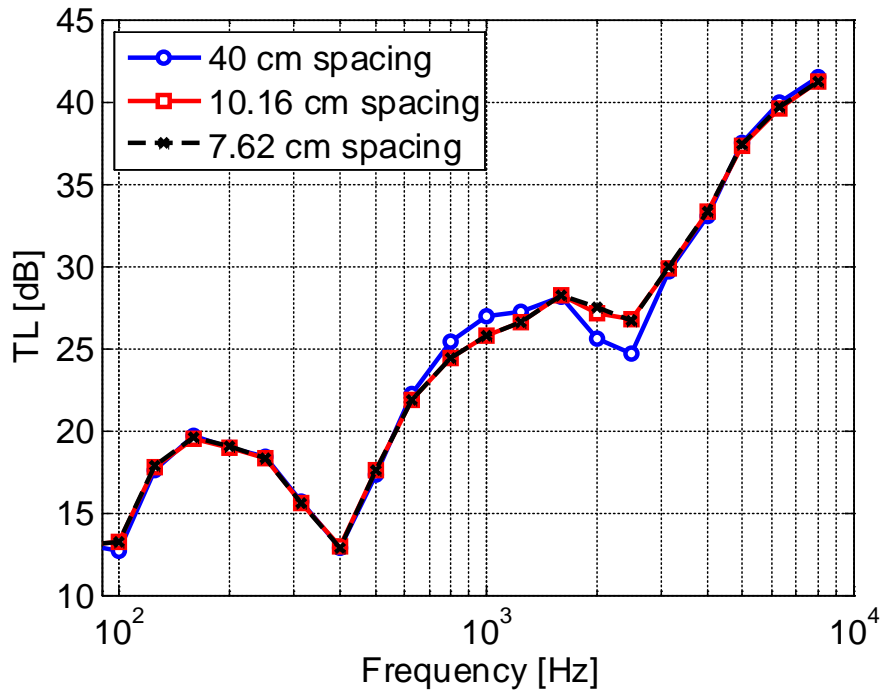


Figure 101. Convergence of sound power measurements for diffuse acoustic field drive on optimized panel in NASA SALT facility with increasing intensity scan resolution.

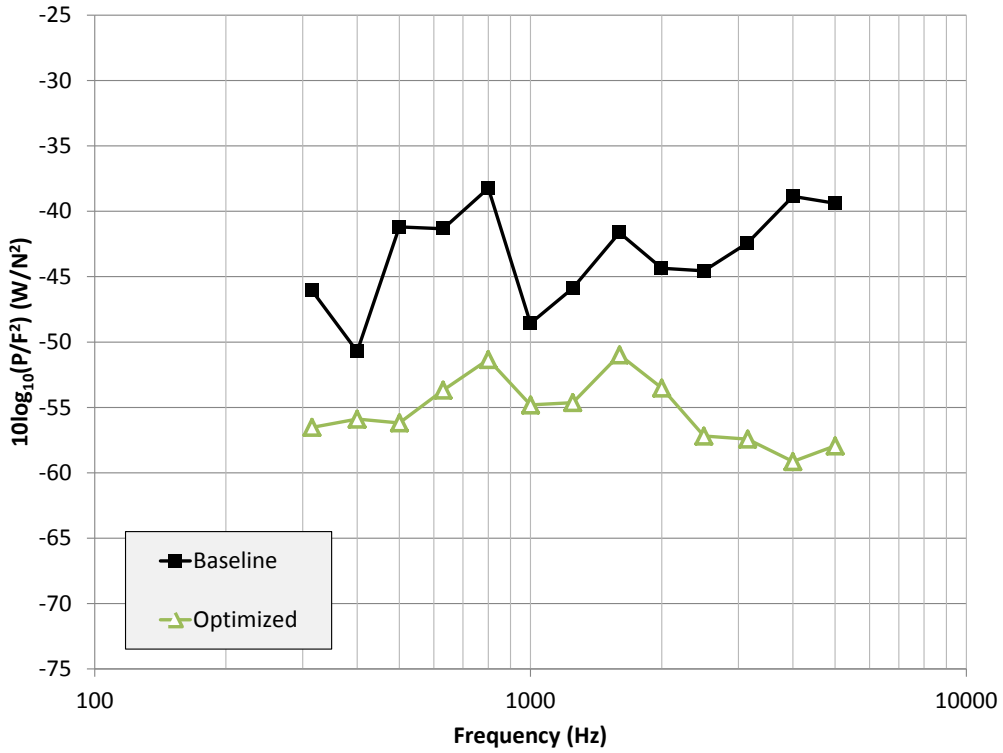


Figure 102. Radiated sound power from a drive at a single joint, optimized vs. baseline panel.

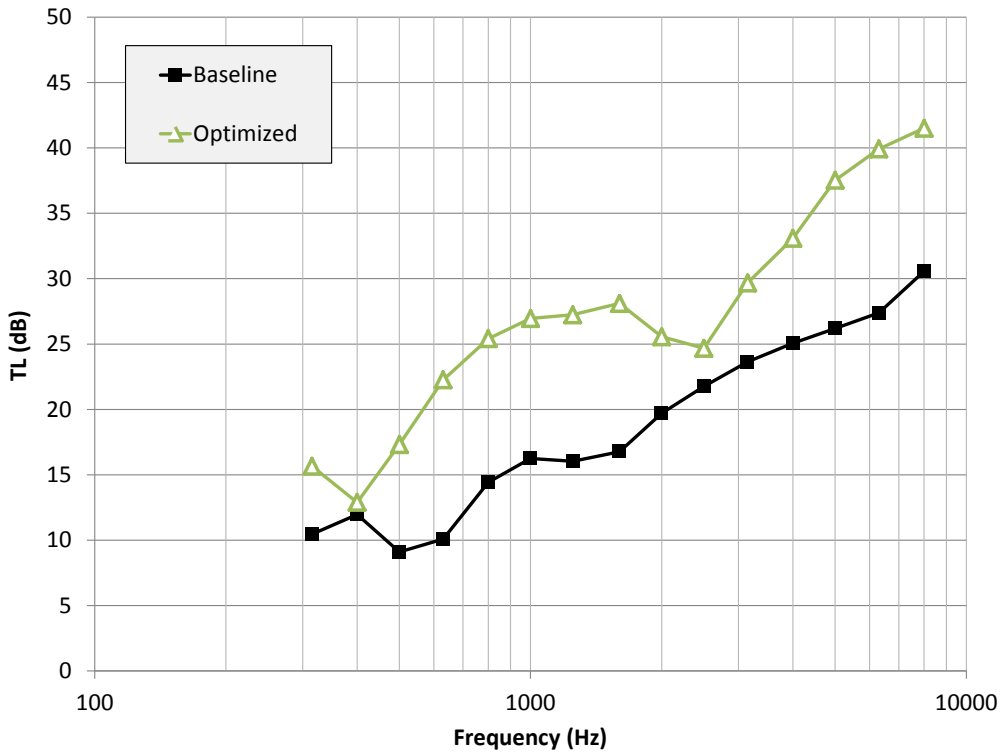


Figure 103. Sound power transmission loss, diffuse field excitation, for optimized and baseline panels.

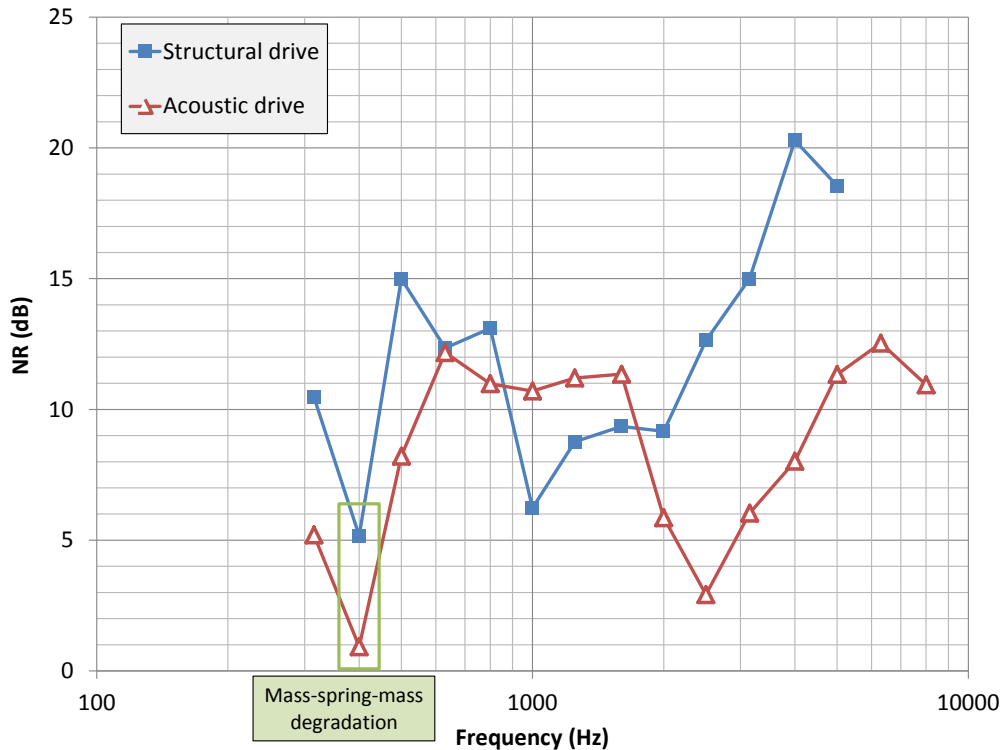


Figure 104. Noise reduction for structural and acoustic (diffuse field) drives.

4.3 Analytic Diffuse Field Panel TL Modeling

The high panel damping and resulting high modal overlap at frequencies above 500 Hz allows the use of simple analytic models to estimate sound power transmission loss. This simplification results in significant computational savings, both in model construction and computer analysis. Infinite panel transmission loss theory is therefore used for both the center sandwich panel region, as well as the edge region to estimate transmitted sound power.

Incident power is computed simply as the product of the surface incident intensity and the panel region areas (30 in x 36 in = 1080 in² for the center panel, and 2 x 5 in x 46 in + 2 x 3 in x 36 in = 676 in² for the edge regions; see Figure 6 for panel dimensions and subtract a one inch wide frame around the panel when clamped in the NASA SALT facility).

The edge region of the optimized panel is constructed of 12 layers of 0.0079 inch thick carbon fiber sheets (the same materials used for the center panel), sandwiched around a single layer of the 0.005 inch thick VHB material. Each set of six layers above and below the VHB is oriented to give nearly quasi-isotropic elastic behavior. The total edge thickness is 0.1 inches. The equivalent Young's modulus of the optimized panel edge region is assumed to be 80% that of the baseline panel due to the flexibility of the VHB. The measured loss factor of 0.30 is applied to the optimized edge panel analytic model, and the lower bound of the measured center panel loss factors – 0.04 – is applied to the center panel.

The transmitted powers are summed, and combined with the total incident power to compute overall panel TL. Figure 105 shows the incident power, power transmitted through the center panel region, and

power transmitted through the edge panel regions for the optimized panel. No correction is made for the mass-spring-mass resonance of the center panel, which occurs near 500 Hz. The added transmission loss of the MicroLite is included in the center panel radiated power. Due to the improved transmission loss of the center panel region, the power radiated through the edge is dominant over most of the frequency range, with the exception of the coincidence frequency of the center panel near 2 kHz.

Figure 106 compares the simulated TL for the center panel regions to those of the overall panel TL. Clearly, the overall panel TL improvements are not as significant as those of the center panel regions alone. Figure 107 compares the analytic total sound power transmission loss for the optimized and baseline panels to those measured in the SALT. The agreement is reasonable between 400 and 4 kHz - within 3 dB. The center panel coincidence dip is sharper in the measured data, suggesting that the MicroLite gap fill material may not be providing the anticipated additional TL reductions. The measured edge region coincidence dip in the optimized panel seems to actually be near 8 kHz, instead of near 5 kHz in the analytic model. This difference distorts the analytic TL curve above 5 kHz, worsening the agreement between simulation and measurement.

The figures indicate that the optimized panel TL is limited by transmission through the edge panels, such that the large increases in TL in the center panel do not fully translate to comparable improvements in the overall panel. This is particularly true of the MicroLite, which has only a small impact on total panel TL near coincidence (and which is not observed in the measured data). Future design improvements to roof panels should therefore be complemented by accompanying noise control studies on other fuselage panels, which may cause flanking noise transmission paths which are stronger than those through the roof panel.

To investigate the impact of the added damping in the center and edge panels, the optimized panel analytic TL is recomputed using the lower damping of the baseline panel. The results in Figure 108 show that, consistent with panel theory, added damping increases random incidence TL at and above the center and edge panel coincidence dips. The improved TL at 1 kHz is due solely to the split panel concept, whereas the TL at 3 kHz is slightly enhanced by the added damping. Above 3 kHz, the edge panel damping benefits are more significant.

In the future, higher fidelity simulations of both TL, as well as sound power induced by structural drives, may be made using FE/BE (which is expensive), or SEA modeling (which is more economical). The beams, center panel, and edge panel regions may be represented by statistical models of mode types, and coupling coefficients to include the effects of the beams in the TL calculations.

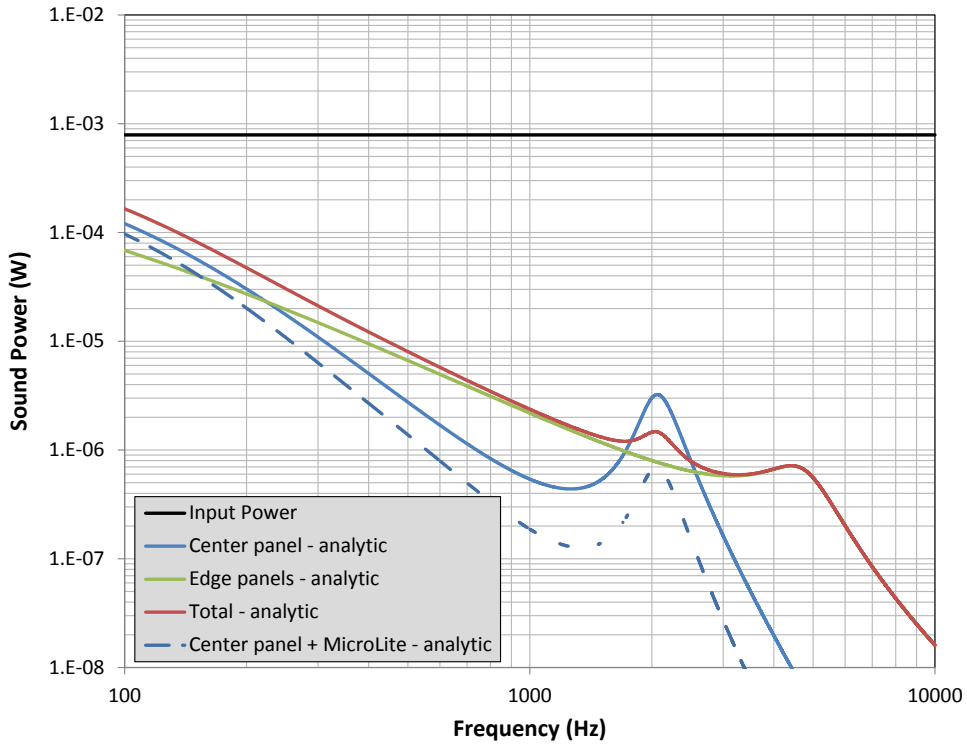


Figure 105. Incident and transmitted powers for optimized panel.

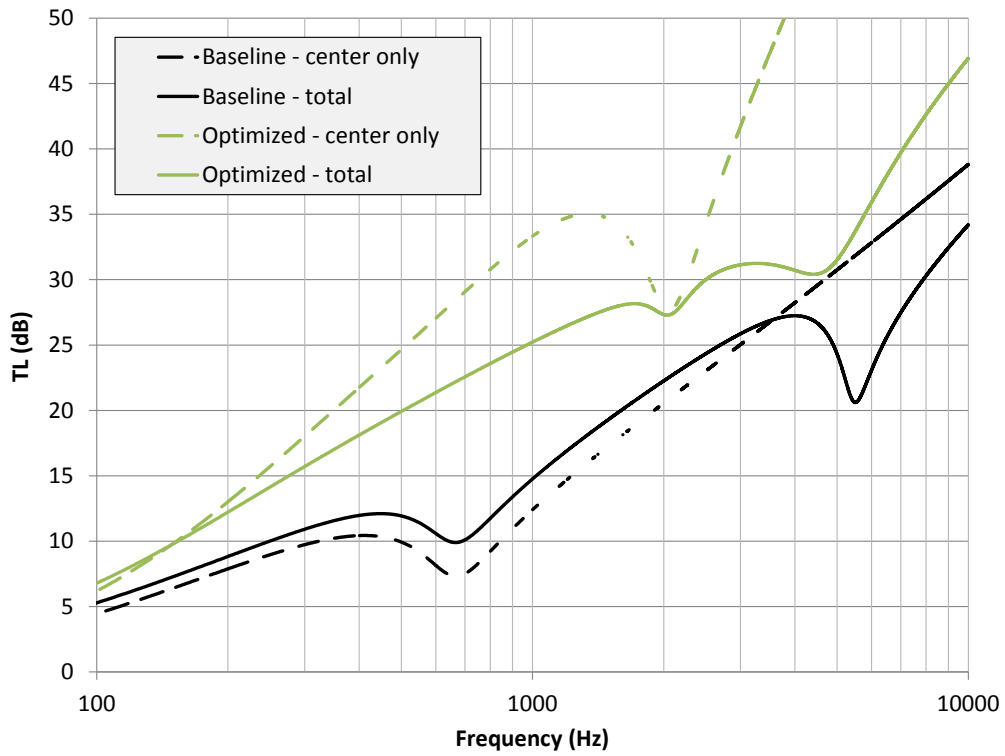


Figure 106. Transmission loss for baseline and optimized panels.

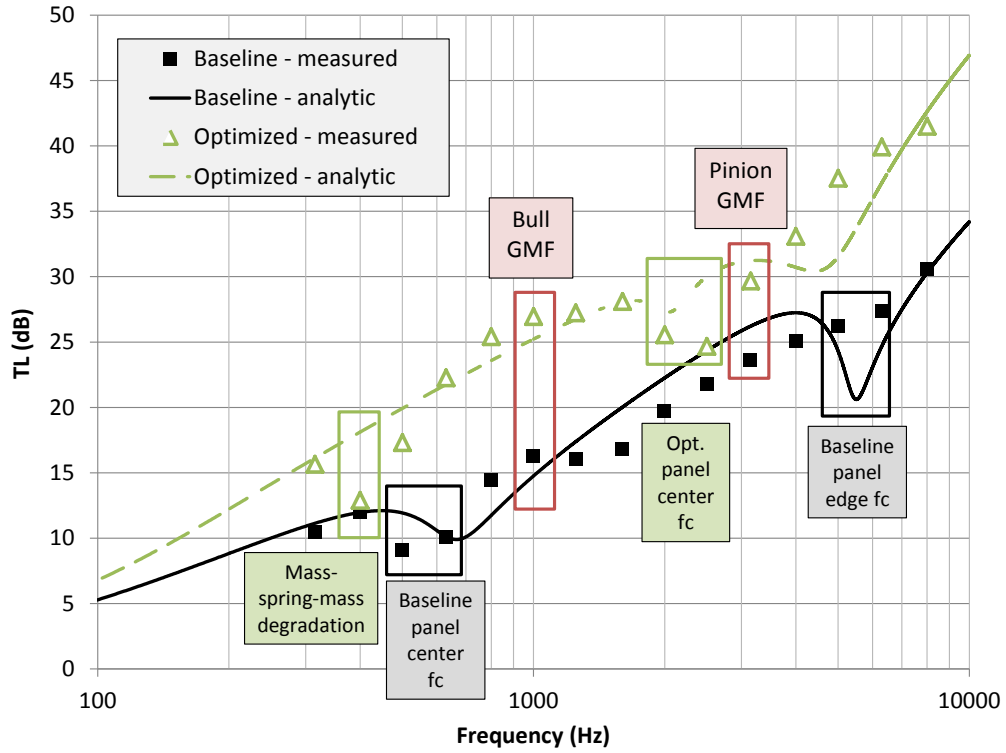


Figure 107. TL of baseline and optimized (including MicroLite) panels, simulations and measurements.

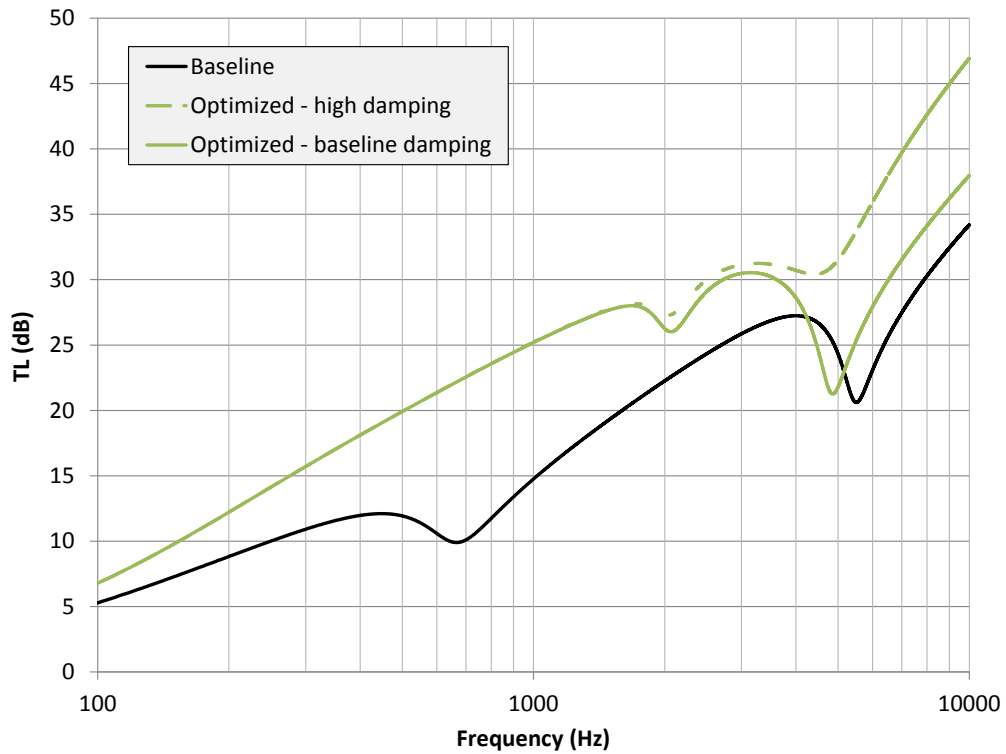


Figure 108. Analytic TL of baseline and optimized (including MicroLite) panels with variable damping.

5 Summary and Conclusions

Baseline and optimized composite roof panels representative of those used on Bell helicopters have been designed, constructed, analyzed, and tested. A structural-acoustic model of the baseline panel has been created and analyzed using finite element and boundary element models. Modes of vibration, forced vibration response, and sound power transmission loss (TL) all compare well with corresponding measurements made on the physical panel in NASA's SALT facility. The numerical modeling approach, or Virtual Transmission Loss (VTL) modeling, has therefore been confirmed using the baseline panel data. Analytic models of the TL also compare well to the measured and numerical data, showing that the simpler analytic approaches may be used to design and assess the optimized panel.

The analysis and testing results show that the center sandwich panel region of the baseline panel is extremely stiff and lightweight, with bending waves supersonic above the coincidence frequency of about 700 Hz. Since the transmission tones of interest are between 1 and 4 kHz, this means the baseline panel center region would reradiate those tones perfectly. To reduce radiated sound, we have reduced structural vibration with added damping, and subdivided the panel into thinner panels separated by an airgap to reduce airborne sound transmission. The final optimized panel has face sheets with embedded layers of 3M VHB material, increasing structural damping in the center sandwich panel from about 0.01 to 0.05, and two subpanels, nearly doubling sound power transmission loss through the center sandwich panel region. The optimized panel mass density is less than that of the baseline panel with added acoustic treatments, but is slightly thicker. To accommodate the extra thickness, the panel is offset slightly upward toward the transmission to maintain the same cabin roof height. Several structural integrity assessments were conducted on the optimized panel to ensure its suitability for use in a commercial rotorcraft.

Analytic studies of the potential vibration reduction benefits of arrays of inclusions in infinite panels were promising, but did not translate well to finite panels with low wavenumber vibrations. The inclusion arrays were therefore not manufactured in the optimized panel. The analytic procedures, however, have been updated to allow for finite panel effects, and may be used in the future to pursue other more effective potential noise reduction designs.

The optimized panel was tested in the NASA SALT facility, and shows structure-borne noise improvements of 6-20 dB, and airborne noise improvements of 6-12 dB. Analytic transmission loss studies agree well with the measurements, and show that the edge paneling dominates sound power transmission in the optimized panel, limiting the benefits of the center panel quieting measures.

Several key lessons learned from this study are listed below.

- Material properties of sandwich panels are not always well understood, even when provided by suppliers of the component materials. Constructing small test coupons, measuring structural mode shapes and frequencies, and updating material properties using a corresponding FE model is therefore essential.

- When designing roof panels (or other panels), the thicknesses and material properties should be adjusted to tune coincidence dips to lie between key transmission noise tonal frequencies.
- Highly damped structures with moderately high modal densities may be assessed using simple infinite panel transmission loss theory, at significant computational and manpower savings compared to FE/BE modeling.
- Minimizing the sound radiated by one component of a complex multi-component structure does not translate to similar total structure noise reduction. In the case of the roof panel investigated here, the optimized panel TL is dominated by edge panel sound radiation. Including additional MicroLite, therefore, had little added noise reduction benefit. In future designs, all components must be considered simultaneously when minimizing sound radiation.

6 References

1. S.D. Garvey, "The vibrational behavior of laminated components in electrical machines," 4th *International Conference on Electrical Machines and Drives*, London, UK, 13-15 Sep 1989, pp. 226-231.
2. G.H. Koopmann and J.B. Fahline, *Designing Quiet Structures*, Academic Press, 1996.
3. S.A. Hambric et. al, "Simulating the vibro-acoustic power of fluid-loaded structures excited by randomly distributed fluctuating forces," *Proceedings of NOVEM 2005*, St. Raphael, France, 18-21 April 2005.
4. Hambric, S.A., Boger, D.A., Fahline, J.B., and Campbell, R.L., "Structure- and fluid-borne acoustic power sources induced by turbulent flow in 90 degree piping elbows," *Journal of Fluids and Structures*, 26, 121-147, 2010.
5. F.W. Grosveld, "Calibration of the structural acoustics loads and transmission facility at NASA Langley Research Center," *Internoise 99*, Fort Lauderdale, Florida, 6-8 December 1999.
6. F.Fahy and P. Gardonio, *Sound and Structural Vibration*, 2nd Edition, Academic Press, 2007.
7. Davis, E.B., "Designing Honeycomb Panels for Noise Control," *AIAA/CEAS Aeroacoustics Conference*, A99-27801, 792-800, 1999.
8. Peters, P.R., Rajaram, S., and Nutt, S., "Sound transmission loss of damped honeycomb sandwich panels," *Proceedings of Internoise 2006*, Honolulu, HI, 3-6 December 2006.
9. Palumbo, D., and Klos, J., "The effects of voids and recesses on the transmission loss of honeycomb sandwich panels," *Noise Control Engineering Journal*, 59 (6), 631-640, Nov-Dec 2011.
10. A.D. Pierce, *Acoustics: An Introduction to its Physical Processes and Applications*, Acoustical Society of America, 1994.
11. B.F. Cron and C.H. Sherman, "Spatial Correlation Functions for Various Noise Models," *Journal of the Acoustical Society of America*, 1962.
12. M.R. Shepherd and S.A. Hambric, "Comment on plate wavenumber transforms in *Sound and Structural Vibration*," *J. Acoust. Soc. Am.* **132**(4), 2155-2157, 2012.
13. E.G. Williams, *Fourier Acoustics: Sound Radiation and Nearfield Acoustical Holography*, Academic Press, San Diego, 1999.
14. C. Y. Shih, Y. G. Tsuei, R. J. Allemang, and D. L. Brown, "Complex mode indication function and its applications to spacial domain parameter estimation," in *Proceedings of the Seventh International Modal Analysis Conference*, pp. 533-540, 1989.
15. J. B. Fahline, R. L. Campbell, S. A. Hambric, "Modal Analysis Using the Singular Value Decomposition and Rational Fraction Polynomials", Technical Report 10-003 (2010)
16. ANSI S12.55-2006/ISO 3745: 2003, "Acoustics- determination of sound power levels of noise sources using sound pressure- precision methods for anechoic and hemi-anechoic rooms."
17. ASTM EE 2249-02: 2008, "Laboratory Measurement of Airborne Transmission Loss of Building Partitions and Elements Using Sound Intensity."
18. G. Del Galdo, M. Taseska, O. Thiergart, J. Ahonen and V. Pulkki, "The diffuse sound field in energetic analysis," *J.Acoust. Soc. Am.* **131**(2), 2012.

19. R.V. Waterhouse, "Interference patterns in reverberant sound fields," *J.Acoust. Soc. Am.* **27**, 1955.
20. F. Jacobsen and T. Roisin, "The coherence of reverberant sound fields," *J.Acoust. Soc. Am.* **108**(1), 2000.
21. H. Kang, J. Ih, J. Kim and H. Kim, "Prediction of sound transmission loss through multilayered panels by using Gaussian distribution of directional incident energy," *J.Acoust. Soc. Am.* **107**(3), 2000.
22. K. Lynch, P. Bauch, S.A. Hambric and A.R. Barnard, "A proposed correction for incident sound intensity distribution for diffuse field panel excitation and transmission loss simulations," *Proceedings of Noise-Con 2014*, Ft. Lauderdale, 2014.
23. F. Fahy, "Comment on 'An experimental investigation of the directional distribution of incident energy for the predicted of sound transmission'," *Appl. Acoust.* **64**, 2003.
24. B. Xu and S.D. Sommerfeldt, "Generalized Energy Density," *J.Acoust. Soc. Am.* **130**(3), 2011.
25. B. Xu and S.D. Sommerfeldt "A Hybrid modal analysis for enclosed sound fields," *J. Acoust. Soc. Am.* **128**(5), 2010.
26. F. Jacobsen and A.R. Molaes, "Ensemble statistics of active and reactive sound intensity in reverberation rooms," *J.Acoust. Soc. Am.* **129**(1), 2011.
27. R.V. Waterhouse, "Statistical properties of reverberant sound fields," *J.Acoust. Soc. Am.* **43**, 1968.

Appendix A – Baseline and Optimized Panel Testing

Structural acoustics measurements of the baseline and optimized panels were made to help validate the numerical models, and confirm improvements in structure-borne and air-borne sound power transmission loss. The free-free modal analyses were conducted at Penn State ARL and transmission loss testing was performed in the SALT facility at NASA Langley.

A.1 Modal Analysis

Experimental modal analysis was performed on the panel with free boundary conditions, and installed in the TL window. The results from these tests included natural frequencies, mode shapes, loss factors, energy, conductance, radiated sound power and estimates of material stiffness (E_x , E_y). The effects of the ribs on the vibration were quantified and the modeling procedure for the panel was verified and refined based on the test results. The free boundary condition tests were used to confirm the panel modeling, and the installed tests used to confirm the boundary condition simulations (ideally clamped, but more realistically slightly different from purely clamped).

The modal test was performed using the roaming hammer approach with six reference accelerometers. One of the accelerometer locations was at a vertical location consistent with previous Bell flight measurements of a Bell 429. A grid of drive points with approximate spacing of 2" was laid up on the flat side of the panel. The grid points were refined near the I-beams and cross-beams so that there are 3 points across the beam. This required approximately 600 drive points on the panel surface. Additional drive points were specified on the beam surfaces, after examination of computational modal analysis results from the FE model of the baseline panel. The accelerometers were placed at various heights and widths along the panel with at least one on/near each I-beam. Three averages were obtained at each drive point to reduce measurement noise. Point mobility and conductance measurements were obtained at the reference accelerometer locations, as well as at each of the four beam intersection points using a refined procedure with 16 averages which circle around the accelerometer. For the modal test conducted while installed in the TL suite, sound intensity sweeps were also performed for shaker drives at the reference accelerometer locations (see below).

The hammer and accelerometer data were collected using PSU in-house software at a sampling frequency of 20 kHz for approximately 1.5 sec to achieve a frequency resolution of less than 1 Hz. Frequency response and coherence data was checked to ensure data quality. The data were processed using PSU in-house modal software which uses singular value decomposition together with rational fraction polynomial fitting to produce clean modal data. Time data were also processed using a decay method to confirm the modal damping values.

The free boundary condition test was performed at Penn State prior to arrival at the SALT facility. At SALT, the set up time was 4-8 hrs and the estimated measurement time was 8-16 hrs, including background noise measurements. The TL tests were performed twice, once before the Transmission Loss tests, and again afterward (removing and re-installing all sensors) to establish repeatability uncertainty. Several hammer excitations were also repeated.

List of hardware (PSU)

- Force hammer (PCB 086CO2, 50 mV/lbf)
- Six accelerometers (PCB 352-C67, 100 mV/g)
- Data acquisition (NI PXI w/ PXI 8106 controller & 2 PXI 4496 16 channel cards)
- Monitor, keyboard & mouse
- Glue and accelerator
- BNC cables and connectors
- Chalk line/marker

List required hardware (SALT)

- 12 Microphones
- 5 Intensity probes
- DAQ

List required software (PSU)

- Data acquisition software (PSU developed)
- Modal analysis software (PSU developed [15])
- Matlab

A.2 Transmission Loss Testing

Transmission loss measurements were performed on the panels using the intensity technique [16]. The panels were mounted with the stiffening beams facing the source (reverberant) room to be prototypical of rotorcraft conditions. The reverberant room was excited with an array of loudspeakers and the transmitted power were measured using a set of intensity probe measurements on the anechoic side. Accelerometers were installed at the same positions as used in the modal test in order to estimate the forcing function [17] and correlate TL measurements to the modal tests. The accelerometer data were acquired for 1 minute every 10 minutes for ensure adequate averaging and repeatability.

The frequency range was from 70 Hz – 8 kHz (for the 80 Hz – 12.5 kHz useable octave band frequencies) and the sampling frequency was at least 20 kHz. Sound intensity measurements were obtained over a 5' x 5' area with a 3" spacing between measurement locations. The tests were conducted with two intensity probe spacers to increase the frequency range. Multiple tests were conducted to establish repeatability bounds, and with different source levels to establish linearity. The estimated set up time was 1-2 hrs and the estimated measurement time was 8 hrs.

List of hardware (PSU)

- Six accelerometers (PCB 352-C67, 100 mV/g)
- Data acquisition (NI PXI w/ PXI 8106 controller & 2 PXI 4496 16 channel cards)
- Monitor, keyboard & mouse

- Glue and accelerator
- BNC cables and connectors

List of hardware (SALT)

- Five intensity probe kits (B&K 3595, consisting of a ½” microphone pair (B&K 4197) dual preamplifier (B&K 2683) and either a 8.5 mm, 12 mm, or 50 mm spacers)
- Intensity probe traverse controlled by LabVIEW
- Sound intensity calibrator (B&K 4297)
- Three sound intensity conditioning amplifiers (B&K Nexus 2691 4 channel conditioning amplifiers)
- Twelve microphones (GRAS Type 40AQ ½-inch prepolarized, random-incidence microphones with Type 26CA preamplifiers)
- Signal conditioner (PCB 584A 16-channel signal conditioner)
- Switch board (Precision Filters Inc. 464k switching system)
- Data acquisition (NI PXI-1045 chassis with 5 PXI 4472B 24-Bit 8 channel cards)
- Eighteen high frequency sound sources (Three JBL 2446H and Fifteen BMS 2” compression drivers)
- Six low-frequency sound sources (JBL JRX 115I 15-inch two-way speakers)
- Four multichannel amplifiers (RANE MA6S amplifiers)

List of software (SALT)

- MATLAB Data Acquisition Toolbox
- Custom MATLAB GUI
- Microsoft Excel
- NI LabVIEW

A.3 Shaker Testing

A vibration shaker was used to excite the structure. First, a random noise excitation was used with the shaker mounted on the bracket. The shaker was hung perpendicular to the panel from a PSU fixture. Intensity sweeps were performed to determine the sound radiation.

List of hardware (PSU)

- Six accelerometers (PCB 352-C67, 100 mV/g)
- Data acquisition (NI PXI w/ PXI 8106 controller & 2 PXI 4496 16 channel cards)
- Monitor, keyboard & mouse
- Glue and accelerator
- BNC cables and connectors
- Shaker (Wilcoxon F4, 100 mV/g, 100 mV/lb)
- Shaker mounting fixture

Frame Adaptor

UNIT: INCH

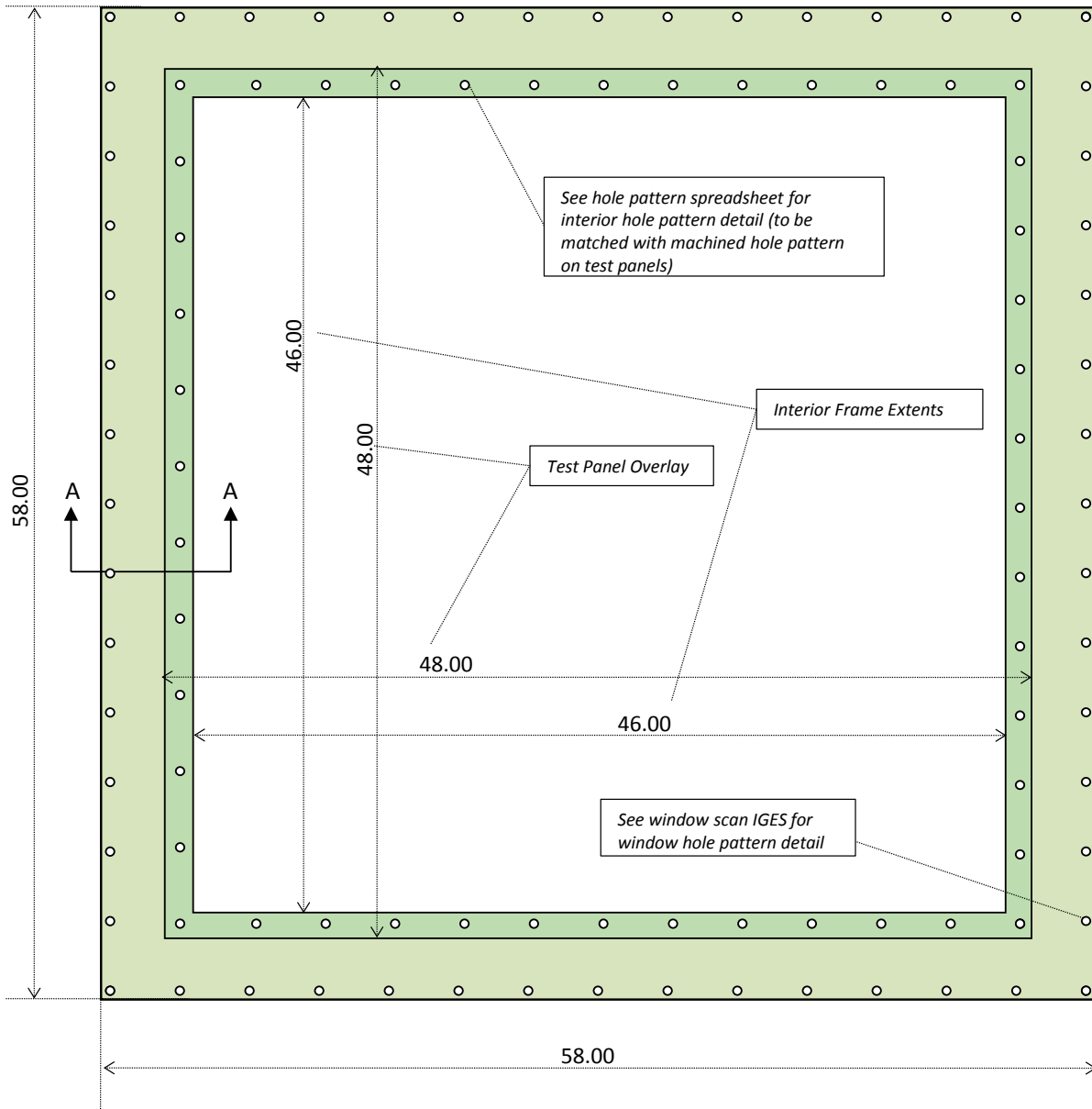


Figure A.1 – NASA Salt frame adaptor.

Appendix B – Virtual Transmission Loss for an Aluminum Panel

The sound power transmission loss of an aluminum panel was simulated using a modal approach. The physical and material properties used for the panel are listed in Table B-1. The panel was modeled using finite elements with simply-supported boundary conditions. 1225 linear plate elements were used. The normal modes were computed up to 3000 Hz using NX NASTRAN (93 total modes). The FE mesh is shown with a few representative modes in Fig. B-1. A one-to-one boundary element mesh of the plate was also created in the baffled condition. The critical frequency of the panel is 1212 Hz.

Table B-1. Properties of the aluminum panel

Dimensions	1.0 x 1.0 x 0.01 m
Loss Factor	0.01
Density	2700 kg/m ³
Modulus of Elasticity	69e9 GPa

To simulate a transmission loss measurement, the panel was excited with a virtual diffuse field pressure. Since the spatial correlation of a perfectly diffuse field is a sinc function [11], the pressure cross-spectral density matrix of the forcing function can be written as

$$G_{FF} = \sqrt{G_{p_i} G_{p_j}} \frac{\sin(k_0 \Delta_{ij})}{k_0 \Delta_{ij}}, \quad (\text{B-1})$$

where Δ_{ij} is the separation distance between points i and j , k_0 is the acoustic wavenumber and G_{p_i} is the power spectral density (PSD) at point i . Assuming unit PSDs at all points, the sound radiation due to the diffuse field was calculated using the CHAMP approach [3].

To compute a transmission coefficient, the power incident on the panel was estimated. For a perfectly diffuse field in a room, the power incident on an area S is defined as

$$P_{inc} = \frac{c w_{in}}{4} S, \quad (\text{B-2})$$

where w_{in} is the reverberant energy density and c is the sound speed [3]. Using the blocked pressure assumption we can approximate w_{in} as:

$$w_{in} \cong \frac{|p|^2}{\rho_0 c^2}, \quad (\text{B-3})$$

where p is the acoustic pressure at the boundary and ρ_0 is the fluid density. Since we apply a unit pressure loading to the panel, the squared pressure in Eq. B-3 must be unity. The transmission coefficient then becomes

$$\tau = \frac{P_{rad}}{S / 4\rho_0 c} \quad (B-4)$$

and the virtual transmission loss (VTL) becomes

$$VTL = 10 \log \left(\frac{S / 4\rho_0 c}{P_{rad}} \right). \quad (B-5)$$

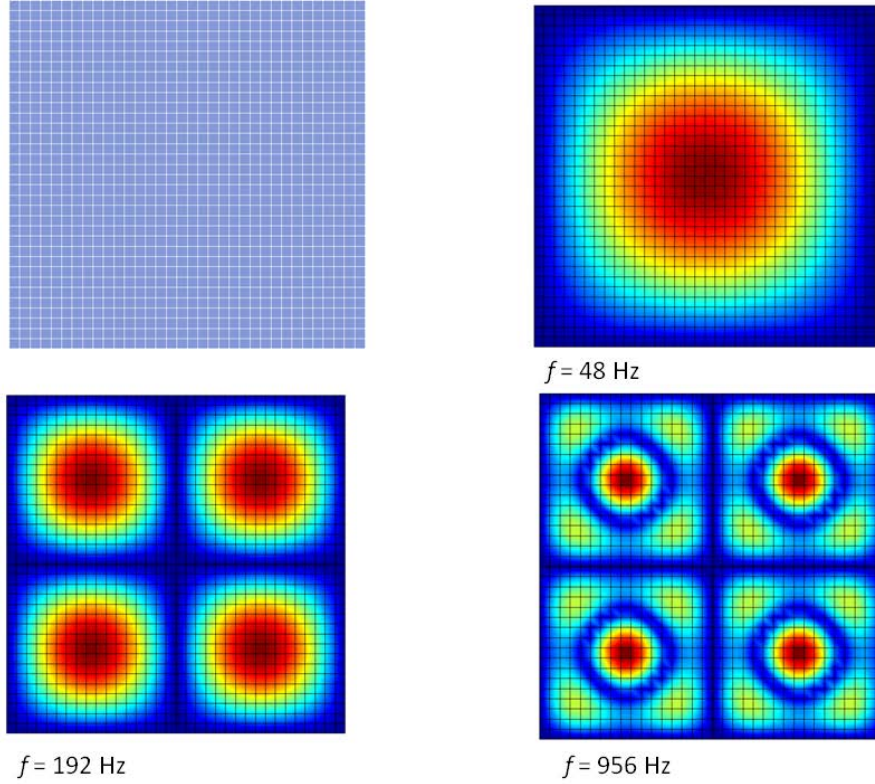


Figure B-1. The finite element mesh of the simply supported aluminum panel with 3 representative modes.

As a theoretical comparison, we computed the oblique angle of incidence transmission coefficient for an infinite panel defined as

$$\tau(\phi, \omega) = \frac{[2\rho_0 c / \sin \phi]^2}{\left[2\rho_0 c / \sin \phi + (D/\omega)\eta(k_0 \sin \phi)^4 \right]^2 + \left[\omega\rho h - (D/\omega)(k_0 \sin \phi)^4 \right]^2} \quad (B-6)$$

where ω is the angular frequency, ϕ is the angle of incidence, D is the structural rigidity, η is the structural loss factor and ρh is the plate surface density [6]. For honeycomb sandwich panels, an effective thin panel D may be inferred from the effective wavespeed described in 2.6.1. The diffuse field transmission coefficient is then found using

$$\tau_d(\omega) = \frac{\int_0^{\pi/2} \tau(\phi, \omega) \sin \phi \cos \phi d\phi}{\int_0^{\pi/2} \sin \phi \cos \phi d\phi} = \int_0^{\pi/2} \tau(\phi, \omega) \sin 2\phi d\phi. \quad (\text{B-7})$$

Figure B-2 shows the VTL compared to the random incident transmission loss for an infinite panel as well as the theoretical mass-law up to 2 kHz. The virtual TL curve captures the coincidence dip well and generally follows the mass-control law at low frequencies and the stiffness-control law at high frequencies. Due to the low modal overlap at low frequencies, dips in the VTL are seen at the natural frequencies. Fig B-3 shows the one-third octave band VTL. To convert VTL to one-third octave band frequencies, the mean transmission coefficient within each band was calculated. This is equivalent to computing the OTO band spectrum for the radiated power spectrum and the incident power spectrum and taking the ratio.

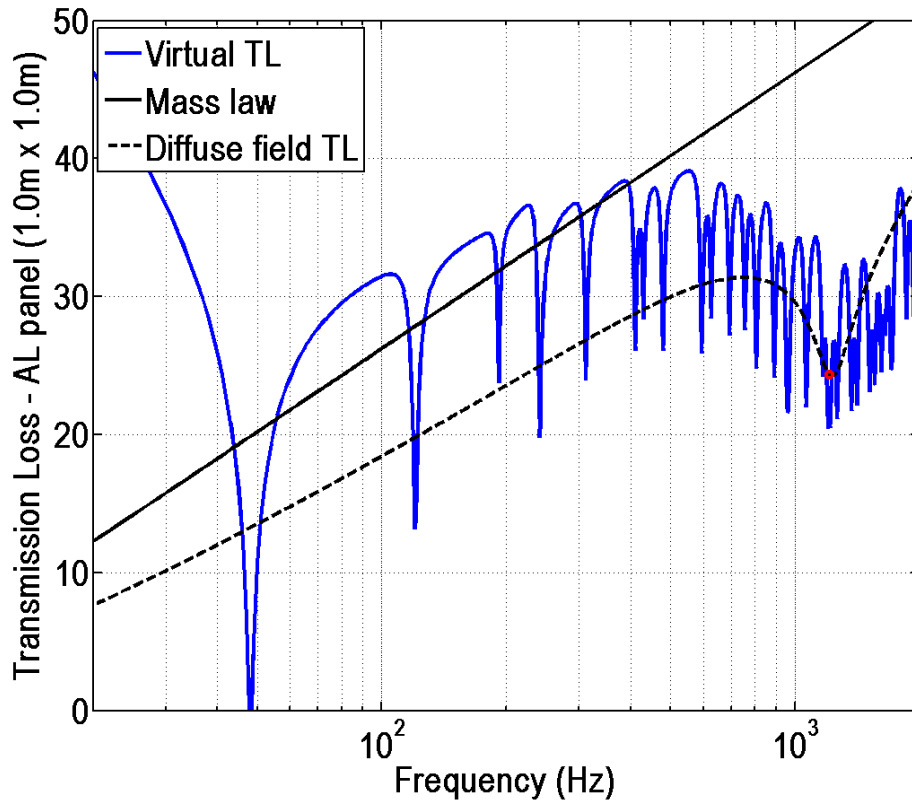


Figure B-2. Virtual transmission loss for the aluminum panel shown with the theoretical mass law and random-incidence transmission loss curve for an infinite panel with the same material properties. The value at the critical frequency is shown as a red circle.

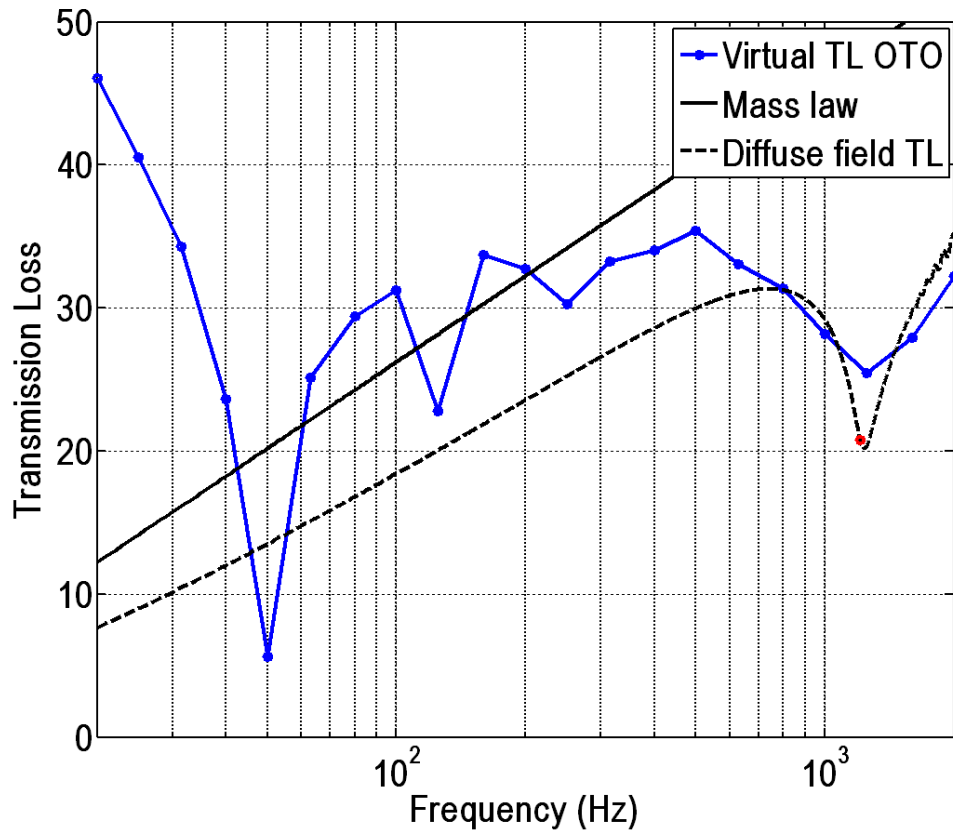


Figure B-3. Virtual transmission loss for the aluminum panel in one-third octave bands.

Appendix C – Determination of Panel Wavespeed and Young’s Modulus

C.1 Theory

The Young’s modulus (E) of a material partially determines the bending wavespeed (c_b) of that structure. Using the expression for wavespeed of a thin or thick plate, E can then be computed once c_b is known or estimated. The following section describes an approach to estimate c_b based on the wavenumber transform.

Shepherd and Hambric recently showed the modal wavenumber (k_m) of a thin, rectangular plate with simply supported boundaries can be found using wavenumber transform [12]. After taking the one-dimensional wavenumber transform of the plate’s mode-shape in the x or y direction, the modal wavenumber is found using

$$k_m = k_{z1} - 2\pi / L, \tag{C.1}$$

where k_{z1} is the wavenumber of the first zero after the peak in the wavenumber spectrum and L is the length of the plate in the dimension of interest. The modal wavenumber can equivalently be determined by adding $2\pi / L$ to the wavenumber at the first zero preceding the peak. This relationship is shown graphically in Fig. C.1 for mode orders 1 and 2. As shown in Eq. C.1, the accuracy of the wavespeed estimate then depends on the ability to compute accurately the zeros in the wavenumber spectrum.

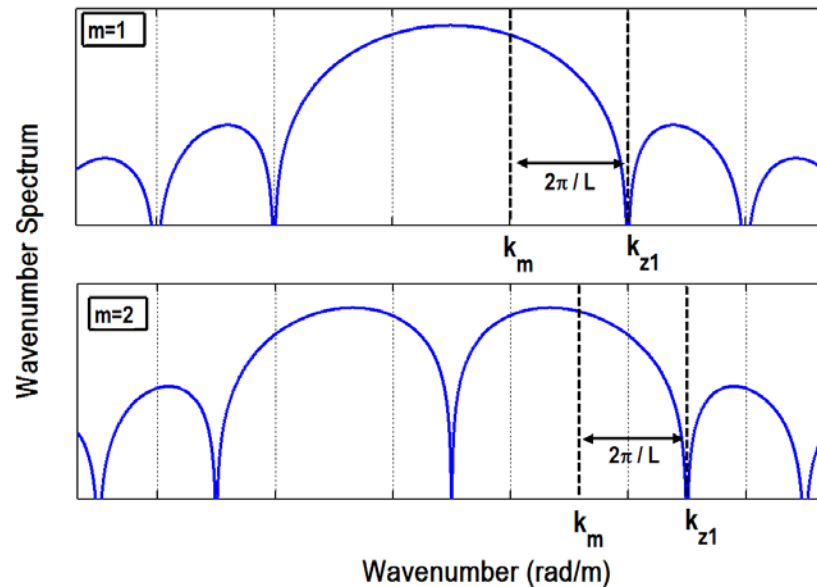


Fig. C.1. The wavenumber spectrum for the first- and second-order modes of a simply-supported rectangular plate. The spacing between zeros $2\pi / L$ can be used to determine the modal wavenumber by finding the first zero after the peak wavenumber and subtracting $2\pi / L$.

Since the modal wavenumbers in each direction are estimated separately, the total wavenumber is taken as the square root of the sum of the squares, $k = \sqrt{k_x^2 + k_y^2}$. The modal wavenumber is associated with the natural frequency of the mode so that the wavespeed at that frequency is

easily computed as $c_{b,n} = \omega_n / k_n$, where ω_n is the n^{th} natural frequency. The Young's modulus can then be estimated using thin plate theory:

$$E = \frac{12\rho(1-\nu^2)c_b}{h^2\omega^2}, \quad (\text{C.2})$$

where ρ represents the material density and h is the plate thickness. If the plate thickness is large enough such that shear effects and rotary inertia cannot be neglected, thick plate theory should be used. For non-isotropic materials, an estimate of E using Eq. C.2 would represent an effective modulus. The independent estimates of k_x and k_y could also be used to estimate effective orthotropic material properties.

C.2 Implementation using measured mode shapes

For most practical problems, structural mode shapes are measured using spatially discrete data such that the discrete Fourier transform (DFT) must be used for wavenumber analysis. Using the analogy from time domain signal processing, the wavenumber resolution will be defined by the length of the plate, $dk = 2\pi / L$. Since many practical structures are smaller than $2\pi \approx 6.28$, the wavenumber resolution will be poor without introducing zero padding. The wavenumber resolution will thus be increased by the zeropad factor z_p [13]. Additionally, the maximum wavenumber will be set by the spatial sampling and is related to spatial aliasing of the modeshape. An equivalent Nyquist wavenumber can be defined as $k_{nyq} = \pi/dx$, where dx is the spacing between known vibration points in a coordinate direction. Therefore, for any given structure, the wavenumber resolution can be arbitrarily reduced while the maximum wavenumber is fixed.

Mode shapes are best estimated using experimental modal analysis techniques, which typically involves acquiring acceleration to force transfer functions at points distributed of the structure and computing the complex mode indicator function (CMIF) [14]. Optical methods could also be used to estimate the mode shapes after which the wavenumber transform is used to estimate the wavespeed for each mode. The individual wavespeed estimates can then be used together to perform a least-squares fit of the data such that E is estimated by minimizing the error over all the wavenumber estimates. Simply supported boundary conditions are difficult to create in practice so that exact modal wavenumber estimates cannot be achieved. However, mode shapes for plates with free or clamped boundaries anecdotally to follow similar trends such that the reasonably accurate wavespeed estimates are achieved using Eq. C.1 as long as the mode shape data is accurate. Additionally, using a least-squares fit procedure can reduce the biases of individual modal wavenumber estimates.

Wavespeeds were estimated using the discrete wavenumber transform for a 1.0 x 0.7 x 0.005 m simply-supported aluminum panel ($E=69$ GPa, $\rho=2700$ kg/m³) up to 1 kHz. Analytical mode shapes up to 1 kHz were discretized with 41 points in the x direction and 29 points in the y direction. The Nyquist wavenumber was 125.7 1/m with a zeropad factor of 20, corresponding to a wavenumber resolution of 0.3142 1/m. The structural wavelength at 1 kHz is 0.2204 m which equates to nearly 9 points per wavelength (ppw).

Figure C.2 shows the exact wavespeed (using thin plate theory) with the wavespeeds inferred using the wavenumber transforms. To determine the effect of the discretization on wavespeed estimates, the modeshapes were downsampled by a factor of two ($dx=0.05$ m, $ppw=4.4$) and four ($dx=0.1$ m, $ppw=2.2$) and the wavespeed estimates were repeated. All estimates show good accuracy indicating that the Nyquist criteria of 2 points per wavelength is acceptable for inferring wavespeeds using wavenumber transforms. Additionally, the estimates were repeated with a reduced zeropad factor of five ($dk=1.26$) as shown in Figure C.3. The error in wavespeed estimate increases since the resolution in wavenumber decreases and the nulls used to infer the wavenumbers are not well resolved. This suggests that minimum zeropad factor is required to achieve the appropriate level of wavenumber resolution. A zeropad factor is therefore suggested of at least $4\pi/L$ ($dk<0.5$) as a rule of thumb.

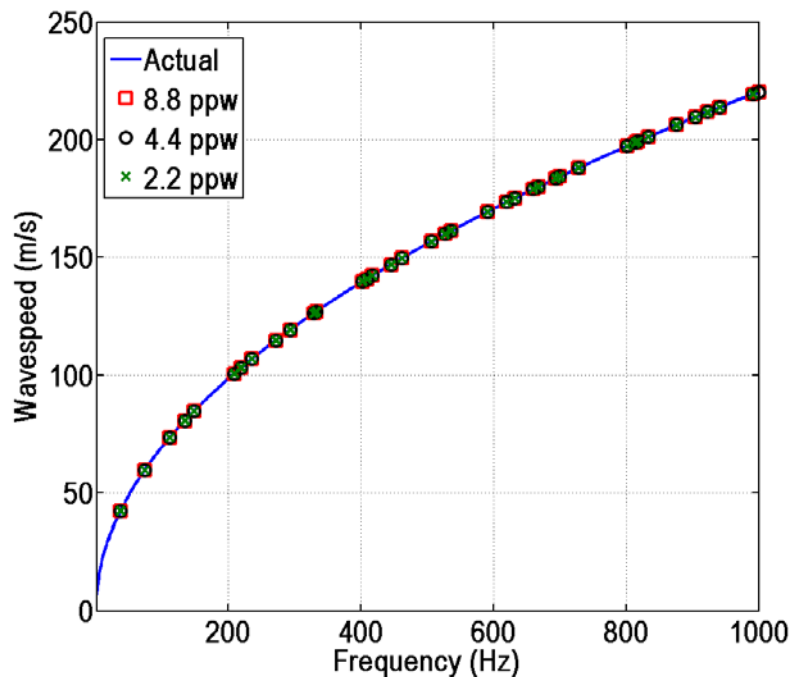


Fig. C.2. Wavespeed estimates of an aluminum plate for different mesh discretizations. Wavenumber analysis of the lowest mesh density (2.2 ppw) predicts the wave speed correctly, since the modes are not aliased in space. The number of points per wavelength is referenced to the flexural wavelength at 1 kHz.

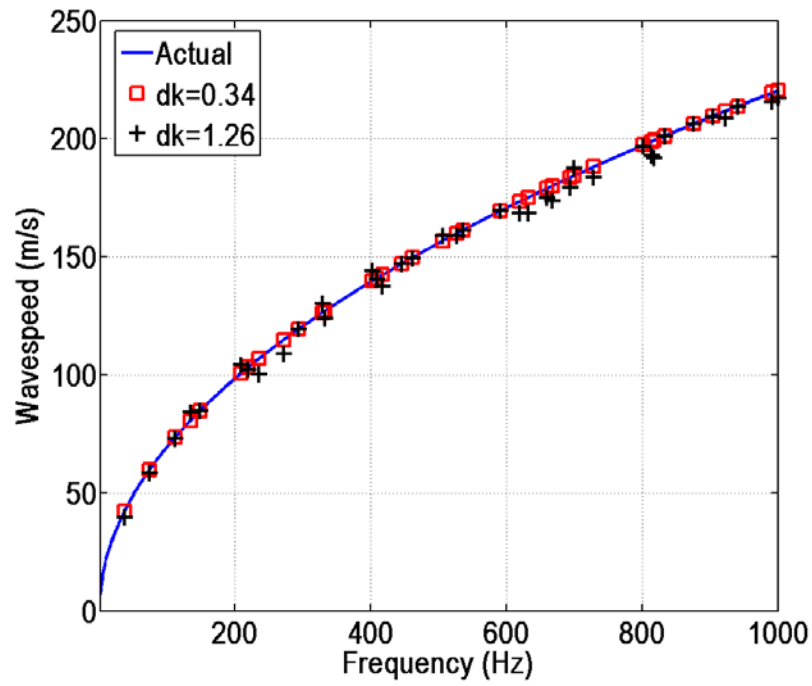


Fig. C.3. Wavespeed estimates of an aluminum plate for wavenumber resolution of 0.34 ($z_p=20$) and 1.26 ($z_p=5$). The larger dk produces errors in the estimate due to an inability to accurately resolve the zeros of the wavenumber spectrum.

Appendix D: Evaluation of Diffusivity and Angular Weighting Factors using Intensity Measurements

D.1 Introduction

Theoretical transmission loss (TL) calculations assume that the acoustic field exciting the structure is diffuse [6]. The power flow in a diffuse field has equal probability to be incident from any angle, making the time-averaged intensity equal to zero. Additionally, the energy density in a diffuse field is spatially uniform [18]. These assumptions are nearly true in large rooms with hard walls and low damping at frequencies above the Schroeder frequency.

However, the sound field in these types of rooms is influenced by specular reflections near the walls so that the field can no longer be considered diffuse. Waterhouse determined that the actual mean-square pressure can significantly vary from the diffuse field mean-square pressure when the distance from the boundary is less than $\lambda/5$ [19]. For analysis at 100Hz and 500Hz, the distance from the wall required to obtain diffuse field conditions should be at least 0.68m (26.5 in) and 0.14m (5.5 in) respectively.

Given these conditions, one may question the accuracy of applying a diffuse sound field excitation to a structure for predicting TL and whether an appropriate correction factor can be determined experimentally. Another issue is how the presence of an elastic panel or an open window impacts the diffusivity. This section details a set of intensity measurements that were made in an effort to examine these questions.

D.2 Intensity Measurements

Using a 2-microphone intensity probe, the diffusivity of the sound field in the reverberant chamber of the NASA LaRC structural-acoustic loads and transmission (SALT) facility was investigated. Measurements were made both with the optimized panel installed and with an open aperture. A GRAS 50AI-C intensity probe was used with a 12 mm spacer. Pressure was recorded for 120 s with the standard TL sources turned on (see Fig D.1).

Measurements were taken from 0° to 180° in approximately 22.5° increments. The 0° locations was oriented parallel with the installed panel. Since the probe is located on a thin rod extended out from a mounting handle, it was not possible to rotate about the acoustic center of the probe. Instead the probe was rotated about its handle. Intensity was acquired at four measurement positions when the panel was installed. These locations are listed in Fig. D.2. The measurement location was as close to the panel as physically possible but was nonetheless several inches from the panel.

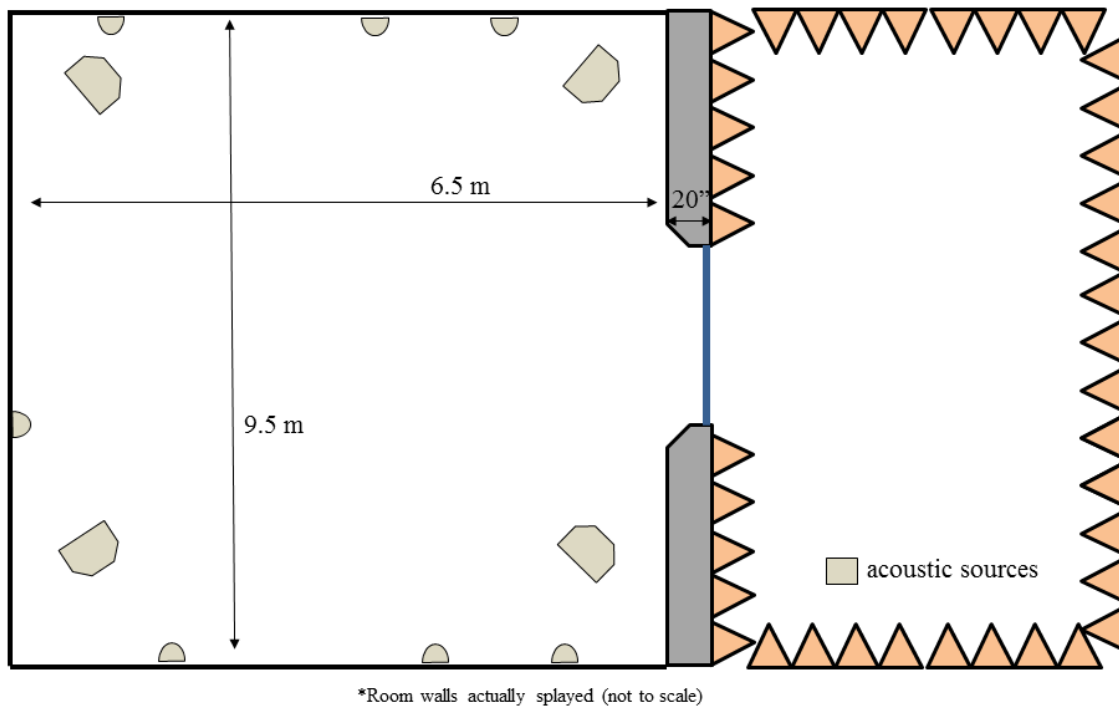


Figure D.1. A diagram of structural-acoustic loads and transmission facility (SALT), not drawn to scale.

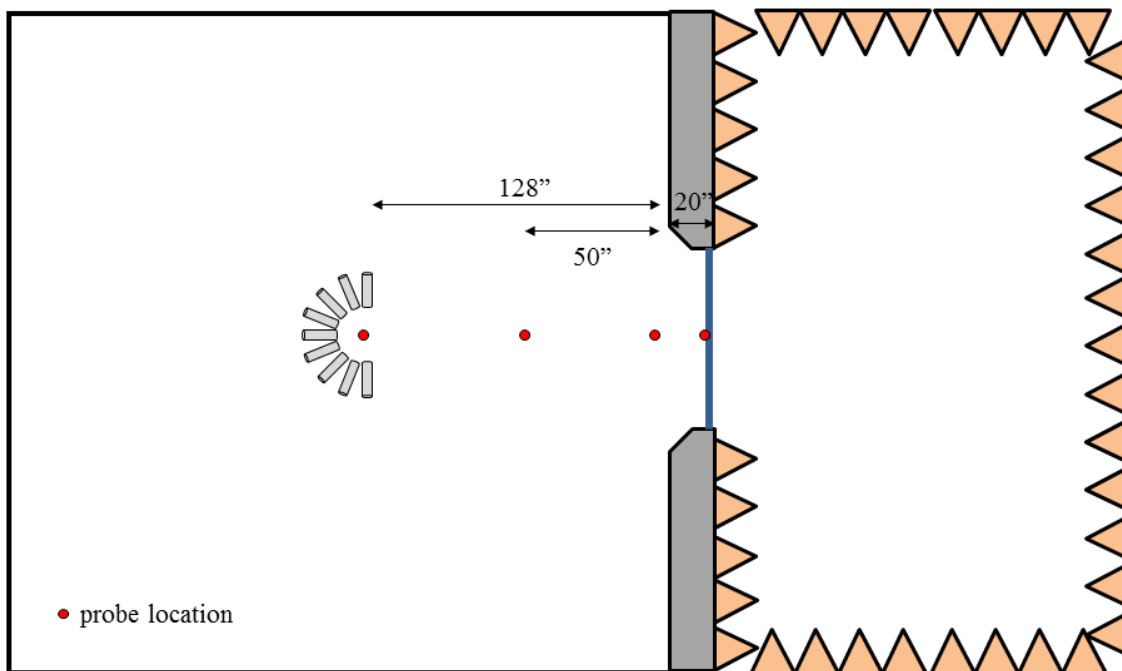


Figure D.2 Measurement locations of the intensity probe with the panel installed in SALT.

Intensity was computed using both the cross-spectral density (CSD) method (Eq. D.1) and by estimating the particle velocity using Euler's equation, the latter method allowing for investigation of both reactive and active intensity (Eq. D.2). The active intensity computed using each method was found to be in nearly perfect agreement. For the CSD computations, a Hanning window was used with 50% overlap and 2^{15} points per block. Intensity was then filtered into one-third octave (OTO) bands, a common practice which has been shown to reduce statistical variance [20, 10].

$$I(f) = -\frac{\text{Im}\{G_{xy}(f)\}}{(2\pi)f\rho\Delta x} \quad (\text{D.1})$$

$$I_a(f) = -\frac{1}{2}\text{Re}\{PU^*\} \quad (\text{D.2})$$

D.3 Limitations of intensity measurements

The intensity computed from these measurements is subject to several limitations. First, the diffuse field is only partially correlated over space. This will cause the pressure at one microphone to be uncorrelated at the second microphone above some frequency. The correlation function of the diffuse field pressure between two points is a sinc function:

$$\frac{\sin(k\Delta x)}{k\Delta x}, \quad (\text{D.3})$$

where Δx is the separation distance (fixed here by the 12 mm spacer) and k is the wavenumber [10]. The quantity $k\Delta x$ can be thought of as the scaled ratio of the separation distance to the wavelength. For frequencies below 2.4 kHz, the correlation between the microphones is greater than 0.95 ($\Delta x = \lambda/12$). This occurs when $k\Delta x = \pi/6$ (or $\Delta x = \lambda/12$) making the measurements only good up to the 2 kHz octave band. This is shown graphically in Fig. D.3.

Another limitation of the intensity measurement is caused by the finite measurement time. The time-averaged intensity is zero in a diffuse field only when averaged over infinite time. For finite-time measurements, the relative amplitude and apparent direction can still be compared for qualitative assessment but will exhibit randomness in amplitude and direction. An additional error is caused by the influence of non-normal intensity incident on the microphones. The cardioid directivity pattern of the microphones helps to limit this error but does not eliminate it.

A final limitation comes from measuring intensity in only one-dimension. Energy density cannot be measured without knowledge of the particle velocity in the three Cartesian directions and the acoustic pressure. Directional energy density, on the other hand, is more appropriate for an intensity probe but requires knowledge of the associated solid angle. Such measurements were not practically feasible for this setup and time table.

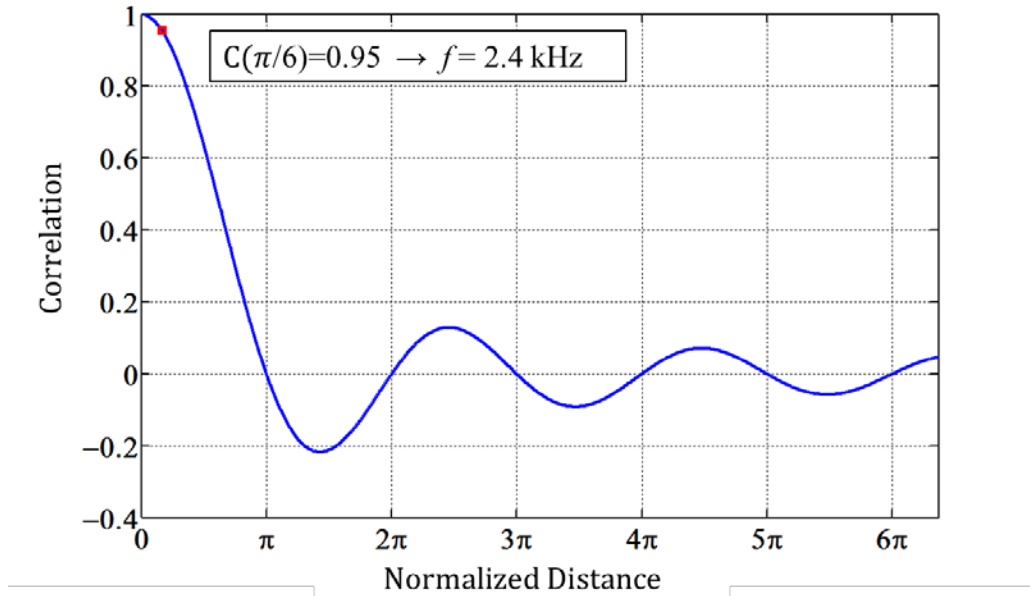


Figure D.3. The partial correlation of the diffuse field limits the frequency range of intensity using the 2-microphone technique.

D.4 Intensity Results – Panel Installed

The response of three accelerometers was acquired during the transmission loss testing. The accelerometers were located on the reverberant chamber side of the panel and show the panel’s vibration response during TL testing (Fig. D.4a). The transmission loss is shown in Fig. D.4b for reference.

The intensity diagrams for the OTO bands from 400 Hz to 4 kHz are shown in Figs. D.5-15. The direction of the vector indicates the orientation of the intensity probe and the length designates the level reference 1 pW/m². The dB scale shows the level for approximate vector length. The measured intensity varies over space, angle and frequency partially due to the random nature of the sound field.

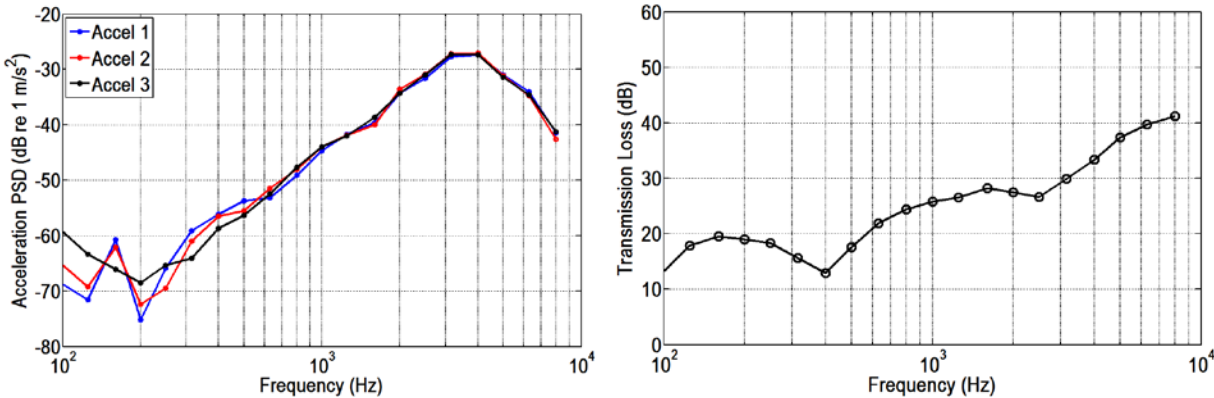


Figure D.4a. The accelerometer response recorded during transmission loss testing. b) The measured transmission loss of the optimized panel.

Several interesting observations will be given rather than detailing the features of each plot. First, the relative amplitudes of the intensity in the middle of the room are small with respect to the intensities near the panel for all measurements below 2 kHz. At 2kHz and above, the dominant direction and amplitude of the intensity appears to be random at all locations. This is likely caused by the partial correlation of the sound field between the microphones. The intensity at the panel shows a dominant intensity direction which varies with frequency, sometime switching directions entirely from one OTO band to the next. Also, the intensity at the wall (20" from the panel) shows strong power flow at some frequencies (e.g. 500 and 800 Hz) but very little at other frequencies (e.g. 400 and 1250 Hz).

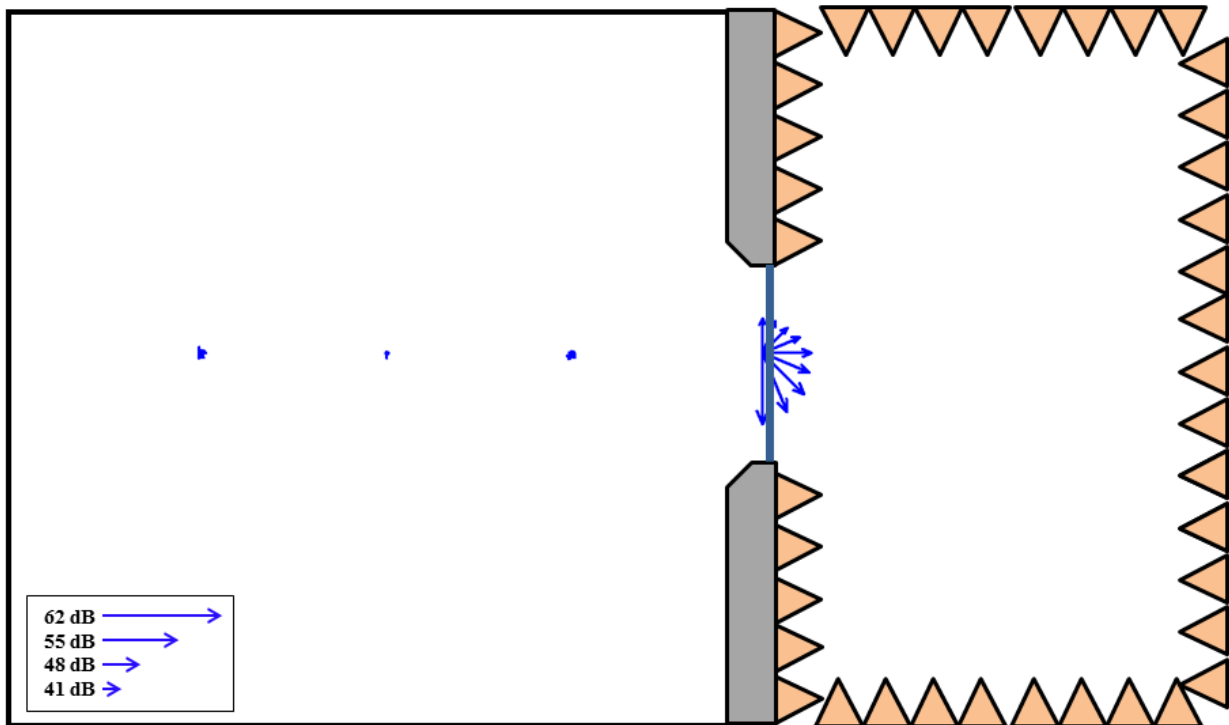


Figure D.5. Intensity field at 400 Hz with the optimized panel installed.

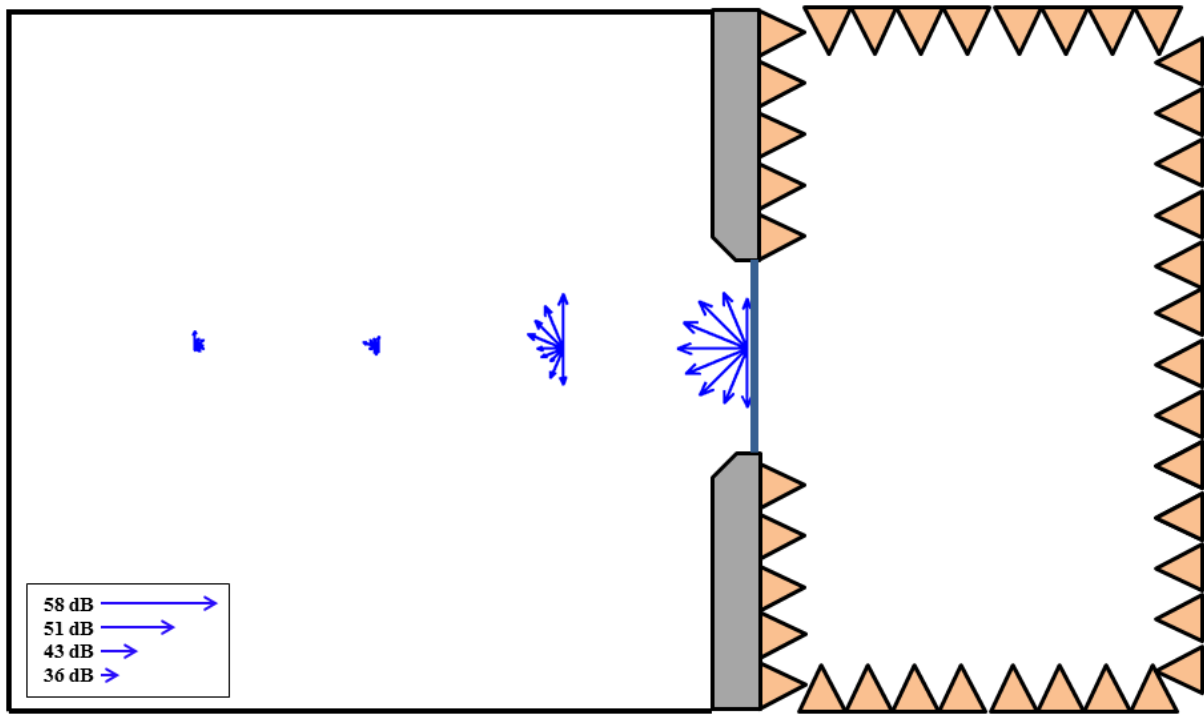


Figure D.6. Intensity field at 500 Hz with the optimized panel installed.

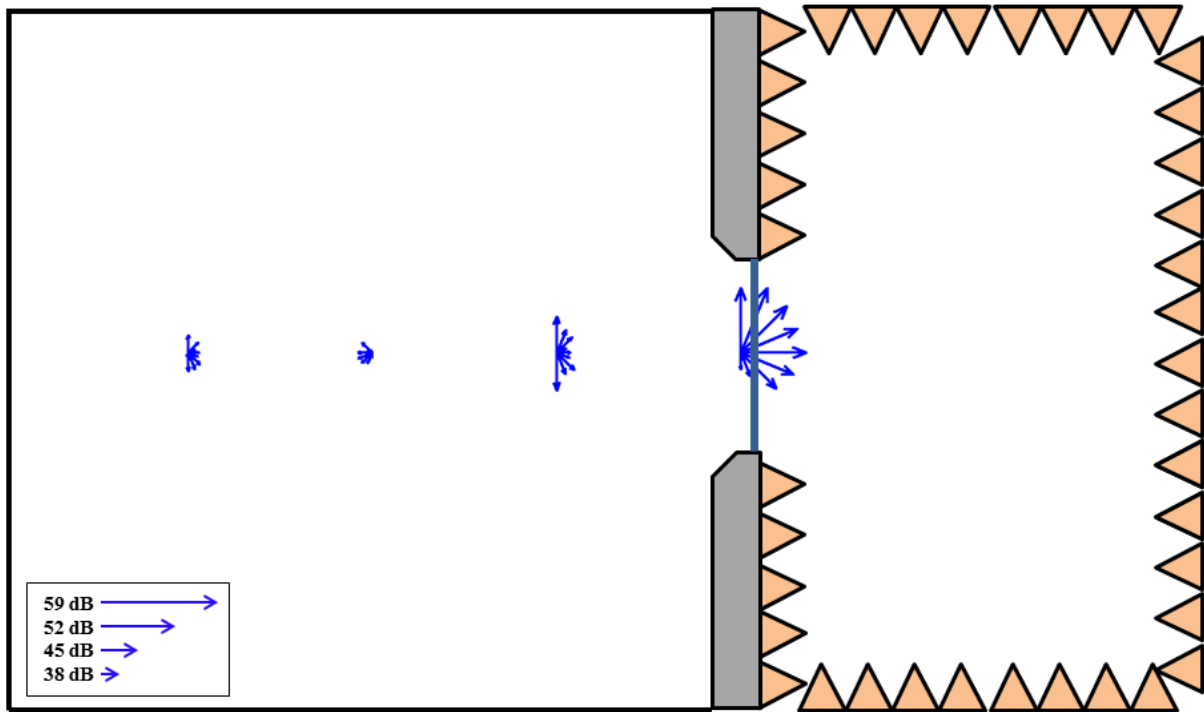


Figure D.7. Intensity field at 630 Hz with the optimized panel installed.

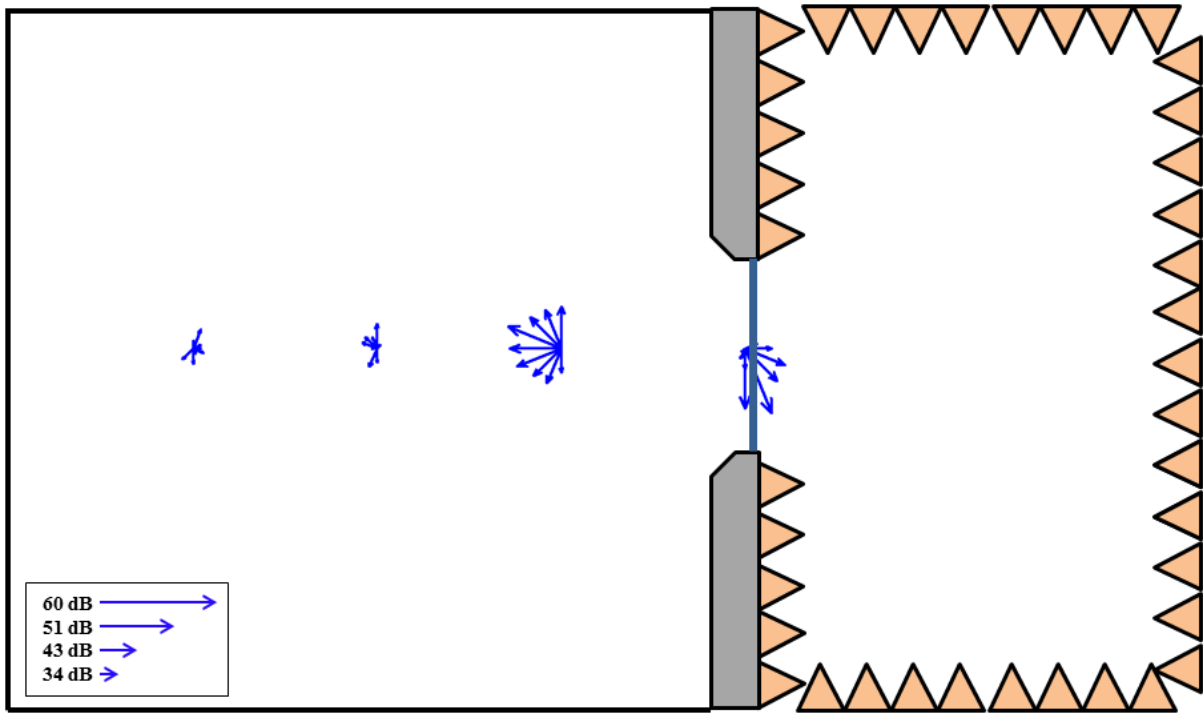


Figure D.8. Intensity field at 800 Hz with the optimized panel installed.

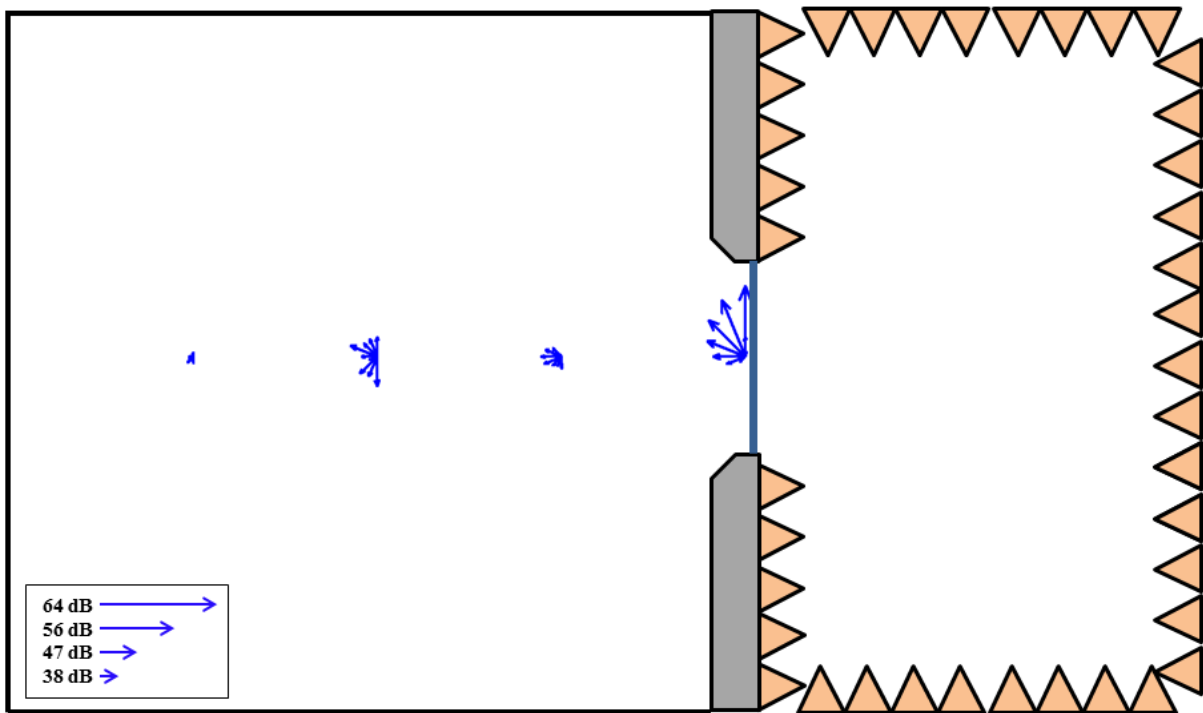


Figure D.9. Intensity field at 1 kHz with the optimized panel installed.

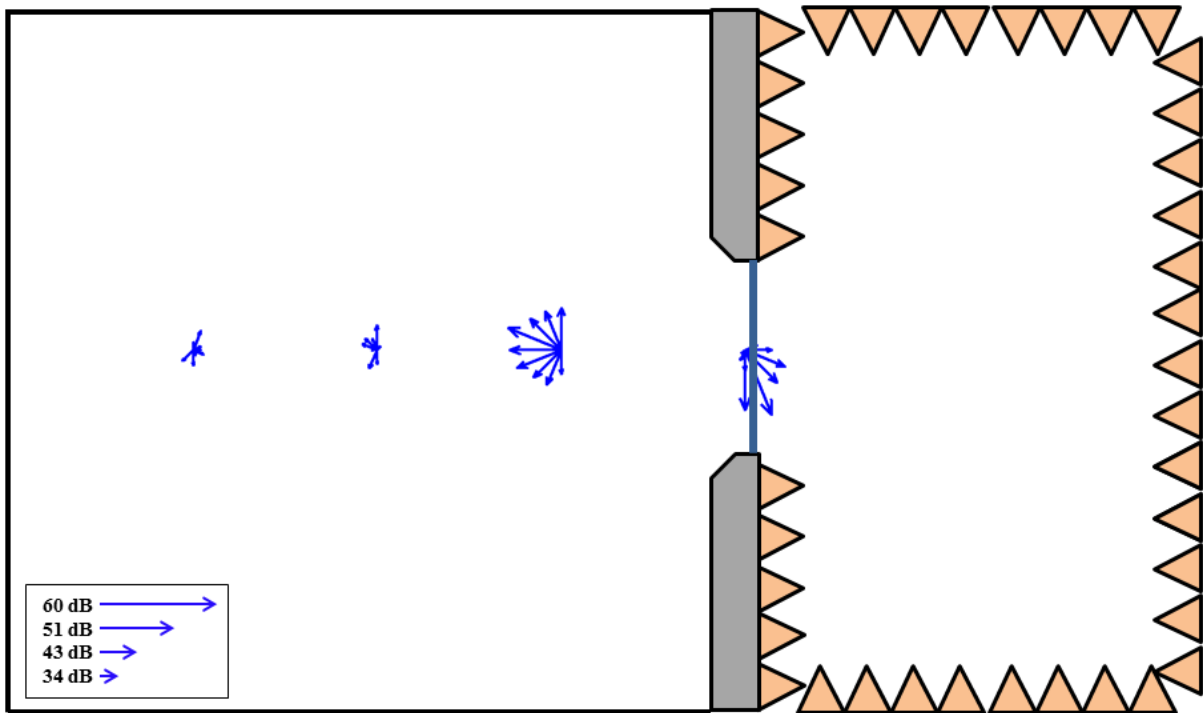


Figure D.10. Intensity field at 1.25 kHz with the optimized panel installed.

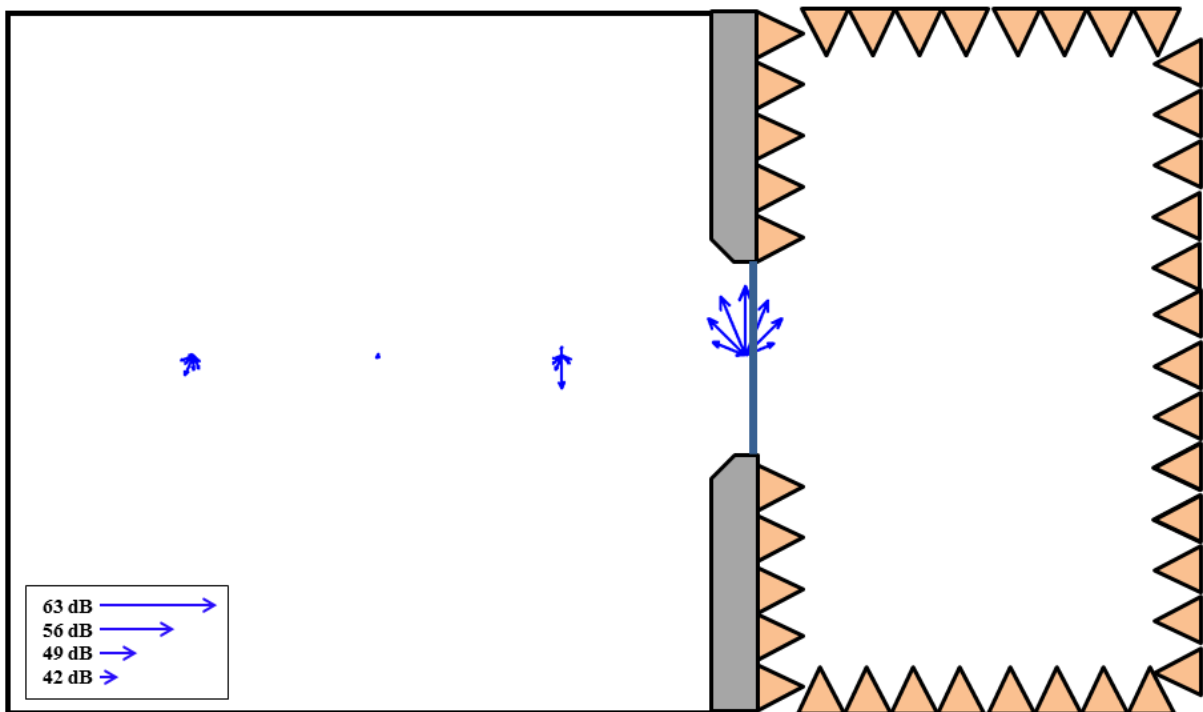


Figure D.11. Intensity field at 1.6 kHz with the optimized panel installed.

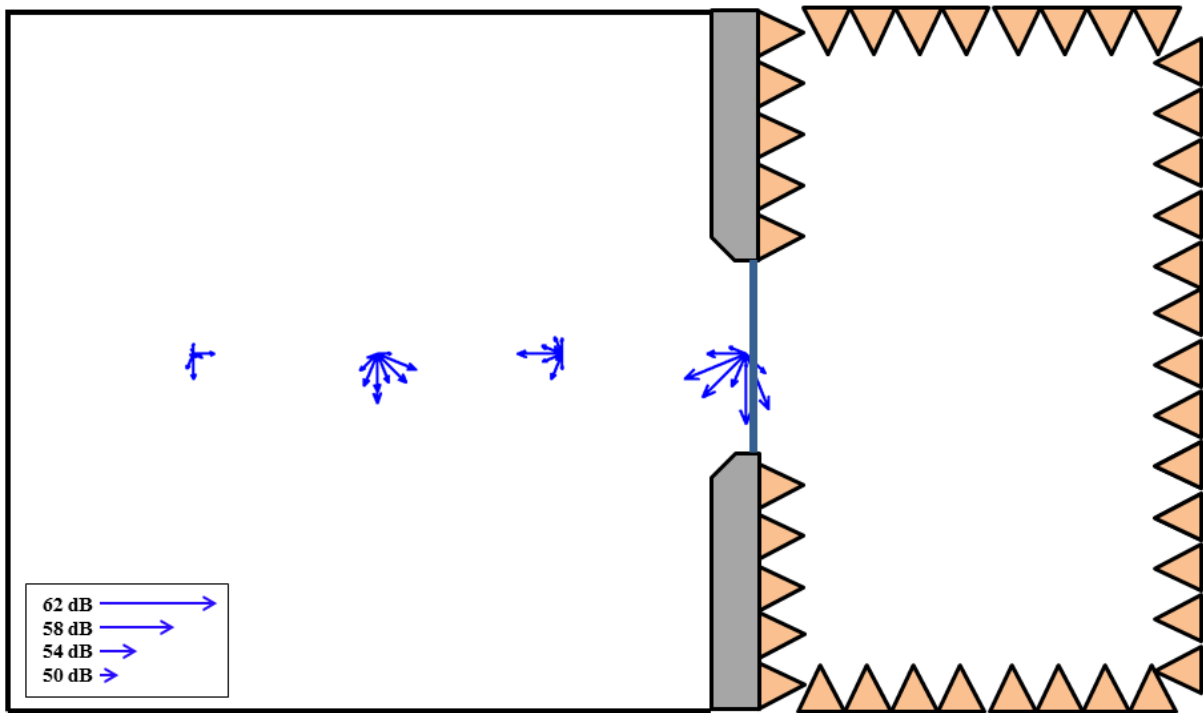


Figure D.12. Intensity field at 2 kHz with the optimized panel installed.

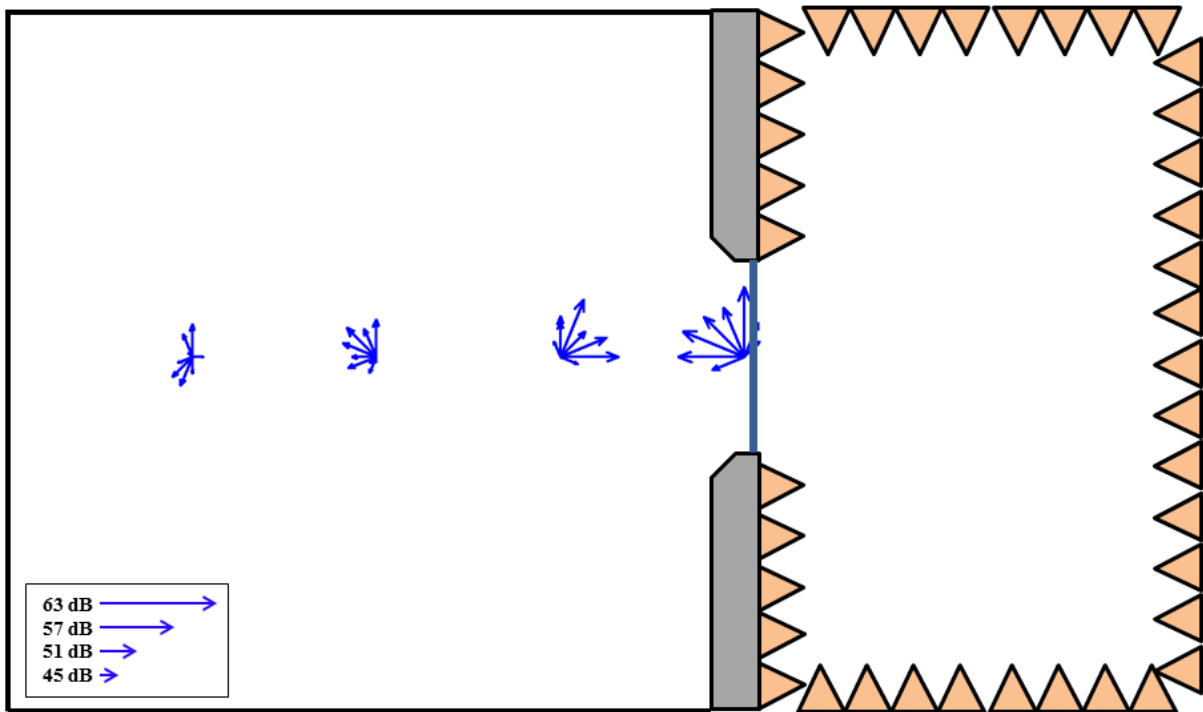


Figure D.13. Intensity field at 2.5 kHz with the optimized panel installed.

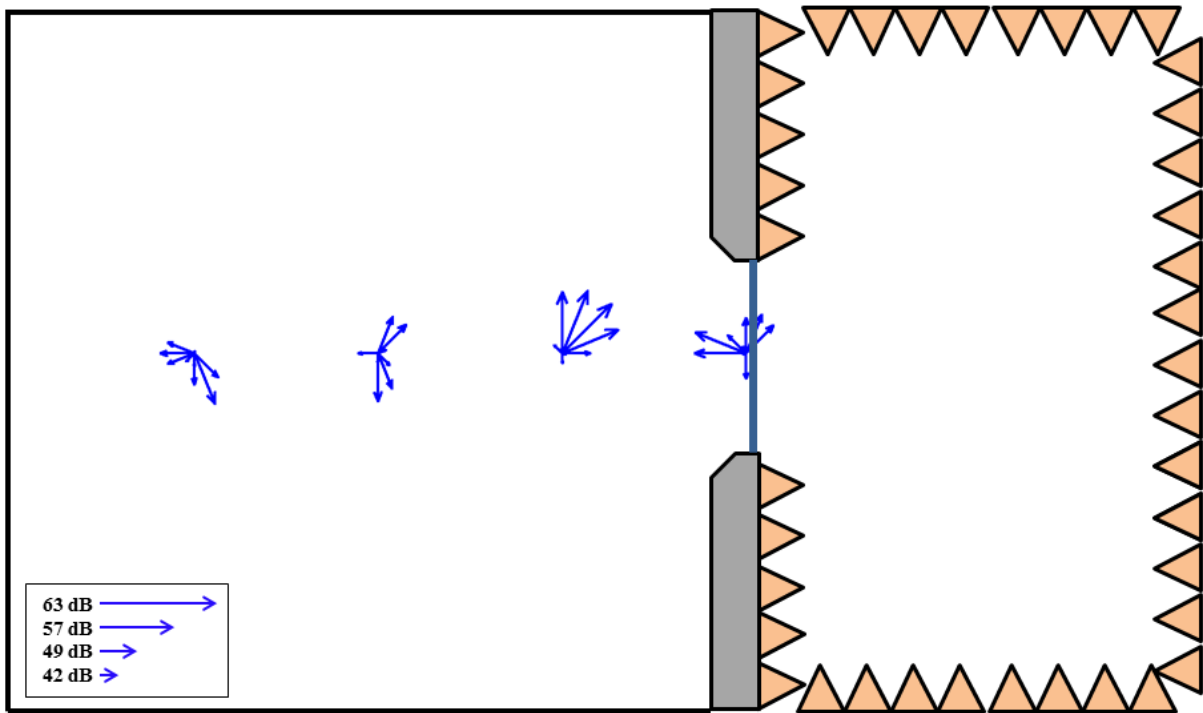


Figure D.14. Intensity field at 3.15 kHz with the optimized panel installed.

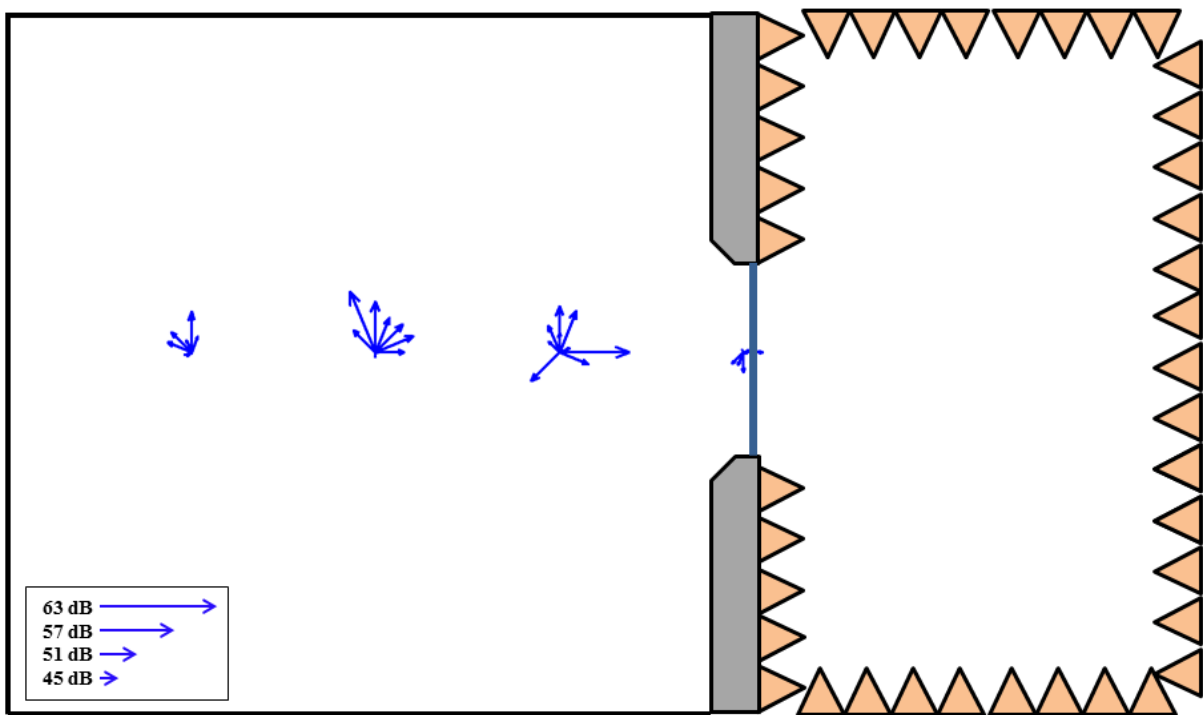


Figure D.15. Intensity field at 4 kHz with the optimized panel installed.

D.5 Intensity Results – Open Aperture

The panel was then removed from the window and intensity measurements were repeated. Measurements at the open window (where the panel would have been located) and ~15” inside the anechoic chamber were acquired at all the angles used from the previous measurements. Intensity measurements were made only at 0° and 90° for the locations in the reverberation chamber and at 0°, 45° and 90° for an additional position located approximately 5’ inside the anechoic chamber. The results are shown for the 1 kHz OTO band in Fig. D.17. As expected, the intensity in the middle of the reverberant room is small but acoustic power clearly flows from the reverberant room to the anechoic room. A similar trend is seen for all OTO frequency bands.

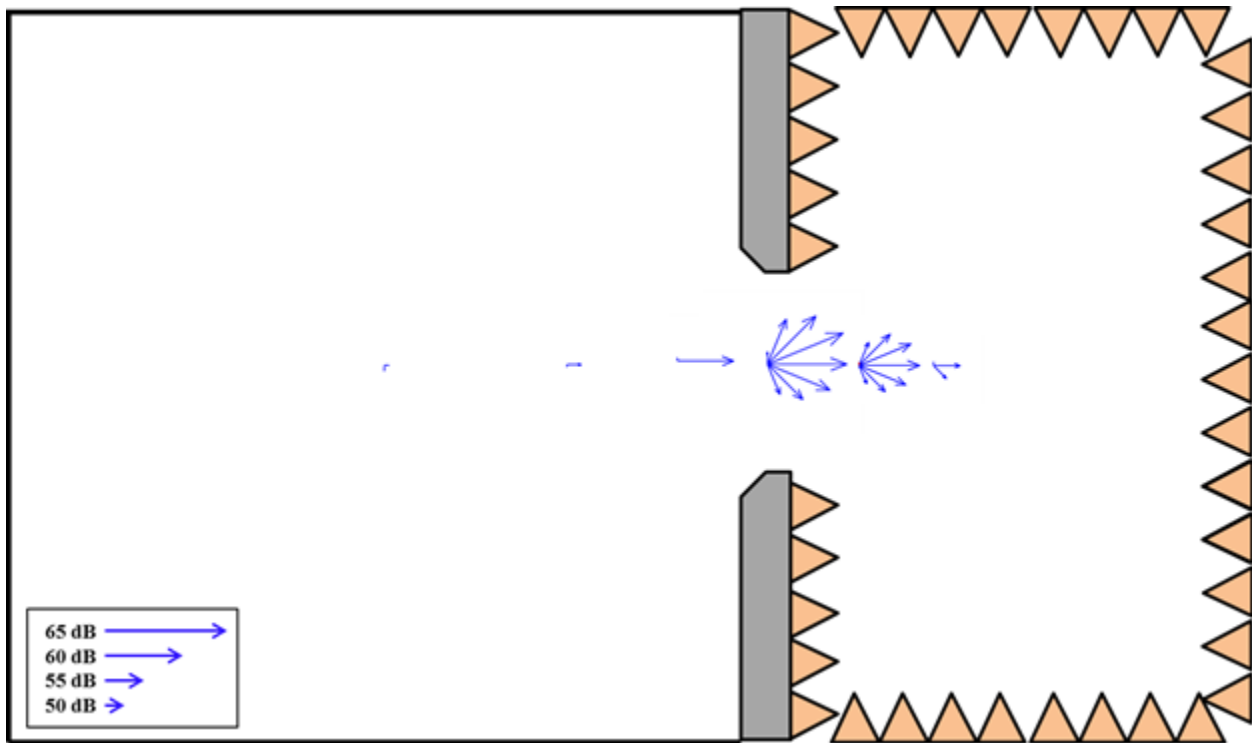


Figure D.17. Intensity field at 1 kHz with an open aperture.

The open aperture measurements were used to estimate an angle-dependent correction factor using a procedure similar to that in references [21] and [22]. The normalized intensity was averaged over all the OTO bands and is shown in Fig. D.18. The correction factors proposed by references [21] and [22] are:

$$\cos^{1.2}(\theta) \tag{D.4}$$
$$e^{-0.5\theta}$$

and are also shown in the Figure.

The exponential coefficient was modified to 0.5 to provide a better fit than the value of 1.5 used in reference [6]. Both correction factors show good agreement from angles from 0° to 45° but deviate slightly at larger angles.

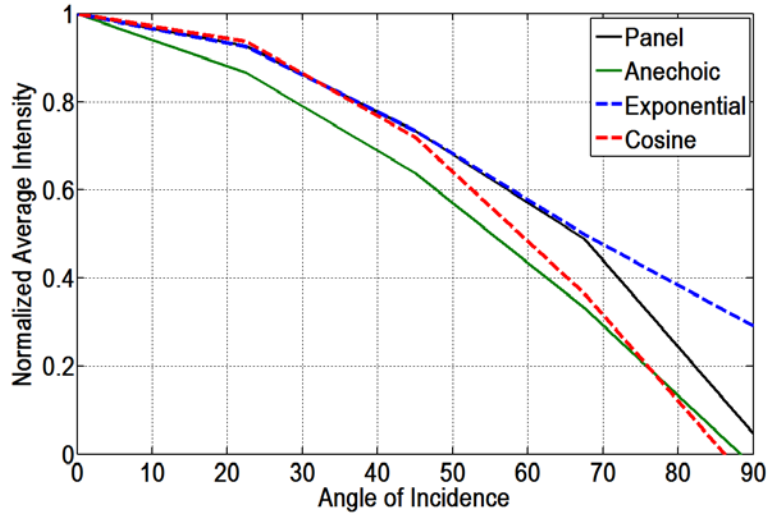


Figure D.17. Normalized intensity averaged over OTO bands with the open aperture for two positions: 'Panel', which is the open window (where the panel would be) and 'Anechoic', which is inside the anechoic chamber. Two possible weighting functions are also shown.

Simulations for the transmission through a thin aluminum panel (0.813 mm) were then updated using the cosine weighting coefficient as shown in Fig. D.18, and compared to measurements made in the NASA SALT facility. The simulations were made using the fully integrated diffuse field sound power transmission coefficient (DAF theory) and its accompanying low frequency approximate form (DAF approx.) as well as the normal incident mass law (equations 5.50, 5.51 and 5.20, respectively from reference [6]). The TL estimate is improved above 400 Hz when including the angular weighting. This case only illustrates agreement for transmission below the panel's coincidence frequency.

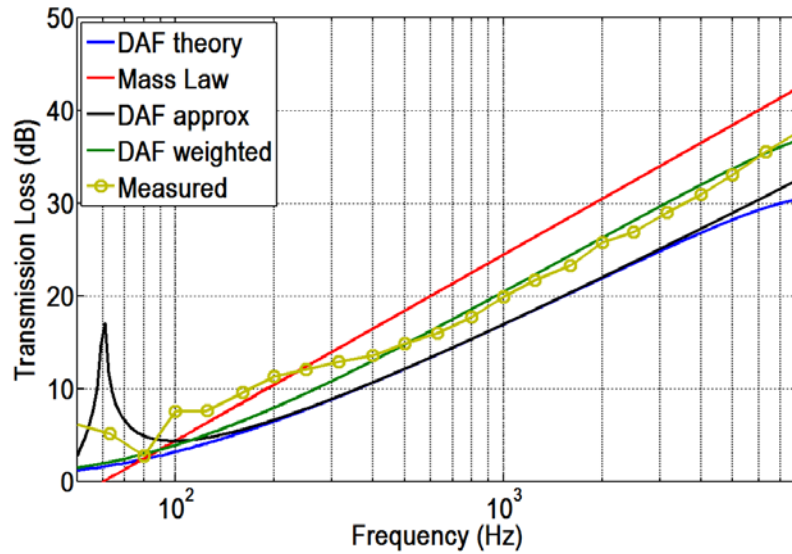


Figure D.18. Simulated and measured TL for an aluminum panel. The simulation is improved when using the cosine weighting function.

It should be noted that using the open aperture intensity field to determine an angular weighting function for TL testing has been questioned by Fahy [23]. He states that the intensity in a hemi-diffuse field incident on a non-reflecting plate inherently has a $\cos(\theta)$ dependence and therefore assigning a weighting function for TL measurements from an open window measurement is not physically justifiable. This idea is consistent with Pierce's derivation of diffuse field intensity through an open window [10]. However, the predicted [21] and measured [22] weighting factors (using beamforming) are obtained without the use of an open aperture and are still valid.

D.6 Future work

Additional experimental and numerical work could be performed to characterize the diffusivity of the reverberation chamber and improve TL simulations. Improved particle velocity measurements should be made using 3-D velocity probes to accurately measure generalized energy density at a point, which has been shown to have lower spatial variance than pressure measurements [24, 25]. However, the expense of such probes is somewhat prohibitive such that other measurement techniques should be developed.

One such procedure could measure pressure at points near a hard wall to map out the spatial correlation and statistics of the sound field. The measurement points would vary over the three axes (x, y and z) to show a complete representation of the sound field and then be compared to existing theory [19,26, 27]. The measurements could then be repeated near an elastic structure operating below coincidence and compared to those for a hard wall. The measurements would also be used to evaluate two proposed weighing functions [21, 22]. Additionally, more advanced metrics for diffusivity could also be computed [18, 20].

Additional theoretical modeling could also be performed to determine the effect of an elastic panel or open window on the sound field in a room. An analytical model could be developed by modifying a hybrid Green's function / modal summation method for computing the sound field in a reverberant room [25]. The hybrid approach has been shown to improve convergence for rigid-walled rooms. A generalized impedance boundary would be included in the model to include the effect of an elastic panel or open aperture. Using an analytical model, the sound field could then be computed in a reverberant room near and away from rigid boundaries to assess the diffusivity and the general impact of the incident intensity on TL could be predicted.

Appendix E – Formulation for Multiple Scattering of Flexural Waves in a Thin Plate

From Dr. Liang-Wu Cai, Kansas State University

Formulation of Multiple Scattering Problems of Flexural Waves in Thin Plates

Liang-Wu Cai — Kansas State University

for the *Acoustically Tailored Composite Rotorcraft Fuselage Panels* Project

Last Updated: November 2014

I. Introduction

There are several types of waves that can exist in a plate. In this report, only the flexural waves are considered.

The justification for limiting the consideration to flexural wave is that the primary concern for the present project is at lower frequencies, for which the wave length is expected to be longer than the plate thickness. For example, the frequency of the primary concern is approximately 3 kHz. Assuming a wave speed in the order of 1000 m/s, the wavelength would be in the order of 0.5 m. Other types of waves, most prominently, the Lamb waves, will become important when the wavelength is in the same order as the plate thickness, which is in the order of $10^{-3} \sim 10^{-2}$ m.

A good design feature in the plate geometry is that the flexural wave speed is highly designable, although frequency-dependent, by varying the thickness of the plate and in turn its rigidity, as it shall become clear in the expression for the wave number. It would be highly desirable to reduce the flexural wave speed so to bring the wave length down to the order of 0.1 m. Even in this wave length, it is still at least one order of magnitude longer than when the Lamb waves become a concern.

II. Governing Equation and General Solution

II.1 General Solution

The governing equation for a wave propagating in a thin plate can be written as (Pao and Mow, 1971, p. 326)

$$D\nabla^4 w + \rho h \frac{\partial^2 w}{\partial t^2} = q \quad (1)$$

where $w(r, t)$ is the deflection (out-of-plane displacement) of the plate, h and ρ are the thickness and the mass density, respectively, of the plate, q is the distributed lateral pressure, and D is the plate's rigidity or flexural stiffness. For classic plate theory, the flexural stiffness for a uniform plate is given as

$$D = \frac{Eh^3}{12(1 - \nu^2)} \quad (2)$$

where E is the Young's modulus, and ν is Poisson's ratio. For a composite sandwich panel with two identical isotropic face sheets and an isotropic core (Vinson, *Plate and Panel Structures of Isotropic, Composite and Piezoelectric Materials, Including Sandwich Construction*, Springer, 2005, p. 296.)

$$D = \frac{E_f h_c^2 t_f}{2(1 - \nu_f^2)} \left[1 + \frac{1}{6} \frac{E_c (1 - \nu_f^2) h_c}{E_f (1 - \nu_c^2) t_f} \right] \quad (3)$$

where parameters with a subscript f belong to the face sheets and parameters with subscript c belong to the core, t_f is the thickness of one of the face sheets.

With the absence of a lateral loading, the equation becomes homogeneous. In the steady state, assuming

$$w(\mathbf{r}, t) = W(\mathbf{r})e^{-i\omega t} \quad (4)$$

eqn. (1) becomes

$$\nabla^4 W - \frac{\rho h}{D} \omega^2 W = 0 \quad (5)$$

which can be split into two equations

$$\nabla^2 W_1 + k^2 W_1 = 0 \quad \text{and} \quad \nabla^2 W_2 - k^2 W_2 = 0 \quad (6)$$

where $k^2 = \omega \sqrt{\rho h / D}$. They are the *Helmholtz equation* and the *Modified Helmholtz equation*, respectively. In a polar coordinate system, their solutions are linear combinations of cylindrical Bessel functions with kr and $i kr$ as respective arguments. Alternatively, the Bessel functions with imaginary arguments can be replaced by the modified Bessel functions. Thus, the most general solution in the polar coordinate system can be written as

$$W(r, \theta) = \sum_{n=-\infty}^{\infty} [A_n J_n(kr) + B_n H_n(kr) + C_n I_n(kr) + D_n K_n(kr)] e^{in\theta} \quad (7)$$

where $H_n(\cdot)$ is the Hankel function of the first kind, $I_n(\cdot)$ and $K_n(\cdot)$ are the modified Bessel function of the first and the second kinds, respectively.

Matrix notation is introduced such that a set of wave expansion bases $\{\mathcal{Z}(r, \theta)\}$ is defined as

$$\{\mathcal{Z}(r, \theta)\}_n = \{\mathcal{Z}_n(kr) e^{in\theta}\} \quad (8)$$

with the index n running from $-\infty$ to ∞ , where $\mathcal{Z}_n(\cdot)$ represents any of the Bessel functions. Then, the general solution can be written as

$$W(r, \theta) = \{\mathbf{A}\}^T \{\mathbf{J}(r, \theta)\} + \{\mathbf{B}\}^T \{\mathbf{H}(r, \theta)\} + \{\mathbf{C}\}^T \{\mathbf{I}(r, \theta)\} + \{\mathbf{D}\}^T \{\mathbf{K}(r, \theta)\} \quad (9)$$

II.2 Modified Bessel Function

The modified Bessel functions are defined as the following

$$I_n(z) = \hat{i}^{-n} J_n(\hat{i}z) \quad (10)$$

$$K_n(z) = \frac{\pi}{2} \hat{i}^{n+1} H_n^{(1)}(\hat{i}z) = \frac{\pi}{2} (-\hat{i})^{n+1} H_n^{(2)}(-\hat{i}z) \quad (11)$$

The general behaviors of these functions are similar to exponential functions: as z increases, $I_n(z)$ increases without bound, while $K_n(z)$ decreases. Thus, for a problem defined in an infinite domain, $I_n(z)$ would not appear, and $K_n(z)$ represents motions confined in the vicinity of the origin ($z = 0$). On the other hand, for a problem whose domain includes the origin, $K_n(z)$ would not appear, as it is singular at the origin.

II.3 Moments and Shear Forces Across Thickness of Plate

The moments and shear forces across the thickness of the plate can be written in terms of displacement w as (Pao & Mow, 1971, p 329)

$$\begin{aligned} M_r &= -D \left[\nu \nabla^2 W + (1 - \nu) \frac{\partial^2 W}{\partial r^2} \right] \\ M_\theta &= -D \left[\nabla^2 W - (1 - \nu) \frac{\partial^2 W}{\partial r^2} \right] \\ M_{r\theta} &= D(1 - \nu) \frac{\partial}{\partial r} \left(\frac{1}{r} \frac{\partial W}{\partial \theta} \right) \\ Q_r &= -D \frac{\partial}{\partial r} (\nabla^2 W) \\ Q_\theta &= -D \frac{\partial}{r \partial \theta} (\nabla^2 W) \\ V_r &= Q_r - \frac{1}{r} \frac{\partial M_{r\theta}}{\partial \theta} \end{aligned} \quad (12)$$

where, Q 's are the shear forces on the cross-section of the panel, and V_r is the so-called total (net) shear force that combines the contributions from the shear force and the in-plane moment $M_{r\theta}$ (Graff, *Wave Motions in Elastic Solids*, Dover, 1975, pp. 234-235).

Among these quantities, the most important ones are those used in the boundary conditions. They are M_r , M_θ and V_r . Correspondingly, a set of special functions $\mathfrak{C}_s^t(n, z)$ is defined and the corresponding wave expansion bases $\{\mathfrak{C}_s^t(r, \theta)\}$ are defined as

$$\{\mathfrak{C}_s^t(r, \theta)\}_n = \mathfrak{C}_s^t(n, kr) e^{in\theta} \quad (13)$$

where the superscript t denotes the type of Bessel functions: 1 for $J_n(z)$, 2 for $H_n(z)$, 3 for $I_n(z)$, and 4 for $K_n(z)$; and the subscript s denotes the sequence of moment-force component: 1 for M_r , 2 for M_θ , and 3 for V_r . Detailed definition for these \mathfrak{C} -functions are given in Appendix A.

With this set of \mathfrak{E} -function, if a deflection is expressible as

$$W = \{\alpha\}^T \{\mathfrak{Z}(r, \theta)\} \quad (14)$$

The corresponding moments and shear force are expressible as

$$\begin{aligned} M_r &= -\frac{1}{r^2} \{\alpha\}^T \{\mathfrak{E}_1(r, \theta)\} \\ M_\theta &= -\frac{1}{r^2} \{\alpha\}^T \{\mathfrak{E}_2(r, \theta)\} \\ V_r &= -\frac{1}{r^3} \{\alpha\}^T \{\mathfrak{E}_3(r, \theta)\} \end{aligned} \quad (15)$$

III. Single Scattering Problems

The single scattering problem lays the foundation for the multiple scattering analysis. The analysis of a single scattering problem leads to the establishment of the so-called T -matrix of the scatterer; and in the process, the matrix notation is defined

III.1 T -Matrix in Generalized Matrix Notation

Consider a single circular scatterer of radius a that is located at the origin, and subjected to a planar incident wave. The incident wave is expressible as

$$W^{\text{inc}} = \{A^p\}^T \{J(r, \theta)\} + \{A^e\}^T \{I(r, \theta)\} \quad (16)$$

and the scatterer wave, which exists in the infinite domain, is expressible as

$$W^{\text{scr}} = \{B^p\}^T \{H(r, \theta)\} + \{B^e\}^T \{K(r, \theta)\} \quad (17)$$

where the superscript p and e in the wave expansion coefficient signify the propagating and evanescent components, respectively.

Physically the $\{A^e\}$ component of the incident wave would not exist in the single scattering problem since this component is localized. But in multiple scattering, the wave scattered from nearby scatterer would contain this component and acts as a part of the incident wave.

As with any scattering problems in a linear system, the incident and the scattered waves form a cause-result causality relation, and can be represented by a matrix, conventionally called the T -matrix. For the problem at hand, there are two components in each of the incident and the scattered waves. They form the following set of four relations

$$\{B^{pp}\} = [T^{pp}]\{A^p\} \quad \{B^{ep}\} = [T^{ep}]\{A^p\} \quad (18)$$

$$\{B^{pe}\} = [T^{pe}]\{A^e\} \quad \{B^{ee}\} = [T^{ee}]\{A^e\} \quad (19)$$

where the first pair of equations determines the scattered wave due to an incident propagating wave, and the second pair is due to an incident evanescent wave. In the double superscripts for $\{B\}$ and $[T]$ matrices, the first superscript signifies the type of the incident wave, and the second superscript signifies the type of the scattered wave.

In order to maintain the conventional form of the T -matrix relation, the above relations can be combined into the following relation in generalized matrices

$$\{\mathfrak{B}\} = [\mathfrak{T}]\{\mathfrak{A}\} \quad (20)$$

where the generalized matrices are define as

$$\{\mathfrak{B}\} = \begin{Bmatrix} \{B^p\} \\ \{B^e\} \end{Bmatrix} \quad \{\mathfrak{A}\} = \begin{Bmatrix} \{A^p\} \\ \{A^e\} \end{Bmatrix} \quad [\mathfrak{T}] = \begin{bmatrix} [T^{pp}] & [T^{pe}] \\ [T^{ep}] & [T^{ee}] \end{bmatrix} \quad (21)$$

Correspondingly, the wave expansion bases can also be concatenated to form the *generalized wave expansion matrices* such that

$$\{\mathfrak{J}(r)\} = \begin{Bmatrix} \{J(r, \theta)\} \\ \{I(r, \theta)\} \end{Bmatrix} \quad \{\mathfrak{K}(r)\} = \begin{Bmatrix} \{H(r, \theta)\} \\ \{K(r, \theta)\} \end{Bmatrix} \quad (22)$$

Then, the incident and the scattered waves are representable as

$$W^{\text{inc}} = \{\mathfrak{A}\}^T \{\mathfrak{J}(r, \theta)\} \quad W^{\text{scr}} = \{\mathfrak{B}\}^T \{\mathfrak{K}(r, \theta)\} \quad (23)$$

III.2 Rigid Inclusion

For a rigid inclusion, the boundary conditions are that the plate is clamped at the edge of the inclusion. That is $W = 0$ and $\partial W / \partial r = 0$. This leads to the following equations

$$B_n^p H_n(ka) + B_n^e K_n(ka) = -A_n^p J_n(ka) - A_n^e I_n(ka) \quad (24)$$

$$B_n^p H_n'(ka) + B_n^e K_n'(ka) = -A_n^p J_n'(ka) - A_n^e I_n'(ka) \quad (25)$$

which can be readily solved as a set of linear equations subjected to two different sets of right-hand sides. The solutions can be written as

$$[T^{pp}]_{nn} \equiv \frac{B_n^{pp}}{A_n^p} = \frac{-J_n(ka)K_n'(ka) + J_n'(ka)K_n(ka)}{\Delta_n} \quad (26)$$

$$[T^{ep}]_{nn} \equiv \frac{B_n^{ep}}{A_n^p} = \frac{J_n(ka)H_n'(ka) - J_n'(ka)H_n(ka)}{\Delta_n} = \frac{2\hat{i}}{\pi ka} \frac{1}{\Delta_n} \quad (27)$$

$$[T^{pe}]_{nn} \equiv \frac{B_n^{pe}}{A_n^e} = \frac{-I_n(ka)K_n'(ka) + I_n'(ka)K_n(ka)}{\Delta_n} = \frac{1}{ka} \frac{1}{\Delta_n} \quad (28)$$

$$[T^{ee}]_{nn} \equiv \frac{B_n^{ee}}{A_n^e} = \frac{I_n(ka)H_n'(ka) - I_n'(ka)H_n(ka)}{\Delta_n} \quad (29)$$

where

$$\Delta_n = H_n(ka)K_n'(ka) - H_n'(ka)K_n(ka) \quad (30)$$

and the Wronskian relations of Bessel functions have been used

$$J_n(z)H_n'(z) - J_n'(z)H_n(z) = \frac{2\hat{i}}{\pi z} \quad (31)$$

$$I_n(z)K_n'(z) - I_n'(z)K_n(z) = -\frac{1}{z} \quad (32)$$

III.3 Void Inclusion

For a void inclusion, the boundary conditions are that the moment and the force along the hole's edge vanish. That is $M_r = 0$ and $V_r = 0$. This leads to the following equations

$$B_n^p \mathfrak{G}_1^2(n, ka) + B_n^e \mathfrak{G}_1^4(n, ka) = -A_n^p \mathfrak{G}_1^1(n, ka) - A_n^e \mathfrak{G}_1^3(n, ka) \quad (33)$$

$$B_n^p \mathfrak{G}_3^2(n, ka) + B_n^e \mathfrak{G}_3^4(n, ka) = -A_n^p \mathfrak{G}_3^1(n, ka) - A_n^e \mathfrak{G}_3^3(n, ka) \quad (34)$$

which can be readily solved to give

$$[T^{pp}]_{nn} \equiv \frac{B_n^{pp}}{A_n^p} = \frac{\mathfrak{G}_3^1(n, ka) \mathfrak{G}_1^4(n, ka) - \mathfrak{G}_1^1(n, ka) \mathfrak{G}_3^4(n, ka)}{\Delta_n} \quad (35)$$

$$[T^{ep}]_{nn} \equiv \frac{B_n^{ep}}{A_n^p} = \frac{\mathfrak{G}_3^2(n, ka) \mathfrak{G}_1^1(n, ka) - \mathfrak{G}_1^2(n, ka) \mathfrak{G}_3^1(n, ka)}{\Delta_n} \quad (36)$$

$$[T^{pe}]_{nn} \equiv \frac{B_n^{pe}}{A_n^e} = \frac{\mathfrak{G}_3^3(n, ka) \mathfrak{G}_1^4(n, ka) - \mathfrak{G}_1^3(n, ka) \mathfrak{G}_3^4(n, ka)}{\Delta_n} \quad (37)$$

$$[T^{ee}]_{nn} \equiv \frac{B_n^{ee}}{A_n^e} = \frac{\mathfrak{G}_3^2(n, ka) \mathfrak{G}_1^3(n, ka) - \mathfrak{G}_1^2(n, ka) \mathfrak{G}_3^3(n, ka)}{\Delta_n} \quad (38)$$

where

$$\Delta_n = \mathfrak{G}_1^2(n, ka) \mathfrak{G}_3^4(n, ka) - \mathfrak{G}_1^4(n, ka) \mathfrak{G}_3^2(n, ka) \quad (39)$$

III.4 Elastic Inclusion

For an elastic inclusion, waves exist inside the scatterer. Note that the scatterer include the origin, thus only non-singular Bessel functions can be used in the expression for the wave inside the inclusion; that is

$$W^{\text{ref}} = \{C^p\}^T \{J(\mathbf{r}, \theta)\} + \{C^e\}^T \{I(\mathbf{r}, \theta)\} \quad (40)$$

The boundary conditions require the continuity of W , W' , M_r and V_r . This gives the following set of equations

$$\begin{aligned} A_n^p J_n(ka) + A_n^e I_n(ka) + B_n^p H_n(ka) + B_n^e K_n(ka) &= C_n^p J_n(k_1a) + C_n^e I_n(k_1a) \\ A_n^p J_n'(ka) + A_n^e I_n'(ka) + B_n^p H_n'(ka) + B_n^e K_n'(ka) &= \frac{k_1}{k} [C_n^p J_n'(k_1a) + C_n^e I_n'(k_1a)] \\ A_n^p \mathfrak{G}_1^1(n, ka) + A_n^e \mathfrak{G}_1^3(n, ka) + B_n^p \mathfrak{G}_1^2(n, ka) + B_n^e \mathfrak{G}_1^4(n, ka) &= C_n^p \mathfrak{G}_1^1(n, k_1a) + C_n^e \mathfrak{G}_1^3(n, k_1a) \\ A_n^p \mathfrak{G}_3^1(n, ka) + A_n^e \mathfrak{G}_3^3(n, ka) + B_n^p \mathfrak{G}_3^2(n, ka) + B_n^e \mathfrak{G}_3^4(n, ka) &= C_n^p \mathfrak{G}_3^1(n, k_1a) + C_n^e \mathfrak{G}_3^3(n, k_1a) \end{aligned}$$

which can be converted into the following two sets of linear equation systems and solved

numerically:

$$\begin{bmatrix} -H_n(ka) & -K_n(ka) & J_n(k_1a) & I_n(k_1a) \\ -H'_n(ka) & -K'_n(ka) & \frac{k_1}{k} J'_n(k_1a) & \frac{k_1}{k} I'_n(k_1a) \\ -\mathfrak{C}_1^2(n, ka) & -\mathfrak{C}_1^4(n, ka) & \mathfrak{C}_1^1(n, k_1a) & \mathfrak{C}_1^3(n, k_1a) \\ -\mathfrak{C}_3^2(n, ka) & -\mathfrak{C}_3^4(n, ka) & \mathfrak{C}_3^1(n, k_1a) & \mathfrak{C}_3^3(n, k_1a) \end{bmatrix} \begin{Bmatrix} B_n^p \\ B_n^e \\ C_n^p \\ C_n^e \end{Bmatrix} = \begin{Bmatrix} J_n(ka) \\ J'_n(ka) \\ \mathfrak{C}_1^1(n, ka) \\ \mathfrak{C}_3^1(n, ka) \end{Bmatrix} A_n^p \quad (41)$$

$$\begin{bmatrix} -H_n(ka) & -K_n(ka) & J_n(k_1a) & I_n(k_1a) \\ -H'_n(ka) & -K'_n(ka) & \frac{k_1}{k} J'_n(k_1a) & \frac{k_1}{k} I'_n(k_1a) \\ -\mathfrak{C}_1^2(n, ka) & -\mathfrak{C}_1^4(n, ka) & \mathfrak{C}_1^1(n, k_1a) & \mathfrak{C}_1^3(n, k_1a) \\ -\mathfrak{C}_3^2(n, ka) & -\mathfrak{C}_3^4(n, ka) & \mathfrak{C}_3^1(n, k_1a) & \mathfrak{C}_3^3(n, k_1a) \end{bmatrix} \begin{Bmatrix} B_n^p \\ B_n^e \\ C_n^p \\ C_n^e \end{Bmatrix} = \begin{Bmatrix} I_n(ka) \\ I'_n(ka) \\ \mathfrak{C}_1^3(n, ka) \\ \mathfrak{C}_3^3(n, ka) \end{Bmatrix} A_n^e \quad (42)$$

The solutions will give a set of eight ratios: the ratios between B_n and A_n give the entries of the T -matrices:

$$[T^{xy}]_{nn} \equiv \frac{B^{xy}}{A^y}$$

where x and y is either p or e . The ratios between C_n and A_n define another set of characteristic matrices. More often, they are re-expressed with respect to the T -matrices, as

$$\{\mathfrak{C}\} = [\mathfrak{R}]\{\mathfrak{B}\} \quad \text{with} \quad [R^{xy}]_{nn} \equiv \frac{C^{xy}}{B^{xy}} \quad (43)$$

IV. Multiple Scattering Problems

IV.1 Generalized Matrix Formulation

With the introduction of the generalized matrix notation, the general multiple scattering solution can be readily obtained, following the same solution structure for other types of waves, as long as the system is linear.

In a general problem setup, a set of N scatterers are located within an infinite plate. The incident wave can still be expressed as eqn. (16), although in reality, the evanescent component would not be present. The wave scattered by individual scatterers can be written as

$$W_i^{\text{scr}} = \{\mathbf{B}_i^p\}^T \{\mathbf{H}(r_i, \theta_i)\} + \{\mathbf{B}_i^e\}^T \{\mathbf{K}(r_i, \theta_i)\} \quad (44)$$

which remains similar to the one for the single scattering problem, in eqn. (17), with two differences: the subscript i is used to signify the parameters belonging to scatterer i , and the waves are expressed in local coordinate systems. The ‘‘classic’’ multiple scattering formulation gives the following solutions, in terms of generalized wave expansion coefficient matrices:

$$\{\mathfrak{B}_i\} = [\mathfrak{T}_i] \left(\{\mathfrak{A}_i\} + \sum_{j=1, j \neq i}^N [\mathfrak{R}_{ij}]^T \{\mathfrak{B}_j\} \right) \quad (45)$$

which can be solved by rearranging into a linear equation system as

$$[\mathbb{L}]\{\mathbb{B}\} = \{\mathbb{A}\} \quad (46)$$

where

$$\{\mathbb{B}\} = \begin{Bmatrix} \{\mathfrak{B}_1\} \\ \{\mathfrak{B}_2\} \\ \vdots \\ \{\mathfrak{B}_N\} \end{Bmatrix} \quad \{\mathbb{A}\} = \begin{Bmatrix} [\mathfrak{T}_1]\{\mathfrak{A}_1\} \\ [\mathfrak{T}_2]\{\mathfrak{A}_2\} \\ \vdots \\ [\mathfrak{T}_N]\{\mathfrak{A}_N\} \end{Bmatrix} \quad (47)$$

$$[\mathbb{L}] = \begin{bmatrix} [\mathfrak{S}] & -[\mathfrak{T}_1][\mathfrak{R}_{12}]^T & -[\mathfrak{T}_1][\mathfrak{R}_{13}]^T & \cdots & -[\mathfrak{T}_1][\mathfrak{R}_{1N}]^T \\ -[\mathfrak{T}_2][\mathfrak{R}_{21}]^T & [\mathfrak{S}] & -[\mathfrak{T}_2][\mathfrak{R}_{23}]^T & \cdots & -[\mathfrak{T}_2][\mathfrak{R}_{2N}]^T \\ \cdots & \cdots & \cdots & \cdots & \cdots \\ -[\mathfrak{T}_N][\mathfrak{R}_{N1}]^T & -[\mathfrak{T}_N][\mathfrak{R}_{N2}]^T & -[\mathfrak{T}_N][\mathfrak{R}_{N3}]^T & \cdots & [\mathfrak{S}] \end{bmatrix} \quad (48)$$

The only remaining issues are matrices $[\mathfrak{R}_{ij}]$, which represent the coordinate transformations, and matrices $\{\mathfrak{A}_i\}$, which is the wave expansion coefficient for the incident wave.

IV.2 Coordinate Transformation

The coordinate transformation among the local coordinate systems is obtained from the *Graf's addition theorem* for the Bessel functions. It has been a crucial ingredient for the multiple scattering formulations, and hence it is well known. However, the modified Bessel functions possess most of essential properties of the Bessel functions and yet differ in some properties. Therefore it is useful to trace the derivation process for coordinate transformation for the propagating wave expansion bases, and then follow the same process to derive the coordinate transformation for the evanescent wave expansion bases.

IV.2.A Coordinate Transformation for Propagating Wave Expansion Bases

Recall Graf's addition theorem for the Bessel functions as (Abramowitz & Stegun, 9.1.79, p. 363 1965):

$$J_n(\varpi) \frac{\cos n\beta}{\sin n\alpha} = \sum_{m=-\infty}^{\infty} J_{n+m}(Z) J_m(z) \frac{\cos m\alpha}{\sin m\alpha} \quad (49)$$

and

$$H_n(\varpi) \frac{\cos n\beta}{\sin n\alpha} = \sum_{m=-\infty}^{\infty} H_{n+m}(Z) J_m(z) \frac{\cos m\alpha}{\sin m\alpha} \quad (50)$$

where both n and m are integers. Equation (50) is valid only when $|Z| > |ze^{\pm i\alpha}|$; whereas eqn. (49) is valid throughout the plane. When Z , z and ϖ are real and positive, the geometric relations of the parameters are as sketched in Fig. 1(a), which is compared with geometric relations between two arbitrarily chosen local coordinate systems in Fig. 1(b). An arbitrary field point P can be located by polar coordinates of either (r_i, θ_i) or (r_j, θ_j) . Further, (d_{ij}, θ_{ij})

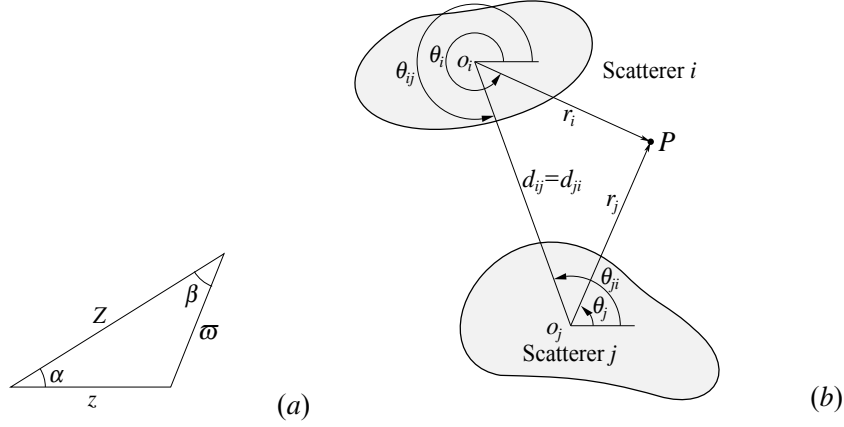


Fig. 1 Geometries in multiple scattering. (a) Geometry for Graf's addition theorem for Bessel functions. (b) Geometric relations between two local coordinate systems.

is the polar coordinates of o_j in the coordinate system originating at o_i , and (d_{ji}, θ_{ji}) is the coordinates of o_i in the coordinate system originating at o_j . From Fig. 1b

$$d_{ij} = d_{ji} \quad \theta_{ij} = \pi + \theta_{ji} \quad (51)$$

First, eqns. (49) and (50) is rewritten using exponential harmonics as

$$\mathcal{C}_n(\varpi) e^{\hat{i}n\beta} = \sum_{m=-\infty}^{\infty} \mathcal{C}_{n+m}(Z) J_m(z) e^{\hat{i}m\alpha} \quad (52)$$

where, following Abramowitz & Stegun, $\mathcal{C}_n(z)$ denotes either $J_n(z)$ or $H_n(z)$.

Comparing the geometries in Fig. 1, after the following parameter substitutions:

$$z \rightarrow k r_j \quad \varpi \rightarrow k r_i \quad Z \rightarrow k d_{ji} \quad \alpha \rightarrow \theta_{ji} - \theta_j \quad \text{and} \quad \beta \rightarrow \theta_i - \theta_{ij},$$

eqn. (52) becomes

$$\mathcal{C}_n(k r_i) e^{\hat{i}n(\theta_i - \theta_{ij})} = \sum_{m=-\infty}^{\infty} \mathcal{C}_{n+m}(k d_{ji}) J_m(k r_j) e^{\hat{i}m(\theta_{ji} - \theta_j)} \quad (53)$$

Moving θ_{ij} from the left-hand side to the right-hand side gives

$$\mathcal{C}_n(k r_i) e^{\hat{i}n\theta_i} = \sum_{m=-\infty}^{\infty} e^{\hat{i}(n\theta_{ij} + m\theta_{ji})} \mathcal{C}_{n+m}(k d_{ji}) J_m(k r_j) e^{-\hat{i}m\theta_j} \quad (54)$$

Since m ranges from $-\infty$ to ∞ , changing $-m$ to m does not change outcome of the summation:

$$\mathcal{C}_n(k r_i) e^{\hat{i}n\theta_i} = \sum_{m=-\infty}^{\infty} e^{\hat{i}(n\theta_{ij} - m\theta_{ji})} \mathcal{C}_{n-m}(k d_{ji}) J_{-m}(k r_j) e^{\hat{i}m\theta_j} \quad (55)$$

Noting that $\theta_{ji} = \theta_{ij} - \pi$, and

$$e^{\hat{i}(n\theta_{ij}-m\theta_{ji})} = e^{\hat{i}[(n-m)\theta_{ij}+m\pi]} = (-1)^m e^{\hat{i}(n-m)\theta_{ij}}$$

and that (A&S, 9.1.5, p. 358)

$$(-1)^m J_{-m}(z) = J_m(z) \quad (56)$$

eqns. (50) and (49) finally become

$$\{\mathbf{J}(r_i, \theta_i)\} = [\mathfrak{R}\mathbf{R}_{ij}^p]\{\mathbf{J}(r_j, \theta_j)\} \quad (57)$$

$$\{\mathbf{H}(r_i, \theta_i)\} = [\mathbf{R}_{ij}^p]\{\mathbf{J}(r_j, \theta_j)\} \quad (58)$$

where the entries of matrices $[\mathbf{R}_{ij}^p]$ and $[\mathfrak{R}\mathbf{R}_{ij}^p]$ at the n -th row and the m -th column are

$$[\mathfrak{R}\mathbf{R}_{ij}^p]_{nm} = e^{\hat{i}(n-m)\theta_{ij}} J_{n-m}(kd_{ij}) \quad (59)$$

$$[\mathbf{R}_{ij}^p]_{nm} = e^{\hat{i}(n-m)\theta_{ij}} H_{n-m}(kd_{ij}) \quad (60)$$

and the validity condition for eqn. (58) is $d_{ij} > r_j$. Matrices $[\mathbf{R}_{ij}^p]$ and $[\mathfrak{R}\mathbf{R}_{ij}^p]$ are called the singular and regular, respectively, *local coordinate translation matrices* for the propagating wave expansion bases. Here, the symbol \mathfrak{R} denotes the *regular counterpart* of the enclosed function, which is, in this case, obtained by replacing the Hankel function of the first kind by the Bessel function of the first kind. (Although $J_n(\cdot)$ is the real part of $H_n(\cdot)$, there is a complex factor in the front, it is not appropriate to call $[\mathfrak{R}\mathbf{R}_{ij}^p]$ as the real part of $[\mathbf{R}_{ij}^p]$. On the other hand, $H_n(\cdot)$ is singular at the origin, while $J_n(\cdot)$ is non-singular.)

IV.2.B Coordinate Transformation for Evanescent Wave Expansion Bases

For the modified Bessel functions, based on the same geometry in Fig. 1(a), the corresponding Graf's addition theorem is (Watson, *A Treatise on the Theory of Bessel Functions*, 2nd edn., Cambridge University Press, 1944, §11.3, p3. 61)

$$I_n(\varpi) \frac{\cos n\beta}{\sin m\alpha} = \sum_{m=-\infty}^{\infty} (-1)^m I_{n+m}(Z) I_m(z) \frac{\cos m\alpha}{\sin n\beta} \quad (61)$$

and

$$K_n(\varpi) \frac{\cos n\beta}{\sin m\alpha} = \sum_{m=-\infty}^{\infty} K_{n+m}(Z) I_m(z) \frac{\cos m\alpha}{\sin n\beta} \quad (62)$$

which can be combined to write

$$I_n(\varpi) e^{\hat{i}n\beta} = \sum_{m=-\infty}^{\infty} (-1)^m I_{n+m}(Z) I_m(z) e^{\hat{i}m\alpha} \quad (63)$$

$$K_n(\varpi) e^{\hat{i}n\beta} = \sum_{m=-\infty}^{\infty} K_{n+m}(Z) I_m(z) e^{\hat{i}m\alpha} \quad (64)$$

Note that a “unified” expression similar to eqn. (52) is not available. However, the same derivation process can be followed exactly without any change, until reaching eqn. (56). The “modified” version of eqn. (56) is (A&S, 9.6.6, p. 375)

$$I_{-m}(z) = I_m(z) \quad (65)$$

Thus,

$$I_n(k r_i) e^{\hat{i} n \theta_i} = \sum_{m=-\infty}^{\infty} e^{\hat{i}(n-m)\theta_{ij}} I_{n-m}(k d_{ij}) I_m(k r_j) e^{\hat{i} m \theta_j} \quad (66)$$

$$K_n(k r_i) e^{\hat{i} n \theta_i} = \sum_{m=-\infty}^{\infty} (-1)^m e^{\hat{i}(n-m)\theta_{ij}} K_{n-m}(k d_{ij}) I_m(k r_j) e^{\hat{i} m \theta_j} \quad (67)$$

In matrix form,

$$\{\mathbf{I}(r_i, \theta_i)\} = [\mathfrak{R} \mathbf{R}_{ij}^e] \{\mathbf{I}(r_j, \theta_j)\} \quad (68)$$

$$\{\mathbf{K}(r_i, \theta_i)\} = [\mathbf{R}_{ij}^e] \{\mathbf{I}(r_j, \theta_j)\} \quad (69)$$

where

$$[\mathfrak{R} \mathbf{R}_{ij}^e]_{nm} = e^{\hat{i}(n-m)\theta_{ij}} I_{n-m}(k d_{ij}) \quad (70)$$

$$[\mathbf{R}_{ij}^e]_{nm} = (-1)^m e^{\hat{i}(n-m)\theta_{ij}} K_{n-m}(k d_{ij}) \quad (71)$$

IV.2.C Coordinate Transformation in Generalized Matrix Form

Finally, in generalized matrix form, the coordinate transformation can be written as

$$[\mathfrak{R} \mathfrak{R}_{ij}] = \begin{bmatrix} [\mathfrak{R} \mathbf{R}_{ij}^p] & 0 \\ 0 & [\mathfrak{R} \mathbf{R}_{ij}^e] \end{bmatrix} \quad [\mathfrak{R}_{ij}] = \begin{bmatrix} [\mathbf{R}_{ij}^p] & 0 \\ 0 & [\mathbf{R}_{ij}^e] \end{bmatrix} \quad (72)$$

Note that there is no off-diagonal blocks. Physically, a propagating wave would not be converted into an evanescent wave by a mere coordinate transformation, and vice versa.

V. Incident Wave Fields

V.1 Wave Expansion for Planar Waves

For the propagating incident wave, a planar wave with unit amplitude propagating in the x -direction, is given by the well-known relation

$$e^{\hat{i} k x} = e^{\hat{i} k r \cos \theta} = \sum_{n=-\infty}^{\infty} \hat{i}^n J_n(k r) e^{\hat{i} n \theta} \quad (73)$$

For the evanescent wave, there is no real meaningful “wave”, rather than a localized vibration, which will be represented by an exponential decaying function. In particular, $e^{-k|x|}$ represents such a vibration localized along the y -axis.

According to the following properties of modified Bessel functions (Abramowitz & Stegun, 9.6.38, p. 3376)

$$e^{z \cos \theta} = I_0(z) + 2 \sum_{n=1}^{\infty} I_n(z) \cos(n\theta) \quad (74)$$

Recall that $I_{-n}(z) = I_n(z)$. Further,

$$I_n(z)e^{in\theta} + I_{-n}(z)e^{-in\theta} = I_n(z)(e^{in\theta} + e^{-in\theta}) = 2I_n(z) \cos(n\theta) \quad (75)$$

Thus, replacing z by kr ,

$$e^{kx} = e^{kr \cos \theta} = \sum_{n=-\infty}^{\infty} I_n(kr) e^{in\theta} \quad (76)$$

Furthermore (Abramowitz & Stegun, 9.6.30 and setting $m = 1$, p. 3376), $I_n(-z) = (-1)^n I_n(z)$

$$e^{-kx} = e^{-kr \cos \theta} = \sum_{n=-\infty}^{\infty} (-1)^n I_n(kr) e^{in\theta} \quad (77)$$

The same relation can be obtained from eqn. (16) by replacing k with $\hat{i}k$, and utilizing the relation between $J_n(z)$ and $I_n(z)$.

In terms of wave expansion, if the incident wave is written as

$$W^{\text{inc}} = \{A_i^p\}^T \{J(r_i, \theta_i)\} + \{A_i^e\}^T \{I(r_i, \theta_i)\} \quad (78)$$

Then, the coefficients are

$$\{A^p\}_n = \hat{i}^n \quad \{A^e\}_n = \begin{cases} (-1)^n & \text{if } \cos \theta \geq 0 \\ 1 & \text{if } \cos \theta < 0 \end{cases} \quad (79)$$

Note that in two-dimensional scattering problems in a free space, the incident wave is often considered as “located at ‘infinity’” its exact location does not matter while the expression remains valid no matter where the origin of the coordinate system is located. However, in a plate, this is no longer true. The evanescent component of the wave comes with a location, which is the y -axis of the coordinate system. For most wave scattering considerations, this is not the main concern and thus be neglected.

V.2 Coordinate Transformation for Planar Incident Waves

In multiple scattering formulation, a same incident wave is expressed in different local coordinate systems. In general, coordinate transformation utilizing the addition theorems of Bessel functions can be used to find the wave expansion coefficient in different coordinate systems. However, it must be noted in the computation, since the infinite series are truncated to finite terms, there are errors introduced into the process. As an alternative, coordinate transformation can be directly applied to the analytical expressions before expanding it into wave expansions.

For example, if the incident wave is expressed in a global coordinate system (without subscript), and in the scatterer i 's local coordinate system, whose origin is located at (X_i, Y_i) in the global Cartesian coordinate system and (R_i, Θ_i) the global polar coordinate system, the following relation can be observed $x = X_i + x_i$. Then,

$$e^{\hat{i}kx} = e^{\hat{i}k(X_i + x_i)} = e^{\hat{i}kX_i} e^{\hat{i}kx_i} \quad e^{-kx} = e^{-kX_i} e^{-\hat{i}kx_i} \quad (80)$$

Then, the wave expansion coefficient for the propagating component of the incident wave in the local coordinate system can be simply written as

$$\{A_i^p\}_n = e^{\hat{i}kX_i} \hat{i}^n \quad (81)$$

This is a much more efficient and accurate approach to obtaining the wave expansion coefficients for the individual scatterers in the multiple scattering problem. However, the expression for the evanescent component has not been sought.

V.3 Planar Wave Reflected by a Boundary

At times it is desirable to consider a wave scattering problem in a finite plate. The simplest geometry of a finite plate would be a rectangular one. In order to consider the wave reflection from a boundary, the reflected wave can be approximated as an incident wave propagating in the $-x$ direction. As with the conventional incident wave, generally considering the propagating component is sufficient but the reflected wave may differ by a certain phase. For a planar wave of unit amplitude traveling in the $-x$ direction, it can be expressed as $e^{\hat{i}k(x_0 - x)}$, where x_0 can be a certain reference point and in turn $kx_0 = \phi_0$ can be viewed as the phase angle. Furthermore, for a reflected planar wave, the amplitude of the reflected wave could be smaller than the incident; and it might differ in phase by a certain angle ϕ_a . (For example: wave reflected by the free-end of the string is known to have a phase change of π .) The real amplitude A and the phase angle $\phi = \phi_0 + \phi_a$ can be combined into a complex amplitude $C = Ae^{\hat{i}\phi}$.

Note that $-x$ direction can be viewed as performing a coordinate transformation of the xy coordinate system by π ; that is,

$$e^{-\hat{i}kx} = e^{\hat{i}kr \cos(\theta + \pi)} \quad (82)$$

Then, this reflected planar wave can be approximated as, according to eqn. (73),

$$C e^{-\hat{i}kx} = C e^{\hat{i}kr \cos(\theta + \pi)} = C \sum_{n=-\infty}^{\infty} \hat{i}^n J_n(kr) e^{\hat{i}n(\theta + \pi)} = C \sum_{n=-\infty}^{\infty} (-\hat{i})^n J_n(kr) e^{\hat{i}n\theta} \quad (83)$$

For individual scatterers, the wave expansion coefficient for the propagation component of the reflected wave can be expressed as

$$\{A_i^p\}_n = C e^{-\hat{i}kX_i} (-\hat{i})^n \quad (84)$$

V.4 Wave Expansion for a Point Load

When a concentrated force F of wave number k is applied at a location denoted as x_0 , the resulting displacement is expressible as (L. Hörchens, *Imaging of Materials Inhomogeneities*

with *Flexural Waves*, Ph. D. Thesis, Delft University of Technology, The Netherlands, 2010, Chapter 4)

$$W^{\text{inc}}(\mathbf{x}) = -\hat{i} \frac{F}{8k^2 D} \left[H_0^{(2)}(k|\mathbf{x} - \mathbf{x}_0|) - H_0^{(2)}(-\hat{i}k|\mathbf{x} - \mathbf{x}_0|) \right] \quad (85)$$

Note that in the derivation for the above expression (in Appendix B), the time-incorporated expression for a general forward-traveling wave is $f(t - x/c)$ for one-dimensional case. Consequently, a harmonic wave would be as $e^{\hat{i}(\omega t - kx)}$, whose time factor is $e^{\hat{i}\omega t}$. In the two-dimensional case, the spatial factor for the an outgoing cylindrical wave in a polar coordinate system would be $H_n^{(2)}(\cdot)$, as the asymptotic expressions for the Hankel functions $H^{(1,2)}(x) = Ce^{\pm \hat{i}x}$ where C is a coefficient the positive sign is for the Hankel function of the first kind, and negative for the second kind. In other words, the Hankel functions of the second kind in eqn. (85) represent out-going waves. This notation differs from most contemporary literature, in which $H_n^{(1)}(\cdot)$ is generally used to represent an outgoing wave, whose time factor, if to be included, is $e^{-\hat{i}\omega t}$. In adopting the above expression for the present analysis, $H_n^{(2)}(\cdot)$'s are simply replaced by the corresponding $H_n^{(1)}(\cdot)$'s with the same arguments.

Furthermore, if a local coordinate system (r_s, θ_s) is constructed such that its origin O_s is located at the point of incident wave, the above expression can be simplified to

$$\begin{aligned} W^{\text{inc}}(r_s) &= -\hat{i} \frac{F}{8k^2 D} \left[H_0^{(1)}(kr_s) - H_0^{(1)}(-\hat{i}kr_s) \right] \\ &= -\frac{F}{8k^2 D} \left[\hat{i} H_0^{(1)}(kr_s) + \frac{2}{\pi} K_0(kr_s) \right] \end{aligned} \quad (86)$$

where the relation between $H_0^{(1)}(\cdot)$ and $K_0(\cdot)$ in eqn. (11) have been used. Note that the incident field is omnidirectional, and is thus independent of θ_s .

In most computations for scattering problems, all the wave amplitudes are normalized by that of the incident wave. In such cases, the constant coefficient in $W^{\text{inc}}(r_i, \theta_i)$ becomes immaterial and can thus be dropped. On the other hand, since the response due to a concentrated force is a singular field the normalization factor can be the field amplitude at a certain characteristic length a from the source, as

$$\overline{W}^{\text{inc}}(r_s) = \frac{W^{\text{inc}}(r_s)}{|W^{\text{inc}}(a)|} = -\frac{1}{\Delta} \left[\hat{i} H_0^{(1)}(kr_s) + \frac{2}{\pi} K_0(kr_s) \right] \quad (87)$$

where

$$\Delta = \left| \hat{i} H_0^{(1)}(ka) + \frac{2}{\pi} K_0(ka) \right| \quad (88)$$

For convenience and in keeping consistency with the case of planar incident wave, the normalized incident wave is simply taken as the incident wave, and the overbar in the above expression will be dropped in the discussions to follow. Using a wave expansion basis based on this source-local coordinate system, the matrix notation for the point source is

$$W_i^{\text{inc}}(r_s, \theta_s) = \{A_s^p\}^T \{H(r_s, \theta_s)\} + \{A_s^e\}^T \{K(r_s, \theta_s)\} \quad (89)$$

Then, coefficient are such that

$$\{A_s^p\}_0 = -\frac{\hat{t}}{\Delta} \quad \{A_s^e\}_0 = -\frac{2}{\pi\Delta} \quad \{A_s^X\}_n = 0 \quad \text{for other } n \quad (90)$$

In scattering computations, it is necessary to express the incident wave in individual scatterers' local coordinate system, say (r_i, θ_i) . Then, coordinate transformations wave wave expansion bases in eqns. (58) and (69),

$$\{A_s^p\}^T \{H(r_s, \theta_s)\} = \{A_s^p\}^T [R_{si}^p] \{J(r_i, \theta_i)\} \quad (91)$$

$$\{A_s^e\}^T \{K(r_s, \theta_s)\} = \{A_s^e\}^T [R_{si}^e] \{I(r_i, \theta_i)\} \quad (92)$$

where $[R_{si}^p]$ and $[R_{si}^e]$ are coordinate translation matrices for the propagating and evanescent components between local coordinate systems (r_s, θ_s) and (r_i, θ_i) , respectively. Note that there is only one non-zero entries in the coefficient matrices $\{A_s^p\}$ and $\{A_s^e\}$. The matrix multiplication can be carried out as zero-th column of the respective $[R]$ matrices. If the point force incident wave is expressed as

$$W_i^{\text{inc}}(r_i, \theta_i) = \{A_i^p\}^T \{J(r_i, \theta_i)\} + \{A_i^e\}^T \{I(r_i, \theta_i)\} \quad (93)$$

the wave expansion coefficient for this incident wave are

$$\{A_i^p\}_n = -\frac{\hat{t}}{\Delta} e^{-\hat{t}n\theta_{si}} H_{-n}(kd_{si}) = (-1)^{n+1} \frac{\hat{t}}{\Delta} e^{-\hat{t}n\theta_{si}} H_n(kd_{si}) \quad (94)$$

$$\{A_i^e\}_n = -\frac{2}{\pi\Delta} (-1)^n e^{-\hat{t}n\theta_{si}} K_{-n}(kd_{si}) = -\frac{2}{\pi\Delta} (-1)^n e^{-\hat{t}n\theta_{si}} K_n(kd_{si}) \quad (95)$$

where (d_{si}, θ_{si}) are the coordinates of the source located in the (r_i, θ_i) coordinate system, and the relation $K_{-n}(z) = K_n(z)$ has been used.

Note that if the evanescent component can be neglected, the propagating component of the incident wave is the same as a point source in a two-dimensional free space.

In the case of multiple wave sources, then only one of the wave will be used to define the normalization factor as described above, and all remaining sources can have a relative amplitude and a phase difference from the one chosen for the normalization. The phase difference is simply expressed by $e^{\hat{t}\phi}$.

V.5 Wave Expansion for a Line Source

A line source can be constructed from an array of identical point sources lined up along the designated segment. This makes sense both physically and mathematically. Mathematically, the sum becomes a *Schlömilch series* if the line is infinitely long, which has been shown by Twersky to turn into (expressible as) planar waves for the propagating components. The complication comes from the normalization, especially when the length of line is finite. This will be dealt with numerically. In the numerical computations, The wave field due to the multiple sources will be calculated along a line a distance a from the line source. The average amplitude of the incident wave along the line segment will be used as the normalization factor.

VI. Computational Considerations

- Since the Young's modulus E does not enter in the formulation except in computing the rigidity D , which have different expressions for a uniform plate and a sandwich panel, in the code, E is not a required material property. Instead, D is used as an input. D can be calculated using a spread-sheet external to the code.
- The thickness h and mass density ρ are needed in relating the wave frequency to the wave number. Note that when the plate is a composite panel, h is the total thickness, and ρ must be the overall mass density. In other words, ρh should forms the areal mass density of the composite panel.
- Poisson's ratio is extensively used. Thus it is needed as an input.
- Since the wave speed is frequency-dependent, the wave number no longer represents a simple (linear) normalization of the frequency. Since it is desirable to have the computational results presented on a linear scale of the frequency, the wave number k is not used as a normalized frequency in the computations. For the lack of a better alternative, the Hertz frequency $f = \omega/(2\pi)$ is used as the input. Correspondingly, all other parameters will be un-normalized, specific in SI units.

A sensible alternative for normalizing the frequency would be to define

$$\omega_0 = \frac{1}{h^2} \sqrt{\frac{D}{\rho h}} \quad (96)$$

such that

$$\frac{\omega}{\omega_0} = (kh)^2 \quad (97)$$

This way, $\omega/\omega_0 = 1$ means $kh = 1$, and in turn the wave length is 2π times of the plate thickness.

- In multiple scattering formation, only $[\mathbf{R}^p]$ and $[\mathbf{R}^e]$ are used (that is, not the regular counter part) for coordinate transformation. They have a unifie expression expressible as

$$[R_{ij}]_{nm} = (-1)^m e^{i(n-m)\theta_{ij}} \mathcal{L}_{n-m}(kd_{ij}) \quad (98)$$

where $\mathcal{L}_n(z)$ will be $H_n(z)$ for $[\mathbf{R}^p]$, and $K_n(z)$ for $[\mathbf{R}^e]$. In other words, they can be computed using a unifie function.

- The following product of generalized matrices are used in the multiple scattering analysis:

$$[\mathfrak{T}_i][\mathfrak{R}_{ij}]^T = \begin{bmatrix} [T_i^{pp}] & [T_i^{pe}] \\ [T_i^{ep}] & [T_i^{ee}] \end{bmatrix} \begin{bmatrix} [R_{ij}^p] & 0 \\ 0 & [R_{ij}^e] \end{bmatrix} = \begin{bmatrix} [T_i^{pp}][R_{ij}^p] & [T_i^{pe}][R_{ij}^p] \\ [T_i^{ep}][R_{ij}^e] & [T_i^{ee}][R_{ij}^e] \end{bmatrix} \quad (99)$$

It is clear that directly constructing the generalized based on the right-most expression is more efficien than constructing the two matrices separately then performing the product of the generalized matrices.

- The wave field can be obtained directly by the product of the generalized matrices for the wave expansion coefficient and bases. Thus the multiple scattering solution, that is, the wave expansion coefficient for individual scatterers, will be stored in the generalized matrix form.
- For an elastic scatterer, it is assumed that the thickness is the same as the host plate. Uneven thickness will cause three-dimensional effects and would be beyond the capability of the current model.

VII. Validations

VI.1 Energy Flux Conservation Validations

According to Norris & Vemula (Scattering of Flexural Waves on Thin Plates, *JSV*, **118**(1), 115–125, 1995), the energy flux conservation for the flexural wave is expressible as

$$\frac{\omega D}{2} \oint_C \left\{ \int_C \left(W \frac{\partial \nabla^2 \bar{W}}{\partial r} - \nabla^2 \bar{W} \frac{\partial W}{\partial r} \right) ds \right\} = 0 \quad (100)$$

The physical meaning of this relation is the principle of energy conservation: if the surface C (a path in a two-dimensional problem) enclosed neither a source nor a sink, the energy entering into the surface should equal to the energy emitted out of the surface.

In general, the wave field on the plate can be divided into propagating and evanescent components,

$$W = W^p + W^e \quad (101)$$

and they satisfy different equations:

$$\nabla^2 W^p + k^2 W^p = 0 \quad \text{and} \quad \nabla^2 W^e - k^2 W^e = 0 \quad (102)$$

or

$$\nabla^2 W^p = -k^2 W^p \quad \text{and} \quad \nabla^2 W^e = k^2 W^e \quad (103)$$

The integral in eqn. (100) can be expressed as

$$\begin{aligned} I &= \int_C \left(W \frac{\partial \nabla^2 \bar{W}}{\partial r} - \nabla^2 \bar{W} \frac{\partial W}{\partial r} \right) ds \\ &= k^2 \int_C \left[(W^p + W^e) \frac{\partial (-\bar{W}^p + \bar{W}^e)}{\partial r} - (-\bar{W}^p + \bar{W}^e) \frac{\partial (W^p + W^e)}{\partial r} \right] ds \\ &= k^2 \int_C \left(-W^p \frac{\partial \bar{W}^p}{\partial r} + W^p \frac{\partial \bar{W}^e}{\partial r} - W^e \frac{\partial \bar{W}^p}{\partial r} + W^e \frac{\partial \bar{W}^e}{\partial r} \right. \\ &\quad \left. + \bar{W}^p \frac{\partial W^p}{\partial r} + \bar{W}^p \frac{\partial W^e}{\partial r} - \bar{W}^e \frac{\partial W^p}{\partial r} - \bar{W}^e \frac{\partial W^e}{\partial r} \right) ds \end{aligned} \quad (104)$$

And in the far field only the propagating component remains, and the inegral becomes

$$I_{\text{far field}} = k^2 \int_C \left(-W^p \frac{\partial \overline{W}^p}{\partial r} + \overline{W}^p \frac{\partial W^p}{\partial r} \right) ds \quad (105)$$

Note that the above relation must hold for all incident waves. It is possible to construct an incident wave that constant only one entry in the wave expansion, leading to a pair of scattered waves. For example, if the incident is $A_n^p = 1$, the resulting total wave field is

$$W^p = J_n(kr) + T_{nn}^{pp} H_n(kr) e^{in\theta} \quad W^e = T_{nn}^{pe} K_n(kr) e^{in\theta} \quad (106)$$

If the integration path is circular with a large radius (far-field) eqn. (100) gives

$$\begin{aligned} 0 &= \Im \left\{ \left(J_n(kr) + T_{nn}^{pp} H_n(kr) \right) \left(J'_n(kr) + \overline{T_{nn}^{pp}} \overline{H'_n(kr)} \right) \right. \\ &\quad \left. - \left(J_n(kr) + \overline{T_{nn}^{pp}} \overline{H_n(kr)} \right) \left(J'_n(kr) + T_{nn}^{pp} H'_n(kr) \right) \right\} \\ &= \Im \left\{ J_n(kr) \left[\overline{T_{nn}^{pp}} \overline{H'_n(kr)} - T_{nn}^{pp} H'_n(kr) \right] \right. \\ &\quad \left. + J'_n(kr) \left[T_{nn}^{pp} H_n(kr) - \overline{T_{nn}^{pp}} \overline{H_n(kr)} \right] \right. \\ &\quad \left. + |T_{nn}^{pp}|^2 \left[H_n(kr) \overline{H'_n(kr)} - H'_n(kr) \overline{H_n(kr)} \right] \right\} \quad (107) \end{aligned}$$

Note that, since $J_n(kr)$ and $J'_n(kr)$ are real,

$$\Im \left[\overline{T_{nn}^{pp}} \overline{H'_n(kr)} - T_{nn}^{pp} H'_n(kr) \right] = -2\Im \{ T_{nn}^{pp} H'_n(kr) \} \quad (108)$$

$$\Im \left[T_{nn}^{pp} H_n(kr) - \overline{T_{nn}^{pp}} \overline{H_n(kr)} \right] = 2\Im \{ T_{nn}^{pp} H_n(kr) \} \quad (109)$$

The equation becomes

$$\begin{aligned} &\Im \{ 2T_{nn}^{pp} [J_n(kr) H'_n(kr) - J'_n(kr) H_n(kr)] \\ &+ |T_{nn}^{pp}|^2 [H_n(kr) H_n^{(2)'}(kr) - H'_n(kr) H_n^{(2)}(kr)] \} = 0 \quad (110) \end{aligned}$$

Recall the Wronkian relations for Bessel and Hankel functions in eqn. (31) and

$$H_n^{(1)}(z) H_n^{(2)'}(z) - H_n^{(1)'}(z) H_n^{(2)}(z) = \frac{4\hat{i}}{\pi z} \quad (111)$$

Then,

$$\Im \left\{ 2T_{nn}^{pp} \frac{2\hat{i}}{\pi k r} + |T_{nn}^{pp}|^2 \frac{4\hat{i}}{\pi k r} \right\} = 0 \quad (112)$$

which can be simplifie to

$$\Re \{ T_{nn}^{pp} \} + |T_{nn}^{pp}|^2 = 0 \quad (113)$$

In the near field noting $K_n(kr)$ is real,

$$W^e \frac{\partial \overline{W}^e}{\partial r} - \overline{W}^e \frac{\partial W^e}{\partial r} = 0$$

$$\begin{aligned}
I &= 2\pi k^3 \left\{ \overline{T}_{nn}^{pe} K'_n(kr) [J_n(kr) + T_{nn}^{pp} H_n(kr)] - T_{nn}^{pe} K_n(kr) [J'_n(kr) + \overline{T}_{nn}^{pp} \overline{H}'_n(kr)] \right. \\
&\quad \left. + T_{nn}^{pe} K'_n(kr) [J_n(kr) + \overline{T}_{nn}^{pp} \overline{H}_n(kr)] - \overline{T}_{nn}^{pe} K_n(kr) [J'_n(kr) + T_{nn}^{pp} H'_n(kr)] \right\} \\
&= T_{nn}^{pe} [K'_n(kr) J_n(kr) - K_n(kr) J'_n(kr)] + \overline{T}_{nn}^{pe} [K'_n(kr) J_n(kr) - K_n(kr) J'_n(kr)] \\
&\quad + T_{nn}^{pe} \overline{T}_{nn}^{pp} [K'_n(kr) \overline{H}_n(kr) - K_n(kr) \overline{H}'_n(kr)] \\
&\quad + \overline{T}_{nn}^{pe} T_{nn}^{pp} [K'_n(kr) H_n(kr) - K_n(kr) H'_n(kr)] \\
&= 2\Re \left\{ T_{nn}^{pe} \right\} [K'_n(kr) J_n(kr) - K_n(kr) J'_n(kr)] \\
&\quad + 2\Re \left\{ T_{nn}^{pp} \overline{T}_{nn}^{pe} [K'_n(kr) H_n(kr) - K_n(kr) H'_n(kr)] \right\} \tag{114}
\end{aligned}$$

and the condition is automatically satisfied without posing any conditions on the T -matrices.

Similarly, if the incident is $A_n^e = 1$, the resulting field is

$$W^p = T_{nn}^{ep} H_n(kr) e^{in\theta} \quad W^e = I_n(kr) + T_{nn}^{ee} K_n(kr) e^{in\theta} \tag{115}$$

In the far field with only the propagating component,

$$\begin{aligned}
0 &= \Im \left\{ \int_C \left(W^p \frac{\partial \overline{W}^p}{\partial r} - \overline{W}^p \frac{\partial W^p}{\partial r} \right) ds \right\} \\
&= \Im \left\{ T_{nn}^{ep} H_n(kr) \overline{T}_{nn}^{ep} \overline{H}'_n(kr) - \overline{T}_{nn}^{ep} \overline{H}_n(kr) T_{nn}^{ep} H'_n(kr) \right\} \\
&= \Im \left\{ |T_{nn}^{pe}|^2 \frac{4\hat{i}}{\pi k r} \right\} \tag{116}
\end{aligned}$$

The content is pure imaginary. This would require $|T_{nn}^{pe}| = 0$, which is not correct. This suggests that the condition is not satisfied. This is likely due to the fact that the incident wave is not included; meaning that the path actually includes the source. The source is the evanescent incident, which is localized in the vicinity of the origin.

Thus, to validate the other part of the calculation for the T -matrices, it would be necessary to numerically compute an integral over a closed path that avoids the origin.

VI.2 Optical Theorem Validation

The *scattering form factor* is the far-field angular distribution pattern of the scattered wave when it is subjected to an planar incident wave of unit amplitude. It is defined as (Norris & Vemula, JSV 1995)

$$\lim_{r \rightarrow \infty} W^{\text{scr}} = \frac{1}{\sqrt{2r}} e^{\hat{i}(kr - \pi/4)} f(\theta) \tag{117}$$

For the single scatterer problem, recall the asymptotes for Hankel functions and modified Bessel functions

$$H_n(kr) = \sqrt{\frac{2}{\pi k r}} e^{\hat{i}(kr - n\pi/2 - \pi/4)} = \hat{i}^{-n} \sqrt{\frac{2}{\pi k r}} e^{\hat{i}(kr - \pi/4)} \tag{118}$$

and

$$K_n(kr) = \sqrt{\frac{2}{\pi kr}} e^{-kr} \rightarrow 0 \quad (119)$$

which means that the evanescent waves do not contribute to the far field. Thus, eqn. (17) gives

$$\lim_{r \rightarrow \infty} W^{\text{scr}} = \sum_{n=-\infty}^{\infty} B_n^p H_n(kr) e^{in\theta} = \sqrt{\frac{2}{\pi kr}} e^{i(kr-\pi/4)} \sum_{n=-\infty}^{\infty} B_n^p \hat{i}^{-n} e^{in\theta} \quad (120)$$

Thus,

$$f(\theta) = \frac{2}{\sqrt{\pi k}} \sum_{n=-\infty}^{\infty} B_n^p \hat{i}^{-n} e^{in\theta} \quad (121)$$

The scattering cross section can be calculated as (Norris & Vemula, 1995)

$$\sigma = \frac{1}{2} \int_0^{2\pi} |f(\theta)|^2 d\theta \quad (122)$$

In the mean time, the *optical theorem* for the flural wave is (Norris & Vemula, 1995)

$$\sigma = -2\sqrt{\frac{\pi}{k}} \mathfrak{I}\{f(0)\} \quad (123)$$

which is the consequence of the energy flux conservation in the far-field. Thus, combining the above two equations gives the following identity that is equivalent to the energy flux conservation:

$$\int_0^{2\pi} |f(\theta)|^2 d\theta + 4\sqrt{\frac{\pi}{k}} \mathfrak{I}\{f(0)\} = 0 \quad (124)$$

For a single scatterer problem, the integration in eqn. (122) gives

$$\begin{aligned} \sigma &= \frac{1}{2} \int_0^{2\pi} f(\theta) \bar{f}(\theta) d\theta = \frac{1}{2} \frac{4}{\pi k} \int_0^{2\pi} \left(\sum_{n=-\infty}^{\infty} B_n^p \hat{i}^{-n} e^{in\theta} \right) \left(\sum_{m=-\infty}^{\infty} \bar{B}_m^p \hat{i}^m e^{-im\theta} \right) d\theta \\ &= \frac{2}{\pi k} \int_0^{2\pi} \sum_{n=-\infty}^{\infty} \sum_{m=-\infty}^{\infty} B_n^p \bar{B}_m^p \hat{i}^{m-n} e^{i(n-m)\theta} d\theta \\ &= \frac{2}{\pi k} \sum_{n=-\infty}^{\infty} B_n^p \bar{B}_n^p 2\pi = \frac{4}{k} \sum_{n=-\infty}^{\infty} |B_n^p|^2 \end{aligned} \quad (125)$$

where when expanding the two summations, noting that

$$\int_0^{2\pi} e^{i(n-m)\theta} d\theta = \begin{cases} 2\pi & \text{when } m = n \\ 0 & \text{when } m \neq n \end{cases} \quad (126)$$

On the other hand, the evaluation of eqn. (123) gives

$$\sigma = -2\sqrt{\frac{\pi}{\pi}} \frac{2}{\sqrt{\pi k}} \sum_{n=-\infty}^{\infty} \Re \{B_n^p \hat{i}^{-n}\} = -\frac{4}{k} \sum_{n=-\infty}^{\infty} \Re \{B_n^p \hat{i}^{-n}\} \quad (127)$$

Comparing the above results we have

$$\sum_{n=-\infty}^{\infty} (|B_n^p|^2 + \Re \{B_n^p \hat{i}^{-n}\}) = 0 \quad (128)$$

For the multiple scattering problem, the optical theorem is still valid. Thus, the equivalent validation in eqn. (124) remains valid. It boils down to computing the scattering form factor. One approach is to perform a similar “scatterer polymerization” scheme to turn the scatterer ensemble into one abstract scatterer. Alternatively, it can be performed numerically. In the numerical computations, the evanescent mode can be neglected.

Appendix A. Definitions for \mathcal{C} -Functions

A.1 For Propagating Waves

Consider a serial expression for a deflection is expressed as

$$W(r) = \sum_{n=-\infty}^{\infty} \alpha_n \mathcal{C}_n(kr) e^{in\theta} \quad (A.1)$$

where $\mathcal{C}_n(z)$ the either $J_n(z)$ or $H_n(z)$, and $z = kr$ will be used as an abbreviation.

Recall that in a polar coordinate system,

$$\nabla^2 W = \frac{\partial^2 W}{\partial r^2} + \frac{1}{r} \frac{\partial W}{\partial r} + \frac{1}{r^2} \frac{\partial^2 W}{\partial \theta^2} \quad (A.2)$$

and

$$\frac{1}{r} \frac{\partial W}{\partial r} = \frac{k}{r} \sum_{n=-\infty}^{\infty} \alpha_n \mathcal{C}'_n(kr) e^{in\theta} = z \sum_{n=-\infty}^{\infty} \frac{\alpha_n}{r^2} \mathcal{C}'_n(kr) e^{in\theta} \quad (A.3)$$

$$\frac{1}{r^2} \frac{\partial^2 W}{\partial \theta^2} = - \sum_{n=-\infty}^{\infty} n^2 \frac{\alpha_n}{r^2} \mathcal{C}_n(z) e^{in\theta} \quad (A.4)$$

Then,

$$\nabla^2 W = \frac{\partial^2 W}{\partial r^2} + \sum_{n=-\infty}^{\infty} \frac{\alpha_n}{r^2} [z \mathcal{C}'_n(z) - n^2 \mathcal{C}_n(z)] e^{in\theta} \quad (A.5)$$

On the other hand, W satisfies the Helmholtz equation, that is

$$\nabla^2 W = -k^2 W = -k^2 \sum_{n=-\infty}^{\infty} \alpha_n \mathcal{C}_n(kr) e^{in\theta} = -z^2 \sum_{n=-\infty}^{\infty} \frac{\alpha_n}{r^2} \mathcal{C}_n(z) e^{in\theta} \quad (\text{A.6})$$

Combined, they give

$$\frac{\partial^2 W}{\partial r^2} = \sum_{n=-\infty}^{\infty} \frac{\alpha_n}{r^2} [-z \mathcal{C}'_n(z) + (n^2 - z^2) \mathcal{C}_n(z)] e^{in\theta} \quad (\text{A.7})$$

Thus, following the definition for M_r , M_θ and V_r ,

$$\begin{aligned} M_r &= -D \left[\nu \nabla^2 W + (1 - \nu) \frac{\partial^2 W}{\partial r^2} \right] \\ &= -D \sum_{n=-\infty}^{\infty} \frac{\alpha_n}{r^2} [-\nu z^2 \mathcal{C}_n(z) - (1 - \nu) z \mathcal{C}'_n(z) + (1 - \nu)(n^2 - z^2) \mathcal{C}_n(z)] e^{in\theta} \\ &= -D \sum_{n=-\infty}^{\infty} \frac{\alpha_n}{r^2} \{ -(1 - \nu) z \mathcal{C}'_n(z) + [(1 - \nu)n^2 - z^2] \mathcal{C}_n(z) \} e^{in\theta} \end{aligned} \quad (\text{A.8})$$

$$\begin{aligned} M_\theta &= -D \left[\nabla^2 W - (1 - \nu) \frac{\partial^2 W}{\partial r^2} \right] \\ &= -D \sum_{n=-\infty}^{\infty} \frac{\alpha_n}{r^2} [-z^2 \mathcal{C}_n(z) + (1 - \nu) z \mathcal{C}'_n(z) - (1 - \nu)(n^2 - z^2) \mathcal{C}_n(z)] e^{in\theta} \\ &= -D \sum_{n=-\infty}^{\infty} \frac{\alpha_n}{r^2} \{ (1 - \nu) z \mathcal{C}'_n(z) - [(1 - \nu)n^2 + \nu z^2] \mathcal{C}_n(z) \} e^{in\theta} \end{aligned} \quad (\text{A.9})$$

$$\begin{aligned} V_r &= Q_r - \frac{1}{r} \frac{\partial M_{r\theta}}{\partial \theta} \\ &= -D \left[\frac{\partial}{\partial r} (\nabla^2 W) + \frac{1 - \nu}{r} \frac{\partial^2}{\partial r \partial \theta} \left(\frac{1}{r} \frac{\partial W}{\partial \theta} \right) \right] \\ &= -D \left[\frac{\partial}{\partial r} (\nabla^2 W) + \frac{1 - \nu}{r} \left(-\frac{1}{r^2} \frac{\partial^2 W}{\partial \theta^2} + \frac{1}{r} \frac{\partial^3 W}{\partial r \partial \theta^2} \right) \right] \end{aligned} \quad (\text{A.10})$$

Since

$$\frac{\partial}{\partial r} (\nabla^2 W) = -k^2 \frac{\partial}{\partial r} \left(\sum_{n=-\infty}^{\infty} \alpha_n \mathcal{C}_n(kr) e^{in\theta} \right) = -z^3 \sum_{n=-\infty}^{\infty} \frac{\alpha_n}{r^3} \mathcal{C}'_n(z) e^{in\theta} \quad (\text{A.11})$$

$$\frac{\partial^3 W}{\partial r \partial \theta^2} = -n^2 k \sum_{n=-\infty}^{\infty} \alpha_n \mathcal{C}'_n(kr) e^{in\theta} = -n^2 \frac{z}{r} \sum_{n=-\infty}^{\infty} \alpha_n \mathcal{C}'_n(z) e^{in\theta} \quad (\text{A.12})$$

Then,

$$\begin{aligned}
V_r &= -\frac{D}{r^3} \sum_{n=-\infty}^{\infty} \alpha_n \left[-z^3 \mathcal{C}'_n(z) - (1-\nu)(-n^2) \mathcal{C}_n(z) + (1-\nu)(-n^2 z) \mathcal{C}'_n(z) \right] e^{in\theta} \\
&= -\frac{D}{r^3} \sum_{n=-\infty}^{\infty} \alpha_n \left\{ -[(1-\nu)n^2 + z^2] z \mathcal{C}'_n(z) + (1-\nu)n^2 \mathcal{C}_n(z) \right\} e^{in\theta} \quad (\text{A.13})
\end{aligned}$$

A.2 For Evanescent Waves

Consider a serial expression for an evanescent wave as

$$W(r) = \sum_{n=-\infty}^{\infty} \alpha_n \mathcal{Z}_n(kr) e^{in\theta} \quad (\text{A.14})$$

where $\mathcal{Z}_n(z)$ is either $I_n(z)$ or $K_n(z)$. The evanescent wave satisfies the modified Helmholtz equation, as

$$\nabla^2 W = k^2 W = z^2 \sum_{n=-\infty}^{\infty} \frac{\alpha_n}{r^2} \mathcal{Z}_n(kr) e^{in\theta} \quad (\text{A.15})$$

Thus, other components are as the following

$$\frac{1}{r} \frac{\partial W}{\partial r} = \frac{z}{r^2} \sum_{n=-\infty}^{\infty} \alpha_n \mathcal{Z}'_n(kr) e^{in\theta} \quad (\text{A.16})$$

$$\frac{\partial^2 W}{\partial \theta^2} = - \sum_{n=-\infty}^{\infty} n^2 \alpha_n \mathcal{Z}_n(z) e^{in\theta} \quad (\text{A.17})$$

$$\frac{\partial^2 W}{\partial r^2} = \sum_{n=-\infty}^{\infty} \frac{\alpha_n}{r^2} \left[-z \mathcal{Z}'_n(z) + (n^2 + z^2) \mathcal{Z}_n(z) \right] e^{in\theta} \quad (\text{A.18})$$

$$\frac{\partial}{\partial r} (\nabla^2 W) = z^3 \sum_{n=-\infty}^{\infty} \frac{\alpha_n}{r^3} \mathcal{Z}'_n(z) e^{in\theta} \quad (\text{A.19})$$

$$\frac{\partial^3 W}{\partial r \partial \theta^2} = -n^2 \frac{z}{r} \sum_{n=-\infty}^{\infty} \alpha_n \mathcal{Z}'_n(z) e^{in\theta} \quad (\text{A.20})$$

Thus, following the definition for M_r , M_θ and V_r ,

$$\begin{aligned}
M_r &= -D \left[\nu \nabla^2 W + (1-\nu) \frac{\partial^2 W}{\partial r^2} \right] \\
&= -D \sum_{n=-\infty}^{\infty} \frac{\alpha_n}{r^2} \left[\nu z^2 \mathcal{Z}_n(z) - (1-\nu) z \mathcal{Z}'_n(z) + (1-\nu)(n^2 + z^2) \mathcal{Z}_n(z) \right] e^{in\theta} \\
&= -D \sum_{n=-\infty}^{\infty} \frac{\alpha_n}{r^2} \left\{ -(1-\nu) z \mathcal{Z}'_n(z) + [(1-\nu)n^2 + z^2] \mathcal{Z}_n(kr) \right\} e^{in\theta} \quad (\text{A.21})
\end{aligned}$$

$$\begin{aligned}
M_\theta &= -D \left[\nabla^2 W - (1 - \nu) \frac{\partial^2 W}{\partial r^2} \right] \\
&= -D \sum_{n=-\infty}^{\infty} \frac{\alpha_n}{r^2} \left[z^2 \mathcal{Z}_n(z) + (1 - \nu) z \mathcal{Z}'_n(z) - (1 - \nu)(n^2 + z^2) \mathcal{Z}_n(z) \right] e^{in\theta} \\
&= -D \sum_{n=-\infty}^{\infty} \frac{\alpha_n}{r^2} \left\{ (1 - \nu) z \mathcal{Z}'_n(z) - [(1 - \nu)n^2 - \nu z^2] \mathcal{Z}_n(z) \right\} e^{in\theta} \quad (\text{A.22})
\end{aligned}$$

$$\begin{aligned}
V_r &= -D \left[\frac{\partial}{\partial r} (\nabla^2 W) + \frac{1 - \nu}{r} \left(-\frac{1}{r^2} \frac{\partial^2 W}{\partial \theta^2} + \frac{1}{r} \frac{\partial^3 W}{\partial r \partial \theta^2} \right) \right] \\
&= -\frac{D}{r^3} \sum_{n=-\infty}^{\infty} \alpha_n \left[z^3 \mathcal{Z}'_n(z) - (1 - \nu)(-n^2) \mathcal{Z}_n(z) + (1 - \nu)(-n^2 z) \mathcal{Z}'_n(z) \right] e^{in\theta} \\
&= -\frac{D}{r^3} \sum_{n=-\infty}^{\infty} \alpha_n \left\{ -[(1 - \nu)n^2 - z^2] z \mathcal{Z}'_n(z) + (1 - \nu)n^2 \mathcal{Z}_n(z) \right\} e^{in\theta} \quad (\text{A.23})
\end{aligned}$$

A.3 Unified Notation and Definitions for \mathfrak{E} -Functions

In a unified notation, using $\mathcal{Z}_n^t(\cdot)$ to represent any of Bessel functions. Specifically,

$$\mathcal{Z}_n^1(\cdot) = J_n(\cdot) \quad \mathcal{Z}_n^2(\cdot) = H_n(\cdot) \quad \mathcal{Z}_n^3(\cdot) = I_n(\cdot) \quad \mathcal{Z}_n^4(\cdot) = K_n(\cdot)$$

If a displacement is expressible as

$$W(r) = \sum_{n=-\infty}^{\infty} \alpha_n \mathcal{Z}_n^t(kr) e^{in\theta} \quad (\text{A.24})$$

Then, the resulting moments and shear force can be expressed by a series of \mathfrak{E} -functions such as

$$M_r = -\frac{1}{r^2} \sum_{n=-\infty}^{\infty} \alpha_n \mathfrak{E}_1^t(n, kr) e^{in\theta} \quad (\text{A.25})$$

$$M_\theta = -\frac{1}{r^2} \sum_{n=-\infty}^{\infty} \alpha_n \mathfrak{E}_2^t(n, kr) e^{in\theta} \quad (\text{A.26})$$

$$V_r = -\frac{1}{r^3} \sum_{n=-\infty}^{\infty} \alpha_n \mathfrak{E}_3^t(n, kr) e^{in\theta} \quad (\text{A.27})$$

These \mathfrak{E} -functions are defined as

$$\mathfrak{E}_1^t(n, z) = D \left\{ -(1 - \nu) z \mathcal{Z}_n^{t'}(z) + [(1 - \nu)n^2 \mp z^2] \mathcal{Z}_n^t(z) \right\} \quad (\text{A.28})$$

$$\mathfrak{E}_2^t(n, z) = D \left\{ (1 - \nu) z \mathcal{Z}_n^{t'}(z) - [(1 - \nu)n^2 \pm \nu z^2] \mathcal{Z}_n^t(z) \right\} \quad (\text{A.29})$$

$$\mathfrak{E}_3^t(n, z) = D \left\{ -[(1 - \nu)n^2 \pm z^2] z \mathcal{Z}_n^{t'}(z) + (1 - \nu)n^2 \mathcal{Z}_n^t(z) \right\} \quad (\text{A.30})$$

where the upper sign in front of z^2 is taken when $t = 1$ or 2 , and the lower sign is taken when $t = 3$ or 4 .

REPORT DOCUMENTATION PAGE			Form Approved OMB No. 0704-0188		
<p>The public reporting burden for this collection of information is estimated to average 1 hour per response, including the time for reviewing instructions, searching existing data sources, gathering and maintaining the data needed, and completing and reviewing the collection of information. Send comments regarding this burden estimate or any other aspect of this collection of information, including suggestions for reducing this burden, to Department of Defense, Washington Headquarters Services, Directorate for Information Operations and Reports (0704-0188), 1215 Jefferson Davis Highway, Suite 1204, Arlington, VA 22202-4302. Respondents should be aware that notwithstanding any other provision of law, no person shall be subject to any penalty for failing to comply with a collection of information if it does not display a currently valid OMB control number.</p> <p>PLEASE DO NOT RETURN YOUR FORM TO THE ABOVE ADDRESS.</p>					
1. REPORT DATE (DD-MM-YYYY) 01-07-2015		2. REPORT TYPE Contractor Report		3. DATES COVERED (From - To)	
4. TITLE AND SUBTITLE Acoustically Tailored Composite Rotorcraft Fuselage Panels			5a. CONTRACT NUMBER		
			5b. GRANT NUMBER		
			5c. PROGRAM ELEMENT NUMBER		
6. AUTHOR(S) Hambric, Stephen; Shepherd, Micah; Koudela, Kevin; Wess, Dennis; Snider, Royce; May, Carl; Kendrick, Phil; Lee, Edward; Cai, Liang-Wu			5d. PROJECT NUMBER		
			5e. TASK NUMBER NNL11AA02C		
			5f. WORK UNIT NUMBER 664817.02.07.03.02.02		
7. PERFORMING ORGANIZATION NAME(S) AND ADDRESS(ES) NASA Langley Research Center Hampton, Virginia 23681-2199			8. PERFORMING ORGANIZATION REPORT NUMBER		
9. SPONSORING/MONITORING AGENCY NAME(S) AND ADDRESS(ES) National Aeronautics and Space Administration Washington, DC 20546-0001			10. SPONSOR/MONITOR'S ACRONYM(S) NASA		
			11. SPONSOR/MONITOR'S REPORT NUMBER(S) NASA/CR-2015-218769		
12. DISTRIBUTION/AVAILABILITY STATEMENT Unclassified Subject Category 71 Availability: NASA STI Program (757) 864-9658					
13. SUPPLEMENTARY NOTES FINAL REPORT Langley Technical Monitor: Noah H. Schiller					
14. ABSTRACT A rotorcraft roof sandwich panel has been redesigned to optimize sound power transmission loss (TL) and minimize structure-borne sound for frequencies between 1 and 4 kHz where gear meshing noise from the transmission has the most impact on speech intelligibility. The roof section, framed by a grid of ribs, was originally constructed of a single honeycomb core/composite facesheet panel. The original panel has coincidence frequencies near 700 Hz, leading to poor TL across the frequency range of 1 to 4 kHz. To quiet the panel, the cross section was split into two thinner sandwich subpanels separated by an air gap. The air gap was sized to target the fundamental mass-spring-mass resonance of the double panel system to less than 500 Hz. The panels were designed to withstand structural loading from normal rotorcraft operation, as well as 'man-on-the-roof' static loads experienced during maintenance operations. Thin layers of VHB 9469 viscoelastomer from 3M were also included in the facesheet ply layups, increasing panel damping loss factors from about 0.01 to 0.05. Measurements in the NASA SALT facility show the optimized panel provides 6-11 dB of acoustic transmission loss improvement, and 6-15 dB of structure-borne sound reduction at critical rotorcraft transmission tonal frequencies. Analytic panel TL theory simulates the measured performance quite well. Detailed finite element/boundary element modeling of the baseline panel simulates TL slightly more accurately, and also simulates structure-borne sound well.					
15. SUBJECT TERMS Composite structures; Finite element method; Gap; Honeycomb cores; Noise reduction; Roof; Rotary wing aircraft; Sound transmission					
16. SECURITY CLASSIFICATION OF:			17. LIMITATION OF ABSTRACT	18. NUMBER OF PAGES	19a. NAME OF RESPONSIBLE PERSON
a. REPORT	b. ABSTRACT	c. THIS PAGE			STI Help Desk (email: help@sti.nasa.gov)
U	U	U	UU	160	19b. TELEPHONE NUMBER (Include area code) (757) 864-9658